"AN EXPERIMENTAL INVESTIGATION OF THE BLADE-VORTEX INTERACTION PHENOMENON USING A SINGLE-BLADE NON-LIFTING ROTOR"

A Thesis
Submitted to the Faculty of Engineering
for the Fulfilment of the
Requirements for the Degree
of

Doctor of Philosophy, (Ph.D.)

by

Efstratios Saliveros, B.Sc., M.Sc.

University of Glasgow
Department of Aerospace Engineering
James Watt Building
Glasgow G12 8QQ

June 1991

"In Memory of my dearest cousin Michael"

"Στην Μνημην του αγαπημενου μου ξαδελφου Μιχαλη"

Preface

The work described in this Dissertation was carried out by the author at the Department of Aerospace Engineering, University of Glasgow, between October 1987, and September 1990, and is original in content except where otherwise stated.

University of Glasgow
Department of Aerospace Engineering
James Watt Building
Glasgow G12 8QQ
Scotland

E. Saliveros, B.Sc.,M.Sc.

June 1991

Abstract

This dissertation describes an experimental investigation of the blade-vortex interaction (BVI) phenomenon conducted at the University of Glasgow, Scotland, using a single blade, non-lifting rotor. The vortex is generated by a fixed split-wing mounted vertically upstream of the rotor disc and five circulatory vortex strengths are considered; 1.10, 2.20, 3.40, 5.10 and 6.70m^2/s. The rotor blade is instrumented with highly sensitive miniature pressure transducers which assist in measuring time-dependent surface pressures as the blade passes through or very close to the vortex. Numerous "Parallel" BVI tests are carried out by altering the geometry of the test set-up in order to study the effects of blade-vortex proximity (Y_v/c), circulatory vortex strength (Γ) and blade-radial variations (r/R). "Oblique" BVI tests are also performed, though of a much lesser extent, using similar test set-ups but for a vortex strength of 6.70m^2/s. The blade-vortex proximity distance varied between $\pm$1.00, at an increment of 0.20, whereas the blade span position ranged between 0.62R and 0.94R, at an increment of 0.08R. The large variety of test conditions and the vast amount of data collected in the present study can be described as one of the most comprehensive tests for the investigation of the BVI problem in the controlled environment of a wind tunnel.

In addition to obtaining details of the chordwise pressure variations, the pressures are integrated using a simple Trapezoidal Rule Method to obtain the unsteady rotor section aerodynamic coefficients, namely C_n, $C_{mc/4}$, and C_t. Generally, the qualitative features observed during the blade-vortex interactions are similar to those documented by other researchers. It is found that when the vortex is within one chord length from the blade leading and trailing edges, the most dominant feature is the leading edge pressure pulse, mainly affecting a large portion of the forward chord ($\approx$30%). The magnitudes of the pressure coefficients and consequently those of the airloading coefficients are shown to depend primarily upon the vortex strength and blade-vortex miss distances. It is also observed from pressure distribution data that for

close blade-vortex encounters the vortex either follows the aerofoil contour or being sliced into two smaller vortices during head-on collisions. Finally, the nominal blade section pressures and integrated airloads are compared with existing data obtained either by various numerical methods or from similar wind tunnel facilities, rotary or two-dimensional.

Erratum

The pressure coefficient data presented in this dissertation are subject to an error caused by the inadvertent subtraction of the velocity component due to the blade rotation from the resultant velocity. This apparently occurred during the transducer offset recording process.

Whilst this significantly changes the appearance of the Cp distributions and the magnitude of the force coefficients obtained, it is the opinion of the board of examiners that it in no way alters the conclusions reached on the nature and behaviour of the fundamental flow phenomena which form the basis of this thesis.

Acknowledgements

I wish to express my profound gratitude to my supervisor Dr. R.A.McD. Galbraith for his encouragement, guidance, support and valuable advice and assistance throughout this project and during my undergraduate and postgraduate years at the University of Glasgow.

I owe many special thanks to Drs. A. Kokkalis, A.J. Niven, F.N. Coton, R.B. Green and Messrs. M.B. Horner and R.D. Gordon for their advice, assistance and useful suggestions and comments during the course of this work. The help and advice of Mrs. Elizabeth Leitch during the computational part of this work is gratefully acknowledged.

I would like to thank the technicians, Messrs. Robert Gilmour and Anthony Smedley, for their efforts and goodwill that they have shown to me and for their assistance during the experimental part of the project. Special praise goes to Mr. Gilmour for his excellent job of rebuilding the amplification system. The efforts of the staff of the Photographic Department for developing the pictures that appear in this work are highly appreciated.

I am also grateful to the Royal Aerospace Establishment (R.A.E.), Farnborough, England, for providing the finance of this work under the British Ministry of Defence Research Grant 2048/54.

Finally, I would like to thank my parents Ioannis and Vassiliki and my brothers Vassilis and Antonis for their tremendous support and encouragement that they have given me throughout my life. To my wife Catherine, I extend my thanks for the continuous love, patience and understanding that she has shown during my studies at university and for proof reading this dissertation.

List of Contents

List of Tables

List of Figures

Nomenclature

A	Area, mm^2
AR	Aspect Ratio, R/c
b	Semispan Length, mm
c	Rotor Blade Chord Length, mm
c_v	Chord Length of the Vortex Generator Wing, mm
$C_{m\ le}$	Leading Edge Pitching Moment Coefficient, $2M_{le} / q_{tip}S$
$C_{mc/4}$	Quarter Chord Pitching Moment Coefficient, $2M / q_{tip}S$
$\Delta C_{mc/4}$	Differential Quarter Chord Pitching Moment Coefficient
C_{lv}	Non-dimensionalised Vortex Strength, $2\Gamma/cV_l$
C_n	Normal Force Coefficient, $2N / q_{tip}S$
$dC_n/d(X_v/c)$	Slope of Normal Force Coefficient Variation with Blade-Vortex Chordal Intervals
ΔC_n	Differential Normal Force Coefficient
C_p	Pressure Coefficient, $2P / q_{tip}$
C_t	Pressure Drag Coefficient, $2T / q_{tip}\ S$
d_v	Vortex Core Diameter, mm
d_v/c_v	Vortex Core Diameter to Vortex Generator Chord Ratio
M_{le}	Section Leading Edge Pitching Moment, Nm
M	Section Quarter Chord Pitching Moment, Nm
M_l	Local Mach Number
M_t	Tip Mach Number
M_∞	Freestream Mach Number
N	Section Normal Force, N/m^2
P	Surface Pressure, N/m^2

q_{tip}	Dynamic Pressure Based on Blade Tip Velocity, $(1/2)\rho V_{tip}^2$ (N/m^2)
r	Spanwise Distance Along the Rotor Blade, mm
R	Radial Distance to the Rotor Tip, mm
Re_t	Reynolds Number Based on Blade Tip Velocity, $\rho V_t c/\mu$
Re_c	Reynolds Number Based on Aerofoil Chord, $\rho V_\infty c/\mu$
S	Wing Area, Ac (mm^2)
t	Time, sec
Δt	Differential Time, sec
T	Section Chordal Force or Pressure Drag, N/m^2
V_∞	Free Stream Velocity, m/s
V_l	Local Blade Velocity, m/s
V_{tip}	Rotational Blade Tip Velocity, m/s
V_r	Blade Velocity at Radial Distance r, m/s
x	Chordwise Coordinate
X_v	Shortest Longitudinal Distance from Rotor Leading Edge to the Vortex Center, mm
X_v/c	Blade-Vortex Longitudinal Distance to the Rotor Chord Ratio
y	Distance Along the Length of a Semispan Wing in the Direction from Root to Tip, mm
Y_v	Vertical Separation Distance from Rotor Plane of Rotation to the Vortex Path Line, mm
Y_v/c	Blade/Vortex Vertical Separation Distance to the Rotor Chord Ratio
Z_v	Lateral Separation Distance from Rotor Axes of Rotation to the Vortex Path Line, mm
Z_v/c	Blade/Vortex Lateral Separation Distance to the Rotor Chord Ratio

Greek Symbols

α	Angle of incidence
γ_s	shed vorticity
γ_t	trailed vorticity
Γ	Vortex Strength, m^2/s
δ	Vortex Generator Differential Angle of Incidence, Deg.
Δ	Increment
Λ	Blade-Vortex Intersection Angle, Deg.
μ	Coefficient of Viscosity, Kg/ms, or Rotor Advance Ratio, $V_\infty/R\Omega$
ν	Kinematic Viscosity, ρ/μ (m^2/s)
ρ	Wind Tunnel Air Density, Kg/m^3
Ψ	Rotor Azimuthal Angle, Deg.
Ω	Rotor Rotational Speed, rad/sec

Subscripts

max	Maximum
min	Minimum
v	Vortex

Chapter I

INTRODUCTION

1.1 INTRODUCTION

For the last twenty years the important problem of helicopter rotor aerodynamics and in particular that of blade-vortex interaction (B.V.I.) mechanism has been the focal interest of many researchers. The BVI mechanism can have a significant effect on the aerodynamic loading, aeroacoustics and aeroelasticity of helicopter rotor blades. Compressibility effects, due to high operating tip speeds, also play an important role on the performance of the rotor and add to the complexity of the BVI problem.

Generally, helicopter rotor blades during hover or in forward flight, generate a differential pressure field along their span which provides lift to support the helicopter's weight and supply the required forward thrust. When in motion, two distinct

concentrated vortices roll-up rapidly from the continuous vortex sheet left behind each blade, one at the tip and the other near the hub (Figure 1.1). The tip vortices remain rolled-up for long radial distances behind the blades until they decay, become unstable and finally disperse. The strength of the tip vortex has been found to be approximately equal to the maximum bound circulation of the blade [1] and the maximum tangential velocity induced by a tip vortex can be as high as 50% of the free-stream velocity [2]. The vortex on the inboard section of the blade is considerably weaker, more diffuse than the tip vortex and, in a multi-blade helicopter configuration, is carried down and away from the rotor by the inflow and free-stream. Hence, BVIs seldom occur under such conditions.

However, tip BVIs occur under certain flight conditions, including forward powered descent flight and steep turns with shallow descents. The rotor in such flight configurations, flies through its own shed wake. In such circumstances, the trailing vortex from a rotor blade comes into close proximity or actually collides with other rotor blades for a range of blade azimuth angles. These BVIs can occur over a short period and can produce sudden changes in local pressure or angle of attack or both. These events take place in a flow-field which is generally transonic, unsteady, viscous and three-dimensional and give rise to a sudden impulse or load fluctuations over a small spanwise portion of the blade. Such load fluctuations have been identified as being the major source of rotor higher harmonic loading, significantly affecting rotor and fuselage vibrations [3,4] and also causing operational fatigue problems in the rotor.

Apart from the unsteady loads, BVIs give also rise to an impulsive noise characterised by a highly annoying sound known as "blade-slap" [5,6]. At high

forward speeds "blade-slap" has been associated with the onset of compressibility effects on the advancing blade and the occurrence of local supersonic flow. The tip vortices travel in space in an epicycloid-type pattern, when viewed from above, and interact with either an advancing or a retreating blade or both at various blade azimuthal positions and spanwise stations. Tangler [7] showed, by using a "free-wake" computer code, that there are seven possible blade-vortex interactions (Figure 1.2). In the twin-blade rotor, shown in Figure 1.2, the advancing blade interacts with a clockwise (positive) tip vortex (cases 1-4), while the retreating blade interacts with an anticlockwise (negative) tip vortex (cases 5-7, see also Figure 1.3). BVIs range from the hover case (cases 1 and 5), where the tip vortex is normal to the following blade, to forward flight, when the tip vortex and blade are nearly parallel under certain conditions (cases 3 and 6). Intermediate interactions, i.e. oblique BVIs, occur in almost all cases in one way or another, at different intersection angles and spanwise locations. Hence, three possible types of BVI exist, namely normal, parallel and oblique. The intersection angle (Λ), defined as the angle between the vortex axis and the blade direction, as shown in Figure 1.4, during a normal BVI is equal to zero, while for a nearly parallel BVI is approximately equal to 90°. For an oblique BVI, however, it ranges between 0° and ±90°. The normal type is more likely to affect a small spanwise portion of the blade, whereas parallel, and to some extent oblique types, affect large spanwise areas and are more persistent than their normal counterpart.

As the retreating blade interacts with a negative tip vortex ($180° \geq \Psi \geq 360°$), an upwash effect is introduced over the aerofoil. The aerofoil responds to this upwash as though it is experiencing a rapid increase in the angle of attack. This leads to large pressure variation, particularly over the first 10% of the aerofoil chord (Figure 1.5, Ref. **8**). At 20% of the chord, very few pressure changes are noted. The pressure

level over the upper surface decreases, causing suction, whereas a similar pattern exists for the lower surface where pressure compression takes place [44]. These pressure variations lead to rapid aerodynamic load fluctuations on the blade. The opposite effect occurs when a positive tip vortex interacts with an advancing blade ($0° \geq \Psi \geq 360°$). The severity of the interactions, which affect the magnitudes of the pressure, loads and noise fluctuations has been known to depend on a number of BVI parameters. These parameters are:

a) The Strength of the Tip Vortex

b) The Core Size of the Tip Vortex

c) The Local Interaction Angle between the Blade and the Vortex Line and,

d) The Vertical Separation Height between the Vortex and the Blade [9].

Referring to Figure 1.3, the vertical separation height between the passing vortex and the aerofoil may vary with blade azimuth. When Y_V/c is large, the vortex passes the aerofoil vicinity well outside of the boundary layer around the aerofoil, and the circular shape of the vortex core remains intact. The trajectory of the vortex though is generally displaced due to the presence of the blade and effectively follows a streamline path, whereas blade influence on vortex trajectory decreases with increasing Y_V/c [10]. On the other hand, when Y_V/c is very small, the vortex passes along a path which is so close to the aerofoil that the vorticity contained in the vortex mixes with the vorticity in the boundary layer and the passing vortex is either severely distorted or broken into two or possibly more smaller vortices.

According to the values of the above four BVI parameters, the BVI problem can be divided into two categories; namely "weak" and "strong" interactions. "Weak"

interactions can be described as those in which the blade-vortex separation height is relatively large (i.e. Y_V greater or equal to 0.50c), the shape of the vortex core remains unchanged or the vortex strength and the BVI intersection angle are small. When the vortex collides head-on or passes at a close distance from the aerofoil or the values of the vortex strength and the intersection angle are large, the BVI can be classified as a "strong" interaction. In a "strong" interaction the vortex can be either distorted or split in two or smaller vortices [10,20,21].

1.2 EARLIER INVESTIGATIONS

As described in the above Section, the BVI phenomenon is very important for both the aerodynamics and aeroacoustics effects of helicopter blades. Although the increase and decrease in lift during interaction affects only a small portion of the blade span and is negligibly small when compared with the overall lift generated over the entire rotor disk, can have significant effects on the emission of unwanted and unpleasant impulsive noises [6,7]. Hence, the aerodynamics and aeroacoustics of the BVI are so closely coupled together that the one cannot be treated without considering the other. For this reason, several researchers have attempted to simulate the BVI mechanism by means of various theoretical and experimental methods. A detail review of these studies is presented in the following two Sections 1.2.1 and 1.2.2.

Although the codes for predicting load and pressure variations during a BVI have been largely successful, the requirement for experimental data still exists for the purposes of confirming and validating them. Obtaining such data however, can lead to problems as it is not easy to measure the vortex characteristics and location during

flight. In the controlled environment of a wind tunnel, however, the BVI phenomenon can be studied with relative ease, since the the strength and the location of the interacting vortex can easily be determined.

1.2.1 Theoretical Investigations

Researchers have attempted in the past to predict helicopter rotor performance in various flight configurations. Their attempts start as early as the mid-1920's with Gluert [**11**] who treated the wake influence on the rotor using the Momentum and Blade Element Theories. The resulting model led to simple algebraic equations for the calculation of the induced velocities at the rotor disc. With the induced velocities known, it was then possible to determine the effective angle of attack on each blade segment along the blade span. The resulting angle of attack was then used, in conjunction with tabulated lift, drag and pitching moment data to compute the rotor performance. This approach, classified as Blade Element Integral Method, proved to be very useful for determining total aircraft performance. It was unable though to compute accurately details of the rotor aerodynamic environment. Accurate prediction of these details was not possible before the introduction of high speed computers and therefore digital computing methods introduced during the 1960's.

Simons [**12**] has followed the theoretical approach of simulating the BVI encounter by implementing the lifting line theory. In his method he computed the circulation distribution along the wing span for different vortex locations with respect to the wing and also for different vortex core radii. The effect of BVI is described by two parameters, the blade-vortex separation height and the intensity of the striking vortex. It has been shown that for blade-vortex distances Y_V<0.75c the accuracy of the

method decreases enormously due to its inability to handle the existing viscous effects.

In contrast with Simons method, Johnson [13] applied the planar lifting surface theory to calculate the aerodynamic loads induced on an infinite aspect ratio wing in a subsonic, compressible freestream and a straight, infinitely long vortex at an arbitrary blade-vortex intersection angle. The distortion of the vortex by the flow field and the presence of the wing was not considered. A comparison of the aerodynamic loads calculated for a simplified blade-vortex configuration, using the lifting surface and lifting line theories, showed that the latter was much inferior for blade-vortex encounters closer than five chord lengths. By comparing also lifting surface theory data with experimental data obtained from a single blade rotor, good correlation was indicated when the vortex was not close to the rotor hub [14].

Since the above two methods were not accurate enough, and because BVIs produce unsteady blade loading and aerodynamic noise, knowledge of the interaction flow field has become a common necessity. For this reason several numerical algorithms have been introduced. These algorithms are based on the limiting case of the parallel BVI (Λ=90°) using Transonic Small-Disturbance (TSD), Euler, two-dimensional thin-layer Navier-Stokes and full potential equations. In order to evaluate the accuracy and the ease with which different numerical methods can be applied, several test cases have been calculated at subsonic and transonic flow conditions. The flow geometry is chosen to be simple and consists of a vortex fixed in space or convecting in a uniform free stream.

The TSD approximation to the velocity-potential equation provides the simplest and computationally most efficient approach to capture the essential features of

the BVI phenomena at high tip speeds. It is based upon the assumption of a thin aerofoil in an inviscid, isentropic fluid with a concentrated potential (irrotational) vortex superimposed on a uniform, nearly sonic, free stream. This approach however was proved to be deficient and misleading in the important region near the leading edge of the aerofoil, unless special precautions are taken, such as a correction of the local velocity near the leading edge region. Also it is less robust in coping with very strong vortices and extremely close blade-vortex encounters.

For strong BVIs, however, which are beyond the scope of the TSD assumptions, the problem may be tackled using a more comprehensive set of equations namely, the Euler and the Navier-Stokes equations. Current numerical algorithms for these equations that are used to compute the unsteady vortical flows encountered on helicopter rotors are frequently either inadequate or too costly for routine design analysis because of their large computer time and storage requirements. Numerical algorithms that are based on the Euler equations are suitable for any inviscid flow field simulation. But for flows dominated by viscous effects, the choice is limited to using the Navier-Stokes equations.

McCroskey and Goorjian **[15]** used the unsteady TSD theory to study the BVI problem. In their work, the flow field was considered to be a non-linear combination of the free stream, the velocity field associated with the passing vortex and, the disturbance velocity potential field. They demonstrated how the presence of the passing vortex produces rapid pressure variations on the aerofoil surface and consequently rapidly varying airloads. The results, however, were acknowledged to be inaccurate in the immediate vicinity of the leading edge region due to the extreme over-prediction of the pressure suctions and interactions using the TSD formulation

approach are therefore treated cautiously.

Caradonna et al [16] also made use of the unsteady transonic small disturbance theory to simulate the BVI phenomenon. Instead of using the velocity field to represent the passing vortex, they introduced a point vortex into the computational domain as the passing vortex. Caradonna et al's results are comparable to the results obtained by McCroskey et al [15] because these two approaches are equivalent.

George and Chang [48] have also used a formulation similar to that found in Reference 15. In contrast with the work described in References 15 and 16, they studied the effects of acoustic waves radiating away from the aerofoil into the far field.

In addition to the TSD approximation approach for modelling the BVI flow fields, Srinivasan [17] and Srinivasan et al [18,19] used the unsteady Euler equations and the thin-layer Navier-Stokes equations to study the blade-vortex interaction problem. They have shown that for weak interactions the results of the three computational methods were in good qualitative agreement. For stronger interactions, however, outside the scope of the TSD assumptions, the Navier-Stokes calculations showed a sizable boundary layer separation prior to and well after BVI has occurred. The main feature of the above methods was the tremendous influence of the vortex on the flowfield around the aerofoil generating a sharp suction peak in the pressure distributions in the leading edge region followed by a rapid compression-like wave when the interacting vortex was approximately within one chord upstream of the aerofoil leading edge.

None of the above mentioned methods, however, could handle the BVI cases

where the passing vortex collides head-on with a two-dimensional aerofoil and allows the vortex structure to convect, diffuse, deform or even break-up into smaller vortices during interaction. In the most recent theoretical investigations **[20,21]**, vortex distortion has been studied with very encouraging results.

Panaras **[20]** used the classical conformal transformation method for modelling a Joukowski aerofoil and a number of discrete vortices to simulate the interacting vortex. He showed that the amplitudes of the pressure pulses induced on the surface of the aerofoil and the distortion of the shape of the vortex were strongly related to the vortex vertical separation distance from the aerofoil and at head-on collisions, the vortex is shown to split into two smaller vortices (Figure. 1.6).

Similar results were also obtained by Lee et al **[21]** who studied the effects of vortex distortion during a blade-vortex encounter by using distributed discrete vortices and an adaptive panel distribution method. The flow is assumed to be two-dimensional, incompressible and inviscid. This method was then applied to study the effects of vortex strength and size, vortex-aerofoil separation position and aerofoil angle of attack. It is emphasised that significant distortion of the vortex structure and its trajectory can occur, especially during close and head-on blade-vortex collisions (Figure. 1.7). The amount of vortex distortion, however, was shown to be strongly depended on the strength and size of the vortex core and vortices with weaker strengths or larger sizes were more likely to split.

1.2.2 Experimental Investigations

For the investigation of the various types of BVI, i.e. parallel, normal or

oblique, and their effects on helicopter blades, several experimental studies have been conducted. These studies have taken place in either a closed and controlled environment of a wind tunnel or outdoors using full-scale size helicopters. Generally, the wind tunnel studies have included two- or three-dimensional setups, wherein the interacting vortex was generated upstream of the test model by means of

a) an angled untwisted semispan wing,

b) an aerofoil oscillating at constant pitch rate and,

c) an impulsively pitched aerofoil.

Although rare, other techniques, such as the air jet **[5]** and the shock tube configuration **[22]**, have also been used to generate the interacting vortex.

Furthermore, for improving the limited knowledge of the complex flow field around an aerofoil impinging with an on-coming vortex filament, has led to various flow visualisation and flow modelling investigations.

In the experimental flow visualisation studies only the two possible but extreme BVI cases were examined; a) the two-dimensional case, in which the vortex is parallel to the blade **[10,22]** and b) the three-dimensional case, in which the vortex is normal to the model aerofoil **[23,24]**. These studies presented detail information of the flow patterns and vortex behaviour during a BVI encounter by means of photographic records. It has been shown that the presence of the model aerofoil not only influences the distortion of the vortex at close encounters but, forces the vortex trajectory to follow a streamline path. The aerofoil's influence on the vortex trajectory being the strongest for small blade-vortex separation distances and the presence of the vortex causes premature stalling of the test aerofoil. In addition to the above results, it was observed that when the vortex collides with the aerofoil head-on ($Y_V/c=0.00$), the

vortex splits in two smaller vortices rotating in the same direction [23,24].

The results obtained in References 10 and 22 are in good agreement with those attained by Panaras [20] and Lee and Smith [21] who modelled the vortex behaviour during a two-dimensional BVI, as described above.

Experiments with an angled untwisted semispan wing, as the vortex generator positioned upstream of a two- or three-dimensional test model aerofoil are rather simple to conduct. The passing vortex interacts with the aerofoil perpendicularly and the test conditions are known to be nominally steady. The main disadvantage of this method is that the resulting flows are three-dimensional and extremely difficult to analyse theoretically. However, Seath [25], Ham [26] and Dunagan et al [27] have followed this approach for their pressure measurement investigations. Seath [25] and Ham [26] have shown that due to the presence of the vortex, sections of the wing in the upwash region experienced a decrease in pressure over the upper surface and an increase in the lower surface, while in the downwash region experienced the opposite effect. Dunagan et al [27] also describes similar observations in his work. Furthermore, they report that the lift coefficient, due to the pressure changes, was significantly affected, showing a loss not only close to the BVI location but also further inboard on the blade, when compared with data obtained without the presence of the vortex.

Other experiments have considered in greater detail the aerodynamics and the flow field structure of the parallel BVI problem. For the parallel BVI studies the generated vortex travels across the flow with its axis parallel to the leading edge of the test model. These experiments are known to be unsteady, difficult to conduct but much

easier to analyse theoretically, compared to the normal BVIs.

For some parallel BVI experiments an oscillating [28,29] or an impulsively pitched aerofoil [30], mounted upstream of the model, was utilised to create isolated vortices. These investigations revealed that, for various freestream velocities, vortex strengths and blade-vortex separation positions, the most dominant characteristic of the recorded pressure changes on both the upper and lower surfaces, was the large pressure pulses featured near the leading edge as the vortex passed over the model. The tests also showed that as the blade-vortex separation height was increased the pressure changes were reduced, and as the vortex strength was increased the pressure pulse near the leading edge of the model corespondingly increased.

In addition to the two methods described above an alternate approach was pioneered by Surendraiah [31]. He choose a rotary-wing environment for his investigation of the BVI phenomenon. The test set-up he employed featured a single instrumented rotating blade which interacts with, but does not generate the vortex in question. The rotor blade interacted with a vortex generated upstream of the rotor disc from a vertically mounted wing. He studied both parallel and oblique blade-vortex interaction types for the spanwise station of 0.95R. His tests were carried out for two different rotor speeds and vortex strengths and for a variety of blade-vortex separation height and intersection angles. The outcome of his investigation showed that by increasing the BVI intersection angle, the differential lift during interactions and its time variation also increased, reaching maximum values when the vortex was cut through its centre and was virtually parallel to the rotating blade (ie. Λ=90°). These parameters also increased in magnitude linearly with the vortex strength, while the rate of increase was largely depended on the rotor plane position, namely X_V.

The advantage of this approach has been well recognised since it offers the use of the same facility to study all possible BVI types by simply rearranging the vortex generator to different height and intersection angle settings. Good assessment and control of the vortex strength and trajectory are its most valuable features. Padakannaya [32], Ham [33], Caradonna and his colleagues [34-36] and Kokkalis [37] have all employed Surendraiah's approach.

Padakannaya's [32] work represents an extension of the work described by Surendraiah [31] and it involves parallel and oblique BVI measurements for the spanwise stations of 0.90R, 0.85R and 0.75R.

Ham [33] and Kokkalis [37] studied the effects of the perpendicular and parallel BVI encounters respectively by means of an instrumented rotating single-blade rotor interacting with a streamwise vortex, generated upstream of the rotor. Data were recorded for rotor plane positions above and below the vortex axis for the span stations 0.75R [33] and for 0.78R and 0.94R using five vortex strengths [37]. The BVI facility described in Reference 37 is the one which has been employed throughout the present investigation, details of which are presented in the following Chapter.

Caradonna et al [34] however used a twin-blade teetering rotor for the study of the parallel BVI problem. BVI encounters were recorded by means of 12 absolute miniature pressure transducers placed on one side of the blade. For the recording of both upper and lower surface pressure variations, the blade was turned over, with both the direction of the rotor and the vortex rotation reversed. Tests were performed for a variety of local Mach numbers, blade-vortex distances and vortex strengths. Similar investigations were also conducted by Caradonna et al [35,36] using the same facility

as in Reference **33**, but with parallel and oblique blade-vortex interactions in mind.

Neuwerth and Muller **[38]** also followed the technique of Surendraiah's and investigated a second type of perpendicular BVI encounter such that the vortex axes are normal to the rotor disc using a twin-blade rotor. Pressure data were recorded for two span stations (0.88R and 0.98R), three chordwise positions and a single vortex strength.

In the shock tube experiments **[22]** the two-dimensional vortices were generated by different vortex shedding cylinders in a stationary duct flow or by an aerofoil positioned upstream in the starting flow of the shock tube. In the air jet configuration **[5]**, however, the simulated vortex was generated by means of two air jets mounted one above and below a three-blade rotor disc and in a slightly offset position. The later investigation however dealt with measurements of sound pressure levels rather than detail chordwise or spanwise pressure measurements.

Other experiments have also dealt with the measurement of acoustic or chordwise and spanwise pressures using full-scale size helicopters instead of wind tunnel environments. Such experiments are very useful since they provide direct and real life information for validating numerous prediction codes employed to calculate helicopter impulsive noise, performance and blade aerodynamic loadings.

Scheiman and his colleagues **[3,39,40]** have tabulated both representative and critical helicopter rotor blade airloads measured in flight using a L-61-4196 helicopter instrumented with pressure transducers on one of its four rotor blades. A comparison of the experimental data with the predicted data, obtained from an

elementary uniform inflow theory, indicated discrepancies between the data near the intersection of the blade with the path of the preceding blade's tip vortex. This BVI produced not only large changes to the blade loading for various spanwise and azimuth angle locations but, affected also the vibratory blade loading. It generated harmonic blade loadings of all orders with large higher harmonics. It was also observed that the intensity of the BVI decreases with increasing forward speed.

Large airload pressure fluctuations caused by the interference of the tip vortices of the blade, were also measured in flight by Pruyn and Alexander **[41]**. It was noticed that section pressures were considerably different from those of a two-dimensional aerofoil over extended areas of the rotor disc, apparently because of combined compressibility effects and disturbances from tip vortex interference. It was also found that the influence of the tip vortex increased as the intersection angle approached 90°.

In-flight experiments were also carried out by Brotherhood et al **[42,43]** using a Puma helicopter as a test vehicle. Their work mostly involved detail chordwise and radial pressure measurements for the investigation of blade stall, influenced by the passage of the tip vortex generated from a preceding blade **[42]**. Helicopter rotor aerodynamic and structural load measurements were also obtained aiming for the validation of a prediction code for the computation of rotor loads and performance **[43]**.

Shockey et al **[8]** and Sakowski et al **[44]** used an instrumented AH-1G Cobra helicopter for their measurements. One of the helicopter's blades was modified to incorporate extensive instrumentation. In-flight aerodynamic, structural and

aeroacoustic data were recorded throughout a wide range of operational conditions. It was found that the BVI phenomenon, identified by the large pressure fluctuations, was concentrated close to the leading edge and in particular at the first 10% of the blade chord.

Numerous theoretical and experimental investigations have also dealt with the measuring of impulsive noises generated during a BVI encounter or due to compressibility effects at various helicopter rotor flight configurations. The reader interested in the aeroacoustic aspect of the problem is referred to References **5-7** and **44-52.**

1.3 SCOPE OF THE PRESENT STUDY

The main objective of the present study was to perform a sequence of experiments over a wide range of test conditions for the investigation of the BVI phenomenon. This work is part of the continuing research programme at the Aerospace Engineering Department of University of Glasgow, set to examine blade-vortex encounters using a recently constructed BVI rig **[37]**. In addition to this investigation, comparisons were made with existing data, obtained by other researchers using either computational or experimental techniques. It is hoped what was observed will be valuable to future analysts for validating BVI prediction codes or justifying any resemblances that might exist between the results obtained during the present study and future BVI investigations.

Pressure measurements were collected at five different blade-span positions for various vertical and lateral vortex displacements and vortex intensities. Both

parallel and to lesser extend oblique BVI types were examined. The values of the aerofoil loading coefficients (C_n, C_m, $C_{mc/4}$ and C_t), primarily due to the vortex interaction, were computed and served to study the aerodynamic behaviour of the NACA-0015 aerofoil under such unsteady flow conditions. An assessment of the pressure and vortex behaviour was also performed, particularly for close blade-vortex proximity heights ($-0.20c \leq Y_V \leq 0.20c$). It revealed that the most important observations were the large pressure pulses featured near the leading edge and the splitting of the vortex as it collided head-on with the rotating blade.

Furthermore, in the early stages of this investigation and prior to any data collection, improvements of the computer facilities and the voltage-pressure signal amplification system were required. The improvement of the computer facilities was carried out by replacing the old-fashioned, by today's computer standards DEC MINC PDP 11/23 computer with the modern IBM PS/2. Such a replacement was necessary because of the limited storage capacity offered by the MINC and its inability to handle large amounts of data quickly and efficiently. Modification of the voltage-pressure signal amplification system was also very important since the former system had the tendency of producing high levels of electronic noise and therefore increase the zero-pressure offset. Such an effect caused the operational range for some pressure transducers to be reduced.

1.4 OUTLINE OF DISSERTATION

In the first couple of Sections of this Chapter, a general background information of the blade-vortex interaction phenomenon and a review of earlier BVI investigations, theoretical and experimental, was presented. The main objective and

approach of the present investigation is described in Section 1.3, also presented in this Chapter.

In Chapter II, a detailed description of the University of Glasgow BVI facility is presented. It includes a description of pressure transducer installation and signal conditioning, data acquisition and computer system, as well as, the data acquisition and data reduction software used to execute the necessary computations.

Chapter III presents a detailed description of the experimental procedures used to perform the required blade-vortex interaction tests. A method for the calibration of the pressure transducers is also included.

In the subsequent Chapter, an analysis of selected pressure and aerodynamic load coefficient data, obtained from parallel blade-vortex interactions, is presented and discussed. The most salient features due to blade-vortex proximity, vortex strength and spanwise location are also presented.

In Chapter V, a comparison between the present and existing blade-vortex interaction data is presented, with the major differences and agreements being identified and discussed.

Conclusions arising from the results are summarised in Chapter VI. Several suggestions for further research on the blade-vortex interaction problem are recommended, including modifications of the current facility for studying different aerofoil sections and blade tip shapes.

Chapter II

EXPERIMENTAL APPARATUS

For the investigation of the blade-vortex interaction phenomenon, in the controlled environment of a wind tunnel, numerous tests were performed using the Aerospace Engineering Department's "Handley Page" wind tunnel facilities at the University of Glasgow. A rectangular, untwisted, non-lifting, single blade rotor of a NACA-0015 aerofoil section, instrumented with miniature pressure transducers, interacted with an on-coming vortex filament of various strengths at different blade/vortex positions and interaction angles. The generation of the vortex was obtained from a stationary wing set upstream of the rotor disc. The blade/vortex interactions that were under examination were of two distinct types; parallel and oblique. Amplifiers, slip-rings, comparators, filters and a THORN-EMI-BE256-420 transient data recording system were set in line before voltage-pressure signals were finally transferred to an IBM PS/2 computer system.

2.1 WIND TUNNEL FACILITIES

2.1.1 Wind Tunnel

All tests were conducted in the Aerospace Engineering Department's "Handley Page" low speed wind tunnel. This wind tunnel is an atmospheric-pressure closed-return suction type with an octagonal working section of 2.13m width and 1.61m height (Figures 2.1). Downstream of the working section there is a line of breather slots which serve to maintain the pressure in the tunnel at or near the atmospheric levels. For very short time intervals, the wind tunnel speed could be brought up to its maximum operational level of approx. 60m/s. Furthermore, for velocities below 48m/s the tunnel could be kept functioning for long periods without interruptions. During the present tests, however, the tunnel freestream velocity remained close to approx. 47.5 m/s. The reason for selecting the above velocity level was that it matched that described by Kokkalis [37] so that the magnitudes of the vortex strengths used in the present investigation also matched.

The measurement of the free stream dynamic pressure was performed by using an FC012 micromanometer with ranges of ±19.99mm and ±199.99mm H_2O. The accuracy of the micromanometer, calibrated by the manufacturers using precision water column manometers is 0.2% or 0.3% depending on range pressure. Its linearity is ±0.5% or ±1.0% and its output voltage signal is 0-5.0 VDC (see Reference **58**).

2.1.2 Rotor Configuration

The general configuration of the rotor included a single non-lifting,

rectangular rotor blade with balance weights and a rotor shaft, mounted vertically in the working section (Figure 2.2). The blade was made of Duralluminium type TF30 material and had a NACA-0015 aerofoil section for its profile. It had a chord length of 149mm and span of 942.6mm giving an aspect ratio of 6.3. The aerofoil's coordinates are listed in Table 1.

The blade was constructed from separate upper and lower parts and five removable aerofoil-shaped pods, each of 75x149mm in dimension. One of these pods was carefully grooved to accommodate 26 miniature pressure transducers at its mid-span position, as shown in Figure 2.3. Fifteen of these transducers were placed on the upper surface with the remaining eleven on the lower surface of the pod. The majority of the transducers were accommodated near the leading edge, where the largest pressure gradients were expected. Each transducer was connected to a pressure tapping on the aerofoil surface via a brass tube. The pressure tappings were staggered over the first 20.6% and 18.3% of the chord from the leading edge on the upper and lower surfaces respectively. Staggering the pressure tapping was deliberate to avoid any possible interference which might exist between upstream and downstream pressure tappings. The locations of each pressure transducer relevant to the aerofoil chord is shown in Figure 2.4.

The instrumented pod could be positioned at anyone of five non-dimensional spanwise stations, i.e. 0.62, 0.70, 0.78, 0.86 and 0.94. Once the transducers were installed and the spanwise position chosen, the blade was then assembled and fitted to the hub of the rotor where it was statically balanced and secured on the supporting structure. Diagrams illustrating the rotor supporting structures, placed above and below the wind tunnel working section and secured to the tunnel framework by

specially made brackets, are shown in Figures 2.5(a) and 2.5(b). Details of their construction and assembly, however, is given in Reference **37**. Rotational movement of the rotor was provided by means of a 1.5kW thyristor controlled D.C. motor transmitted via a 3:1 ratio reduction bevel gear.

Prior to setting up the rig configuration to its final position it was detected that the rotor shaft vibrated violently, especially at mid-position where the blade was mounted. Such vibrations were believed to have been transmitted to the blade and subsequently to the instrumentation pod giving pressure measurements with large amounts of unpleasant and uncontrolled errors. So, the rotor shaft had to be dismantled and remachined to the required standards.

2.1.3 Vortex Generator

The vortex which interacted with the rotating blade was created by means of a "differential" vortex generator wing, made-up of two adjoining NACA-0015 model aerofoil sections. The vortex generator was positioned seven chord lengths upstream of the rotor tip location when the rotor was at its 180° azimuthal position. It was aligned with the wind tunnel centre line and mounted vertically from floor to ceiling on two rotating circular steel turntables (Figure 2.6). The two NACA-0015 aerofoil sections, each of 150.0mm chord length and semispan of 750.0mm, were constructed of fibreglass, mounted on two separate aluminium spars and filled with epoxy resin foam. They were joined at the centre section at their quarter chord position by a steel "dowel-pin" aligned with the centre of the circular turntables allowing free rotational movement of the two sections. The required vortex was, therefore, obtained by setting the lower half at an angle of incidence equal and opposite to that of the upper half. The

end of each half, closest to the rotor disc plane, was divided in five equal pods of $0.2c_w$ width each. Furthermore, the pod closest to the rotor disc plane was split even further into two equal parts of $0.1c_w$ width each. By altering the vortex generator "differential" angle of incidence to different magnitudes, numerous vortex strengths could be obtained. The magnitudes of the vortex strengths used in the present study are similar to those used by Kokkalis [37], which were measured by means of a triple hot-wire anemometer. Variations of the vortex strengths with the vortex generator "differential" angle of incidence (δ) are shown in Figure 2.7, which also includes the vortex core diameter (d_v) against δ.

To indicate the relative position of the reference blade section with respect to the path of the oncoming vortex in either parallel and oblique BVIs three geometric parameters were used. The first parameter was the rotor azimuth angle "Ψ" measured between the blade's spanwise axis and the zero-azimuth direction (see Figure 2.8). The second parameter, more appropriate for two-dimensional simulations, represents the upstream (or downstream) distance "X_v" between the leading edge of the reference section and a line parallel to the vortex axis in the plane of rotation of the blade (see Figure 2.8). The +/- signs associated with the distance X_v are only intended to distinguish between instances where the vortex is located ahead (-) or behind (+) the leading edge of the reference blade section. The two parameters Ψ and X_v are geometrically related via a simple relation viz.,

$$X_v = (-1)[r\sin\Psi + (c/2)\cos\Psi \pm Z_v] \qquad (1)$$

or $$X_v/c = (-1)[(r/c)\sin\Psi + (1/2)\cos\Psi \pm Z_v/c] \qquad (2)$$

where the last part of the expression refers to the oblique BVIs and positive or negative

Z_V indicates interactions in the second or third quadrant respectively (see Figure 2.8).

The third parameter, the vertical displacement of the vortex (Y_V/c) with respect to the rotor disc plane, was achieved by rearranging the centre pod sections of the vortex generator so that the juncture moved higher or lower of the rotor disc plane. The outer blade/vortex separation height was one chord length above or below of the rotating blade. The above settings were adapted for all the parallel blade/vortex interactions carried out during this investigation. However, to achieve oblique interactions in the second or third azimuth quadrants, the vortex generator had to be repositioned to either the left or to the right of the tunnel centre line. The procedure for the oblique tests was similar to that of the parallel BVI test cases.

The present vortex generator configuration was the result of a feasibility study carried out by Kokkalis **[37]**. He discovered that the above arrangement will not only create a vortex which will be easy to govern, but its flight path in the tunnel will be almost independent of free stream velocity, "differential" angle of incidence and down stream distance. He explains that , although other vortex generator configurations were considered, such as of a single aerofoil mounted vertically from the tunnel ceiling, difficulties of measuring the vortex strength may have emerged, as other researchers had already found out **[59-61]**. Vortex meandering and interference due to the presence of the measuring triple hot-wire probe were the principal obstacles. To avoid similar problems, it was therefore decided that the most appropriate vortex generator arrangement for a BVI investigation would be the one described by Hoffman et al **[62]**. Smoke flow visualisation and pressure measurements confirmed that by using the Hoffman and Joubert vortex generator arrangement, the generated vortex had a well defined structure and trajectory and insertion of the measuring probe did not alter its

flight path or structure. The vortex generator arrangement, described in References **62** and **37**, is also the one being adapted in the current BVI investigation and explained in the above paragraphs.

2.2 *PRESSURE TRANSDUCERS*

To measure the chordwise pressure distribution around the aerofoil at the various instantaneous azimuthal blade positions, the blade was equipped with twenty six ultra miniature pressure transducers. The location of each pressure transducer, in respect to the aerofoil's chordwise co-ordinate, is shown in Figure 2.4. They are installed just underneath the aerofoil surface in a specially grooved aerofoil section pod (Figure 2.3).

Due to inadequate space between the pod surface and blade spar, the overall size of each transducer had to be as small as possible and the pod had to be machined with extreme care to avoid damaging the pod's outer surface. The transducers employed in the present study were of two types; KULITE-XCS-093-5-SG and ENTRAN-EPIL-80B-5S. All transducers were of the sealed gauged type with one side of the pressure sensitive diaphragm sealed to a reference pressure and fitted with a temperature compensation module, which reduced the change of zero offset and the sensitivity with temperature to a minimum. Their dimensions were 2.03mm in diameter and 9.8mm length for the ENTRAN type and 2.36mm diameter and 9.52mm length for the KULITE type. Each transducer was mounted very carefully in one of the meticulously machined grooves and connected to the aerofoil surface via a brass pipe of 0.813mm and 1.575mm inner and outer bore. The supporting link between transducer and brass pipe was provided by means of a rubber tube of 1.2mm inner bore and the

groove walls. The brass pipes were secured on the model by a special adhesive substance called "ARALDITE" epoxy resin. One end of the brass pipe was facing perpendicularly outwards to the edge of the aerofoil surface. The "ARALDITE" epoxy resin formed a remarkably strong bond between brass pipe and model and sealed any gaps which might have existed.

The present transducer mounting technique is superior to that described by Kokkalis [37] for the following three reasons. Firstly, it provides well sheltered transducers which are able to survive rough treatment during testing, i.e. blade vibrations and rotational acceleration. Secondly, to avoid registering pressure signals due to normal acceleration, the transducer diaphragms were placed in-line with the accelerating motion of the blade. Thirdly, it enables the replacement of damaged transducers easier and faster if required. Due to the secure mounting technique no damaged transducers were reported during the present investigation.

Immediately after the installation of the pressure transducers on to the rotor blade, the instrumented aerofoil pod was subjected to an external pressure of about ±1.5p.s.i. to inspect for possible faults or leaks. If the inspection was successful, calibration of the pressure sensors followed to check their linearity and sensitivity to air pressure. A typical calibration curve is illustrated in Figure 3.3. The output varies linearly with pressure, passing through the origin, independent of voltage excitation. The sensitivity varied in the range from 12mV/p.s.i. to 22mV/p.s.i. for different pressure transducers. Table 2 provides a list of all the pressure transducers used. It includes the type, sensitivity (at manufacture) and present calibrations in mV/p.s.i. of each transducer per radial span position. It is seen that for r/R=0.70 and 0.62 no sensitivity values are presented. Since the transducer sensitivity changes were

generally within 5% for the first three calibrations, it was decided to omit the calibration procedure for the remainder of the spanwise positions examined. The transducer sensitivity values for the last two spanwise cases were identical to those of r/R=0.78. Full description of the pressure transducer calibration procedure is provided in Chapter III, Section 3.1.1.

Power supply to the pressure sensors was provided by means of a 15V D.C. constant current passed through a set of gold-plated slip-rings. The wire leads of each transducer passed through the gap provided between the rear of the span and the trailing edge of the blade and terminated at the amplifiers' rack by a 4 by 32 D-plugs.

The offset drift of each transducer, although varied with time, was found to be in the range from ±1mV to ±10mV when powered-up. Once this offset drift rose to unacceptable levels it was nulled by means of a push button switch at the front panel of the comparators board rack, bringing the output back to zero.

2.3 AMPLIFIERS AND COMPARATORS

2.3.1 Signal Amplifiers

For each of the 26 pressure transducers installed in the rotor blade, a representative amplifier was built. The amplifiers served to condition and amplify the recorded low voltage signals due to aerodynamic pressure and to fully utilise the operational range of the A-to-D converter (±5.0V). A diagram illustrating the amplifier and the amplifier control circuits are presented in Figures 2.9 and 2.10. The present operational amplifiers have been redesigned and replaced those employed by Kokkalis

[37]. The redesigning of the old amplifiers was very important, since the former ones had the tendency to increase the zero-pressure offset with operational time to substantially high levels for the majority of the transducers. Such a rise reduced the operational range of the transducers in question and therefore affected the overall output signal.

Due to limited space in the amplifier rack, located to the lower end of the rotating frame, two amplifiers were incorporated in a single amplifier board (see Figure 2.11). The new boards manufactured and tested in the Aerospace Engineering Department Electronics Workshop, University of Glasgow, had to be made under certain guidelines. The most important of these guidelines was to reduce the electronic noise and the zero-pressure offset to a minimum and to have easy access for the alteration of the gains when required. The gain range of each amplifier was from 1 to 999. It could be adjusted with ease to fit the needs of each transducer so the voltage-pressure signals, recorded during testing, were amplified accordingly without causing possible system overrange (i.e. outside the range ±5.0V).

2.3.2 Voltage Comparators

The voltage signals, after being amplified, travelled from the rotating to the static environment, to a set of voltage comparators via gold-plated slip rings of Michigan Scientific SR36 type. Comparison of the input voltage signals with a standard voltage source of ±5.0V was very important, because the maximum input voltage to the A-to-D converter was fixed at ±5.1V. Therefore, temporary or even permanent damage of the A-to-D converter was prevented. The input voltage signals fed to the comparators were initially pre-filtered and post-filtered by anti-aliasing 2nd-

order Butterworth low-pass filters incorporated in the comparators circuit (Figure 2.12) before being transferred to the A-to-D converter. The use of these filters ensured that high frequencies beyond the fixed range of 7kHz at -3db set by the A-to-D converter were removed. If an input signal fed to the comparator circuit exceeded ±5.0V range, a digital switch (flip-flop) would be activated. A visual warning (via a red LED) would then be provided, indicating that system overrange had occurred. Corrective action then had to be taken by adjusting the amplifier's gain setting to lower levels. Such action was repeated until system overrange came to a halt, and the signal was then inside the permitted limits to be send to the A-to-D converter for digitisation.

2.4 LOW - PASS FILTERS

The main use of the low-pass filters was to remove high frequency components from the input voltage signals and ensure that aliasing during the digitisation process did not occur. The filters used herein were of an 8th-order Butterworth low-pass filters with the cut-off frequency being controlled by a 6-pole dip switch. A diagram showing the circuit of a low-pass filter is presented in Figure 2.13. The cut-off frequency range for the above filters is between 0.5Hz and 12kHz. For the present investigation, however, the cut-off frequency was set at 3kHz. After the filtering process, the voltage signals were then fed back to the voltage comparators for further processing, as described in the Section 2.3.1.

2.5 A - to - D CONVERTER

The voltage signals were digitised from analogue-to-digital form using a THORN-EMI-BE256-420 transient recording system. It is a Multi-Channel Input

system of modular construction comprising of one master controller board and a number of input channel boards occupying up to a maximum of 16 slots (Figure 2.14). The maximum number of analogue input channels accommodated in the module is thirty two, two in each slot. They are complete with input buffer, sample-and-hold circuit, analogue-to-digital converter, memory, a maximum sampling frequency of 50kHz/channel and 12-bit resolution. The BE256 transient recording system is designed to operate from a remote programmable source(host) interfaced with an IEEE-488 data bus.

A simplified block diagram of a typical BE256 transient recording module for a single channel is shown in Figure 2.15. The inputs are d.c. coupled, single-ended and are fed via a buffer amplifier circuit with an input voltage range of ±5.0V. The digitised samples from the A-to-D converter are then stored in successive memory locations ready to be transferred. The timing-circuits control the sampling rate from the A-to-D converter and the address-circuits define the successive memory locations. The memory contents are read out directly as digital outputs for analysis and storage. When recording starts, the specified memory block, of 512 words in length, is continuously refreshed with new samples. When a trigger pulse occurs, which is externally supplied to the system from an optical encoder, the recording process stops after a further count which fills the memory block (Figure 2.16). Furthermore, when recording has terminated, the memory block contains information before and after trigger pulse has occurred, termed as pre-trigger and post-trigger segments respectively. The IEEE-488 data bus, serving as the communicating link between the transient recorder and the computer system, allowed the user to transfer recorded data to the computer at high speed. The data was transferred in binary form of two's compliment format with the least significant byte (L.S.B.) being transferred first, followed by the most significant

byte (M.S.B.).

2.6 *TRIGGERING AND COUNTING MECHANISM*

Triggering was necessitated because of the short time involved in passing the blade through the vortex system, which was approximately 3.5 milliseconds. In order to analyse the results occurring during this period of time, the signal must be triggered at the standard azimuthal position of the blade of 180 degrees, where blade and vortex are in-line with the tunnel centre line. Recording must, therefore, be allowed to take place before and after triggering has occurred and for an appropriate length of time.

The A-to-D converter, discussed above, offered the user three different trigger facilities; "auto - trigger", "manual - trigger" and "external - trigger". By generating the trigger pulse using the "auto -" and "manual -" trigger facilities it would have been virtually impossible to record the BVI events at the proper azimuth position. Therefore, a controllable external trigger mechanism was required.

An Incremental Optical Encoder (Ferranti 24QB type) with its associated decoder circuit was therefore employed to provide the required triggering pulse. The encoder generates eight output signals with 900 pulses per revolution for outputs A, $\bar{A}$,B and $\bar{B}$ and, one pulse per revolution for outputs C,$\bar{C}$,D, and $\bar{D}$ (see Figure 2.17. By counting the positive and negative pulse edges of signals A and B, monitoring of the instantaneous azimuthal position of the rotating blade was provided. Since there were 3600 pulses (two from each signal) per revolution, and a 1.25mV voltage step input per pulse, the voltage output from the counter could vary linearly from 0.0 - 4.5V per revolution. The positive edges of signals C and D provided the starting triggering

pulse for the data acquisition and counting process, resetting the counter to zero after a full revolution has been complete. The outputs from the incremental optical encoder (i.e. the triggering pulse and the counter output) were then passed to the electronic decoder/counter and fed into the A-to-D converter at the proper channels, as shown in Figure 2.18.

2.7 COMPUTER AND SOFTWARE FACILITIES

The computer system used to monitor and control the data acquisition sequence was an IBM PS/2 model 80441, replacing the former DEC MINC PDP-11/23 microcomputer [37]. The present system was chosen as the replacement of the MINC, because it offers a larger storage capacity and a faster and more efficient information movement, all essential for an effective handling of large amounts of data.

The IBM PS/2 is configured with a 32-bit Intel 80386 microprocessor operating at 16MHz, a 44Mb fixed disk drive for software and recorded data storage and finally a 2Mb Random Access Memory (RAM) planar board with 80 nanoseconds (ns) access time. Its internal storage peripherals consisted of a 1.44 Mb 3.5-inch diskette drive and a 200Mb 5.25-inch IBM 3663A12 Optical disk drive. Its external storage peripherals included of a 5.25-inch 360kb diskette drive. Other external peripherals include an IBM PS/2 colour display unit, an IBM keyboard, an OLYMPIA laser-star 6 Printer with a 300x300 dots/inch printing resolution and an IEEE-488 data bus cable connected to the "master" board of the BE256 A-to-D converter. The IEEE-488 bus provided the communicating link between the host computer and the data acquisition module. The BE256 was controlled from the host computer by sending instructions to it via the IEEE-488 data bus. Figure 2.18 provides a general schematic

of the IBM PS/2 computer with its inner- and outer-connections.

After the completion of each set of tests the collected data were stored in an optical disk and transferred to a VAX 11/750 computer system via an ETHERNET low voltage computer cable for data reduction and data analysis. The VAX 11/750 computer system, coupled with a VERSATEC, a BENSON and an H.P. Plotters and using GINO and NAG graphics routines, produced the high quality plots presented in this dissertation. All computer programs used for the data reduction, analysis and presentation were written in FORTRAN 77 under the VAX/VMS operating system. The data acquisition computer program "BVI" was written in 'C' language. A detailed description of each program's task, accompanied with a relevant flowchart, is presented in the following Section.

2.7.1 Data Acquisition Software

The data acquisition program "BVI" was used to perform the principal task of recording, transferring, storing and displaying the BVI test data. It initially prompts the user with a list of a number of integrated tasks, such as, to configure the BE256 A-to-D converter, run a BVI test or plot selected data on the monitor's screen for validation. A flowchart showing the sequence of events during a BVI test-run is presented in Figure 3.4 and a detailed description of the data acquisition procedure is given in Chapter III, Section 3.1.2.

The routine "configure BE256" initialises and resets the IEEE-488 data bus and the internal memory blocks of the A-to-D converter. Furthermore, it identifies and sends the instructions set by the user to the BE256 via the IEEE-488 bus. These

instructions include the block size (512 words/channel), number of blocks to record (8 blocks/channel), type of trigger (external), number of active channels (26), the size of the post-trigger segment and finally the sampling frequency (18kHz).

The routine "run BVI" includes the "configure BE256" routine, which is set automatically and two important subroutines "record Offsets" followed by "record BVI data". Prior to any data recording (Offsets or BVI) the user was requested to enter the filename for the data to be stored. After recording the data were transferred to the IBM hard disk, where it was stored temporarily before being stored permanently on the optical disk.

Finally, the routine "BVI Graphics" was used to plot selected data recorded from an individual transducer at any of the eight recorded blocks to check the validity of the data before pursuing any further with more testings.

2.7.2 Data Conversion and Reduction Software

The data conversion from digital to voltage form was accomplished by executing the routines "VOLTS3" and "OFFCONV", whilst for the data reduction from volts to instantaneous pressure values the routine "CPICONV" was utilised. Both data conversion and reduction routines were performed using the VAX 11/750 computer which also stored the input/output data files.

Commencing the "VOLTS3" routine, a control-file was requested as input. This control-file contained the input (raw data) and output (voltage data) files names which were read and allocated during the data conversion process. The raw data,

which was in the range of -2048 to +2047 binary, was read from the input file sample-by-sample and when converted to real values in the range ±5.0 volts, was stored in rows of 512 samples/channel for each successive block. The conversion sequence was kept going, allocating different input/output data files in the process, until there were no more input files to read raw data from. A flowchart illustrating the BVI data conversion sequence is presented in Figure 2.19.

In a similar fashion, the conversion of offset data from binary to voltages was performed using the routine "OFFCONV" (Figure 2.20). The difference between the two conversion routines, however, is that "OFFCONV" reads data recorded over one blade revolution and produces an averaged voltage value from the 512 samples per channel, prior to storing the data to the output file.

In completion of the above two routines, reduction of the data from voltages to pressure and subsequently to non-dimensional pressure coefficients then followed. The routine used for the data reduction process is called "CPICONV". At routine entry, a control-file was also requested as input. This file consisted of input file names which contained the voltage, offset and gain values and the output file name for storage of the instantaneous pressure values. It also consisted of information for each particular test from which the data was captured (i.e. r/R, Y_V/c, Z_V/c and Γ), as well as information of the test conditions (i.e. free stream dynamic and barometric pressure in mm of H_2O and, wind tunnel temperature readings). The temperature reading was generally used to calculate the air density and free stream velocity at the throat of the wind tunnel working section. Reading the voltage values from the appropriate input file, offsets, amplifier gains and transducer sensitivities (obtained from calibrating the transducers) were applied. Azimuthal position of the blade was then calculated in

degrees and the induced chordwise pressure coefficient values were finally obtained by dividing the pressure values recorded from each transducer (N/m^2) by the dynamic pressure based on the blade's tip speed. Similar method of reducing the pressure data using the rotor tip speed is reported by Surendraiah **[31]** and Kokkalis **[37]** for their experimental BVI studies.

Since the pressure at the trailing edge (x/c=1.00) was not actually recorded, two values were calculated for the upper and lower trailing edge points. These values were based on extrapolating pressure readings obtained from upper and lower surface neighbouring points. At this stage, no averaging of the data was performed and the instantaneous pressure coefficient values were stored in rows of 512 samples/channel/ block. The sequence of events followed by the data reduction process is shown in the flowchart presented in Figure 2.21.

2.7.3 Data Analysis and Presentation Software

Instantaneous pressure coefficient values obtained by executing the routine "CPICONV" were used for the acquisition of instantaneous and averaged normal force (C_n), pressure drag (C_t) and quarter chord pitching moment ($C_{mc/4}$) and averaged C_p coefficients. For the derivation of the above coefficients the program "CNTMNGT" was developed, the flowchart of which is shown in Figure 2.22.

Once again, at entry to the above routine, a control file was requested. This file contained the input and output file names and were allocated during execution. The program then read the test parameters stored at the top of each input file containing instantaneous pressure coefficient values C_p, and allocated the file containing the

chordwise positions of the pressure transducers in the x- and y- coordinates. Instantaneous pressure values were then read and the derivation of the aerodynamic forces and moments was performed. Instantaneous C_p, C_n , C_t and $C_{mc/4}$ values were added to an accumulator and averaged before being stored in the output files. The calculation of the aerodynamic forces and moment coefficients was obtained by integrating the chordwise pressure distribution around the aerofoil using the Trapezoidal Rule approximation method. When using chordwise pressure distributions this method is relatively accurate provided the spacing between pressure measuring points around the aerofoil are close enough to one another. Since this criterion was satisfied for the current set of BVI tests (see Figure 2.4) the trapezoidal rule method was then implemented.

As far as the presentation software is concerned, a variety of programs has been developed to tailor the needs for each data examination case. These programs are written to present the recorded data in a graphical form making use of the customised plotting packages implemented on the VAX 11/750 computer and are used for the Data Base Management of the BVI data.

Chapter III

EXPERIMENTAL PROCEDURE

This Chapter presents a detailed description of the methods adopted to perform the required parallel and oblique BVI experiments so that the unsteady pressures and airloads of the NACA-0015 aerofoil could be examined. Furthermore, a standard transducer calibration procedure was followed to determine the linearity and sensitivity of each transducer when subjected to variable external pressures. The role of some of the previously described software routines is also highlighted and no further detail reference to these will be made.

3.1 PRESSURE DISTRIBUTION MEASUREMENTS

In order to assess the effects of the vortex upon the blade's aerodynamic loading coefficients extensive measurements of the unsteady pressure field around the aerofoil were carried out by means of miniature pressure transducers. These pressure

measurements were performed for a variety of test set-up positions which include constant wind tunnel and blade rotational speeds and different spanwise locations (r/R) and vortex strengths (Γ). Blade-vortex proximity distances in either the vertical (Y_V/c) or horizontal plane (Z_V/c) were also examined.

3.1.1 Transducer Calibration

For the calibration of the 26 pressure transducers installed in the rotating blade a single ENTRAN-EPIL-080B-5S transducer was used, the output of which acted as reference. Calibration of this transducer was simple and performed by using a single Prandtl mercury manometer in conjunction with an air pump, a power supply source of 15.0V DC and a voltmeter. A schematic view of their interconnections is presented in Figure 3.1. The air supplied by the pump was equally delivered via a three-way junction to the manometer and the transducer. Instantaneous readings taken from the voltmeter and the mercury manometer for a variety of pressures showed that the transducer response was 1.5mV/p.s.i.. When the calibration of the reference transducer was complete, calibration of the pressure sensors mounted in the instrumentation pod of the blade promptly followed.

The blade pressure transducers were calibrated by placing the instrumentation pod inside a pressurised chamber and measuring the output at different pressure levels ($\pm$1.5 p.s.i.). The chamber was installed and sealed with care so no air leaks were occurred. On one side two orifices were made, one served as the applied air pressure input to the chamber and the other as the supply pressure to the reference transducer (see Figure 3.2). The calibration procedure was identical to that as to perform an actual BVI test using the "BVI" data acquisition routine described in Section 2.7.1, with the

only exemption being the initiation of the triggering pulse which was sent not by the Optical Encoder, but by an externally connected oscilloscope. The triggering signal was passed to the THORN-EMI-BE256 A/D converter via the "trigger" channel at the front cover of the A/D converter. The frequency of the triggering pulse, for the initiation of data recording, was set at 0.425Hz, the sampling frequency being 1KHz and the pressure signals were amplified by a factor of 100 for all channels. For the computation of the transducer sensitivity in mV/p.s.i. a data reduction program named "TRCALB" was used. A typical calibration curve obtained from channel No. 9 (x/c=0.20604) is shown in Figure 3.3 where the gradient of the line serves for the calculation of the transducer sensitivity value.

3.1.2 Data Acquisition Procedure

The flowchart illustrating the sequence of events during the chordwise pressure distribution measurements for different blade-span locations and test set-ups is shown in Figure 3.4. A schematic representation of the various electronic instruments used and their interconnections is also shown in Figure 2.18.

Before the beginning of each set of tests, a warm-up period of about fifteen to twenty minutes was allowed so that the electronic equipment (amplifiers, filters, etc.) were brought-up to the desired operational temperature levels. Moreover, the wind tunnel was let to run until the air flow temperature level reached at least 20° C. During testing however, the air flow temperature was not allowed to rise beyond the 30° C mark, since the temperature compensation module of each pressure transducer was most effective in the above temperature range.

At the start of each test, the wind tunnel air temperature and atmospheric pressure were recorded and logged-in in the date-to-date BVI log-book. These values served to determine the wind tunnel air density which in turn was utilised for the calculation of the tunnel free stream velocity at the throat of the working section. Extra care was taken to ensure that the tunnel air speed remained within the 47.5±0.5m/s range so that the vortex intensities used throughout the present investigation were as close as possible to those described by Kokkalis [37].

A "BVI test" consisted of the aerofoil's chordal pressure distribution measurements recorded for a specific blade-span station, vortex strength and blade-vortex proximity distance over an azimuthal arc of 102.4°. During each set of tests the data acquisition program "BVI" was used (see Section 2.7.1) and set to record 512 samples per channel for eight consecutive blade revolutions at a sampling frequency of 18KHz. The sampling rate is equivalent to one sample per 0.2° of blade azimuthal angle (4096 samples/channel/test were recorded in total). Each test included the recording of offset and actual BVI data.

It is mentioned in Section 2.2 that when the whole system is switched-on an offset drift of various magnitude for each transducer is constantly present. This offset drift is originally small and rises with operational time. When it reaches unacceptable levels, thus reducing the operational range of each pressure transducer, it is nullified by means of a push button switch, bringing the output back to the original levels similar to those when powered-up. Moreover, unwanted pressure readings due to velocities in the radial direction caused by the rotational movement of the blade had to be eliminated so that a pure BVI signal was recorded.

In order to achieve the pure BVI pressure reading the following procedure was carried out. The rotor was set at full speed (600revs/min) and data were recorded over one blade revolution using the routine "record Offsets". The recorded data is an accumulation of the offset drift and the radial pressure readings. An average value is obtained and subtracted from the pressure readings recorded during the real BVI test to give an acceptable BVI pressure reading. The offset data was then transferred to the 44Mb hard disk of the IBM PS/2 computer via the IEEE-488 data bus (Figure 2.18). When the transfer mode had been completed the wind tunnel air speed was brought-up to the desired value of approx. 47.5 m/s and the routine "record BVI data" of the data acquisition program was activated. The recorded data were then immediately transferred to the IBM hard disk, where it was stored temporarily before being stored permanently on the optical disk together with the offset data. Offset and BVI data were stored in separate file names ending in *.OFF and *.RAW respectively. As the data was transferred after the completion of each test, the rotor drive motor and the wind tunnel fan were shut-down. For the duration of each test the data acquisition process was entirely governed by the IBM PS/2 computer.

With all the recorded data transfered and stored temporarily in the IBM PS/2 hard disc, the routine "BVI Graphics" was activated to inspect the data. Data from individual channels were plotted in the IBM PS/2 display unit.

Between tests of the same radial position, the vortex generator juncture was shifted to the next position of measurement till all blade-vortex proximity distances were examined. To study the effects of different vortex strengths the vortex generator

"differential" angle of incidence was also altered to the required values, following the same procedure as above.

However, for examining the spanwise effects the rotor had to be dismantled from the wind tunnel and the instrumentation pod placed to the new position without removing the transducers from their original locations. During each dismantling and reassembling of the rotor between spanwise repositioning of the instrumentation pod, extra care had to be taken to avoid damaging the pressure transducers or their wire leads and the blade was then positioned back to the rotor hub, ready for testing. A grand total of 495 tests were performed throughout this investigation and are summarised in Table 3.

A full discussion of the results obtained from the present BVI investigation is presented in Chapter IV, whereas comparisons between the present and existing data are discussed in Chapter V.

Chapter IV

PRESENTATION AND DISCUSSION OF EXPERIMENTAL RESULTS

This Chapter presents selected detailed discussions of the most pertinent results obtained from a wide range of Parallel and Oblique Blade/Vortex Interaction pressure measurements. These measurements were attained using an instrumented single blade, non-lifting rotor of a NACA-0015 aerofoil profile which interacted with a vortex, generated upstream of the rotor disc. From the determined pressures, the pressure distribution variations over the aerofoil surface, the aerofoil's general performance with respect to vortex strength, blade-vortex separation height, and span station, were examined. Aerodynamic forces and moment coefficients were obtained by integrating the chordwise pressure distribution using a simple trapezoidal rule method. These coefficients are normalised using the blade tip-speed velocity at 180° azimuth and are presented as a function of blade-vortex longitudinal separation distance (X_V/c) for each BVI test case. It should be noted that the initial lift produced by the

blade without the vortex in the flowfield is zero (non-lifting case) and that any lift generated during the interaction is induced by the oncoming vortex.

Due to the substantial amount of data collected during the present investigation, only the appropriate parallel BVI test cases will be presented in the forthcoming Sections. The complete set of tests, however, is presented in References **53-57**, where pseudo-three-dimensional representations were developed. These illustrate the chordwise pressure distributions over the upper and lower surfaces of the aerofoil for a blade azimuthal range of 102.4°. A typical example of how the C_p data is presented in the above References is shown in Figure 4.1(a) and (b). Graphical presentations of the aerodynamic load coefficients (i.e. C_n, $C_{mc/4}$ and C_t) are also included in the above figure and plotted against X_v/c.

4.1 GENERAL DESCRIPTION OF AEROFOIL PERFORMANCE AS A FUNCTION OF X_v/c AND Y_v/c

In order to study the BVI problem a general knowledge of the sequence and intensity of the events that take place prior to, during, and after the interaction is very important. In a preliminary investigation concerning the aerofoil's pressure distributions with increasing azimuth, it had been noticed that the aerofoil experienced its largest pressure and air-loading coefficient changes, regardless of the blade's span position, when the vortex strength was set at the maximum 6.7m2/s and the trajectory of the vortex was on a near-miss or head-on collision course with the blade. Upon impact with the blade, the vortex either followed a streamline path for near-miss collisions or was sliced into two smaller vortices which were convected above and below the aerofoil during head-on collisions. For the description of some of the above

observations, selected plots have been employed (Figures 4.1.1-9). They illustrate the induced pressure coefficients around the aerofoil over a variety of blade azimuthal positions in a two- and three-dimensional form, as well as the corresponding aerodynamic load coefficients. These plots represent the test cases of parallel B.V.Is for the radial span position of 0.62R portraying the -0.2, 0.0 and 0.2 blade-vortex separation heights (Yv) and for a vortex strength of 6.7m2/s.

a) Case-A : Y_V/c=-0.20

The history of the pressure distribution variations for the parallel BVI test in which the blade-vortex separation height ratio is -0.20, are shown in Figure 4.1.1 for selected X_V/c locations during the interaction process. The position of the vortex relative to the aerofoil's leading edge and the blade's azimuthal position are presented numerically at each plot. By examining the pressure data it is noticed that the presence of the oncoming vortex, which rotates in an anti-clockwise fashion with respect to the blade leading edge, generates an upwash on the aerofoil, which in turn has the same effect as increasing the angle of attack. This induced upwash increases as the blade approaches the vortex. As a consequence of the increasing upwash, pressure expansion and compression formed over the upper and lower surfaces respectively, increase steadily with decreasing aerofoil-vortex longitudinal separation distance ratio (X_V/c). Such pressure behaviour resembles that of a two-dimensional aerofoil with increasing positive angle of attack in a steady two-dimensional flow. The vortex induced upwash continues to enhance its influence on the aerofoil even further until the aerofoil experiences a maximum pressure suction at X_V≈-0.315c. Following the occurrence of maximum pressure suction, a rapid change of events begins to take place. The suction over the upper surface starts to decrease very quickly until it is

observed to subside at $X_V \approx 0.224c$. Similar behaviour is also seen to occur in the lower surface where compression diminishes at approximately the same rate compared with the decreasing suction.

As the vortex advances downstream towards the trailing edge, pressure suction and compression are seen to reestablish themselves over the aerofoil. They now take place over the lower and upper surfaces respectively indicating that the original vortex induced upwash has been switched to a downwash at the leading edge.

From the aerofoil-vortex distance ratio $X_V/c \approx 0.183$ onwards (see Figure 4.1.1), it is observed that the lower surface begins to experience a pressure fluctuation which propagates along the chord of the aerofoil as the vortex convects downstream. This pressure fluctuation is interpreted as the result of the intensified flow effects generated between the vortex and the flow passing the blade surface which forms a bubble owing to the vortex.. This "vortex bubble" can be described as similar to a separation bubble except that the separation bubble is the outcome of vorticity generated at the body surface, whereas a "vortex bubble" is due to the presence of the external vortex. It affects a substantial amount of chordal length which sometimes is as much as 40% of the chord.

It is also noticed that due to the induced downwash at the leading edge, pressure suction rises steadily until a maximum is obtained at $X_V/c \approx 1.320$. In contrast with the leading edge, the trailing edge begins to experience an upwash. This upwash becomes more noticeable with additional vortex progression away from the leading edge. It is identifiable as a slight pressure expansion over the lower surface due to local flow acceleration at the trailing edge. When the vortex advances further

downstream the aerofoil's chordal pressure variation returns to that associated with a two-dimensional aerofoil. The intensity of the interaction is seen to decrease since the vortex induced velocities are reduced as the vortex moves away from the blade leading edge.

The chordwise pressure variations described above, can be seen more clearly in Figure 4.1.2(a) and(b), where chordwise pressure variations of the upper and lower surfaces respectively are plotted in a standard three-dimensional form against X_v/c. From this figure it is noticed that the major pressure changes occur near the leading edge of the aerofoil ($x/c<0.30$). Furthermore, the position of the vortex bubble, described above, is very noticeable as it travels downstream along the chord.

As far as the aerodynamic force and moment coefficients are concerned they vary quite smoothly prior to and after the interaction phase. During the blade-vortex interaction phase, however, abrupt changes are recorded (Figure 4.1.3).

When the position of the vortex is a few chord lengths ahead of the aerofoil's leading edge, C_n starts to increase gradually, due to the increasing upwash. This effect becomes more intense as the vortex moves within one chord length upstream of the aerofoil leading edge. The C_n reaches a maximum at $X_v/c\approx-0.60$ and the peak of the curve has a "round" gentle shape. Further progression of the vortex downstream causes the normal force coefficient to drop. It initially falls at a slow rate followed by a sudden dive. This sudden C_n drop begins when the vortex is approximately 15% chord length upstream of the aerofoil leading edge. The initial induced upwash begins to switch to a downwash in a very short time. When the vortex has travelled a distance of a quarter chord passed the leading edge, the C_n reduction starts to slow down until a

minimum has been obtained at $X_v/c \approx 0.65$. The minimum C_n peak has shown similar behaviour with its maximum counterpart also having a "round" gentle shape. When the vortex progresses towards and away from the trailing edge, C_n begins to rise once again. As long as the vortex is in close contact with the aerofoil the peak's round shape is maintained. When the vortex leaves the trailing edge, and is convected downstream, C_n increases due to the associated reduction in downwash.

The quarter chord pitching moment coefficient ($C_{mc/4}$) performs in a somewhat different manner. When the vortex is a short distance away from the aerofoil leading edge ($X_v/c \approx -0.10$), the $C_{mc/4}$ curve dips to a minimum. As the vortex travels downstream $C_{mc/4}$ gradually increases. The major contributor to this increase is believed to be the trailing edge upwash which causes the flow to accelerate and decelerate over the lower and upper surface respectively. As a consequence of this the aerofoil experiences a nose-up condition. The nose-up condition is maintained until the vortex is right above the mid-chord position of the aerofoil ($X_v/c \approx 0.555$). With further vortex progression downstream, $C_{mc/4}$ begins to decrease, originally at a very slow rate. As the vortex progresses towards the trailing edge (Figure 4.1.1, $X_v/c \approx 0.760$), the contribution of the local upper and lower surface suctions to the pitching moment gradually balances itself out, leaving the leading edge suction as the sole contributor. This causes the aerofoil pitching moment coefficient to undergo a severe nose-down phase until the vortex is believed to be ≈30% of the chord downstream of the trailing edge. It is at this stage ($X_v/c \approx 1.320$) that maximum pressure suction occurs over the lower surface (Figure 4.1.1) and a second $C_{mc/4}$ minimum is obtained.

In the C_t curve, however, it is shown that C_t decreases and increases prior to and after the interaction process. During the blade-vortex interaction encounter, however, it behaves in a similar but opposite manner compared to the C_n (Figure 4.1.3(a)). It reaches a minimum value just before interaction occurs and a maximum when the vortex has travelled a distance of ≈40% of the aerofoil chord downstream of the leading edge.

After interaction has taken place ($X_v/c \geq 1.00$) and the blade travels away from the vortex, all the aerodynamic load coefficients tend to move towards their original values. However, this recovery process is relatively slow compared to the earlier part of the blade-vortex interaction process.

b) Case-B : $Y_v/c = 0.00$

Figures 4.1.4 and 4.1.5 present the surface pressure distributions obtained from a similar test case as the one in case-A, but with the vortex now colliding head-on with the rotating blade. By studying these plots it is noticed that there is a close resemblance with those pressure distributions plotted in Figures 4.1.1 and 4.1.2 respectively, in particular, when the blade has travelled up to the $X_v/c \approx -0.65$ and past the $X_v/c \approx 1.20$ blade-vortex positions. When the blade is at a closer distance to the vortex ($-0.65 \leq X_v/c \leq 1.20$) noticeable differences exist, with the intensity of the induced upwash at the leading edge being more severe prior to interaction. This can be seen more clearly in the development of the leading edge suction peak which moves slightly towards the leading edge as the blade approaches the vortex (Figure 4.1.4). The positive angle of attack owing to the induced upwash is thought to increase steadily causing the suction peak to increase very sharply. When maximum suction is obtained

at $X_V/c \approx -0.066$, it is observed that its magnitude has doubled in size and that the above aerofoil-vortex distance ratio has been substantially reduced compared to the equivalent one of case-A ($X_V/c \approx -0.315$). As the blade approaches closer to the vortex, the vortex affects the flow circulation around the aerofoil and particularly the flow at the aerofoil leading edge region, altering its direction from an upwash to a downwash. The leading edge suction peak starts to decrease very rapidly and crosses from the upper to the lower surface. The collapse of the suction peak process and its reoccurrence over the lower surface leading edge requires a much shorter blade azimuth range ($\approx 4.5°$) and consequently less time to that recorded in the previous case ($\approx 9.0°$). As the vortex advances towards the trailing edge two distinct pressure fluctuations develop on either side of the aerofoil surface. They propagate along the full length of the chord and are interpreted as vortex bubbles, similar to that observed over the lower surface in case-A.

Since for the duration of the experiment there exists only one externally generated vortex, the most obvious explanation for their appearance is that, as the blade is in-line for a head-on collision course with the vortex, the blade slices through the external vortex splitting it into two smaller vortices. The broken vortices are believed to move close to the surface of the aerofoil affecting the boundary layer and thus the surface pressure distribution. The shape, strength, and behaviour of those broken vortices remain to date unknown. An examination of those characteristics has not been carried out, since such an investigation was beyond the scope of the present study.

From the surface pressure traces it is also noted that the vortex bubble on the upper surface travels faster than its counterpart on the lower surface. Since the generated vortex has an anticlockwise rotational mode relative to the aerofoil direction of motion, it is suggested that the sum of the aerofoil and vortex induced velocity must

be higher than that on the lower surface, causing the upper surface flow to accelerate. Therefore, the upper surface vortex must travel at a faster speed. Examining the C_p data very carefully it is believed that this vortex arrives at the aerofoil trailing edge at approximately 30% of the chord ahead of schedule (i.e. at $X_v/c \approx 0.70$ instead of $X_v/c \approx 1.00$). After interaction has taken place, the vortices on both the upper and lower surfaces meet at the trailing edge and merge into the wake.

The history of the aerodynamic loads plotted against X_v/c is shown in Figure 4.1.6. When the vortex is ahead of the aerofoil, the normal force and pressure drag coefficients behave in a similar manner to that experienced in case-A, i.e. increase and decrease respectively due to the increasing upwash. The quarter chord pitching moment coefficient, however, varied significantly. It increased constantly and reached a maximum as the aerofoil leading edge was at a very small distance away from the vortex core. The present aerodynamic load curves, however, were shown to have much sharper peaks. Severe changes were also observed to take place just prior to interaction, with the worst variations occurring when the vortex is within 3/4 of a chord length upstream of the aerofoil.

During the interaction process, and in particular when the vortex has travelled less than a quarter chord downstream from the aerofoil leading edge, C_n and C_t experience their maximum rate of change of approximately 2.0 and -0.26 respectively per travelled chord.

The $C_{mc/4}$ on the other hand, starts to drop slightly as the uninterrupted interaction process begins. For blade-vortex distance ratios between $0.30 \leq X_v/c \leq 0.70$ it behaves in a very erratic fashion. Such turbulent $C_{mc/4}$ behaviour is attributed to the

unsettled performance of the pressure distributions caused by the presence of the two broken vortices travelling along either surface of the aerofoil. It has been mentioned earlier that the upper surface vortex leaves the aerofoil at the calculated blade-vortex distance of $X_v \approx 0.70c$. It is at this blade-vortex location however that the aerofoil begins to experience a second, but less severe, nose-up effect until an additional maximum $C_{mc/4}$ is attained at $X_v/c \approx 0.80$. At this stage the lower surface vortex has moved closer to the trailing edge, still influencing the local pressure distribution (Figure 4.1.4). For greater X_v/c values, the quarter chord pitching moment coefficient undergoes a sharp decrease of ≈ 0.056 per travelled chord, causing the aerofoil to experience a sudden nose-down effect. The constantly increasing leading edge pressure suction has been found to be the main contributor to the nose-down effect. It causes the aerodynamic centre to move forward towards the leading edge, increasing the effective length of the moment arm and therefore intensifying the negative moment effect.

It is also observed from the C_p plots that traces of the lower surface "vortex peak" exist at an even greater blade-vortex distance ratios than $X_v/c=1.00$, indicating that this vortex travels at a slower speed than the aerofoil's rotational speed. It is believed that the lower surface vortex departs from the aerofoil at the much later distance of $X_v/c \approx 1.45$.

After interaction has taken place the aerodynamic load coefficients behave in a similar manner compared to case-A, i.e. tending to return to their original values prior to interaction.

c) Case-C : $Y_V/c= 0.20$

Figures 4.1.7 and 4.1.8 illustrate the chordwise pressure coefficient variations for the near-miss blade-vortex collision when $Y_V/c=0.20$, whereas the corresponding aerodynamic coefficients are presented in Figure 4.1.9.

By examining Figures 4.1.7 and 4.1.8 it is seen that although the surface pressure distribution variations resemble those of the two previous cases, the magnitudes have increased and decreased compared to those obtained in cases A and B respectively. The maximum leading edge suction peak which occurs at $X_V/c=-0.149$ is seen to have been reduced by ≈30% and increased by ≈50% compared to the equivalent one of case-B and -A respectively. Furthermore, the upper surface pressure coefficient histories experience a noticeable perturbation which travels along the chord as the blade passes near the vortex. This pressure perturbation is identified as a "vortex peak", and its presence is clearly visible in Figure 4.1.8. It is similar to the one being described in case-A but it has a distinguishably faster travel speed since it departs the aerofoil at a shorter chordal-time interval ($X_V/c\approx0.940$). Moreover, by studying the present aerodynamic load curves (Figure 4.1.9), it is seen that noticeable disimilarities exist when compared to their equivalent counterparts (case-A and -B). The most distinguishable of them all, however, is the unexpected nose-up pitching moment characteristic occurring as the vortex approaches the trailing edge.

An examination of the chordwise pressure distribution plots has shown that no major changes do exist to suggest any reasons for the unusual pitching moment behaviour. A detail investigation of pressure histories obtained from individual pressure stations and plotted on a magnified scale was therefore used to provide the

user with possible answers.

Selected plots illustrating pressure traces obtained from the lower surface pressure stations, past the mid-chord position, are shown in Figure 4.1.10 and are drawn against X_v/c. It is evident from these plots that a sudden trailing edge pressure expansion has taken place and been recorded from the nearest to the trailing edge pressure transducers (Nos. 25 and 26). The further inward transducers (Nos. 23 and 24) also pick-up a similar pressure expansion which has a much weaker concentration. It is not quite clear what has caused the unexpected trailing edge pressure suction, which is felt from as far upstream as the mid-chord location. It is this extra trailing edge suction presence which causes the quarter chord pitching moment coefficient to experience a second but very abrupt nose-up effect (Figure 4.1.9), reaching a maximum at $X_v/c \approx 0.940$. The magnitude of the secondary $C_{mc/4max}$ almost matches the one obtained prior to interaction and the corresponding differential pitching moment coefficient ($\Delta C_{mc/4}$) is found to be equal to 0.033.

The normal force coefficient has also been influenced by such an effect. It undergoes a small but distinct fall due to the additional lift generated over the lower surface caused by the trailing edge suction. In contrast to the C_n and $C_{mc/4}$, no abrupt changes were observed for the pressure drag coefficient.

Finally, to the author's knowledge very few of the previous experimental methods employed for the investigation of the BVI problem, as discussed in Chapter I, document the vortex progression during near-miss or head-on blade-vortex impingements by means of pressure traces for equivalent BVI encounters. Thus, the present work it can be said to represent one of the most successful pressure data

recordings of the BVI phenomenon in a three-dimensional rotating environment. The vortex behaviour and in particular the splitting during interaction has been visible using only two-dimensional flow visualisation methods and numerical techniques.

4.2 GENERIC BVI RESULTS DUE TO BLADE-VORTEX PROXIMITY

To examine the effects of vortex proximity on the aerodynamic performance of the NACA-0015 aerofoil, comparisons had to be made between identical force and moment coefficients, attained at different blade-vortex separation height ratios (Y_v/c). For all the vortex proximity test cases examined here, the vortex strength was equal to $6.70m^2/s$, the blade-vortex separation height covered the range $-1.00 \leq Y_v/c \leq 1.00$ and the spanwise position was set at 0.86R.

Typical normal force (C_n), quarter chord pitching moment ($C_{mc/4}$) and pressure drag (C_t) coefficient variations obtained under the above parallel BVI conditions are presented in Figures 4.2.1, 4.2.4 and 4.2.6 respectively.

By studying Figure 4.2.1 it is noticed that as the blade approaches the vortex, minor differences exist between C_n curves until the blade is positioned just above a chord length upstream of the vortex centre ($X_v/c \approx -1.30$). The only exception occurs when the blade-vortex separation height equals to -1.00c (Figure 4.2.1(a)) where the C_n curve begins to deviate prematurely from the rest at $X_v/c \approx -2.50$. As the blade passes the $X_v \approx -3.00c$ position, the curves start to rise almost simultaneously at a similar increasing rate. This reflects the effect of the vortex on the surrounding flow field, inducing an upwash at the blade leading edge regardless of blade-vortex separation height.

The C_n rate of increase is maintained for the remainder of the curves until the blade leading edge is ≈130% of a chord length upstream of the vortex core centre. Up to this stage, and for test cases where the rotor flies below the generated vortex filament (i.e. $Y_v/c>0.00$), the C_n magnitudes have shown to be slightly higher than their equivalent counterparts, i.e. when the rotor's plane of rotation is above the vortex path. As the blade continues to approach the vortex centre of rotation, the curves begin to separate in an uneven fashion and reach a maximum prior to the BVI encounter. It is noticed that the magnitude of C_{nmax} increases with decreasing blade-vortex separation height. The greatest value of C_{nmax} is attained when the blade is on a direct collision course with the vortex ($Y_v/c=0.00$). The position of the blade relative to the vortex centre at which C_{nmax} is obtained, differs with Y_v/c. For BVIs in which $Y_v/c\leq-0.60$ and ≥0.80, C_{nmax} is attained when the blade is about a chord length upstream of the vortex. For closer BVI encounters, however, the attainment of C_{nmax} occurs when the blade is only a few percent of the chord from the vortex, with the shortest length ($X_v\approx0.10c$) being when the blade interacts head-on with the vortex (i.e. $Y_v/c=0.00$).

During the BVI phase, however, there is a rapid change in C_n as the blade passes close to the vortex. After reaching a maximum, it reverses sign during the interaction process, passing through zero at about 0.15 chords for $Y_v/c \leq 0.00$ and between 0.15 and 0.30 chords for $Y_v/c \geq 0.00$ (Figure 4.2.1). This change in C_n is due to the aerofoil abrupt change of angle of attack from positive (upwash) to negative (downwash) caused by the oncoming vortex. The transformation of C_n from positive to negative is seen to vary very smoothly for the large Y_v/c values (i.e. $Y_v/c \geq \pm 0.80$). However for smaller Y_v/c values, it varies in a sudden, almost instantaneous pulse-like manner, during near-miss and head-on collisions ($-0.20 \leq Y_v/c \leq 0.20$). This kind of C_n behaviour indicates that the most severe interactions occur when the vortex is at its closest encounter with the rotating blade.

In order to emphasize the above findings, Figure 4.2.3 has been employed. It illustrates the differential normal force coefficient (ΔC_n) experienced by the aerofoil during a BVI, in relation to blade-vortex proximity. ΔC_n is known as the maximum sectional normal force coefficient which is the difference between the maximum positive and negative peaks of C_n. It is evident that the magnitude of ΔC_n increases as the blade-vortex separation height decreases. For $Y_v/c \geq 0.20$ it is also observed that the values of ΔC_n are higher compared to those obtained at a corresponding negative Y_v/c. This is attributed to the higher induced velocities which the aerofoil experiences when the vortex is positioned above the blade.

Returning to Figure 4.2.1, it has also been observed that the magnitude and shape of the negative C_n traces varied with Y_v/c. In particular, the magnitude of C_{nmin} is seen to decrease with decreasing blade-vortex separation height, reaching its lowest value at $Y_v/c=0.00$. The negative C_n curves also produced "round" shape peaks, except for blade-vortex separation heights of $Y_v=0.20c$ and 0.40c. In these two cases "sharp" peaks have been recorded as the blade trailing edge departs from the vortex. As the blade travels further away from the vortex, it is observed that the C_n curves tend to rise towards their original values compared with those prior to interaction.

Finally, it is noticed that as the aerofoil-vortex distance (X_v) is enlarged to more than 2 1/2 chord lengths, very little C_n changes are observed regardless of blade-vortex proximity heights.

In addition to the above observations, a further examination of the blade-vortex proximity effects to the aerofoil's $C_{mc/4}$ and C_t coefficients is performed. In contrast to the normal force coefficients, the pitching moment coefficient ($C_{mc/4}$) variations, shown in Figure 4.2.4, are also presented in individual plots for each Y_v/c case to highlight the immense differences occurring between each test (Figure 4.2.5). Before any examination of the above curves is carried out it should be mentioned that the curve obtained from the head-on BVI has been omitted from Figure 4.2.4. This is due to immense $C_{mc/4}$ variations and large curve fluctuations, particularly during interaction (Figure 4.2.5(f)), blurring the illustration of curve trends and therefore obstructing the identification of critical points between curves. Although small but persistent fluctuations do exist for the remainder of the $C_{mc/4}$ curves, the general patterns are well documented and an observation of the $C_{mc/4}$ behaviour relative to blade-vortex proximity was performed without delay.

By examining Figure 4.2.4, it is noted that the $C_{mc/4}$ curves resemble the shape and magnitude of each other prior to and after interaction takes place. During interaction, however, and for the extreme outer Y_v/c cases examined (i.e. ± 0.80 and ± 1.00), $C_{mc/4}$ undergoes a reasonably gentle transformation from a positive (nose-up) to a negative (nose-down) configuration. As the blade-vortex separation height shortens, the $C_{mc/4}$ curves behaved in a completely different manner for $Y_v/c \geq 0.20$ and ≤ -0.20 respectively.

For test cases where the blade rotates above the vortex line (Figure 4.2.4(a)), it is observed that as the blade rotates towards the vortex, the curves begin to deviate from about $X_v \approx -1.30c$, with the strongest deviation being when $Y_v/c = -0.20$. It is noticed that the initial curve deviation location coincides with that of C_n (Figure 4.2.1(b)). In contrast with the C_n data, however, there is a distinct delay in the $C_{mc/4}$ transformation from positive to negative. Albeit this delay is present in all the negative Y_v/c cases, it is more obvious in BVIs where $-0.60 \leq Y_v/c \leq -0.20$. Initially, the origination of this transformation begins before interaction has taken place for $Y_v/c \leq -0.80$. For the test cases where $Y_v/c \geq -0.60$ it forms immediately after the vortex passes the mid-chord location of the aerofoil. The above delay has been attributed to the presence of the vortex which strongly affects the aerofoil pressure distribution, especially that of the lower surface, detailed description of which has been presented in Section 4.1, case-A.

Although the change from a nose-up to nose-down configuration takes place over an approximately similar chord-transit interval (i.e. $0.55 \leq X_v/c \leq 1.20$) for the stronger interactions, the rate of change has been increased significantly during the closest aerofoil-vortex encounter ($Y_v/c = -0.20$). The differential quarter chord pitching

moment coefficient ($\Delta C_{mc/4}$), defined as the maximum $C_{mc/4}$ difference between the positive and the negative peak of $C_{mc/4}$, is observed to vary between $\approx$0.020 and $\approx$0.043 during weak and strong interactions respectively.

Furthermore, for those BVIs in which the blade's plane of rotation lies below the vortex line (Figure 4.2.4(b)), it is seen that before and after interaction takes place the $C_{mc/4}$ traces also behave in a similar fashion, attaining almost identical magnitudes. However, as the blade approaches the oncoming vortex filament, $C_{mc/4}$ starts to increase very gradually for $Y_v/c \geq 0.60$. For closer blade-vortex encounters, however, the increase in $C_{mc/4}$ becomes very sudden, especially for $Y_v/c=0.00$ and 0.20, where maximum magnitudes of approximately 0.029 and 0.032 respectively are obtained (Figure 4.2.5(f)-(g)). It is also seen that after the occurrence of a maximum, $C_{mc/4}$ decreases very rapidly as the vortex convects downstream, particularly for $0.20 \leq Y_v/c \leq 0.60$. However, the sharpest reduction has been observed to take place during the $Y_v/c=0.20$ test case, where $\Delta C_{mc/4}$ obtained its greatest magnitude of $\approx$0.055 for all Y_v/c cases considered here.

As the vortex advances further downstream, the aerofoil experiences an additional and much sharper nose-up pitching moment. This second nose-up (pulse-like) pitching moment is very abrupt and is only perceptible during the $Y_v/c=0.20$ and 0.40 BVI test cases (Figure 4.2.5(g)-(h)). The magnitude of $\Delta C_{mc/4}$ during this pulse-like pitching moment behaviour is at its highest when $Y_v/c=0.20$ has a value of $\approx$0.042, which is almost 2 1/2 times higher when compared to that of the $Y_v/c=0.40$ case. Possible explanation of what has caused the pitching moment coefficient to behave in such manner has been presented in the earlier Section 4.1, case-C.

The pressure drag coefficient variations obtained at different blade-vortex heights and plotted against X_v/c are presented in Figure 4.2.6. By examining the above figure it is noticed that C_t remains unresponsive to the blade-vortex proximity effect. It follows a similar behaviour to that described earlier for the other two aerodynamic loading coefficients. Further studies of the C_t behaviour relative to Y_v/c settings revealed that, once again the maximum variations were obtained when $Y_v/c=0.00$. The pressure drag coefficient, although it decreased very sharply prior to interaction and reached a minimum at $X_v/c\approx-0.035$, increased very rapidly as interaction begun to take place. The location of C_{tmin} also varied with Y_v/c, occurring at an earlier blade azimuthal position as Y_v/c enlarged. The sharp C_t increase has only been observed to occur during the stronger BVIs (i.e. $-0.20\leq Y_v/c\leq 0.20$), whereas for the remainder of the Y_v/c cases C_t increased in a much gentler fashion. In addition to the above observations, the maximum value of the differential pressure drag coefficient (ΔC_t) measured during the interaction process, has been found to be approximately equal to 0.076.

Finally, the corresponding pressure histories recorded from two leading edge pressure transducers stationed at x/c=0.0261 (No.13) and 0.0255 (No.17) over the upper and lower surface respectively, are also shown in Figure 4.2.7 and 4.2.8. It may be noted that the salient features of these pressure plots, especially those from transducer no. 13, are very similar compared with those observed for the C_n. The intensity of the interaction becomes less severe as the blade-vortex separation height increases. Furthermore, as the blade-vortex distance ratio (X_v/c) exceeds the 4.0 value, the pressures recorded from transducer no. 17 (Figure 4.2.8) almost recover to their original values. In contrast to the above observation, pressures obtained from transducer no. 13 (Figure 4.2.7) appear to be not even near to their initial values for the

same azimuthal length. Detail examination of the above figure has also revealed that pressures of similar magnitude were measured for different Y_V/c settings, i.e. Y_V/c=0.00 and 0.20 (see Figure 4.2.7(b)).

4.3 VORTEX STRENGTH VARIATION EFFECTS

In the previous Sections, the blade-vortex proximity problem was examined and described in a generic form. Its effect on the aerofoil's chordal pressure distributions and aerodynamic loadings were highlighted using numerous selective plots. The intensity of the generated vortex remained unchanged throughout the discussion and was equal to $6.7m^2/s$. In this Section, an attempt is made to study the BVI effects on the blade's airloading coefficients by altering the intensity of the generated vortex. In the forthcoming discussion the presented data were obtained from a blade span location of 0.62R and for five different vortex strengths. Figures 4.3.1, 4.3.2 and 4.3.3 are presented to illustrate the integrated aerodynamic load coefficients variations as the blade passes over the vortex at a blade-vortex separation distance of 0.20c. In general terms, these figures indicate that the coefficient magnitudes increase substantially with increasing blade azimuthal location, and also with increasing vortex intensity. This is due to the enhancement of the resultant free stream velocity caused by the presence of the vortex and its intensity increases, which in turn strengthen the flow circulation around the advancing blade resulting in higher suction and in higher aerodynamic forces and moments. Detailed examination of the above figures however has revealed that some distinguished features do exist between plots and are described in the following paragraphs.

The vortex strength variation effect upon the normal force coefficient is

portrayed in Figure 4.3.1. From this figure it can be seen that by far the most prominent event of the BVI encounter is the occurrence of the C_n perturbation from positive to negative as the blade passes at a close distance from the vortex. As the vortex strength intensifies between tests, the C_n impulsive change becomes more abrupt. For weaker BVI encounters however (see Figures 4.3.1(a) and (b)), the C_n transformation can be described as a much gentler affair. During these weaker BVIs, the $dC_n/d(X_v/c)$ slope obtains its minimum values of $\approx$0.27 and $\approx$0.54 per travelled chord respectively and the positive and negative curve peaks have developed "round" shapes. The highest slope magnitude was found to be $\approx$1.20 per travelled chord and corresponded to the strongest vortex ($6.7m^2/s$). For BVIs at which the vortex strength is greater than $3.40m^2/s$, the curve peaks have developed pointed summits.

Furthermore, another distinctive feature of the C_n data is observed to take place, as the vortex interacts with the rear part of the blade, being identified as an additional negative lift. The extra negative lift is noticeable for most of the vortex intensity cases and its variation in magnitude solely depends on the vortex strength. Although C_n tends to move towards its original value after the occurrence of interaction, its magnitude never recovers fully, in the azimuthal test range, to that obtained prior to interaction, except perhaps for the weakest BVI (Figure 4.3.1(a)).

The quarter chord pitching moment coefficient histories obtained for five different vortex strengths and for the same blade-vortex separation distance ratio as above, are presented in Figure 4.3.2. Although there is a noticeable noise-like fluctuation for all curves, the underlying trends with respect to vortex strength are well defined and are fairly similar. It is obvious from the above figure that as the blade

approaches the vortex core, $C_{mc/4}$ gradually increases until it reaches a maximum when the vortex is virtually next to the aerofoil leading edge. The strongest pitching moment is obtained just before interaction occurs and for a vortex strength of $6.70m^2/s$. As interaction starts to take place between blade and vortex, $C_{mc/4}$ begins to reduce very gently for the weakest BVI and in a sharp almost pulse like manner for the strongest BVIs. The rate of reduction varies between $\approx$0.004 and $\approx$0.067 per travelled chord for the lowest and highest vortex intensities respectively. With further vortex progression downstream the aerofoil experiences its smallest pitching moment, well ahead of the vortex departure from the blade. Following the attainment of $C_{mc/4min}$ a sudden nose-up pitching moment comes into effect, identifiable only from the stronger vortex cases.

It is well known that $C_{mc/4}$ is not simply related to the induced pressure loading but is also a function to the chordwise location of that loading. Therefore, generally small pressure variations near the trailing edge region can play a significant role in the pitching moment behaviour, as well as, in the overall aerofoil's aerodynamic performance. A detailed examination of pressure traces from individual pressure sensors, described in Section 4.1.1(c), has revealed that an additional pressure suction takes place over the lower surface (opposite side) as the vortex travels towards the aerofoil trailing edge (Figure 4.1.10). The great similarities between pressure and pitching moment traces, have left no doubt that the major contributor to the extraordinary nose-up pitching moment behaviour is no other than the lower surface trailing edge suction. Furthermore, the event in which $C_{mc/4min}$ occurs appears to take place at an earlier blade-vortex (X_v/c) location as the vortex strength increases. This is expected since the vortex induced velocities progressively increase with increasing strength, causing the travelling vortex to accelerate at a much faster speed

towards the trailing edge and therefore speed-up the blade-vortex interaction process.

The effects of vortex strength on the pressure drag coefficient are illustrated in Figure 4.3.3. It is shown that as the blade's instrumented section proceeds towards the vortex the pressure drag coefficient histories are dominated by the large forward force generated by the vortex. C_t varies in an almost linear fashion, except for the strongest vortex strength cases where substantial and precipitate changes are observed a few percent of the chord prior to the occurrence of interaction (Figure 4.3.3(d) and (e)). For these stongest BVIs the location at which C_{tmin} occurs, relative to aerofoil-vortex distance ratio (X_v/c), matches that of the corresponding C_{nmax} (Figure 4.3.1(d) and (e)). During interaction the pressure drag coefficient variations become more severe and a second C_{tmin} is obtained as the blade moves away from the vortex. The significance of the second minimum peak, which becomes more noticeable for the stronger BVIs, is not at present understood.

4.4 SPANWISE VARIATION EFFECTS

To study the effects of spanwise variation on the induced airloading coefficients, BVI test data obtained from five different blade-span locations, ranging from 62% to 94% at an increment of 8%, were examined. BVI parameters such as vortex strengths and blade-vortex miss distances (Y_v/c) were also considered. Typical results are presented in Figures 4.4.1 to 4.4.9. These figures illustrate the integrated normal force, quarter chord pitching moment and pressure drag coefficients plotted against X_v/c for three blade-vortex separation heights; -0.20, 0.00 and 0.20. Because the general variations and trends of the airloading coefficients have shown great similarities for all vortex intensities, only the results obtained under the strongest vortex

strength ($6.70m^2/s$) will be presented in the current discussion.

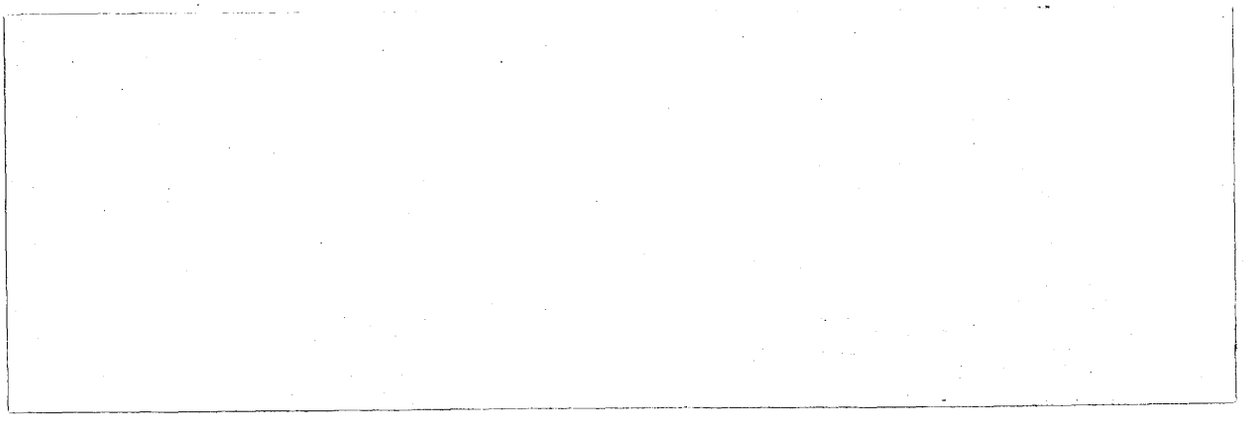

By studying the above Figures 4.4.1 to 4.4.9 a number of interesting observations may be seen. Firstly, although the C_n variations and trends behave in a similar fashion to that described in the earlier Section of 4.1 for various blade-vortex separation heights, distinct variations do exist when compared to those of different blade-radial positions. These variations include a slight increase in magnitude from the inboard to the outward blade-span stations. This increase is more obvious for the maximum negative lift during and after the occurrence of interaction. In contrast with the negative lift, the maximum positive lift remains almost unaffected for all the radial positions examined. In the latter observation, however, there is an apparent inconsistency, particularly for the head-on and near-miss collision of $Y_v/c=0.20$ (Figures 4.4.2 and 3). This may be attributed to possible meandering of the oncoming vortex, which as a result, affects the intensity of the interaction from time to time and therefore the airloading coefficients along the length of the blade span.

Furthermore, when the blade tip sections (r/R=0.86 and 0.94) are positioned well upstream of the vortex filament, C_n values are slightly smaller compared to their equivalent inboard counterparts. Similar behaviour appears to exist also in the C_m and

C_t curves. Additionally, as the blade trailing edge departs from the vortex, the distinct instantaneous perturbation in lift becomes almost imperceptible for the outermost span station of 0.94R (Figure 4.4.3(e)).

As far as the quarter chord pitching moment coefficient is concerned (Figures 4.4.4-6), it is observed that its overall behaviour remained consistent for most of the spanwise positions, with the obvious exception of that nearest to the tip. It is not surprising to find that there are negligible differences between the inner sections of the blade since the flow in that region is said to behave in a highly two-dimensional manner. At the tip region, however, the airflow becomes more complex and the presence of three-dimensionality is believed to be sufficiently large, resulting in the airloading coefficients differing from those on the remainder of the blade.

One might have expected the three-dimensionality of the flow to be universal, affecting all airload coefficients, but detailed examination of the C_n and C_t variations has shown otherwise (see Figures 4.4.1-3 and 4.4.7-9 respectively). Although there are some minor discrepancies in C_n and C_t between the tip and the inboard sections, the general trends of the curves have remained almost unchanged. This is not the case for the $C_{mc/4}$ where significant changes are observed and its behaviour at the outer section of the blade varies from the rest, except perhaps when $Y_v/c=0.20$ (Figure 4.4.6), where similarities exist in the early part of the interaction (up to $X_v/c=0.90$). In the latter part of the interaction process the distinct nose-up/nose-down pitching moment featured between r/R=0.62 and 0.86, disappears from sight. When the blade has fully departed from the vicinity of the vortex, the aerofoil appears to experience a positive pitching moment for all blade-vortex proximities which in turn tends to return gradually to its original value prior to interaction.

Referring to Figure 4.4.6 one notices that the duration between $C_{mc/4max}$ and $C_{mc/4min}$, in terms of blade chord travel intervals during the BVI encounter and for all radial stations, is $\approx 0.75c \pm 0.05c$. Since $C_{mc/4min}$ has been found to coincide with vortex departure from the blade trailing edge (see Section 4.1) the above finding suggests that the vortex speed of travel past the blade surface remains almost unaffected regardless of spanwise position.

Finally, by examining the Figures 4.4.7-9 it is seen that the pressure drag coefficient varies in a qualitatively similar fashion for all span stations with the most dominant feature being the large negative overshoot just prior to the interaction process. The amplitude of this overshoot is at its greatest value when the blade is on a head-on collision course and drops quite substantially when the blade-vortex proximity height is enlarged by the smallest possible margin of 0.20c from the blade's rotational plane. This decrease is more evident near the tip (r/R=0.94) where a reduction of approximately 400% and 330% are recorded for Y_v/c=-0.20 and 0.20 respectively.

4.5 ΔC_n AND $\Delta C_n/\Delta t$ VARIATIONS WITH BLADE-VORTEX PROXIMITY AND VORTEX STRENGTH

In the preceding Sections of this Chapter, a discussion and analysis of the pressure and airloading coefficient data has been presented. Emphasis was directed towards the blade-vortex interaction parameters, such as votrex strength and blade-vortex proximity and their immediate effects on the blade performance for a variety of spanwise locations. Another parameter, equally important to those mentioned above, is the maximum section lift coefficent difference (ΔC_l or ΔC_n) which plays a very important role in estimating the structural and fatigue life of a rotor blade. Moreover, it has been shown that due to the impulsive load variation during BVI, a sharp cracking

sound known as "blade slap" can be generated [5-7 and 44-52]. By referring to the results of Reference 5, it is shown that the total sound energy radiated into the far field is proportional to the square of the time-rate-change of the fluctuating load per unit span. A measure of this fluctuating load is the quantity $\Delta C_l/\Delta t$ or $\Delta C_n/\Delta t$. Therefore, for the remainder of this Chapter, the variations of the above two parameters (ΔC_n and $\Delta C_n/\Delta t$) with respect to blade-vortex proximity and vortex strength will be discussed.

Figure 4.5.1 illustrates the variations of ΔC_n with Y_v/c, for various vortex intensities, Γ, and for each of the spanwise positions examined. It is noted that as blade-vortex proximity decreases the magnitude of ΔC_n increases in an non-symmetrical fashion. For the majority of vortex strengths and radial stations, ΔC_{nmax} is observed to occur when the vortex interacts head-on with the blade ($Y_v/c=0.00$), except perhaps for the inboard radial stations, i.e. r/R=0.70 and 0.62, where ΔC_{nmax} takes place when the vortex axis is located 20% of the chord above the blade's rotational plane and only for some vortex strengths. It is interesting to note that such a shift of the ΔC_{nmax} position is only evident for $Y_v/c=0.20$. This may be attributed to the higher induced velocities and effective angles of incidence which the aerofoil experiences when the rolled-up vortex is positioned above the blade, therefore producing higher induced airloads. This is seemingly true, since for $Y_v/c\geq0.20$ the ΔC_n values are generally higher compared to those obtained at a corresponding negative Y_v/c. If the direction of rotation of the rolled-up vortex was reversed (i.e. rotating clockwise with respect to aerofoil leading edge), it would have created the opposite effect. Moreover, the magnitude of ΔC_n is reduced with decreasing vortex strength regardless of spanwise position. It is at its smallest value for the weaker vortex strength and for the extreme blade-vortex separation distances (i.e. $Y_v/c\pm1.00$).

The effect of blade-span location on the parameter ΔC_n, for a variety of blade-vortex proximities and a vortex strength of $6.70 m^2/s$ is illustrated in Figure 4.5.2. It is noted that the values of ΔC_n are lower for the inboard blade-span stations compared to the outboard ones under similar test conditions. As explained earlier in Section 4.4, this is mainly due to an increase in the negative peak normal force coefficient as the vortex convects downstream during interaction process. It is also noticed that the rate of change varies uniformly in an almost linear manner for all Y_v/c cases, with the exception of the strongest interactions (Y_v/c=0.00 and 0.20) where a sudden increase is observed for the outer radial stations of 0.86R and 0.94R. Although not shown in this dissertation, similar results are obtained for the remainder of the vortex strength cases.

Figure 4.5.3 shows the variation of $\Delta C_n/\Delta t$ ratio with blade-vortex proximity for each of the vortex strengths and radial stations examined. It is seen that the general variation and trend is very similar to that of ΔC_n, as expected, and shown in Figure 4.5.1. There is however a distinguishable increase in the rate of change of $\Delta C_n/\Delta t$, not only with increasing vortex strength but with decreasing blade-vortex separation distance. Particularly for $-0.20c \leq Y_v \leq 0.20c$, where maximum $\Delta C_n/\Delta t$ rate of change is observed. Outside this blade-vortex proximity range the rate of change is reduced and the curves drop off gradually.

Finally, the effect of vortex strength on the parameter ΔC_n is presented in Figures 4.5.4 to 4.5.8, for each spanwise station and selected blade-vortex separation distances. The vortex strengths are non-dimensionalised with the blade radius and the rotor's tip speed. By studying the above figure it is noted that ΔC_n varies linearly with vortex strength for all blade-vortex separation distances examined. The maximum rate

of increase, however, occurs when the blade slices through the rolled-up vortex. For the near-miss BVI however, i.e. $Y_V/c=0.20$, it is apparent that the gradient of the curve is very close or almost coincides with that of $Y_V/c=0.00$, as it happened for the radial station 0.78R (see Figure 4.5.6(b)). It is also observed that for positive miss-distance interactions, i.e. $Y_V/c>0.00$, the rate of change is greater compared to equivalent miss-distances below the rotor's rotational plane under similar test conditions.

Chapter V

COMPARISONS BETWEEN PRESENT AND EXISTING B.V.I. DATA

In the previous chapter, a detailed discussion and analysis of selected pressure and aerodynamic coefficient data corresponding to the NACA-0015 aerofoil blade-vortex interaction characteristics, was presented. The discussion included the aerofoil performance as a function of blade-vortex proximity in both longitudinal and vertical direction for a variety of vortex strengths and blade-span locations. During this analysis the most important observations were underlined and discussed.

In the present chapter, however, pressure and aerodynamic coefficient data obtained under the current BVI investigation are compared with those published by other researchers, obtained either by using similar experimental techniques or from computational methods.

Prior to any data comparison it is worth mentioning that the majority of the aerodynamic data obtained experimentally in the past, for the investigation of the BVI problem, a NACA-0012 aerofoil section was used as the test model [29, 34-36]. The only available data, however, obtained from a profile identical to that of the present investigation is of Surendraiah [31] and Padakannaya [32]. The required tests were performed using either two-dimensional [29] or rotary wing environment facilities [31, 32 and 34-36]. Although these tests were dissimilar to those of the present study, as far as vortex strength and tip Mach numbers are concerned, it is still instructive to compare the results from these investigations for approximately similar blade-vortex parameters, i.e. Y_v/c, X_v/c and r/R. Other blade-vortex interaction data, obtained by means of numerical methods [21,36], are also presented in the forthcoming sections for comparison. In the following comparison only the data obtained from parallel BVI investigations are considered.

5.1 COMPARISONS OF PRESSURE VARIATIONS

A selection of pressure measurements attained in the present study are compared with those acquired by Caradonna and his colleagues (References 34 and 35). The test set-up was identical for both of the above references and consisted of a two-bladed teetering-rotor of 7 ft. in diameter and 6 in. in chord. Each blade was untwisted and with a constant chord of NACA-0012 profile. The test conditions under which the experiments were performed were of much higher Mach numbers compared to the present study. It should also be mentioned that the vortex rotation in the above references is in a clockwise direction, whereas in the present study the vortex rotates anti-clockwise in relation to the blade leading edge. In order to have a more realistic comparison the blade-vortex proximity distances chosen from the present study are of

nearly equal but opposite magnitudes.

Figure 5.1.1 shows the whole set of the pressure variation histories for (a) the upper surface and (b) the lower or "vortex side" surface attained in Reference **34** and for a blade/vortex separation distance of Y_V/c=-0.22. Figure 5.1.2 also illustrates the pressure coefficient variations for both aerofoil surfaces from selected chordwise pressure stations obtained in the present study under the test conditions Y_V/c=0.20, r/R=0.86 and Γ=5.10 m^2/s.

By examining the above figure it is seen that in both sets of data the most significant event is the sharp pressure reduction and rise over the "vortex side" surface of the blade as it approaches the vortex (Figures 5.1.1(b) and 5.1.2(a)), particularly over the first 30% of the chord. For the remainder of the chord the pressure variation diminishes drastically and alters its character. Moreover, as the blade moves even further past the vortex, the disturbances described by Caradonna et al **[34]** as "propagated" and "convective", are also observed to exist in the present data, with the "convective" disturbance or "vortex peak" as it was labelled in the present study, being the clearer of the two. For the reverse side of the blade, however, the pressure perturbation signals also change very rapidly near the leading edge region and have the opposite sign of that on the "vortex side" (Figures 5.1.1(a) and 5.1.2(b)).

Figure 5.1.3 shows the effect of vortex proximity on the BVI and compares the leading edge (x/c=0.02) transducer outputs collected in Reference **35** and in the present investigation (x/c=0.0260) at three different blade-vortex separation distances. It is noticed that in both cases the trends of the curves are very similar. The strongest vortex effect is observed to take place during a head-on interaction for both sets of data. As

the blade-vortex distance increases the magnitude of the pressure pulse decreases, with the greatest reduction being between 0.00 and 0.25 (Fig. 5.1.3(a)) and -0.20 (Fig. 5.1.3(b)). It is also noticed that in the present data minimum pressure occurs approximately four degrees earlier than that of Caradonna et al **[35]**. Furthermore, the pressure variations in the present data are shown to exhibit larger magnitudes compared to their equivalent counterparts for similar blade-vortex separation distances.

Finally, pressure results obtained from the experimental investigation of Chigier et al **[69]** at r/R=0.9720 were compared with the present data (r/R=0.9443). The flow conditions and the wing geometry of Reference **69** consist of an untwisted-untapered rectangular wing with an aspect ratio 2.67 (based on semispan), set at an angle of incidence of 12° and inserted into a uniform flow of M_∞= 0.0897, producing a chord Reynolds number of Re_c=953,000.

Figure 5.1.4 shows the upper surface pressure distribution for the two test cases. It is seen that the pressure data of Reference **69**, shown in Figure 5.1.4(a), levels-off near the 40% chord and a secondary suction peak starts to form aft of the mid-chord location. This secondary peak has been shown to be associated with the formation and lift-off of a tip vortex and its subsequent roll-up in the downstream wake. Although the above data were obtained for an angle of incidence of 12°, the present data also show similar behaviour, with the secondary peak being developed between the 40% chord location and the trailing edge. One may speculate, however, that the shape of the secondary peak of the present data is more akin to a trailing edge separation bubble **[70]** than to a strong tip vortex formation. Without the support of more detailed and of higher resolution pressure measurements, no definite answer can be provided at present.

In Section 4.4, it was also suggested that tip effects may have influenced the pitching moment coefficient to vary so differently between the outermost and the inboard radial sections for all vortex intensities and blade-vortex proximities examined (Figure 4.4.4-6). If this is true, more conclusive evidence would therefore be required before an explicit statement can be given.

5.2 COMPARISONS OF AIRLOAD VARIATIONS

5.2.1 Airloading Variations with Instantaneous Blade Azimuth Position

In this Section the aerodynamic coefficient data obtained in References **21** and **36** using computational methods are presented and compared with the present data. It should be noted that the vortex in the above References has a clockwise orientation and as it approaches the aerofoil it continuously induces varying velocities that result in negative angles of attack. The generated lift therefore has opposite values compared to the present data.

Figure 5.2.1 shows the variation of lift and normal force coefficients with the instantaneous X_v position of the vortex relative to the aerofoil leading edge. It is observed that C_l and C_n are qualitatively similar. The change in lift is seen to be steeper for the data of Reference **21** as the vortex approaches the aerofoil (Figure 5.2.1(a)). As the vortex passes the aerofoil trailing edge, however, an additional negative lift is generated in both sets of data. For further progressions of the vortex downstream, the lift of the present data increases towards its initial value before interaction took place, whereas no such changes are shown to exist in the data from Reference **21** for similar vortex displacements.

Figures 5.2.2 shows a comparison of lift coefficient variations for a parallel (head-on) blade-vortex interaction, obtained theoretically by Caradonna et al **[36]** and the present investigation for the test conditions : $Y_v/c=0.00$, $r/R=0.944$ and $\Gamma=6.70$ m^2/s. Whilst differences are apparent, particularly after initial interaction, the changes in lift are, in general, very similar but with the present data exhibiting much higher magnitudes and a larger rate of change from C_{nmax} to C_{nmin}. The noticeable shift between curves, seen also in Figure 5.2.3, may be attributed to the fact that in the present study the radial axis, which passes through the mid-chord position of the aerofoil for the whole length of the blade span, was in parallel to the vortex path line at $\Psi=180.0°$. For the computed data of Reference **36**, however, it is the author's opinion that aerofoil-vortex interactions are allowed to occur when the aerofoil leading edge is exactly parallel to the vortex path line.

Figure 5.2.3 illustrates a comparison of the corresponding quarter chord pitching moment coefficient variations for the parallel blade-vortex interaction described above. Although the data obtained in Reference **36** are for a much higher Mach number, the most striking feature of Figure 5.2.3 is the great resemblance of the pitching moments. Both cases show similar behaviour, exhibiting an increasing positive pitching moment as the blade advances towards the vortex, followed by a rapid oscillatory performance as the blade slices through the vortex and a gradual recovery as it departs away from it.

Individual pressure measurements corresponding to the above comparison of the airload variation are graphically represented in Figure 5.2.4 for the chord locations $x/c=0.020$ and 0.830 **[36]** and in Figure 5.2.5 for $x/c=0.026$ and 0.886 of the present study. It is seen that in both cases there is also a striking resemblance between curves. The most interesting similarities, however, exist for the trailing edge transducers where

the curves almost match each other, particularly for an azimuth interval of approximately 8° to the right of the plots (Figures 5.2.4(b) and 5.2.5(b)).

Figures 5.2.6 and 5.2.7 illustrate the lift and leading edge pitching moment coefficient variations respectively obtained from the present investigation under the parallel BVI parameters $Y_v/c=0.20$, $\Gamma=5.10m^2/s$ and $r/R=0.70$, and those obtained experimentally by Straus et al **[29]**. In both investigations the vortex rotates in a counterclockwise sense relative to the aerofoil's leading edge. The data are plotted against non-dimensional time, i.e. Ut/c. The parameter U in the present study represents the rotational speed of the blade at the appropriate radial station (V_r), whereas in Straus et al **[29]** it represents the freestream velocity (V_∞).

By examining the above figures it is observed that the trends of the curves are qualitatively similar to each other. The lift and pitching moment coefficients gradually increase and decrease respectively as the rolled-up vortex approaches the aerofoil leading edge and produces an incident flow of higher angle of attack. It is interesting to note that as the vortex departs from the aerofoil trailing edge the curves in both cases agree very well and show the distinct feature of the additional negative lift and the abrupt increase in pitching moment coefficients. This abrupt change in lift and pitching moment is a very important result signifying the validity of the present data and the ability of the facility to capture critical events only seen so far in two-dimensional flows; either experimentally, as seen here, or numerically (Figure 5.2.1), discussed in earlier paragraphs of this Section.

As the vortex convects further downstream a noticeable lift and moment recovery is observed for both sets of data, with that of the present study having the

fastest rate of change. Furthermore, the time interval between maximum and minimum lift and pitching moment is shorter compared with that of Reference **29**. The magnitudes are also higher, exceeding in some occasions the order of two. The increase in magnitudes was not surprising since the vortex in the present investigation is almost ten times stronger and therefore produces a more powerful interaction.

5.2.2 *Variations of Differential Normal Force with Vortex Strength and Blade-Vortex Proximity*

In this Section a comparison of differential normal force coefficient variations, ΔC_n, and their time-rate variations, $\Delta C_n/\Delta t$, is carried out between existing **[31,32]** and present data. The data in the above references were obtained from a comparatively similar BVI facility and Reynolds number (6.0×10^5), but for different vortex strengths. Also, due to limitation of the facility only four pressure transducers were installed on one surface of the blade at four spanwise stations; 0.95R, 0.90R, 0.85R, 0.75R. In the following discussion, data for the spanwise stations 0.95R and 0.85R, reproduced from References **31** and **32,** are compared with those of similar radial positions (i.e. 0.94R and 0.86R) of the present study and presented in Figures 5.2.8 to 5.2.13.

Figure 5.2.8 shows a comparison of the ΔC_l and ΔC_n variations for a range of blade-vortex miss-distances, for two different vortex strengths and for the spanwise locations 0.95R **[31]** and 0.94R. The results in the above figure demonstrate quite clearly that ΔC_l and ΔC_n follow a qualitatively similar performance, that is, they decrease with increasing blade-vortex separation heights and are higher for the higher vortex strength. It is also observed that although ΔC_l and ΔC_n vary almost uniformly for different vortex intensities and identical miss-distances, the uniformity seems to

break-out as the interactions become more severe, i.e., for near-miss or head-on collisions. Similar behaviour, however, is also seen to occur for the corresponding time-rate changes of ΔC_l and ΔC_n, shown in Figure 5.2.9.

Figure 5.2.10 illustrates a comparison of ΔC_l and ΔC_n respectively, for various vortex intensities, for the same spanwise locations as above and three blade-vortex miss-distances, i.e., Y_v/c=0.00, 0.25 and 0.50 (Figure 5.2.10(a), **[31]**) and Y_v/c=0.00, 0.20 and 0.40 from the present study (Figure 5.2.10(b)). It is noticed that the differential lift and normal force coefficients vary in a linear fashion, increasing with increasing vortex strength, for both sets of data. The highest changes are observed to occur when Y_v/c=0.00, for all vortex intensities. The analogous $\Delta C_l/\Delta t$ and $\Delta C_n/\Delta t$ for the conditions of Figure 5.2.10 are shown in Figure 5.2.11. It is seen that their behaviour is also qualitatively similar, with the rate of change being much stronger for the present data, for similar blade-vortex miss-distances.

Figure 5.2.12 shows a comparison of the ΔC_l and ΔC_n variations alongside their equvalent $\Delta C_l/\Delta t$ and $\Delta C_n/\Delta t$ for a range of blade-vortex miss-distances, for two different vortex strengths and for the spanwise positions 0.85R **[32]** and 0.86R. The results once more are in good qualitative agreement, showing an increasing lift with decreasing blade-vortex separation heights (Y_v/c). The large increments between ΔC_n and $\Delta C_n/\Delta t$, compared to ΔC_l and $\Delta C_l/\Delta t$ (Figure 5.2.12(a)), may be attributed to larger time intervals between ΔC_{nmax} and ΔC_{nmin} in the present investigation.

Finally, Figure 5.2.13 shows the results of the ΔC_n variations for a variety of vortex intensities, three blade-vortex miss-distances, i.e., Y_v/c=0.00, 0.25 and 0.50 (Figure 5.2.13(a), **[32]**) and Y_v/c=0.00, 0.20 and 0.40 from the present study (Figure

5.2.13(b)) and for the same spanwise positions described in Figure 5.2.12. It is clearly seen that although ΔC_n is increasing linearly with intensifying vortex strength, the incremental changes for different Y_v/c locations, vary in a non-linear manner, with those of Reference **32** (Figure 5.2.13(a)) having the largest offset values from the mean-line.

In conclusion it may be said that although the existing theoretical and experimental test conditions were dissimilar to those of the present study, the general behaviour of the present pressures and normal force coefficients remained qualitatively similar for approximately matching BVI parameters.

Chapter VI

CONCLUSIONS AND RECOMMENDATIONS FOR FURTHER STUDIES

An experimental approach to study the blade-vortex interaction phenomenon has been conducted in the present dissertation. The primary objective of this investigation has been to examine the BVI problem within the controlled environment of a wind tunnel. The experimental method employed consists of a highly instrumented single-blade non-lifting model rotor interacting with a well defined vortex filament generated from a vortex generator wing mounted vertically and upstream of the rotor disc. The method permits good control of the vortex, whose position and strength can easily be altered to satisfy the requirements of each test. Blade-vortex encounters have been recorded using sensitive ultra miniature pressure transducers for various combinations of vortex strengths, blade spanwise positions, blade-vortex interaction angles and blade-vortex proximities varying from -1.00c to 1.00c with an increment of 0.20c. The results were quite repetitive and consistent. The recorded

pressure data were used to determine chordwise pressure distributions around the aerofoil for different blade span stations and azimuthal airload coefficient variations.

Furthermore, the pressure and airload coefficients obtained in the present investigation were compared with those obtained by other researchers using similar test facilities or newly developed computational methods.

6.1 SUMMARY OF CONCLUSIONS

Prior to any data recording a number of important modifications were required to improve the existing University of Glasgow BVI facility. The most major modifications included the redesigning of the signal amplification system, the introduction of a more powerful computer in terms of computational speeds and storage capacity and last but not least the transducer installation technique.

The pressure transducers used, proved to be very reliable throughout the experimental investigation of the BVI phenomenon despite the harsh treatment to which they were subjected during testing. Their reliability can also be seen in the recorded data, where meaningful and consistent results were obtained.

Due to limitations of the present BVI facility the results are not representative of self-generated blade-vortex interactions for rotors in flight, but the general blade-vortex interaction effects are very well documented. The primary objectives, set for investigating the BVI phenomenon, were predominantly fulfilled and the recorded data are more accurate and less "noisy" compared to those obtained by Kokkalis **[37]**. Moreover, the results presented here are but a small sample of the data that has been

acquired during the length of this investigation.

It has been noted that the interaction resulting from a rotating blade and an upstream generated vortex rotating in a counter-clockwise fashion relative to the blade leading edge, is characterised by an abrupt suction followed by a rapid compression of the leading edge pressures as the vortex passes near the blade's leading edge. This sudden change of the leading edge pressure results in the rapid variation of the sectional forces and moment coefficients which in turn are responsible for the increase in blade vibrational levels during blade-vortex interaction.

Although significant distortion of the vortex, and even splitting, can occur during close blade-vortex interactions, the current pressure measurement technique was able to record very successfully the splitting of the vortex during head-on collisions. It is also shown that when a vortex is on a near-miss collision course ($Y_V/c=\pm 0.20$) a "vortex peak" is produced over the vortex side of the blade. It is found that this "vortex peak" convects downstream at a much faster speed over the aerofoil when $Y_V/c=0.20$. This is attributed to the direction of rotation of the vortex as it interacts with the rotating blade. Due to an increase in the vortex induced velocities, past the aerofoil, the flow accelerates over the whole length of the upper surface.

The impulsive airloads caused by the blade-vortex interactions were clearly identified and their behaviour was found to depend quite strongly on the convective movement of the vortex. Their intensity and shape was little affected by the blade-span location. Moreover, their behaviour was found to be strongly dependent upon the vortex strength and blade-vortex proximity. In general, the effect of increasing the vortex strength or reducing the blade-vortex separation height led to an increase of the

interaction intensity.

The most obvious effects appear to occur during the immediate interaction phase, i.e. when the vortex is within one chord length of the blade ($-1.00 \leq X_v/c \leq 1.00$). The main features are the rapid increase and subsequent decrease of the lift, a result caused by the variation of the effective angle of attack of the blade induced by the oncoming vortex. Similar behaviour due to the effective angle of attack variation, were also found to exist for the quarter chord pitching moment and pressure drag coefficients. The variations in the pitching moment coefficient however, were found to differ substantially between lower ($Y_v/c \leq -0.20$) and higher ($Y_v/c \geq 0.20$) blade-vortex miss distances.

Furthermore, it is seen that as the blade trailing edge departs from the vortex, the influence of the vortex on the surrounding flow field remains the most dominant feature. This was demonstrated in the local surface pressure variation plots where additional pressure suction was observed to occur over the rear section of the aerofoil and on the opposite vortex side. Such pressure behaviour affected the section airloading performance where characteristic abrupt changes were observed, particularly in the normal force and quarter chord pitching moment coefficient and for vortex miss distances 0.20c and 0.40c.

The maximum section lift coefficient difference parameter was shown to increase significantly with decreasing blade-vortex miss-distance and increasing vortex strength. The most important changes, however, were observed to occur when the blade passed through the vortex core and when the vortex was at its greatest intensity. Higher ΔC_n values were obtained for positive Y_v/c locations than the corresponding

negative ones.

Furthermore, ΔC_n and $\Delta C_n/\Delta t$ values varied in a linear fashion with vortex strength producing different slopes for different Y_v/c positions. The maximum slope has been obtained during head-on interactions. ΔC_n was also shown to vary linearly with radial station. The rate of change, however, was found to be similar for all spanwise positions with the exception of 0.86R and 0.94R and for one of the strongest interactions examined, i.e. Y_v/c=0.00 and 0.20.

Finally, in a further analysis of the present BVI results, comparisons were made with data obtained either by means of experimental or numerical methods. In general, the behaviour of the NACA-0015 aerofoil, interacting with a vortex of various strengths, was found to be qualitatively similar with that of identical or different aerofoil sections obtained by other researchers. These included the azimuthal variation of both chordwise pressure and airload coefficients, with data obtained at considerably higher Mach numbers.

6.2 RECOMMENDATIONS FOR FURTHER STUDY

To date, most of the BVI experimental studies are related to the requirement of an extensive knowledge about the induced pressures and airloads. The results obtained from such investigations are used for validating newly developed or existing aerodynamic force prediction codes and an adequate data base has already started to emerge. However, due to the complexity of the flow during a BVI (i.e. excessive flow turbulence, three-dimensional effects of yaw and rotational accelerations) very little is known about the flow field past the surface of the aerofoil. Therefore, detailed

measurements of the aerofoil's boundary layer characteristics would be useful. Although, as it was shown in the present study, meaningful information can be drawn from pressure distribution histories, inside knowledge of the aerofoil's boundary layer remains virtually untouched.

In order to achieve that additional information hot-film sensors, positioned around the aerofoil surface, are suggested. They are known to be highly sensitive devices with the ability to respond to flow fluctuations at high frequencies. The recording of flow reversal, from which flow separation can be implied, is their most significant contribution. Other advantages of the hot-film measuring technique are the low cost and simplicity to install on large body surfaces. Their main disadvantage however, is the self-generated "turbulence wedge" which may modify the boundary layer behaviour at low speeds. However, the difficulty to install such devices on the present BVI model rotor, due to limited aerofoil surface available, is well appreciated and understood.

Since the rotor blade airloads were shown to be very sensitive to the vortex locations and strength, the most important issue however must be the development of practical means to alleviate the vortex effect on the blade's airloads. To reduce the vortex effect it is therefore sensible to either increase the distance between blade and vortex or reduce the vortex strength which in turn will result to weaker interactions and improving the overall rotor performance.

In the last decade, such measures have already been applied with the introduction of new blade-tip planforms and tip aerofoil geometries **[63-68]**. The RAE Puma swept tip **[65]**, the British Experimental Rotor Program (BERP) **[66]** and

the SPP8 [67,68] configurations are the most well known. As far as alleviating the vortex effect onto the blade's airloads is concerned, the inclusion of an evolutive anhedral at the tip of the blade has been the most favourable design. By inclining the blade-tip downward, the vortex is shed at a lower level and passes further beneath the next blade, reducing the interaction and enhancing the blade performance. In particular during hover, where perpendicular BVIs have been known to occur on a regular basis, the rotor performance has been greatly improved [67,68].

Although large amounts of data have been acquired from wind tunnel and in-flight experiments, to study the aerodynamic performance of the modified rotors at different flight envelopes, to the author's knowledge little is known about the BVI effect on the new blade-tip designs. Since the rotor's blade-tip of the present BVI facility can incorporate tips of different designs and geometries, it is therefore recommended that an investigation of the BVI phenomenon on these new tips would be worth looking into.

Further research may also be conducted to examine the extent of the BVI effect on different blade sections. The introduction of a tilt twin rotor to replace the present single-bladed rotor, so that a general picture is obtained for different blade angles of incidence, may also prove useful.

6.3 CONCLUDING REMARKS

The current BVI facility has fulfilled the objectives set at the start of this investigation. Modifications of the BVI facility were performed, suggested in the dissertation of Kokkalis [37] or identified during the course of this work. The

acquired results provided valuable information about the aerodynamic characteristics of the NACA-0015 aerofoil section tested in a rotary wing environment. The main BVI effects, such as of different blade-vortex proximities, vortex strength and spanwise variations, were thoroughly examined. It is rather unfortunate, however, that speculations may arise about the validity of the results, mainly because of the low blade-tip Reynolds numbers involved. It is hoped that the results obtained in this investigation will encourage future researchers towards the development or improvement of similar test facilities associated with the study of the BVI problem.

References

[1] Johnson, W.
"Helicopter Theory"
Princeton University Press, New Jersey, 1980.

[2] McCormick, B.W., Tangler, J.L. and Sherrieb, H.E.
"Structure of Trailing Vortices"
AIAA Journal of Aircraft, Volume 5, No. 3, pp. 260-267, May-June 1968.

[3] Scheiman, J. and Ludi, L.H.
"Qualitative Evaluation of the Effect of Helicopter Blade Tip Vortex on Blade Airloads"
NASA TN D-1673, 1963.

[4] Hooper, W.E.
"The Vibratory Airloading of Helicopter Rotors"
Proceedings of the 9th European Rotorcraft and Powered Lift Aircraft Forum, Stresa, Italy, September, 1983.

[5] Leverton, J.W. and Taylor, F.W.
"Helicopter Blade Slap"
Journal of Sound and Vibration, Volume 4, No. 3, pp. 345-357, 1966.

[6] Schmitz, F.H. and Boxwell, D.A.
"In-Flight Far Field Measurement of Helicopter Impulsive Noise"
Journal of the American Helicopter Society, Volume 21, No. 4, October 1976.

[7] Tangler, J.L.
"Schlieren and Noise Studies of Rotor in Forward Flight"
Presented at the 33rd Annual National V/STOL Forum of the American Helicopter Society, Washington D.C., May 1977.

[8] Shockey, G.A., Williamson, J.W. and Cox, C.R.
"Helicopter Aerodynamics and Structural Loads Survey"
Presented at the 33rd Annual National V/STOL Forum of the American Helicopter Society, Washington D.C., May 1976.

[9] Schmitz, F.H. and Yu, Y.H.
"Helicopter Impulsive Noise: Theoretical and Experimental Status"
NASA TM-84390, November 1983.

[10] Booth, E.R.Jr. and Yu, J.C.
"Two-Dimensional Blade-Vortex Flow Visualisation Investigation"
AIAA Journal, Volume 24, No. 9, pp. 1468-1473, September 1986.

[11] Glauert, H.
"The Elements of Aerofoil and Airscrew Theory"
Cambridge University Press, 1926.

[12] Simons, I.A.
"Some Aspects of Blade/Vortex Interaction on Helicopter Rotors in Forward Flight"
Journal of Sound and Vibration, Volume 4, No. 3, pp. 268-281, 1966.

[13] Johnson, W.
"A Lifting Surface Solution for Vortex Induced Airloads and its Application to Rotary Wing Airloads Calculations"
ASRL TR 153-2, M.I.T. Aeroelastic and Structures Lab., April 1970.

[14] Johnson, W.
"A Comparison Between Experimental Data and a Lifting Surface Theory Calculation of Vortex Induced Loads"
ASRL TR 153-3. M.I.T. Aeroelastic and Structures Lab., August 1970.

[15] McCroskey, J.W. and Goorjian, P.M.
"Interactions of Airfoils with Gusts and Concentrated Vortices In Unsteady Transonic Flow"
AIAA Paper 83-1691, AIAA 16th Fluid and Plasma Dynamics Conference, Danvers, Massachusetts, July 12-14, 1983.

[16] Caradonna, F.X., Desopper, A., Tung, C.
"Finite Difference Modelling of Rotor Flows Including Wake Effects"
Proceedings of the 8th European Rotorcraft and Powered Lift Aircraft Forum, Aix-en-Provence, France, August 1982.

[17] Srinivasan G.R.
"Computations of Two-Dimensional Airfoil-Vortex Interactions"
NASA CR 3885, May 1985.

[18] Srinivasan, G.R., McCroskey, J.W. and Baeder, J.D.
"Aerodynamics of Two-Dimensional Blade-Vortex Interaction"
AIAA Journal, Vol. 24, No. 10, pp. 1569-1576, October 1986.

[19] Srinivasan, G.R. and McCroskey, J.W.
"Numerical Simulations of Unsteady Airfoil-Vortex Interactions"
Vertica, Vol. 11, No. 1/2, pp. 3-28, 1987.

[20] Panaras, A.G.
"Modelling of the Vortex-Airfoil Interaction"
AIAA Journal, Vol. 25, pp. 5-11, January 1987.

[21] Lee, D.J. and Smith, C.A.
"Distortion of the Vortex Core During Blade/Vortex Interaction"
AIAA Paper 87-1243, AIAA 19th Fluid Dynamics, Plasma Dynamics and Laser Conference, Honolulu, Hawaii, June 8-10, 1987.

[22] Meier, G.E.A. and Timm, R.
"Unsteady Vortex Airfoil Interaction"
AGARD CP-386, AGARD Symposium on Unsteady Aerodynamics: Fundamentals and Applications to Aircraft Dynamics, May 1985.

[23] McAlister, K.W. and Tung, C.
"Airfoil Interaction with an Impinging Vortex"
NASA TP-2273, 1984.

[24] Kantha, H.L., Lewellen, W.S. and Durgin, F.H.
"Qualitative Responses of a Vortex Core to Tip Blowing and Intersecting Airfoils"
NASA CR-126675, August 1971.

[25] Seath, D.D.
"Vortex-Airfoil Interaction Tests"
2nd Atmospheric Flight Mechanics Conference, Palo Alto and Moffet Field, California, September 11-13, 1972.

[26] Ham, N.D.
"Some Conclusions from an Investigation of Blade-Vortex Interaction"
Journal of the American Helicopter Society, Volume 20, pp. 45-48, October 1975.

[27] Dunagan, S.E. and Norman, T.R.
"Lift Distributions and Velocity Field Measurements for a Three-Dimension-al, Steady Blade/Vortex Interaction"
NASA TM-100013, November 1987.

[28] Booth, E.R., Jr.
"Surface Pressure Measurement During Low Speed Two-Dimensional Blade Vortex Interaction"
AIAA Paper 86-1856, AIAA 10th Aeroacoustics Conference, Seattle, Washington, July 9-11, 1986.

[29] Straus, J., Renzoni, P. and Mayle, R.E.
"Airfoil Pressure Measurements During a Blade Vortex Interaction and a Comparison with Theory"
AIAA Journal, Vol. 28, No. 2, pp. 222-228, February 1990.

[30] Seath, D.D., Kim, J.M. and Wilson, D.R.
"An Investigation of the Parallel Blade-Vortex Interaction in Low-Speed Wind Tunnel"
AIAA Paper 87-1345, AIAA 19th Fluid Dynamics, Plasma Dynamics and Laser Conference, Honolulu, Hawaii, June 8-10, 1987.

[31] Surendraiah, M.
"An Experimental Study of Rotor Blade-Vortex Interaction"
NASA CR-1573, May 1970.

[32] Padakannaya, R.
"Experimental Study of Rotor Unsteady Airloads due to Blade-Vortex Interaction"
NASA CR-1909, November 1971.

[33] Ham, N.D.
"Some Preliminary Results from an Investigation of BladeVortex Interaction"
Journal of the American Helicopter Society, Vol . 19, pp. 45-48, April 1974.

[34] Caradonna, F.X., Laub, G.H. and Tung, C.
"An Experimental Investigation of the Parallel Blade-Vortex Interaction"
Proceedings of the 10th European Rotorcraft and Powered Lift Aircraft Forum, The Hague, The Netherlands, August 1984.

[35] Caradonna, F.X., Lautenschlager, J.L. and Silva, M.J.
"An Experimental Study of Rotor-Vortex Interactions"
AIAA Paper 88-0045 , AIAA 26th Aerospace Sciences Meeting, Reno, Nevada, January 11-14, 1988.

[36] Caradonna, F.X., Strawn, R.C. and Bridgeman, J.O.
"An Experimental and Computational Study of Rotor-Vortex Interactions"
Proceedings of the 14th European Rotorcraft and Powered Lift Aircraft Forum, Milano, Italy, September 20-23, 1988.

[37] Kokkalis, A.
"An Experimental Investigation of Parallel Blade/Vortex Interaction for a NACA-0015 Airfoil"
Ph.D. Thesis, Department of Aerospace Engineering, University of Glasgow, Scotland, United Kingdom, April 1988.

[38] Neuwerth, G. and Muller, R.
"Pressure Fluctuations on Rotor Blades Generated by Blade-Vortex Interaction"
Vertica, Vol. 9, No. 3, pp. 227-239, 1985.

[39] Scheiman, J. and Kelly, H.L.
"Comparison of Flight-Measured Helicopter Rotor Blade Chordwise Pressure Distributions with Static Two-Dimensional Airfoil Characteristics"
NASA TN D-3936, May 1967.

[40] Scheiman, J.
"A Tabulation of Helicopter Rotor-Blade Differential Pressures, Stresses and Motions as Measured in Flight"
NASA TM X-952, 1964.

[41] Pruyn, R.R. and Alexander, W.T., Jr.
"USAALABS Tandem Rotor Airloads Measurement Program"
Journal of Aircraft, Volume 4, No. 3, May-June, 1967.

[42] Brotherhood, P. and Riely, M.J.
"Flight Experiments on Aerodynamic Features Affecting Helicopter Blade Design"
Vertica, Volume 2, pp. 27-42, 1978.

[43] Brotherhood, P. and Young, C.
"The Measurement and Interpretation of Rotor Blade Pressures and Loads on a Puma Helicopter in Flight"
Proceedings of the 7th European Rotorcraft and Powered Lift Aircraft Forum, Garmisch-Partenkirchen, Federal Republic of Germany, September 8-11, 1981.

[44] Sakowski, P. and Charles, B.
"Noise Measurement Test Results for AH-1G Operational Loads Survey"
Volumes I and II, Report 299-099-831, Bell Helicopter Co., 1976.

[45] Leverton, J.W., Pollard, J.S. and Wills, C.R.
"Main Rotor Wake/Tail Rotor Interaction"
Vertica, Vol. 1, pp. 213-221, 1977.

[46] Nakamura, Y.
"Prediction of Blade-Vortex Interaction Noise From Measured Blade Pressure"
Proceedings of the 7th European Rotorcraft and Powered Lift Aircraft Forum, Garmisch-Partenkirchen, Federal Republic of Germany, September 8-11, 1981.

[47] Boxwell, D.A. and Schmitz, F.H.
"Full Scale Measurements of Blade-Vortex Interaction Noise"
Journal of the American Helicopter Society, October 1982.

[48] George, A.R. and Chang, B.
"Flow Field and Acoustics of Two-Dimensional Transonic Blade-Vortex Interactions"
AIAA-84-2309 , AIAA/NASA 9th Aeroacoustics Conference, Willamsburg, Virginia, October 15-17, 1984.

[49] Fontana, R.R. and Hubbard, J.E., Jr.
"A Comparison with Theory of Peak-to-Peak Sound Level for a Model Helicopter Rotor Generating Blade Slap at Low Tip Speeds"
Vertica, Vol. 9, No. 2, pp. 101-125, 1985.

[50] Lee, D.J.
"An Analysis of Blade Vortex Interaction Aerodynamics and Acoustics"
NASA CR-177016, September 1985.

[51] Brooks, T.F. and Marcolini, M.A.
"Airfoil Tip Vortex Formation Noise"
AIAA Journal, Vol. 24, No. 2, pp. 246-252, February 1986.

[52] Hoad, D.R., Elliot, S.W. and Orie, N.M.
"Rotor Performance Characteristics from Aeroacoustic Helicopter Wind- Tunnel Test Program"
NASA TM-87661, May 1986.

[53] Saliveros, E. and Galbraith, R.A.McD.
"Collected Data From Blade Vortex Interaction Tests Using a Single-Blade, Non-Lifting Rotor (r/R=0.94)"
G.U. Aero. Report 9007, Department of Aerospace Engineering, University of Glasgow, Scotland, United Kingdom, March 1990.

[54] Saliveros, E. and Galbraith, R.A.McD.
"Collected Data From Blade Vortex Interaction Tests Using a Single-Blade, Non-Lifting Rotor (r/R=0.86)"
G.U. Aero. Report 9008, Department of Aerospace Engineering, University of Glasgow, Scotland, United Kingdom, March 1990.

[55] Saliveros, E. and Galbraith, R.A.McD.
"Collected Data From Blade Vortex Interaction Tests Using a Single-Blade, Non-Lifting Rotor (r/R=0.78)"
G.U. Aero. Report 9009, Department Of Aerospace Engineering, University of Glasgow, Scotland, United Kingdom, March 1990.

[56] Saliveros, E. and Galbraith, R.A.McD.
"Collected Data From Blade Vortex Interaction Tests Using a Single-Blade, Non-Lifting Rotor (r/R=0.70)"
G.U. Aero. Report 9010, Department of Aerospace Engineering, University of Glasgow, Scotland, United Kingdom, March 1990.

[57] Saliveros, E. and Galbraith, R.A.McD.
"Collected Data From Blade Vortex Interaction Tests Using a Single-Blade, Non-Lifting Rotor (r/R=0.62)"
G.U. Aero. Report 9011, Department of Aerospace Engineering, University of Glasgow, Scotland, United Kingdom, March 1990.

[58] Furness Controls Limited.
"Instruction Manual of the FC012 Micromanometer"

[59] Mason, W.H., Marchman, J.F.
"Farfield Structure of an Aircraft Trailing Vortex Including Effects of Mass Injection"
NASA CR-62078, 1972.

[60] Reed, R.E., Jr.
"Properties of the lateral Random Oscillations of Trailing Vortices Observed in Wind Tunnel Tests"
Technical Report 47, NEAR inc., Mountain View, California, U.S.A., January 1973.

[61] Corsiglia, V.R., Schwind, R.G., Chigier, N.A.
"Rapid Scanning, Three-dimensional Hot-Wire Anemometer Surveys of Wing-tip Vortices"
Journal of Aircraft, Vol. 10, No. 12, pp. 752-757, December 1973.

[62] Hoffman, E.R., Joubert, P.N.
"Turbulent Line Vortices"
Journal of Fluid Mechanics, Vol. 16, No. 3, pp. 395-411, July 1963.

[63] Muller, R.H.G.
"The Influence of winglets on Rotor Aerodynamics"
Proceedings of the 12th European Rotorcraft and Powered Lift Aircraft Forum, Garmisch-Partenkirchen, Federal Republic of Germany, September 22-25, 1986.

[64] Muller, R.H.G.
"Winglets on Rotorblades in Forward Flight: A Theoretical and Experimental Investigation"
Proceedings of the 14h European Rotorcraft and Powered Lift Aircraft Forum, Milano, Italy, September 20-23, 1988.

[65] Riley, M.J., Miller, J.V.
"Pressure Distributions on a Helicopter Swept Tip from Flight Tests and from Calculations"
Proceedings of the 9th European Rotorcraft and Powered Lift Aircraft Forum, Stresa, Italy, September, 1983.

[66] Hansford, R.E.
"Rotor Load Correletion with the British Experimental Rotor Program Blade"
Journal of the American Helicopter Society, Volume 32, No. 3, July 1987.

[67] Desopper, A., Lafon, P., Philippe, J.J., Prieur, J.
"Effects of an Anhedral Sweptback Tip on the Performace of a Helicopter Rotor"
Vertica, Vol. 12, No. 4, pp. 345-355, 1988.

[68] Vuillet, A., Allongue, M., Philippe, J.J., Desopper, A.
"Performance and Aerodynamic Development of the Super Puma Mk II Main Rotor with New SPP8 Blade Tip Design"
Proceedings of the 15th European Rotorcraft and Powered Lift Aircraft Forum, Amsterdam, The Netherlands, 12-15 September, 1989.

[69] Chigier, N.A., Corsiglia, V.R.
"Tip Vortices - Velocity Distributions"
NASA TM X-62087, September 1971.

[70] Saliveros, E.
"The Aerodynamic Performance of the NACA-4415 Aerofoil Section at Low Reynolds Numbers"
M.Sc. Thesis, Department of Aerospace Engineering, University of Glasgow, Scotland, United Kingdom, November 1988.

TABLE 1

Coordinates of NACA-0015 Aerofoil Section

x/c	y/c
0.00000	0.00000
0.01000	0.02129
0.02000	0.02949
0.03000	0.03550
0.05000	0.04443
0.07500	0.05250
0.10000	0.05853
0.12500	0.06319
0.15000	0.06681
0.17500	0.06961
0.20000	0.07172
0.24000	0.07391
0.28000	0.07490
0.32000	0.07490
0.36000	0.07408
0.40000	0.07253
0.45000	0.06976
0.50000	0.06617
0.55000	0.06190
0.60000	0.05704
0.65000	0.05165
0.70000	0.04579
0.75000	0.03950
0.80000	0.03279
0.85000	0.02567
0.90000	0.01809
0.95000	0.01008
1.00000	0.00157

TABLE 2 Pressure Transducer Calibration Information

Transducer Model & Serial Number	Chordwise Location (x/c)	Transducer Sensitivity (mV/p.s.i.)			
		Manufacture	0.9443R	0.8647R	0.7851R
ENTRAN - 2491	0.97383(US)	14.500	15.846	15.892	15.798
ENTRAN - 2512	0.89195	13.860	15.391	15.976	15.785
ENTRAN - 2503	0.80121	15.730	16.951	16.015	15.759
ENTRAN - 2514	0.70000	14.480	14.581	15.209	14.737
ENTRAN - 2522	0.60174	14.060	14.415	14.844	14.667
ENTRAN - 2487	0.50624	13.700	13.540	13.797	13.587
ENTRAN - 2516	0.40201	13.990	13.861	12.192	13.999
ENTRAN - 2519	0.29799	13.770	14.447	15.852	14.898
ENTRAN - 2513	0.20604	14.910	16.079	16.940	16.327
ENTRAN - 2489	0.13960	14.300	15.513	15.912	15.535
ENTRAN - 2494	0.09396	14.370	15.765	16.209	16.088
ENTRAN - 2488	0.05101	13.820	19.263	19.674	19.756
KULITE - 239	0.02617	14.980	14.990	15.636	15.108
KULITE - 236	0.00671	14.810	14.807	15.554	14.954
KULITE - 237	0.00000	14.480	16.217	15.965	15.337
KULITE - 240	0.00671(LS)	14.960	14.435	14.245	14.708
ENTRAN - 2495	0.02550	14.870	20.518	21.244	21.102
ENTRAN - 2506	0.06477	15.010	15.843	16.019	16.110
ENTRAN - 2498	0.10805	16.180	15.189	15.297	15.094
ENTRAN - 2504	0.18322	15.276	16.247	16.816	16.518
ENTRAN - 2511	0.28121	13.800	14.739	15.449	15.049
ENTRAN - 2492	0.38993	13.910	14.910	15.035	15.035
ENTRAN - 2515	0.51141	14.520	16.274	16.479	16.506
ENTRAN - 2500	0.64228	14.800	16.539	16.920	16.847
ENTRAN - 2497	0.78993	15.420	15.959	16.175	16.075
ENTRAN - 2523	0.95436	13.974	14.208	14.839	14.384

US : Upper Surface

LS : Lower Surface

TABLE 3. Details of Parallel and Oblique B.V.I. Tests

TABLE 3.1 Summary of Parallel B.V.I. Tests

Spanwise Position (r/R)	0.9443		0.8647		0.7851		0.7056		0.6260	
Vortex Strength (m^2/s)	1.10		2.20		3.40		5.10		6.70	
Blade/Vortex Miss Distance	-1.00	-0.80	-0.60	-0.40	-0.20	0.00	0.20	0.40	0.60	0.80	1.00

(All Perturbations)

TABLE 3.2 Summary of Oblique B.V.I. Tests

Spanwise Position (r/R)	0.9443		0.8647		0.7851		0.7056		0.6260	
Vortex Strength (m^2/s)	6.70									
Blade/Vortex Lateral Distance	2.00		1.00		-1.00		-2.00			
Blade/Vortex Miss Distance	-1.00	-0.80	-0.60	-0.40	-0.20	0.00	0.20	0.40	0.60	0.80	1.00

(All Perturbations)

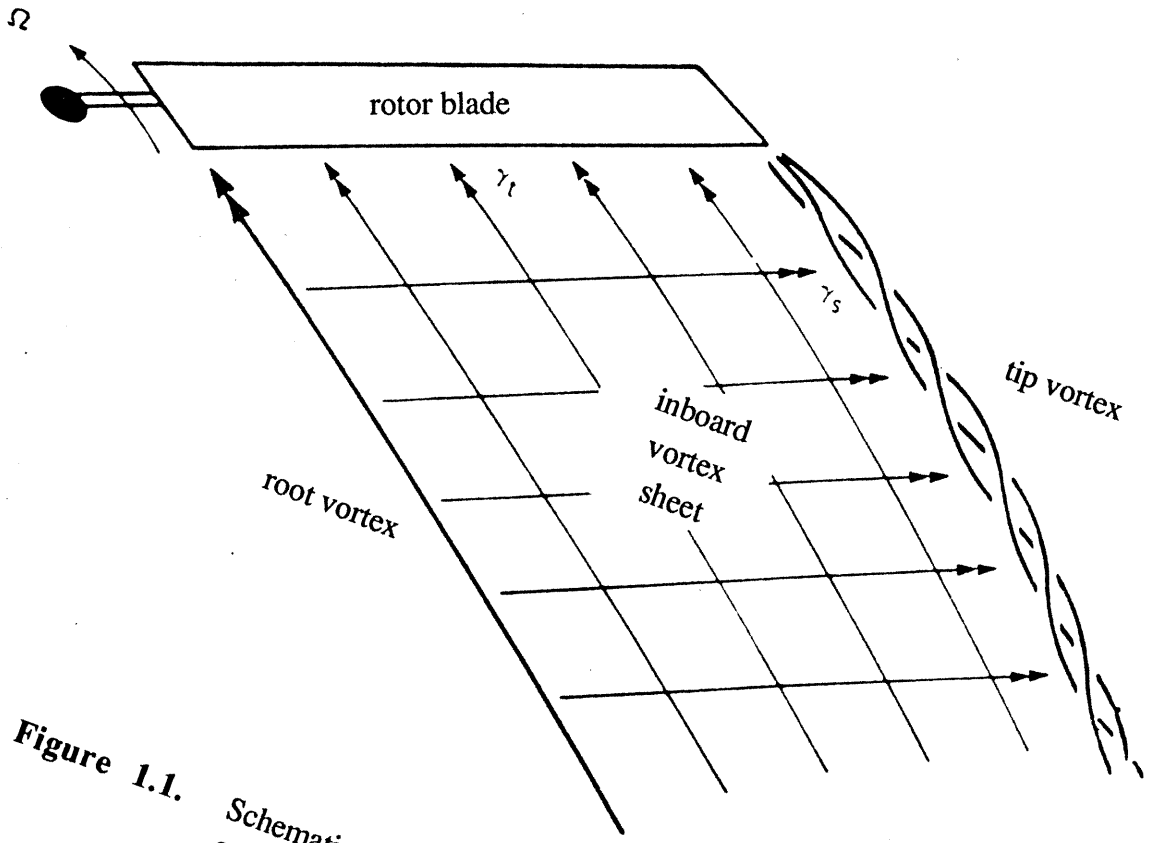

Figure 1.1. Schematic of Trailed and Shed Vorticities for a Single Blade

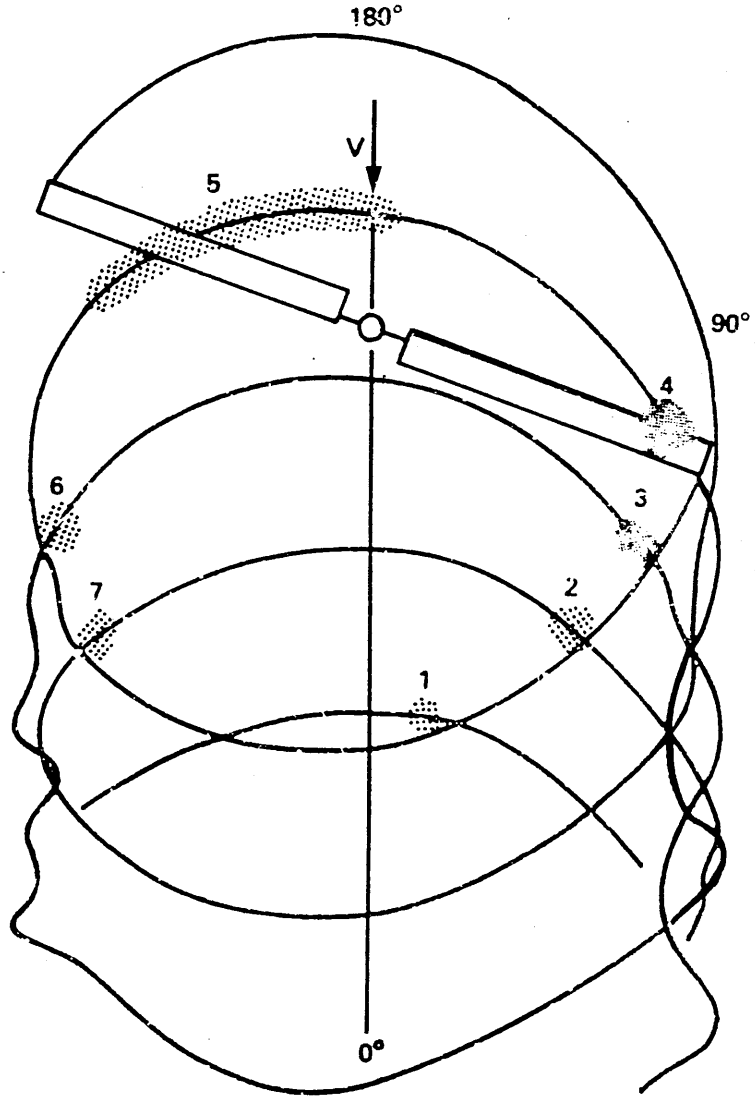

Figure 1.2. Blade-Vortex Interactions During Partial Power Descent (Ref. 7)

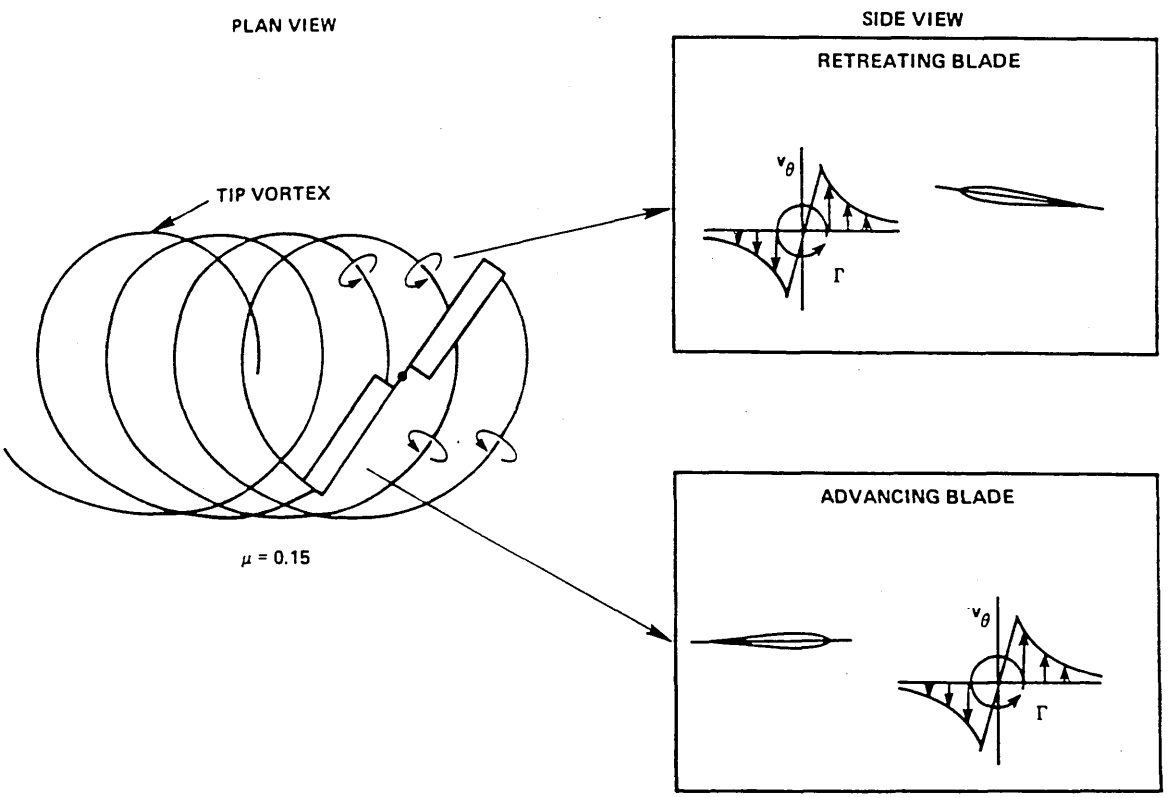

Figure 1.3. Blade-Vortex Interactions on Advancing and on Retreating Sides (Ref. **4 5**)

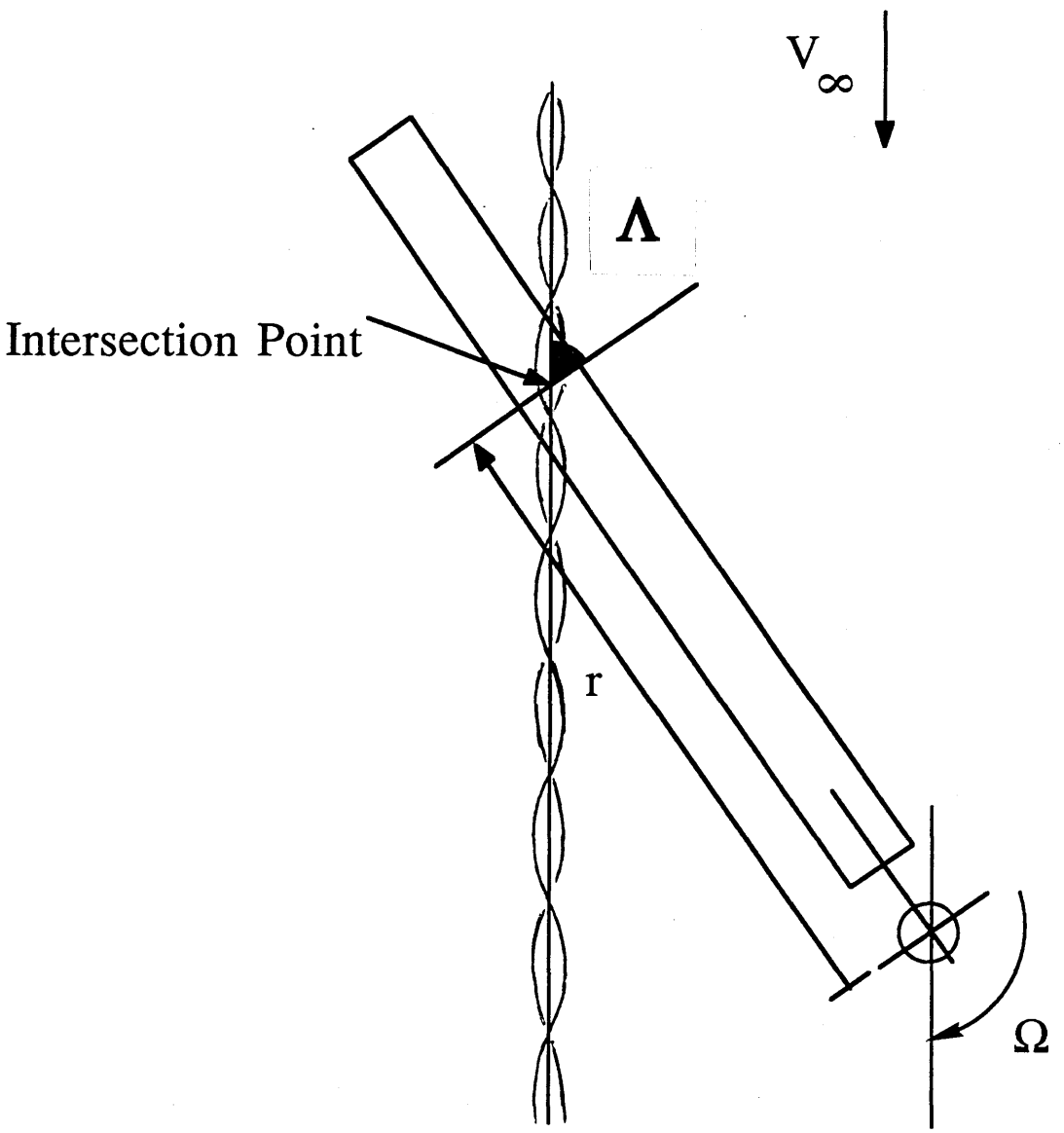

Figure 1.4. A Schematic of Blade Passing Through a Tip Vortex

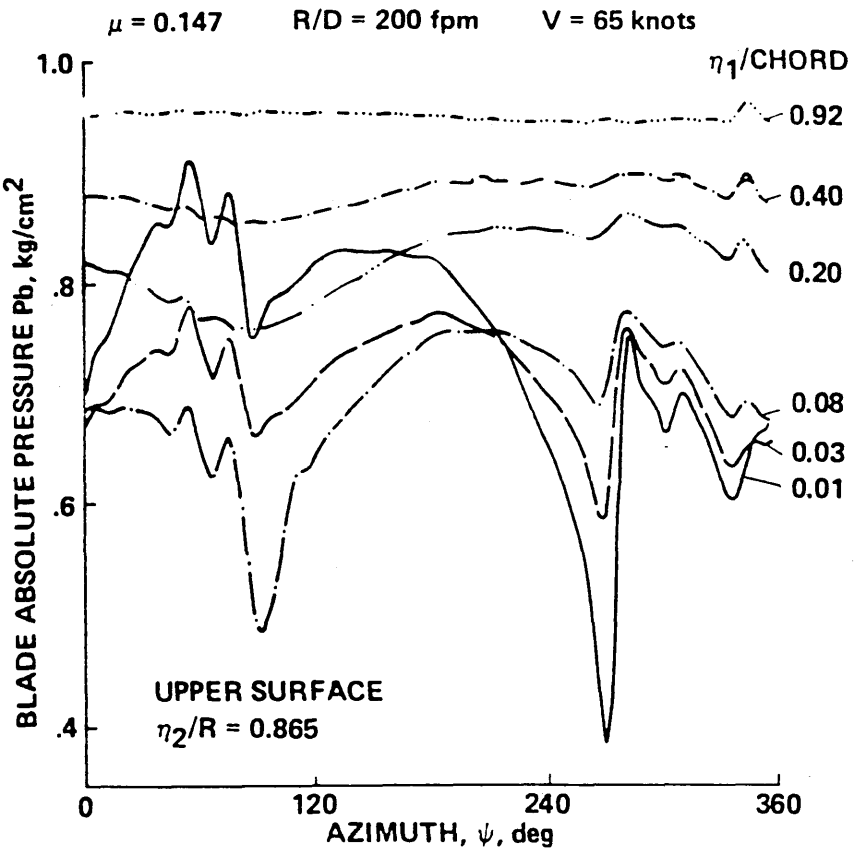

Figure 1.5. Example of Blade Surface Pressure Histories at Different Chord Positions (Ref. 8)

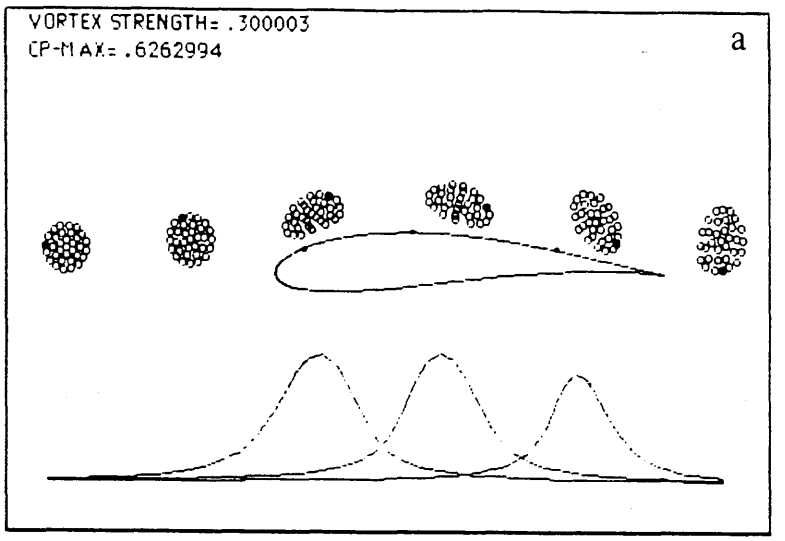

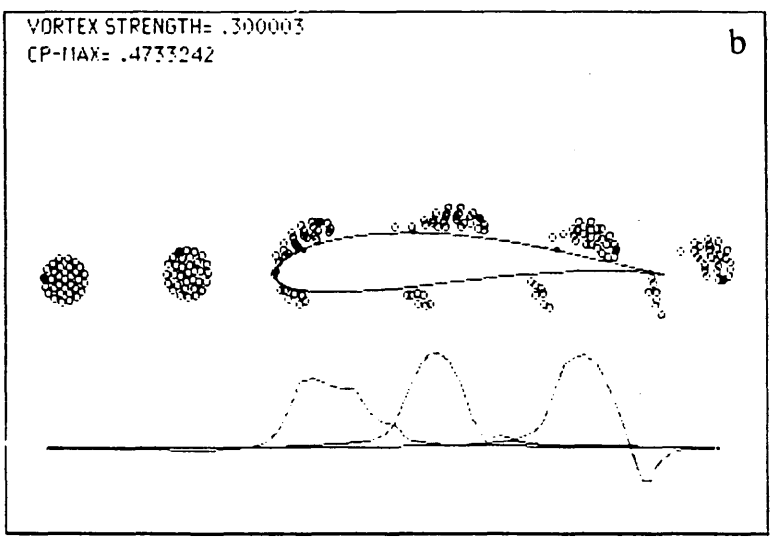

Figure 1.6. An Illustration of Vortex Distortion During (a) a Near-miss and (b) a Head-on Aerofoil-Vortex Interaction (Ref. **20**)

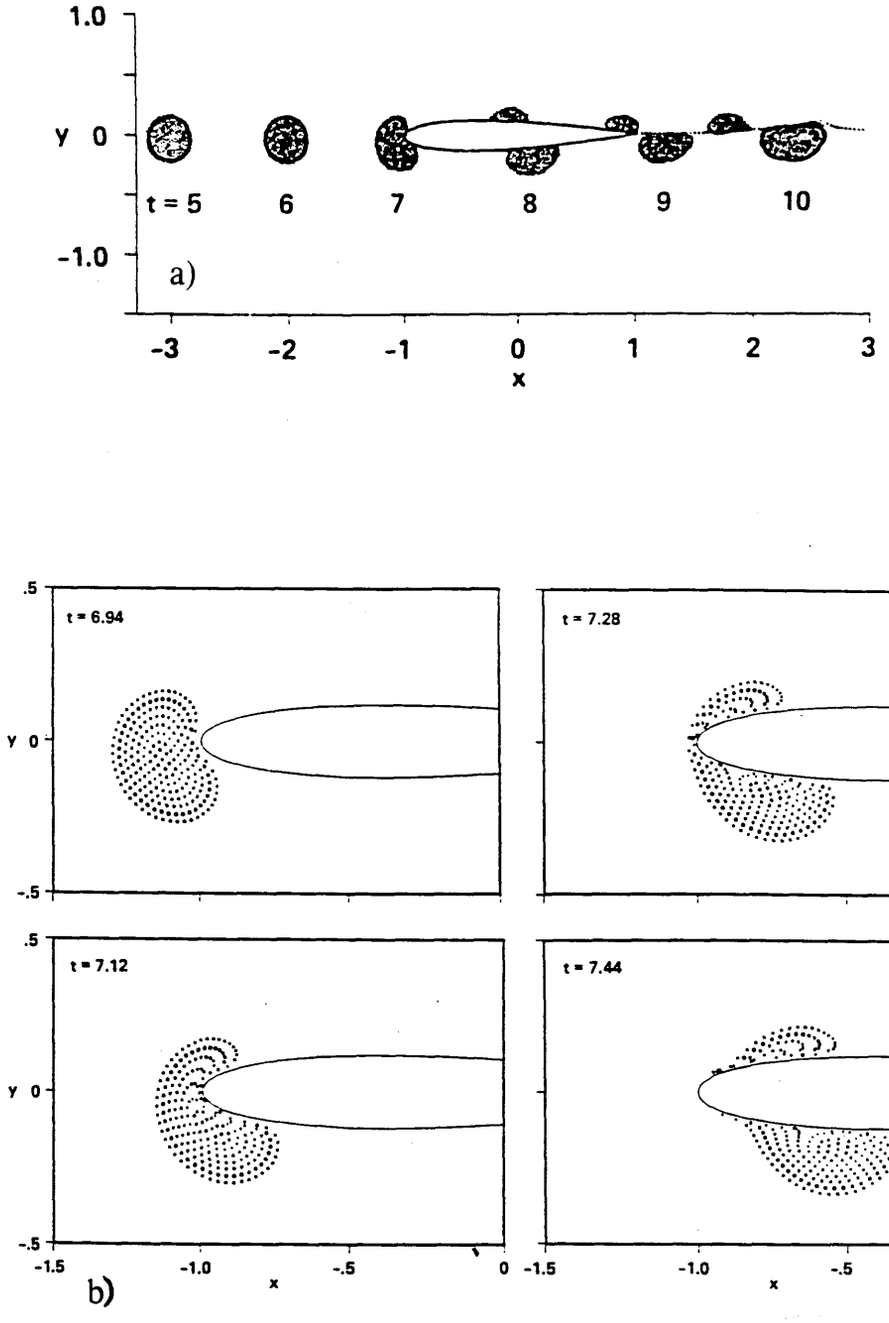

Figure 1.7. Blade-Vortex Interaction for Zero Vertical Separation Distance - (a) Vortex Trajectory and (b) Vortex Distortion at the Leading edge (Ref. 21)

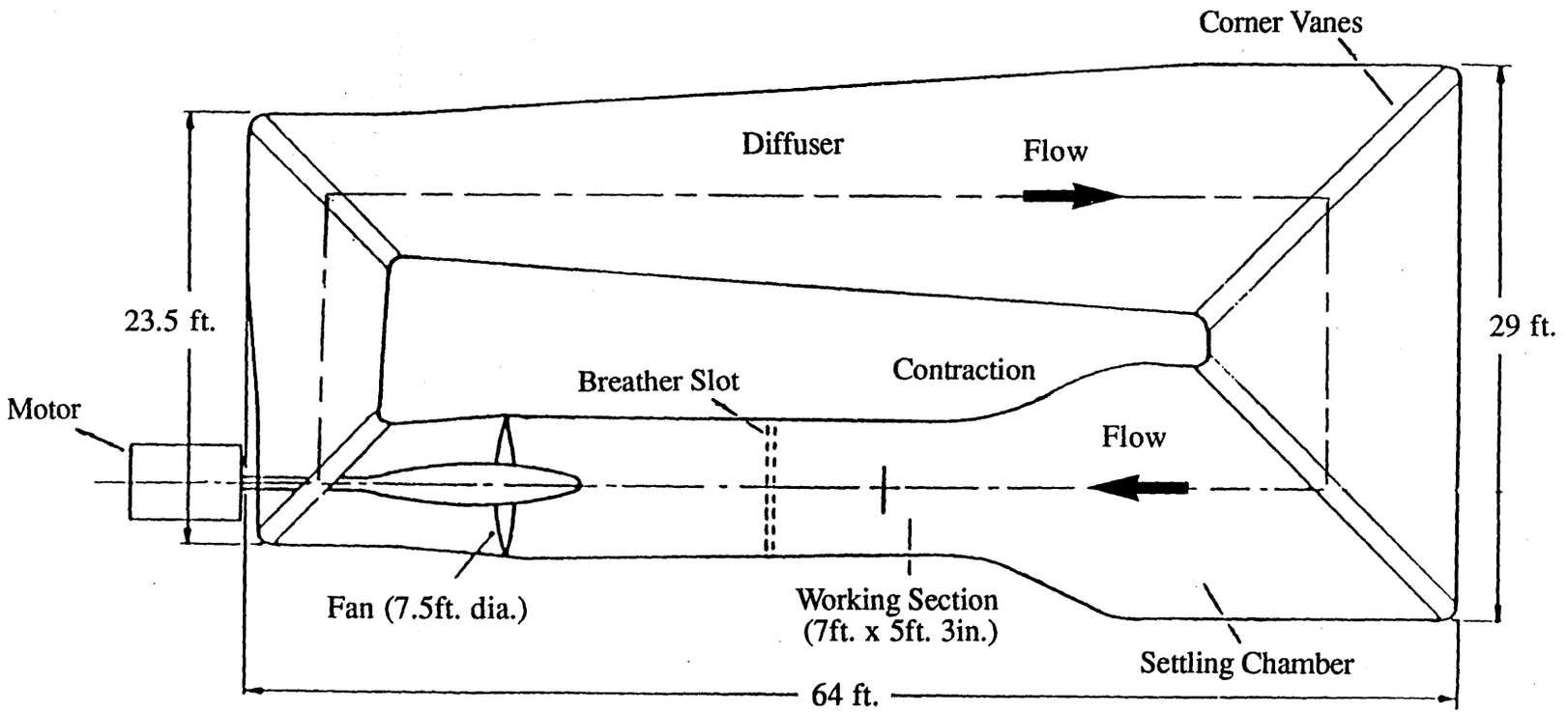

Figure 2.1. A Plan View of the University of Glasgow 'Handley Page' Wind Tunnel

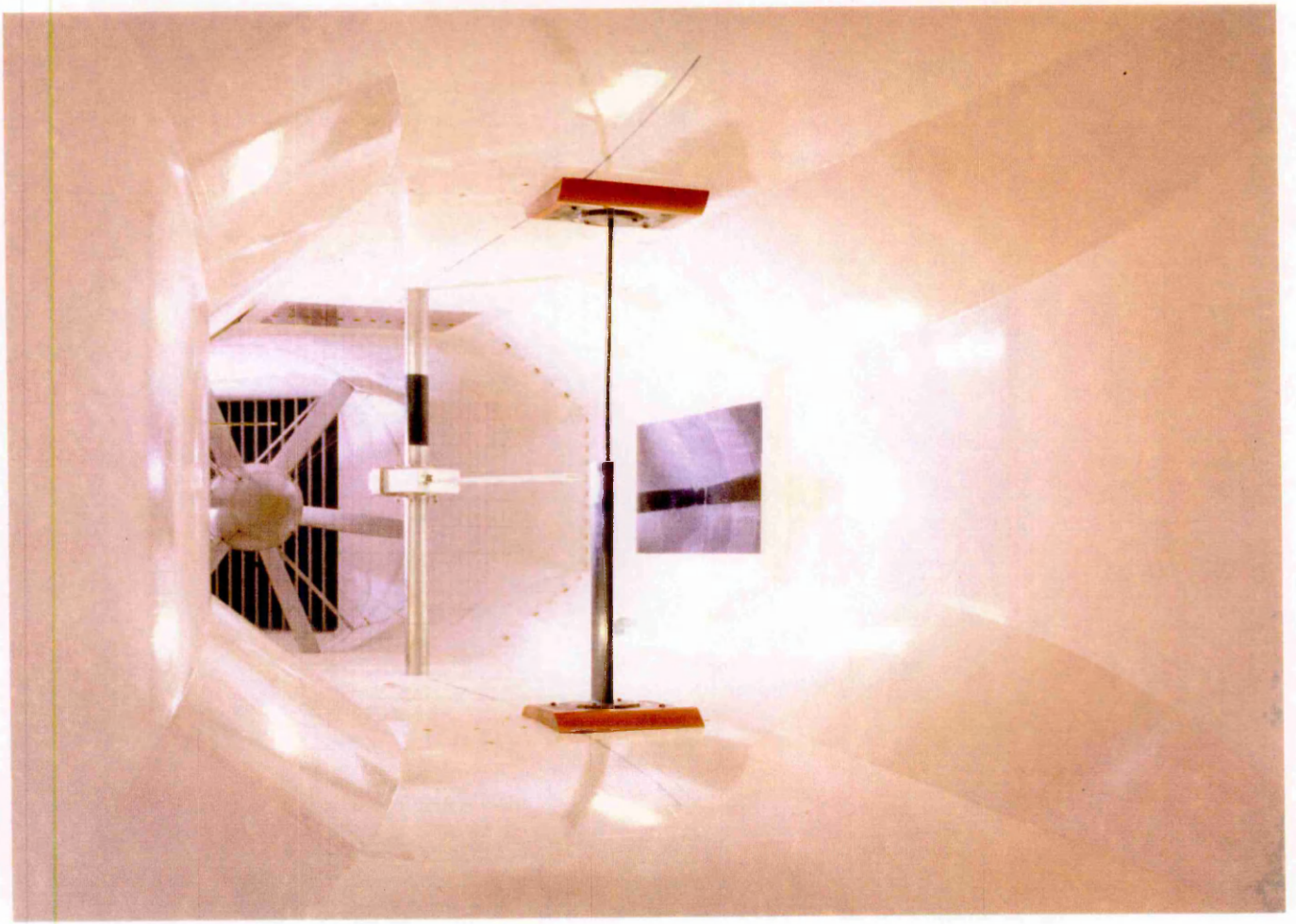

Figure 2.2. Installation of the BVI Facility in the Tunnel's Working Section

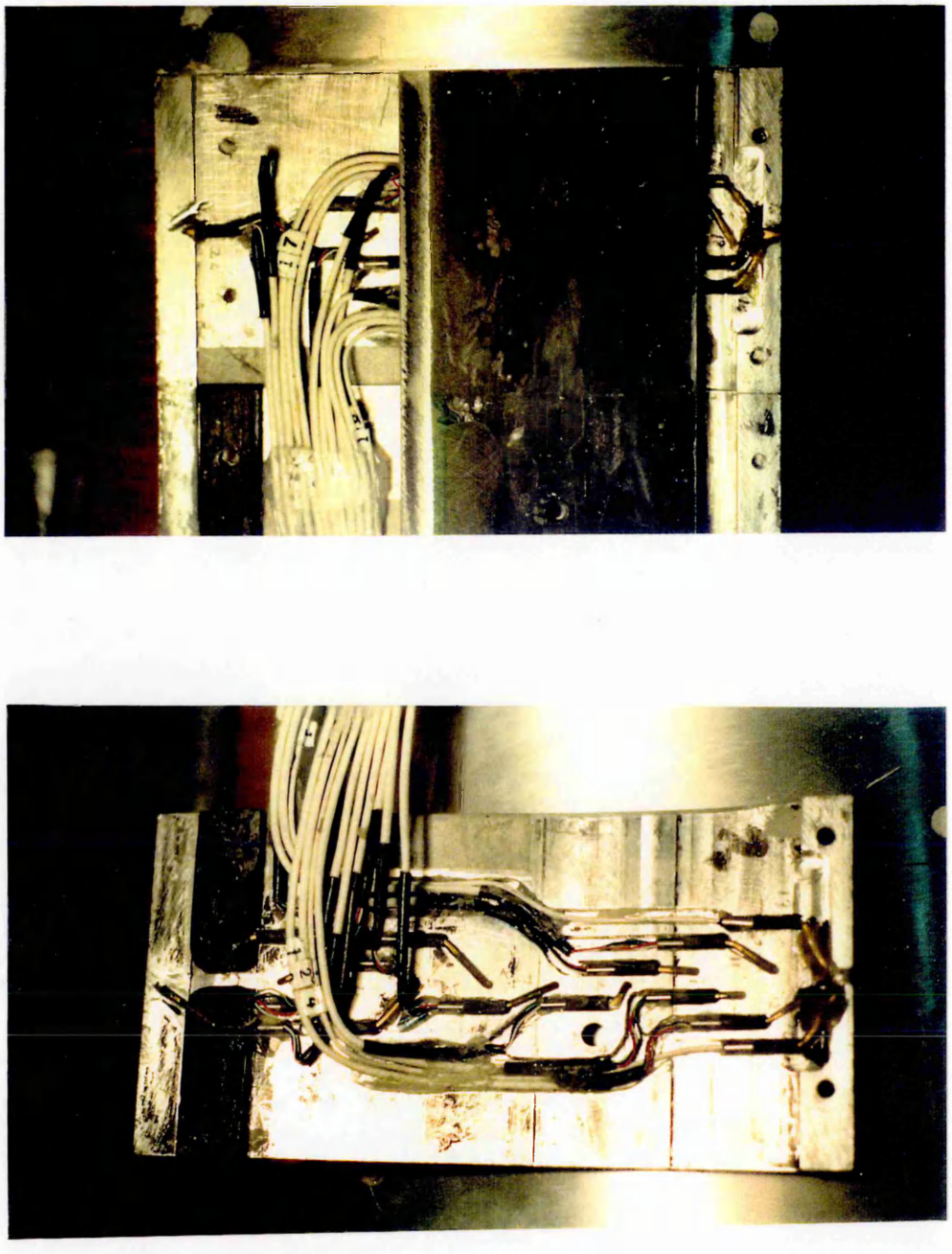

Figure 2.3. Installation of 26 Pressure Transducers Inside an Instrumentation Pod

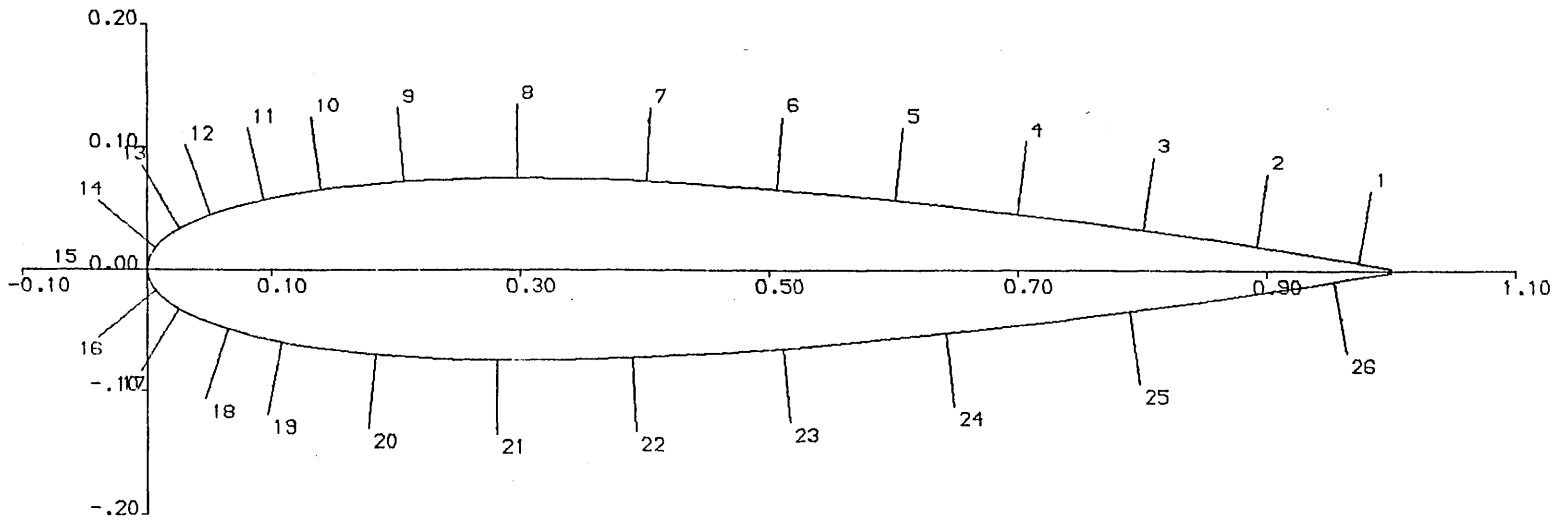

X(1)/C= 0.97383	X(10)/C= 0.13960	X(19)/C= 0.10805
X(2)/C= 0.89195	X(11)/C= 0.09396	X(20)/C= 0.18322
X(3)/C= 0.80121	X(12)/C= 0.05101	X(21)/C= 0.28121
X(4)/C= 0.70000	X(13)/C= 0.02617	X(22)/C= 0.38993
X(5)/C= 0.60174	X(14)/C= 0.00671	X(23)/C= 0.51141
X(6)/C= 0.50624	X(15)/C= 0.00000	X(24)/C= 0.64228
X(7)/C= 0.40201	X(16)/C= 0.00671	X(25)/C= 0.78993
X(8)/C= 0.29799	X(17)/C= 0.02550	X(26)/C= 0.95436
X(9)/C= 0.20604	X(18)/C= 0.06477	

Figure 2.4. Location of Pressure Transducers around the NACA-0015 Aerofoil Section

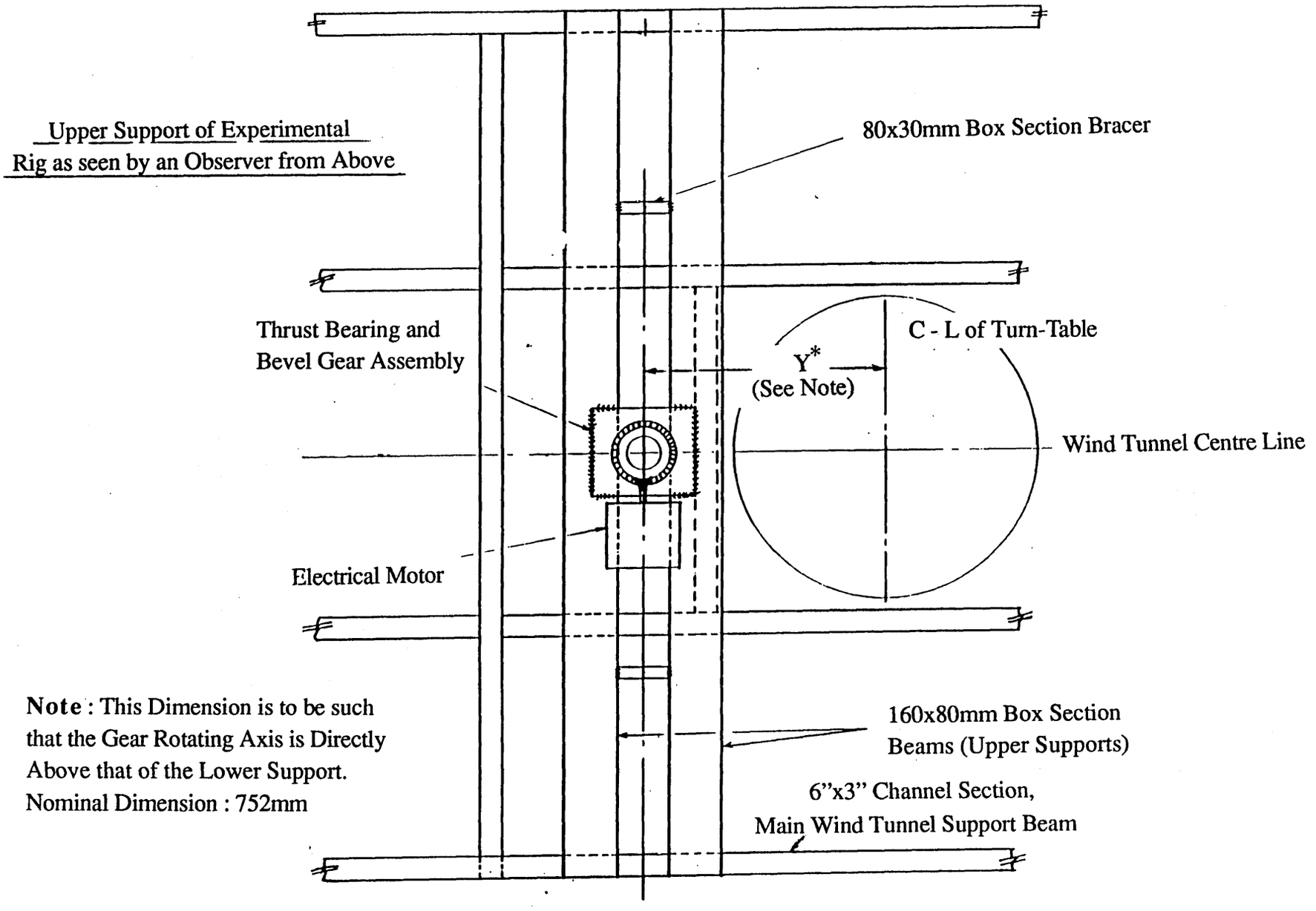

Figure 2.5(a) Graphic Illustration of the Rotor Supporting Structure above the Wind Tunnel Working Section

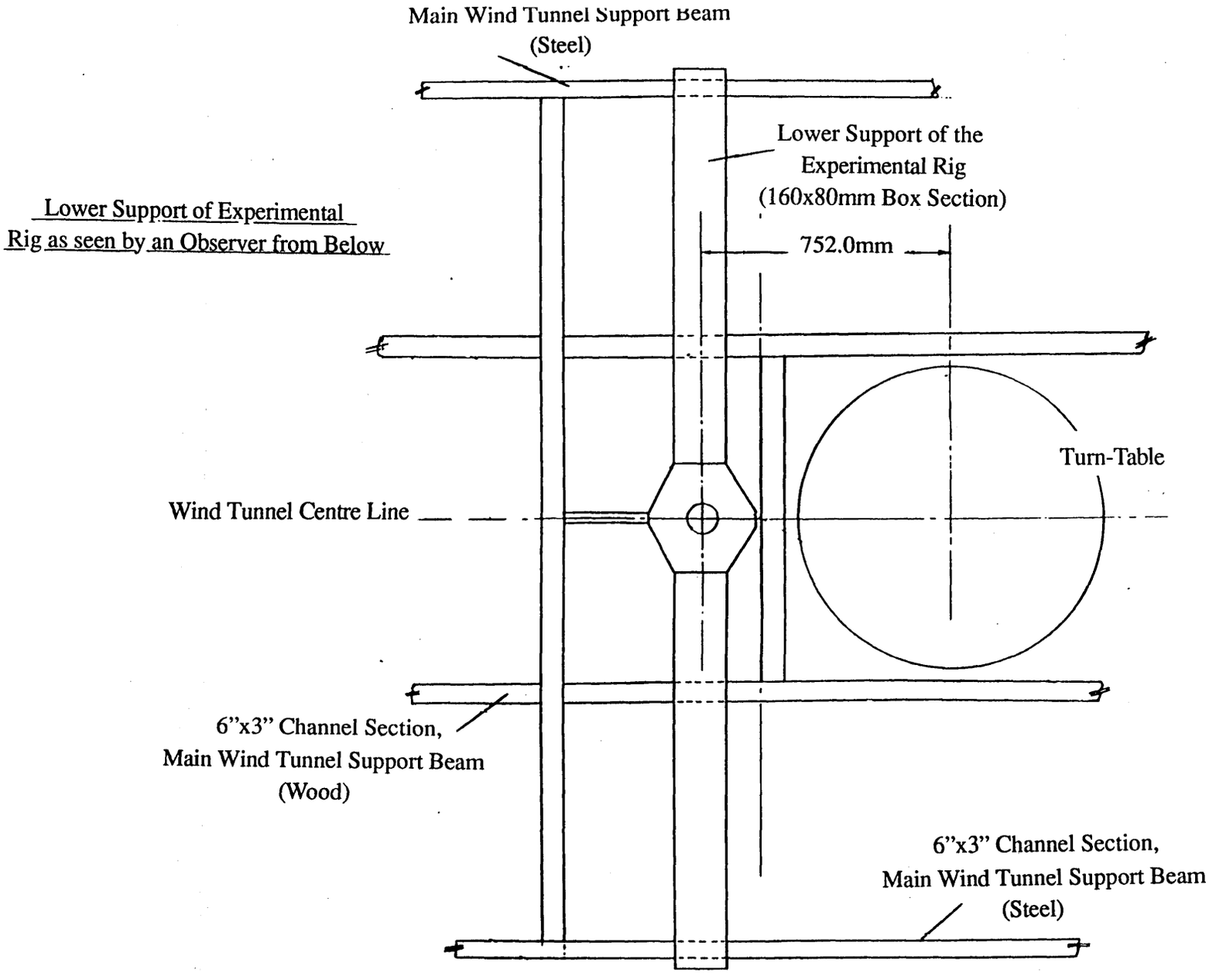

Figure 2.5(b) Graphic Illustration of the Rotor Supporting Structure below the Wind Tunnel Working Section

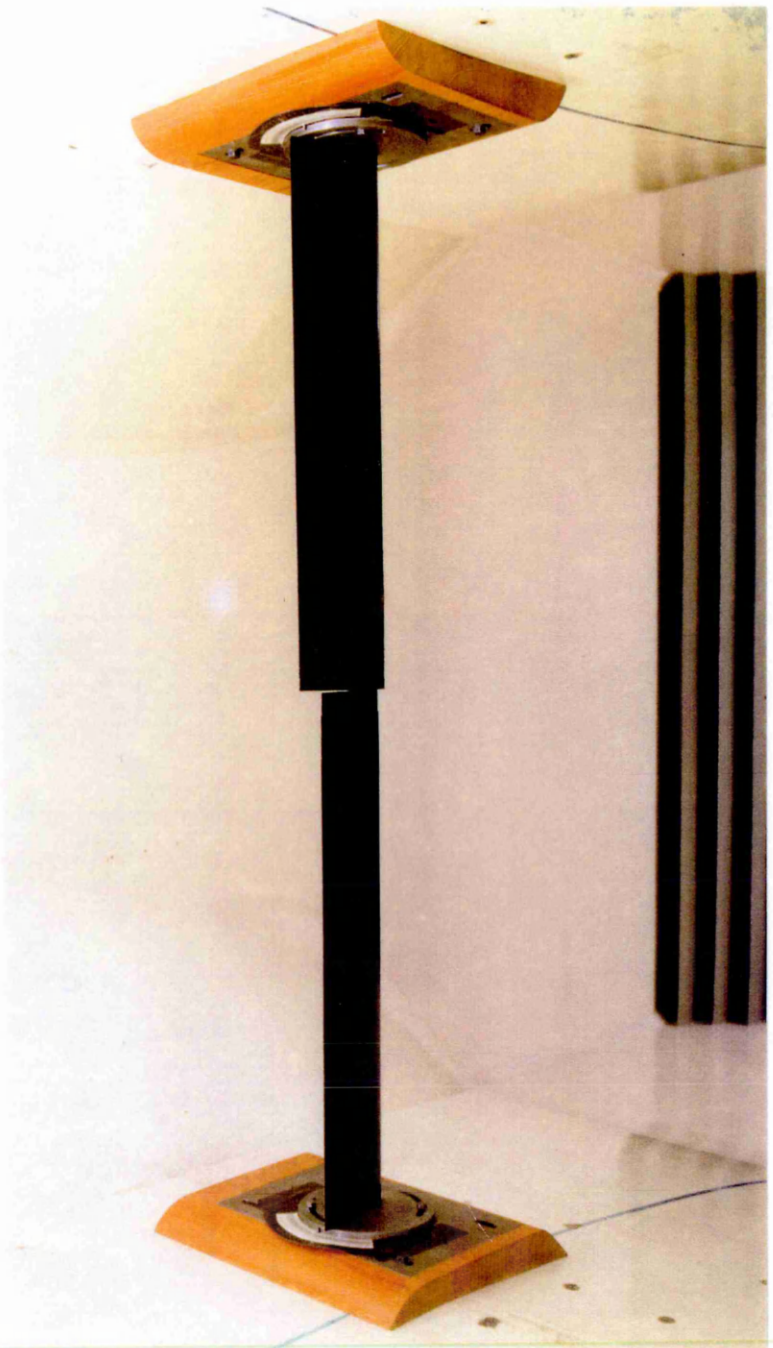

Figure 2.6. Blade-Vortex Generator Installation Upstream of the Rotor

LEGEND			
δ	Γ (m^2/s)	$\Gamma/V_\infty c_w$	d_v/c_w
5.00	1.10	0.16	0.340
10.00	2.20	0.32	0.280
15.00	3.40	0.49	0.270
20.00	5.10	0.73	0.260
25.00	6.70	0.96	0.260

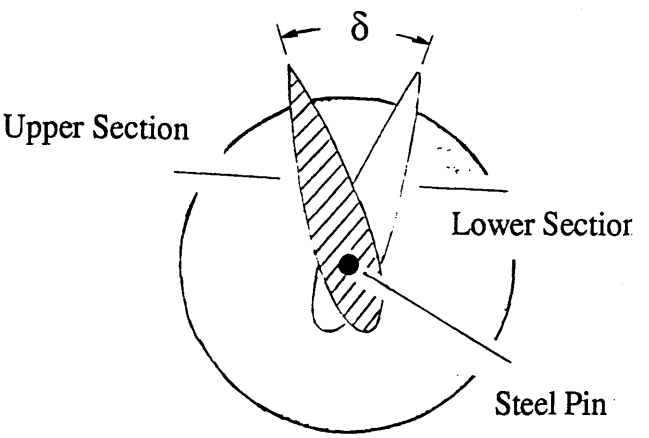

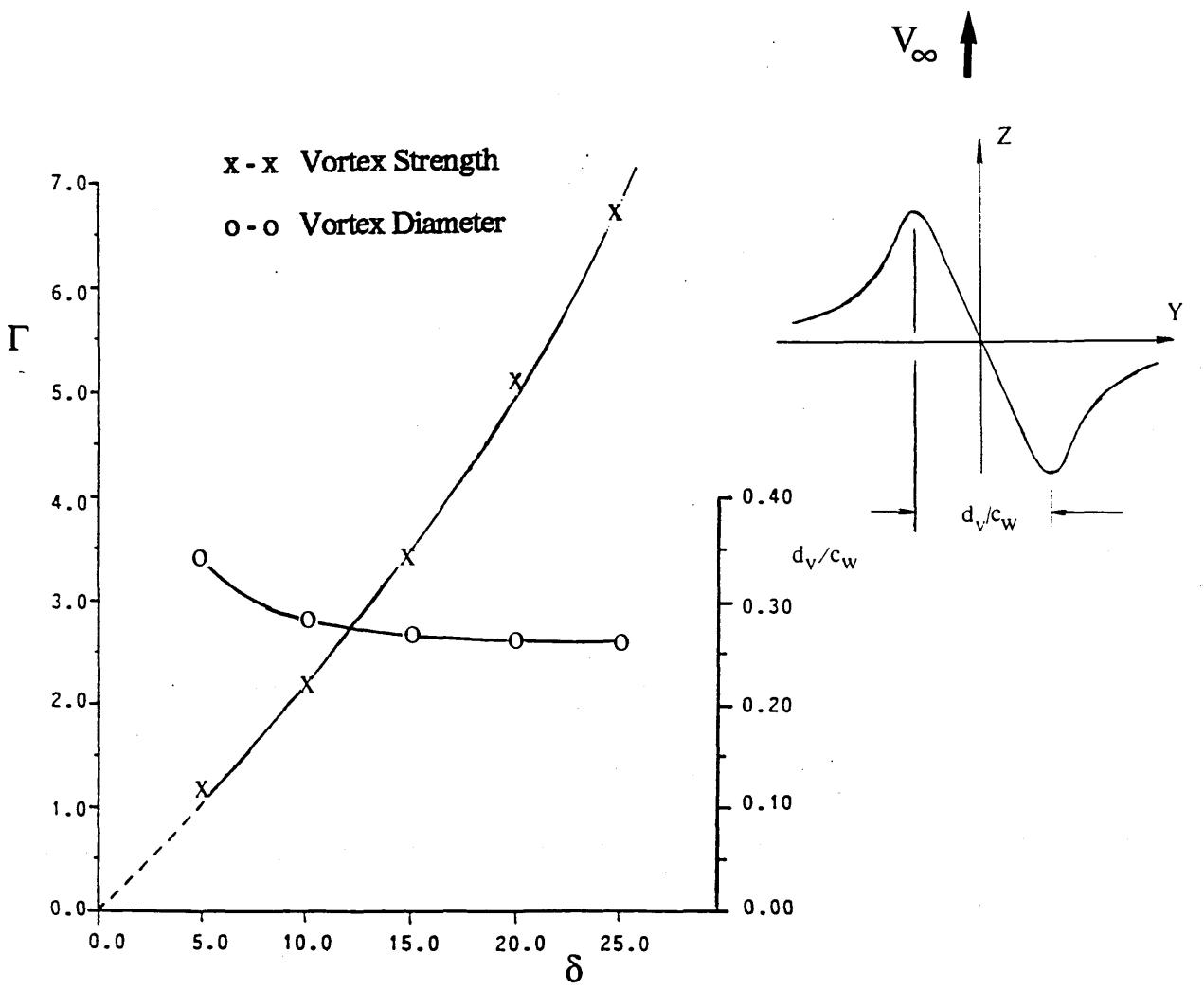

Figure 2.7. Variation of Vortex Strength and Core Diameter with Vortex Generator "Differential" Angle of Incidence

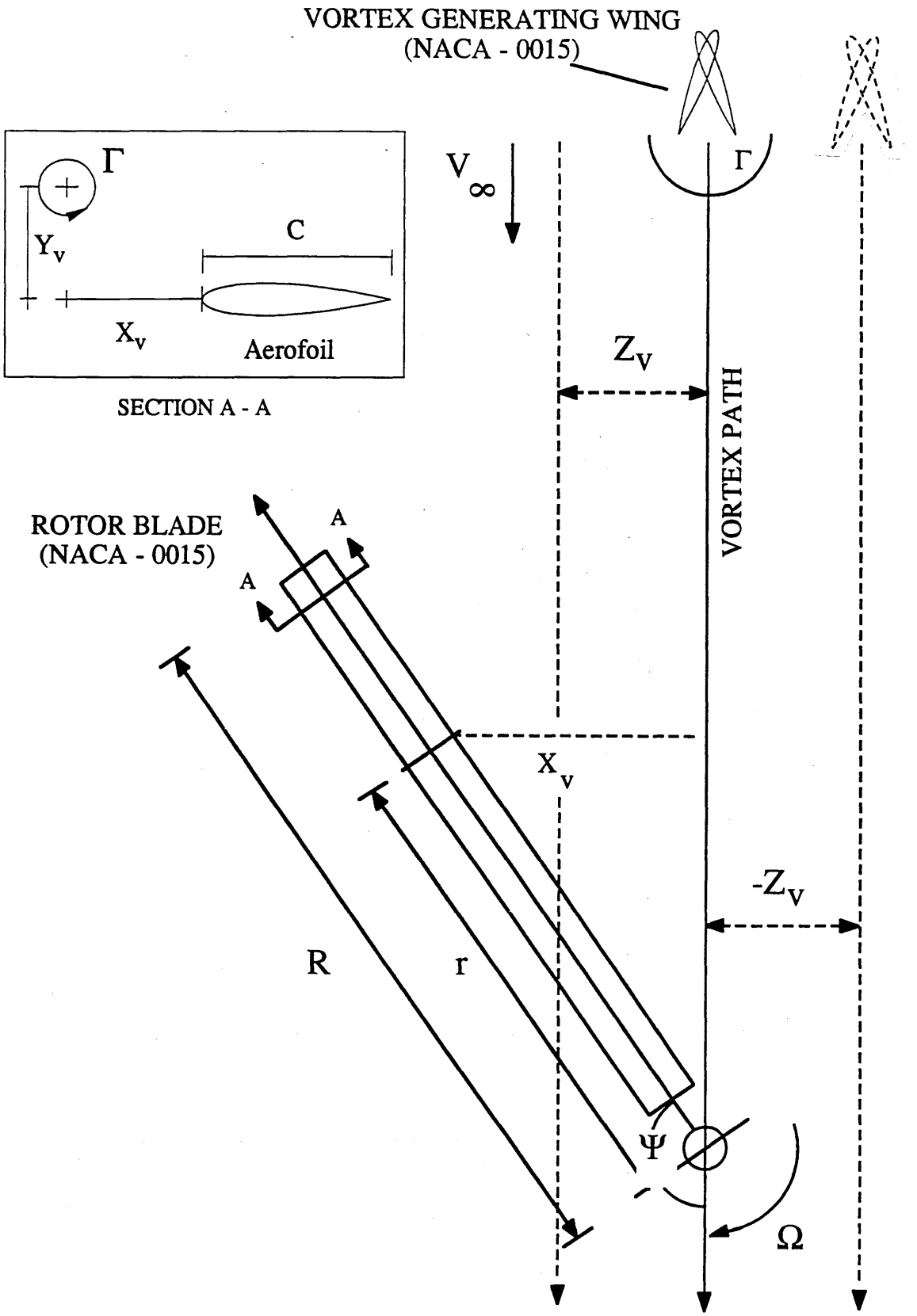

Figure 2.8. Illustration of Relative Position of Vortex Axis with Respect to Blade Leading Edge and Tunnel Centre Line

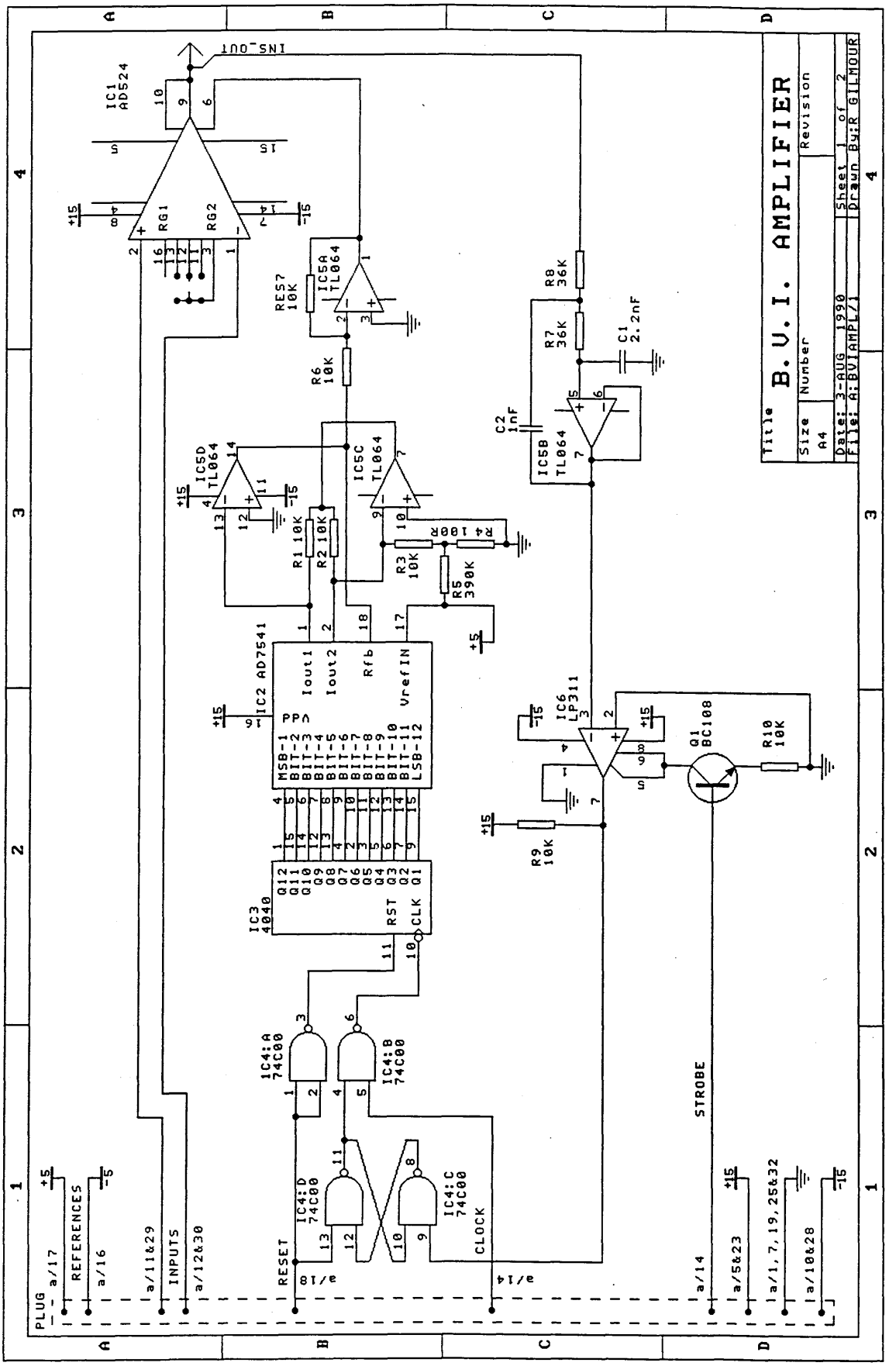

Figure 2.9. Schematic of an Electronic Amplifier Circuit

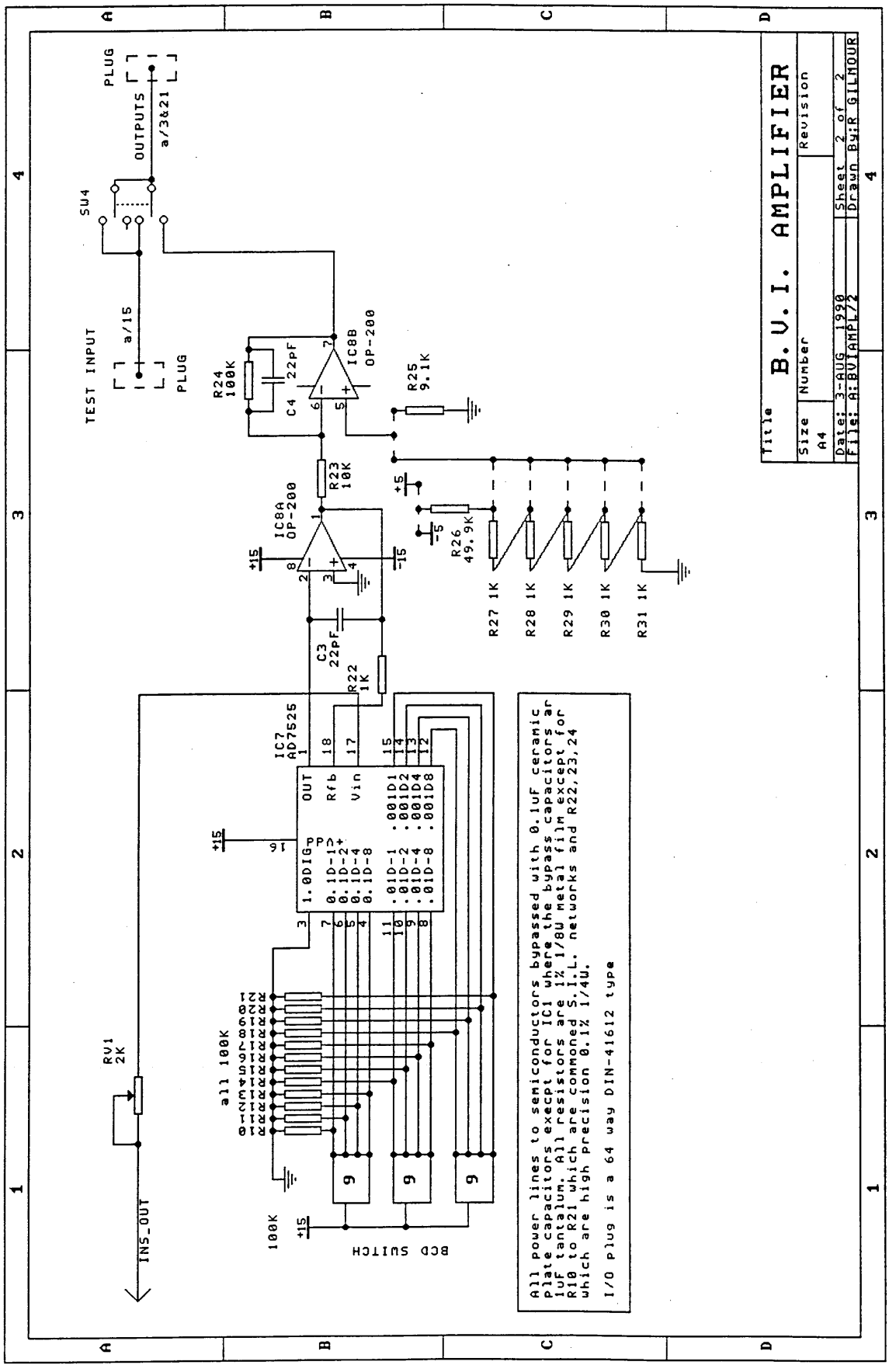

Figure 2.9. Concluded

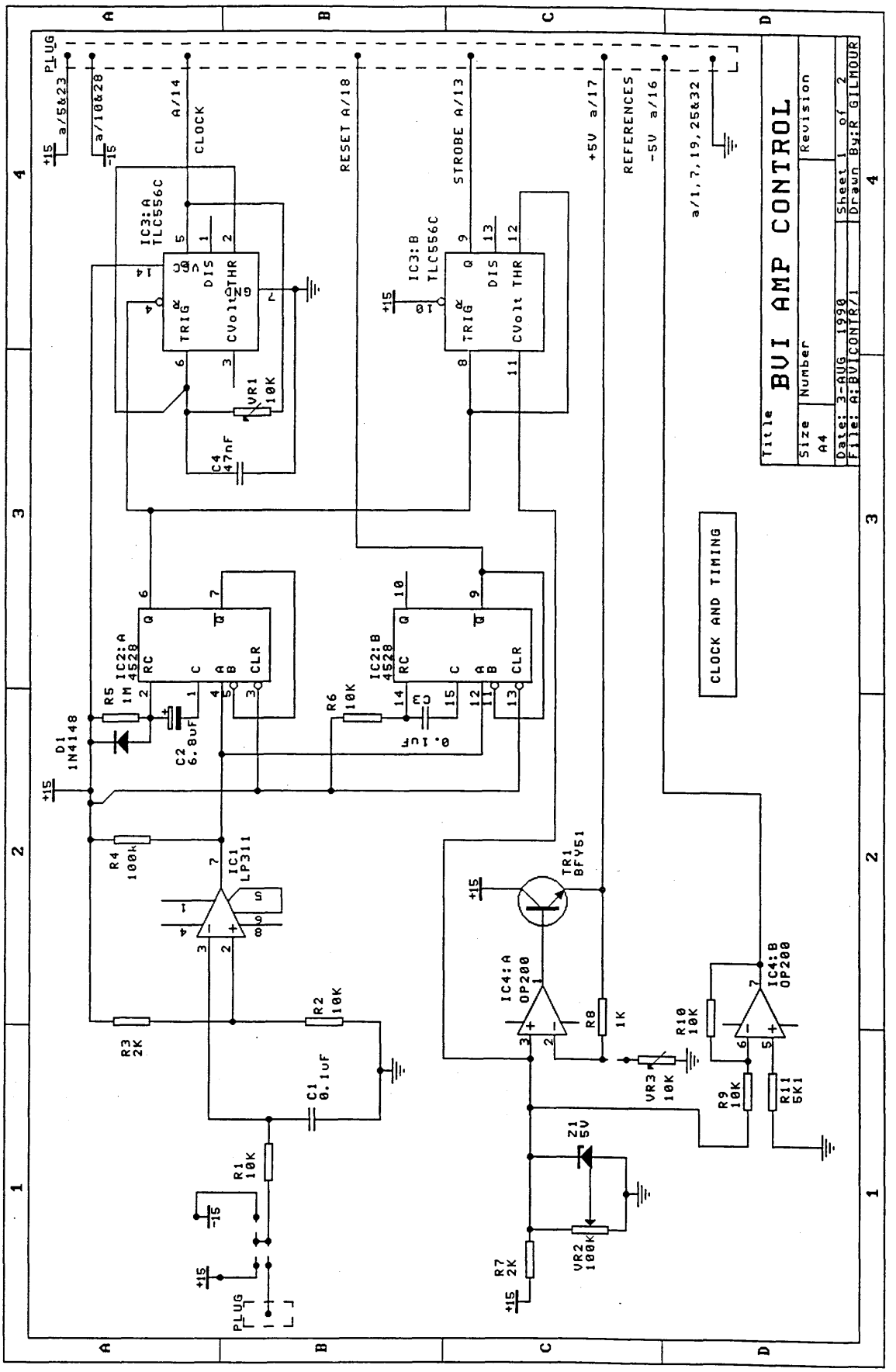

Figure 2.10. Schematic of an Electronic Amplifier Control Circuit

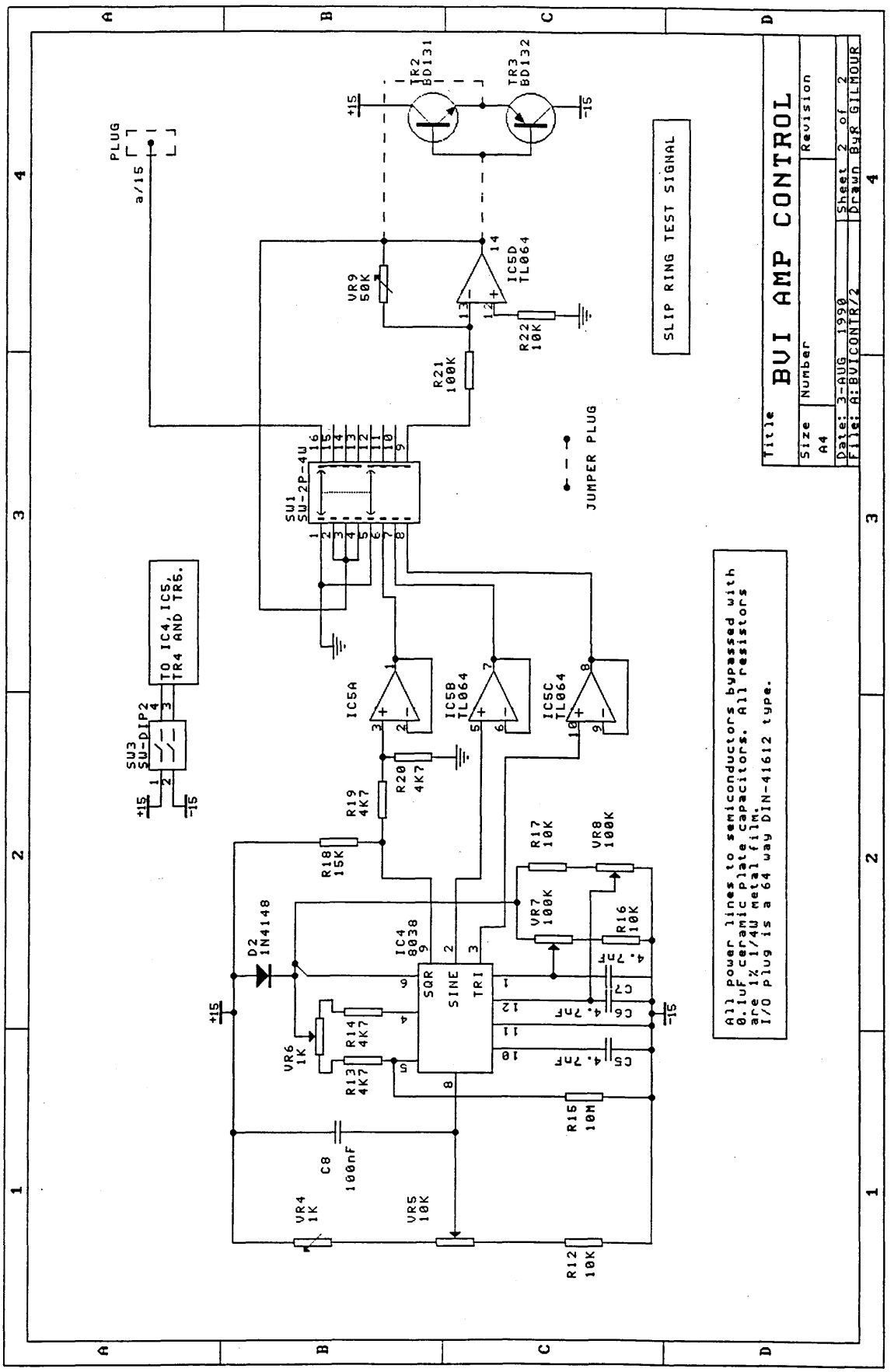

Figure 2.10. Concluded

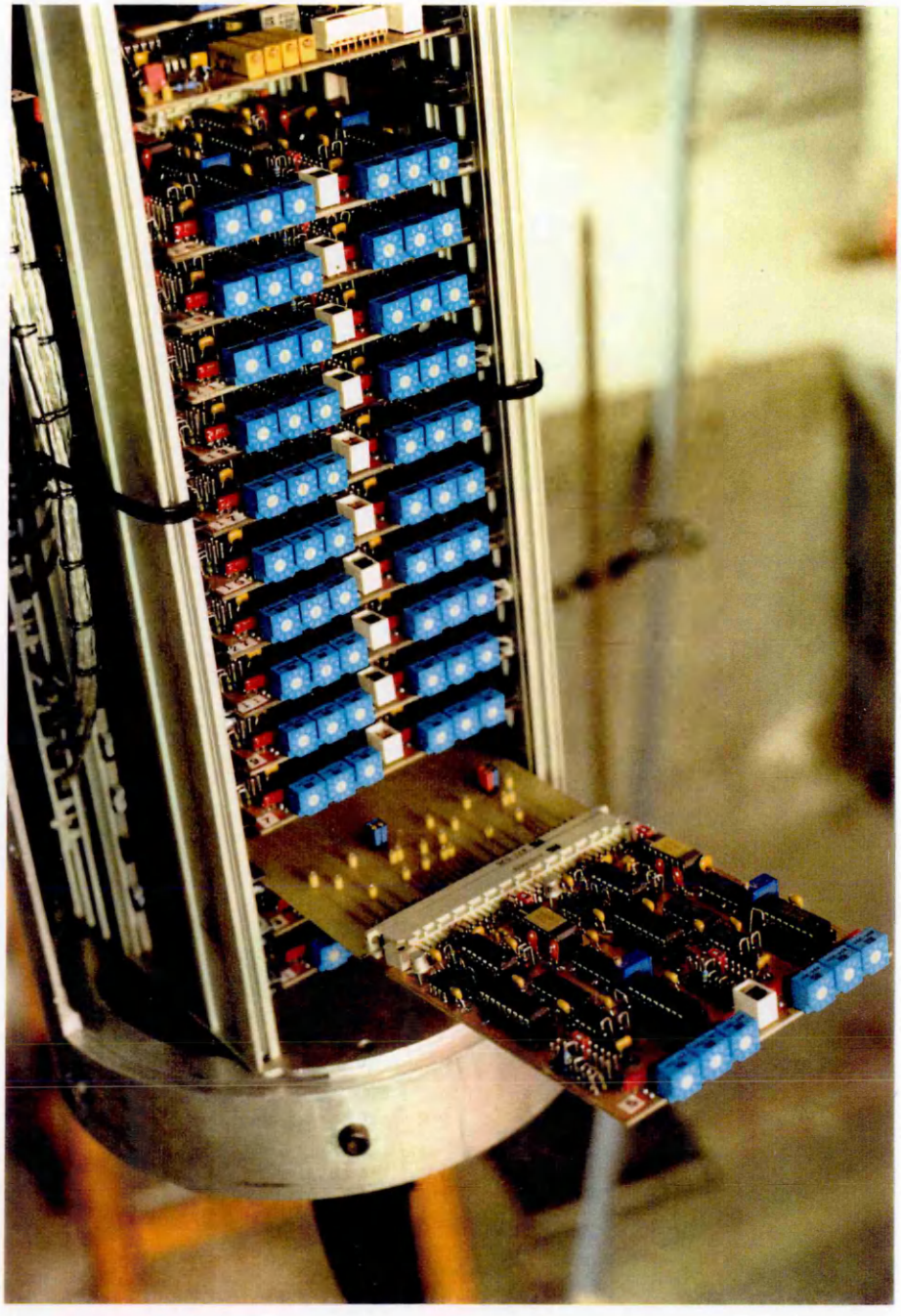

Figure 2.11. Installation of Amplifier Board Circuits onto an Amplifier Rack

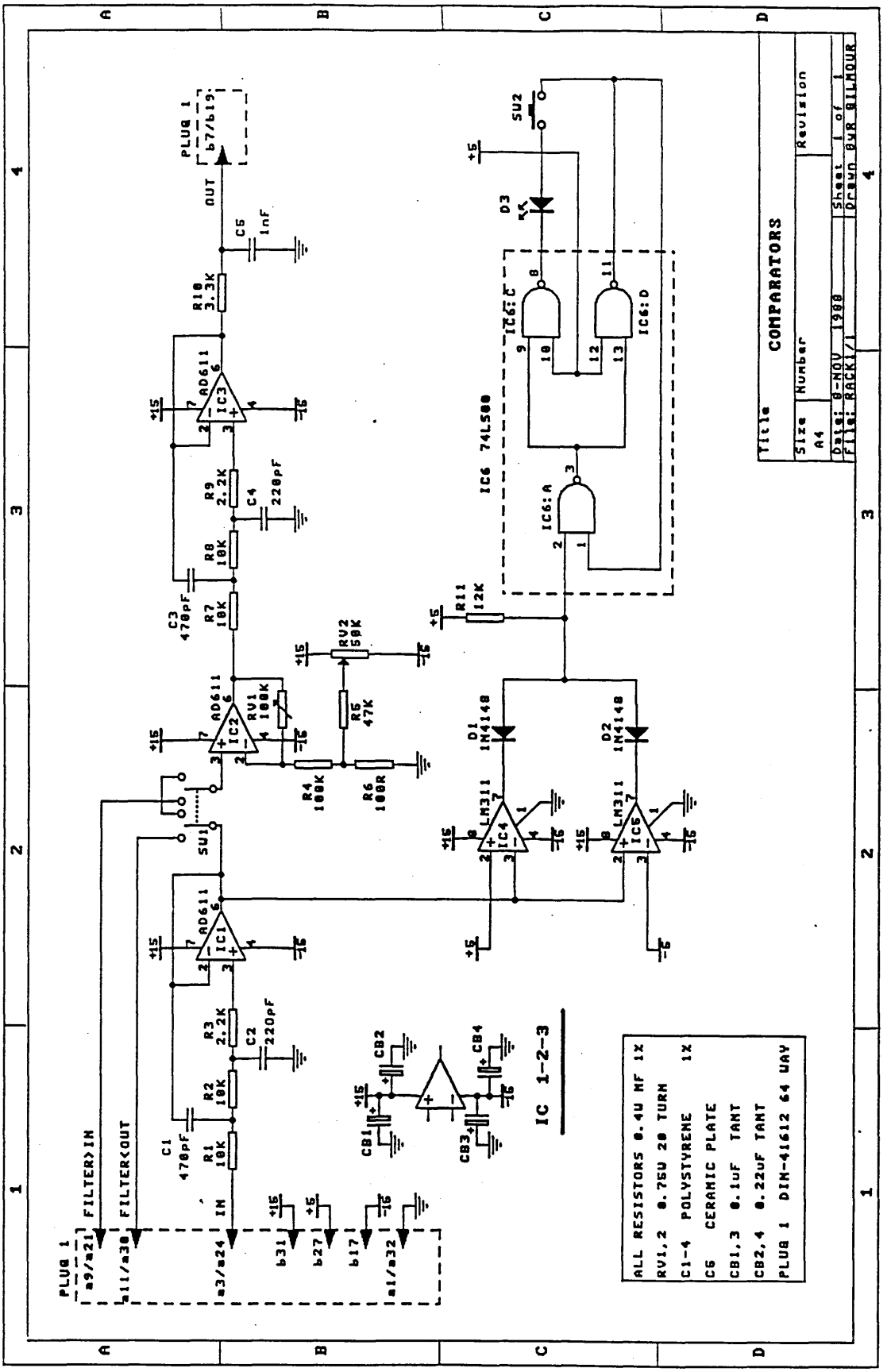

Figure 2.12. Schematic of a Voltage Comparator Circuit

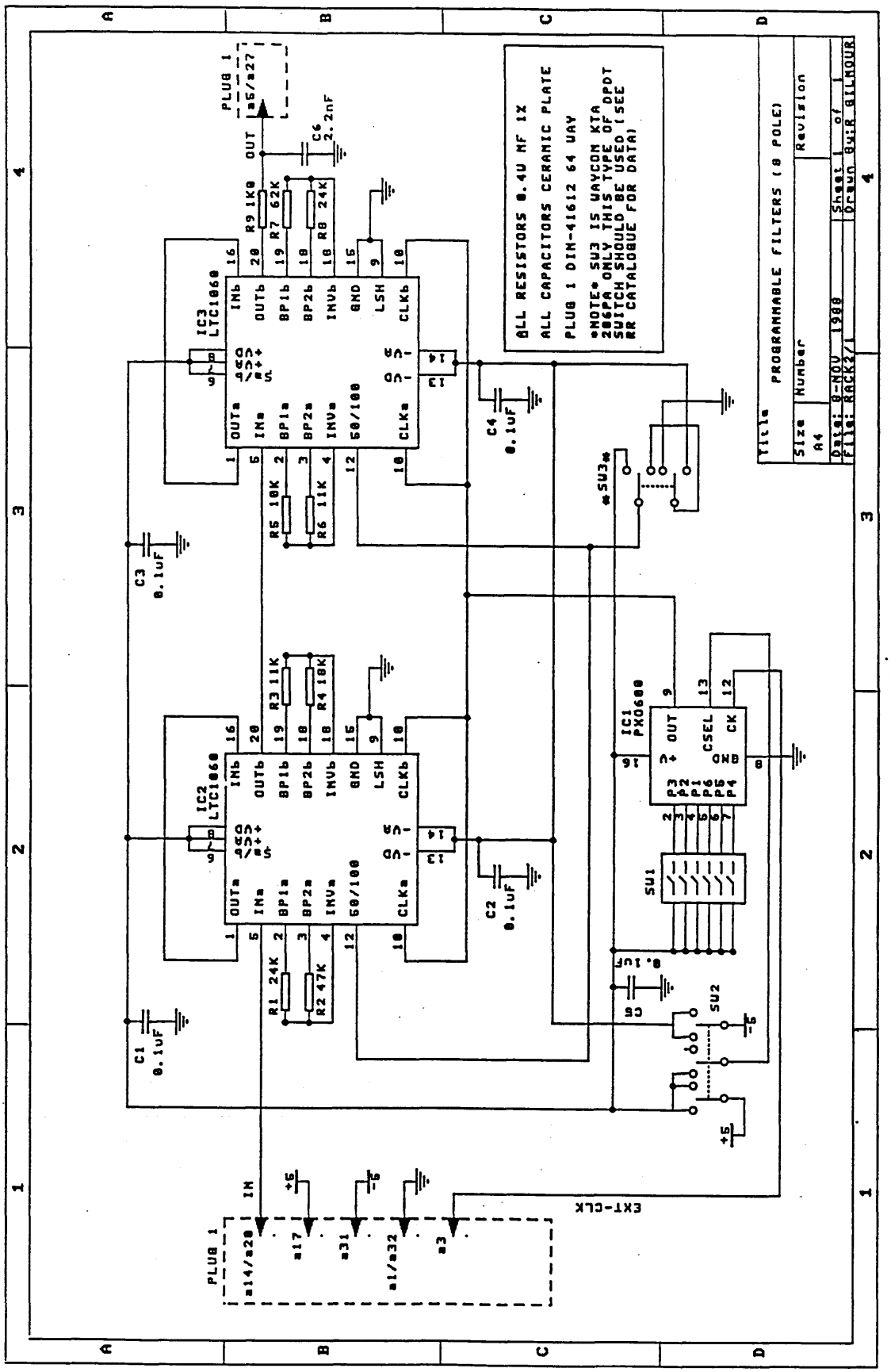

Figure 2.13. Schematic of a Low - Pass Filter Circuit

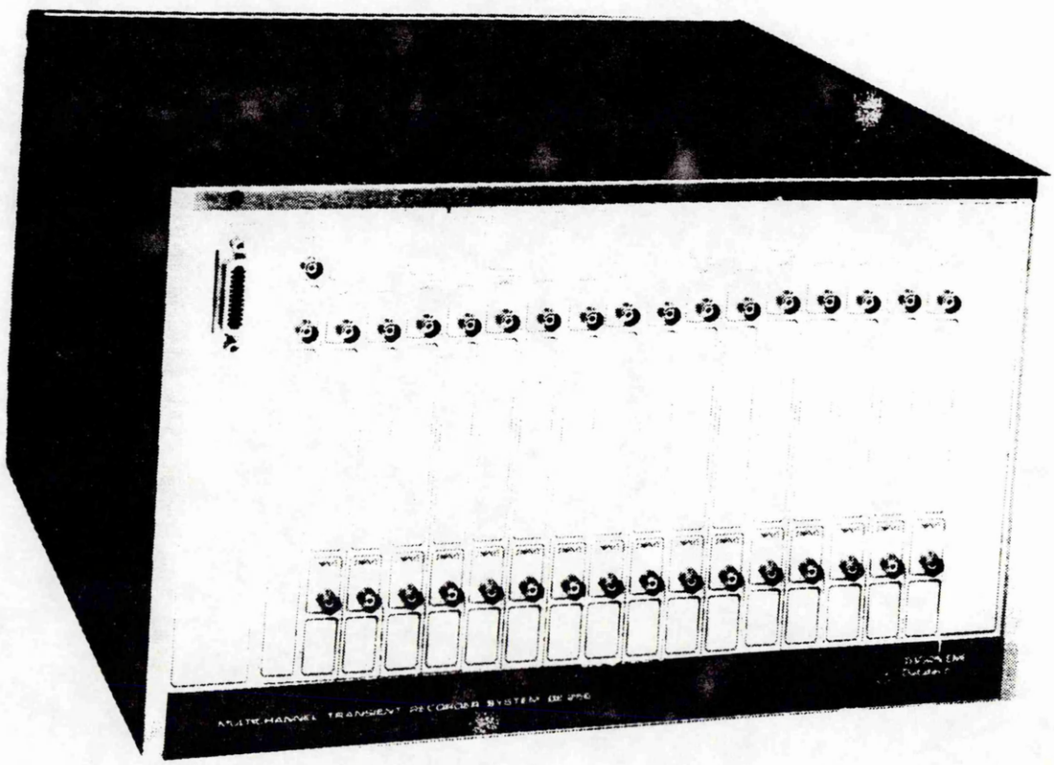

Figure 2.14. Illustration of the BE256-420 Multi-channel Transient Recording System

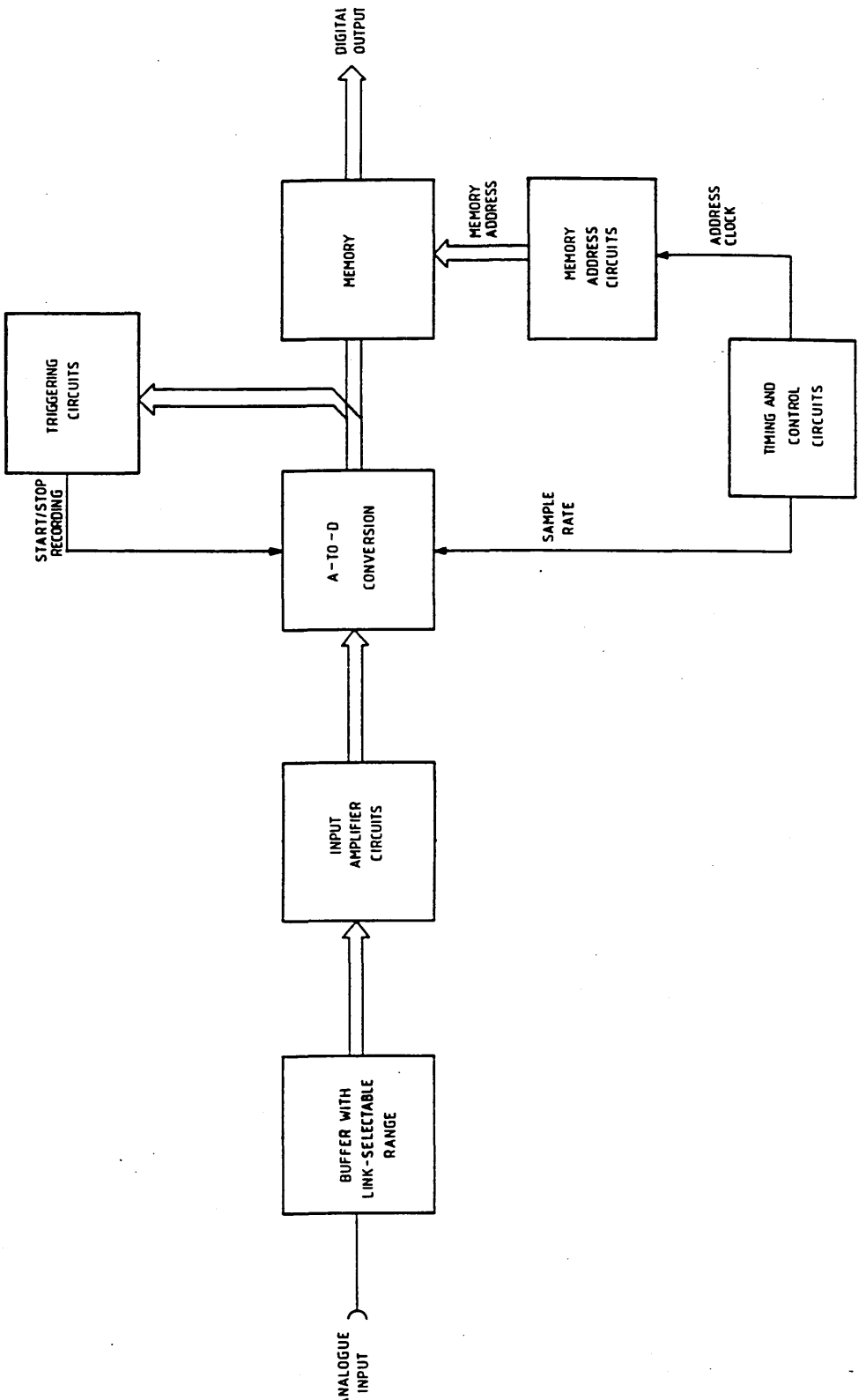

Figure 2.15(a) Block Diagram of a Typical BE256 Transient Recording Module

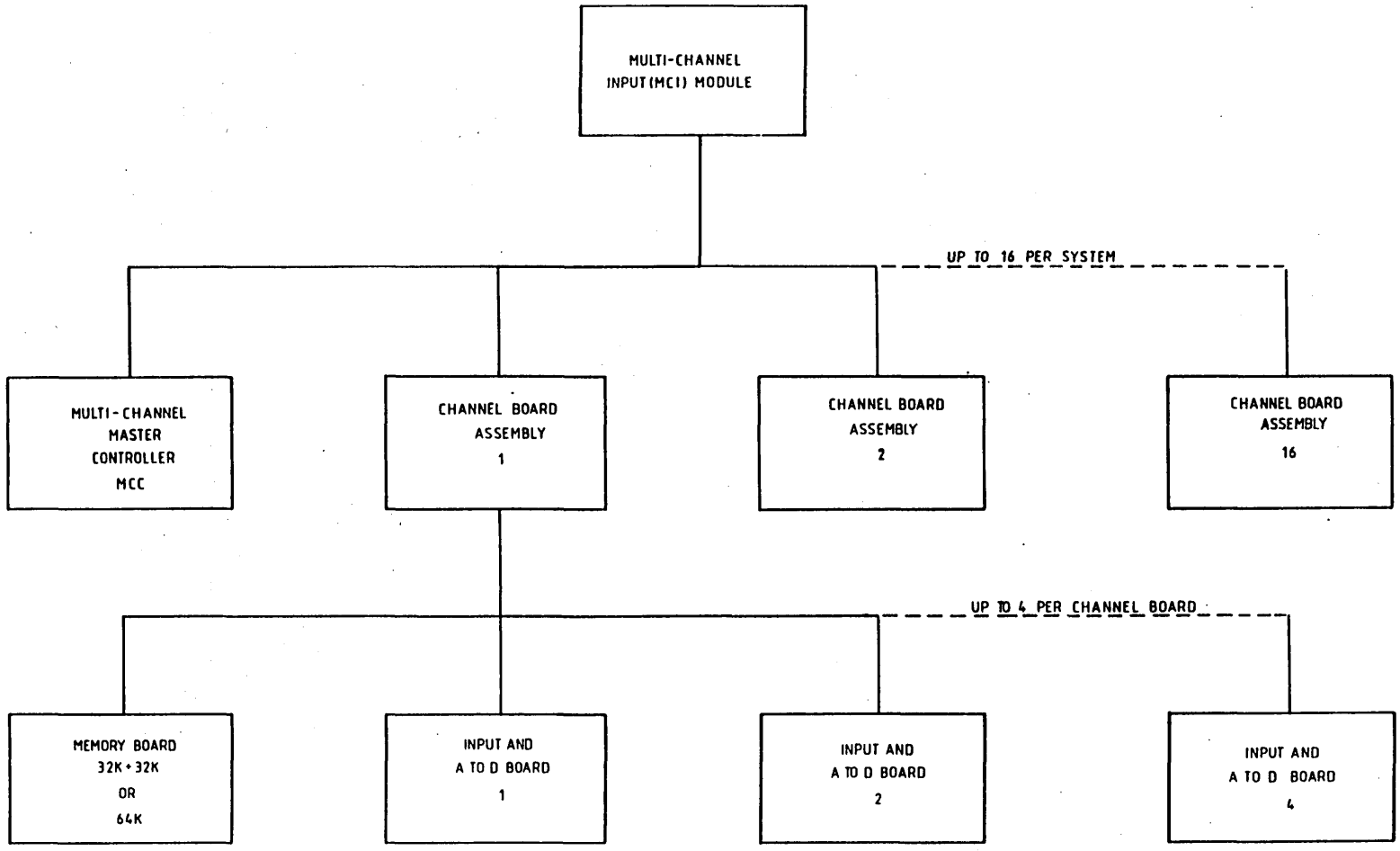

Figure 2.15(b) Block Diagram of a Typical BE256 Multi-Channel Input Module Structure

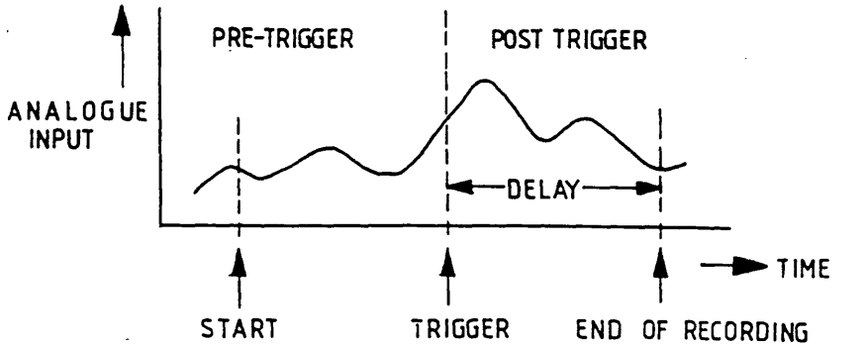

Figure 2.16(a) Pre-Trigger Feature

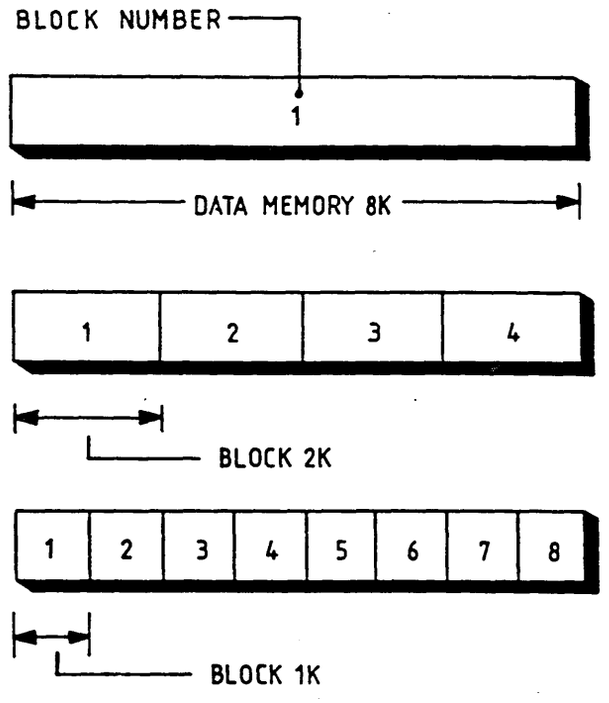

Figure 2.16(b) Recording In Single Block Mode

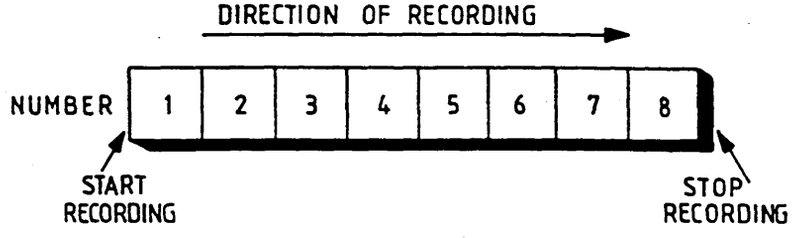

Figure 2.16(c) Recording All Block Modes

Figure 2.16. Recording Modes of the BE256 Transient Recording Module

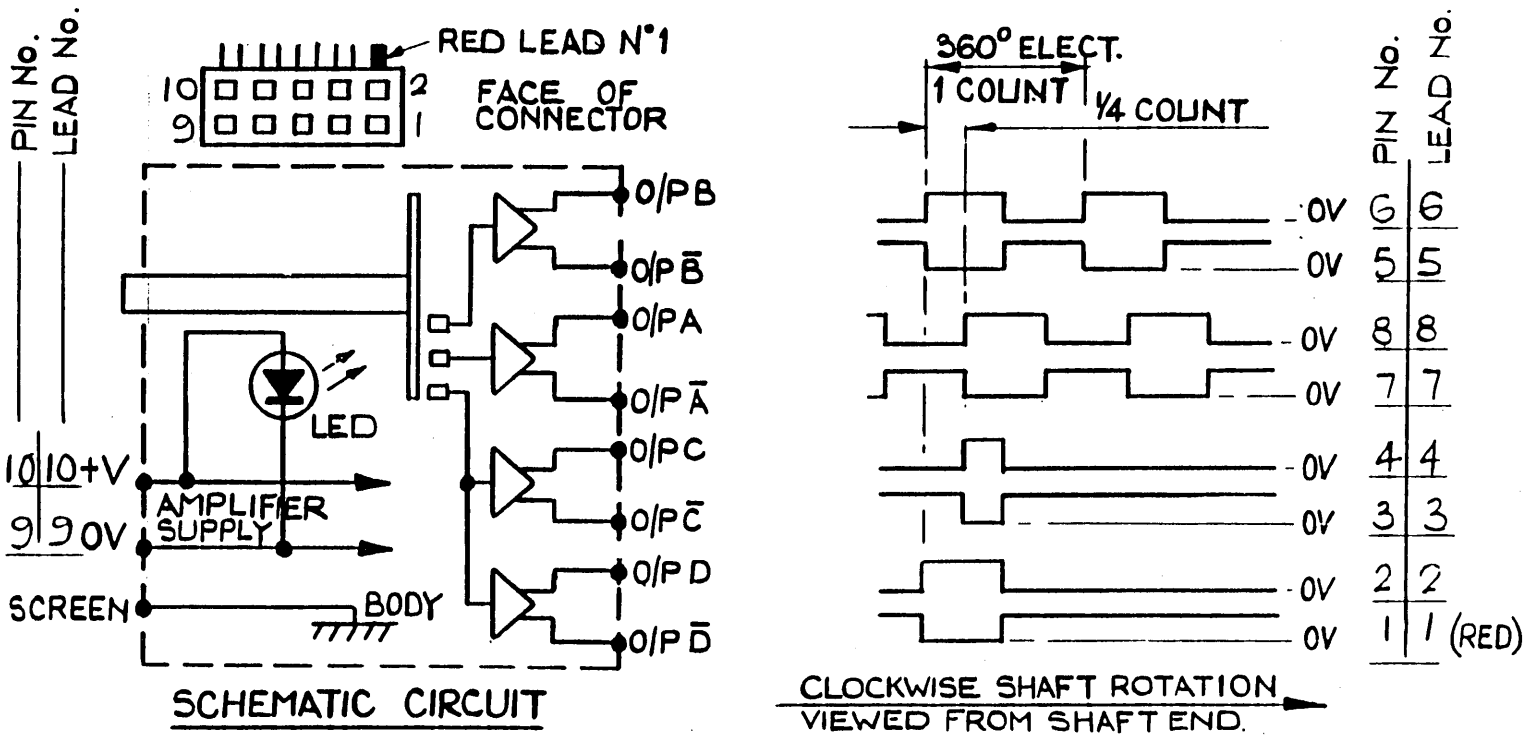

Figure 2.17. Schematic Circuit and Signal Output of the Incremental Optical Encoder

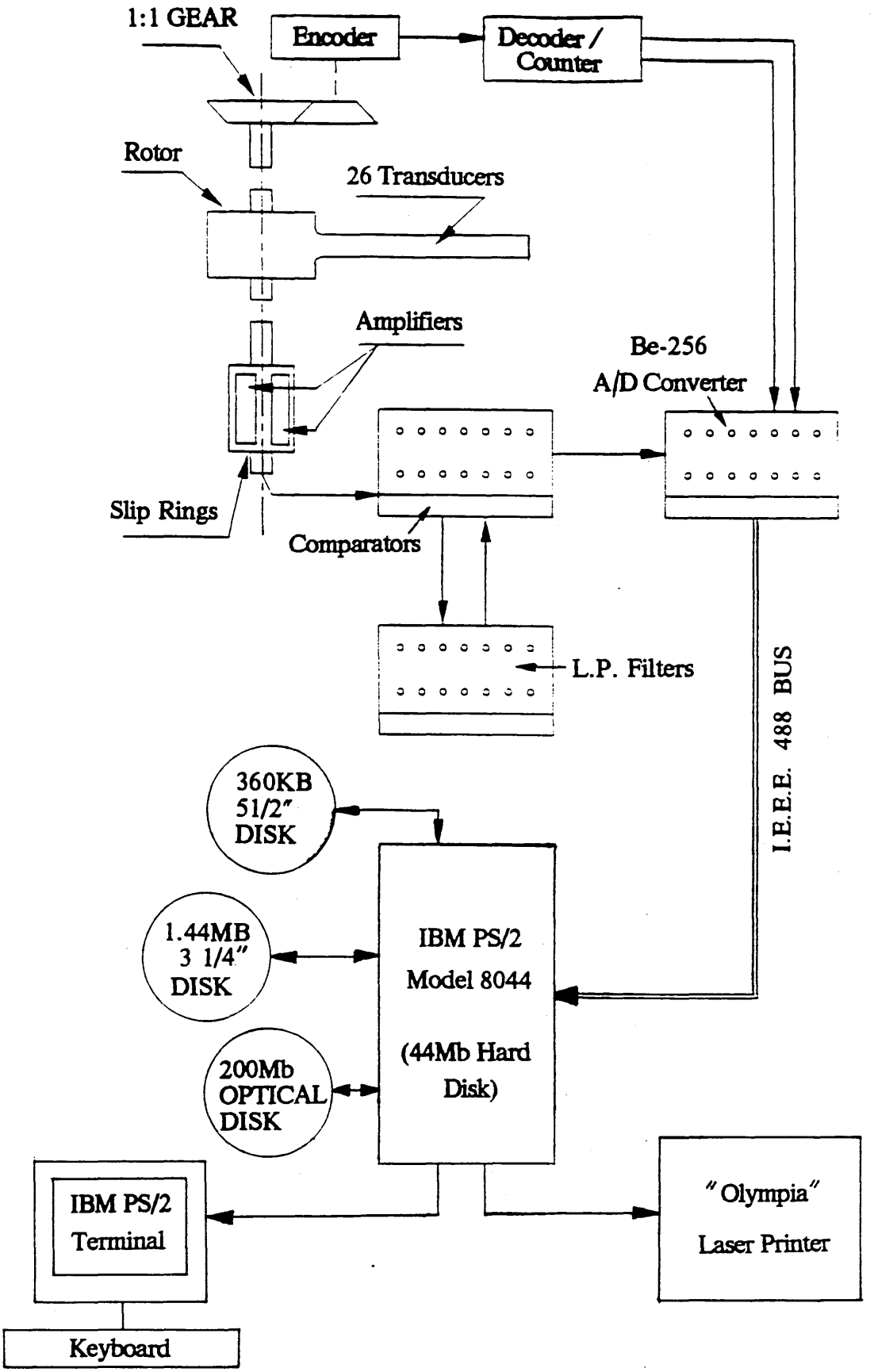

Figure 2.18. Schematic of the BVI Data Acquisition System

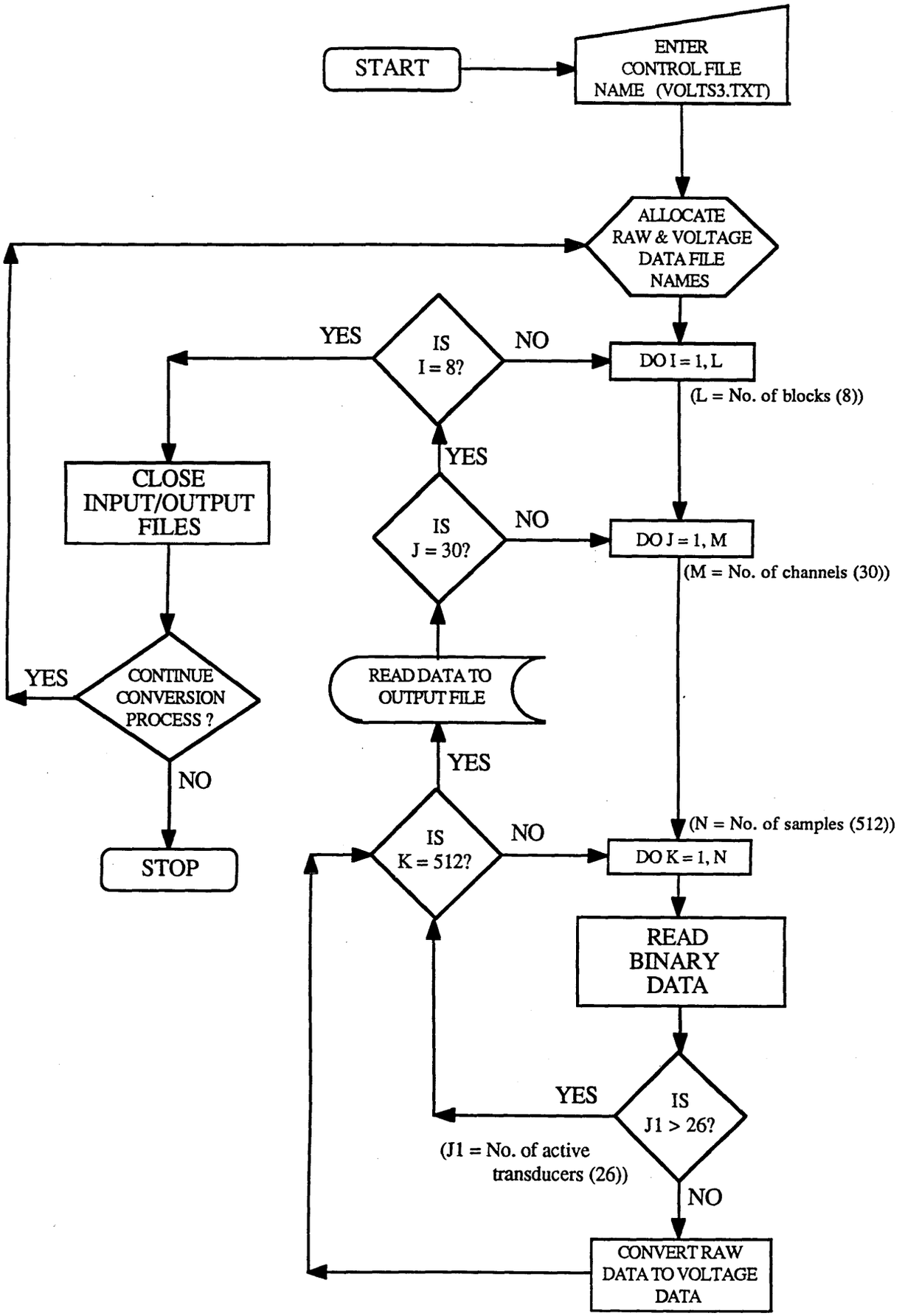

Figure 2.19. Flowchart for the BVI Data Conversion to Voltages (Program VOLTS3.FOR)

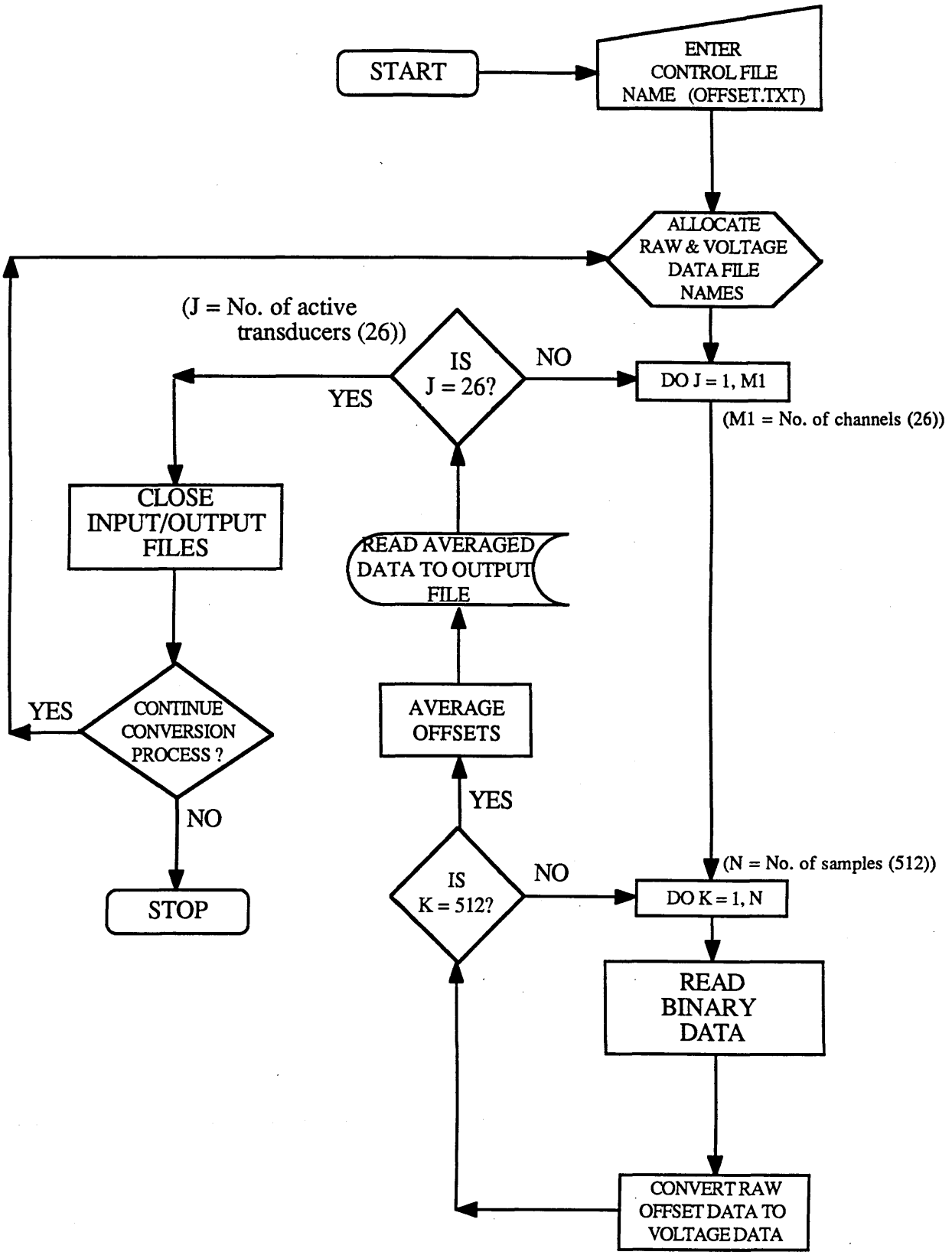

Figure 2.20. Flowchart for the OFFSET Data Conversion to Voltages (Program OFFCONV.FOR)

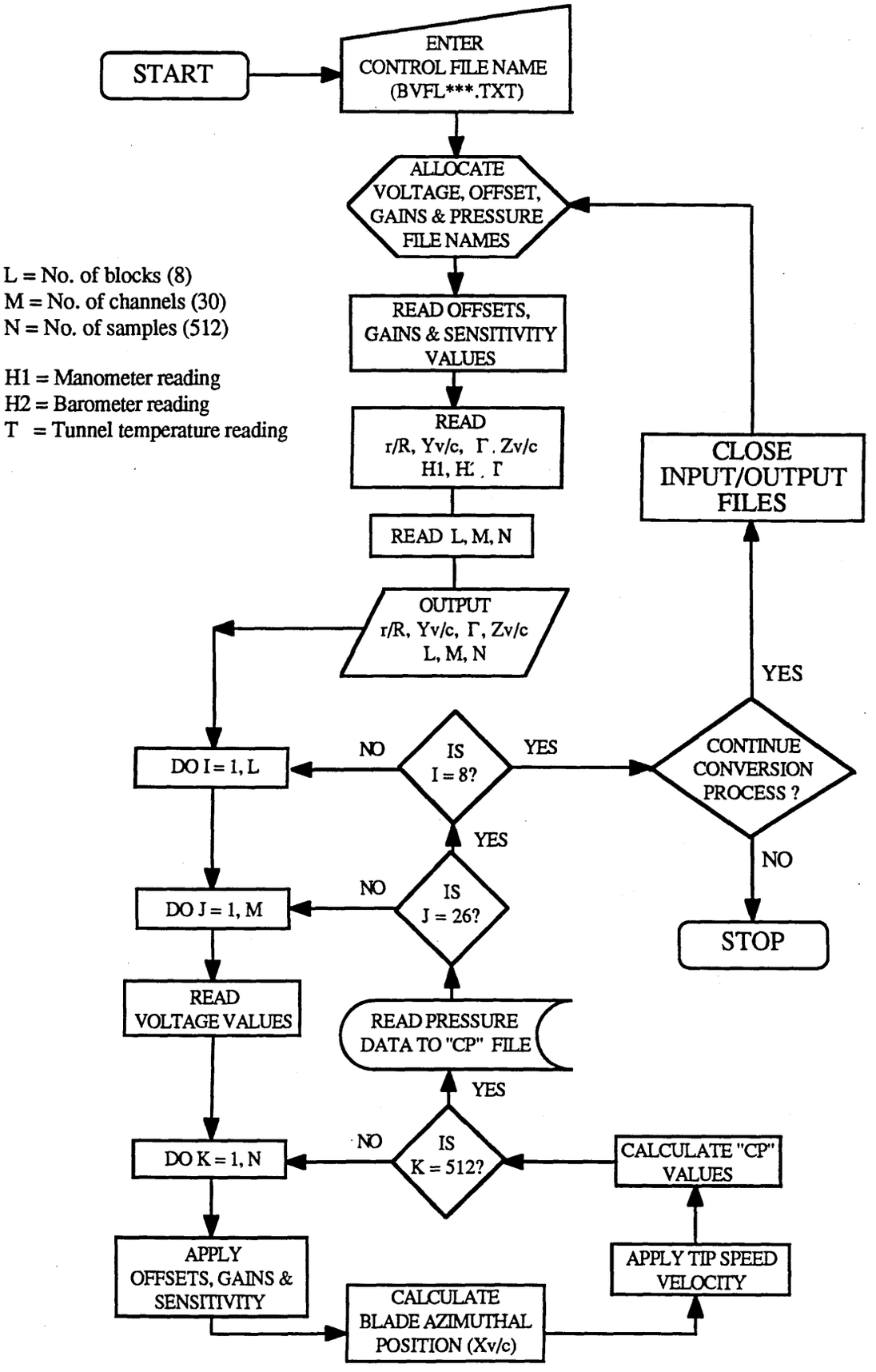

Figure 2.21. Flowchart for Reducing the BVI Data from Voltages to Pressure Coefficients values (Program CPICONV.FOR)

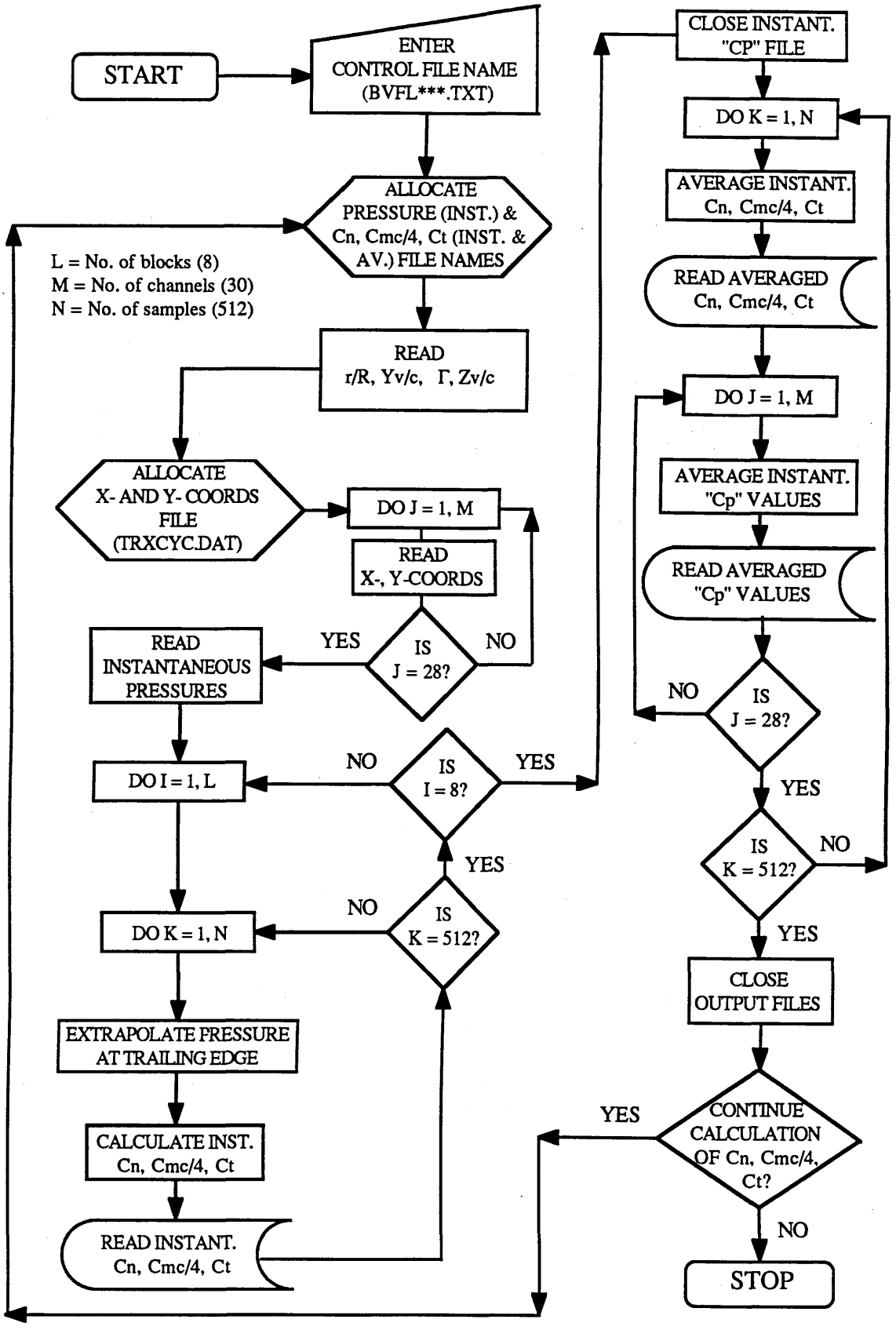

Figure 2.22. Flowchart for the Calculation of the Instantaneous and Averaged C_n, $C_{mc/4}$, C_t and Averaged Pressure Coefficients (Program CNTMNGT.FOR)

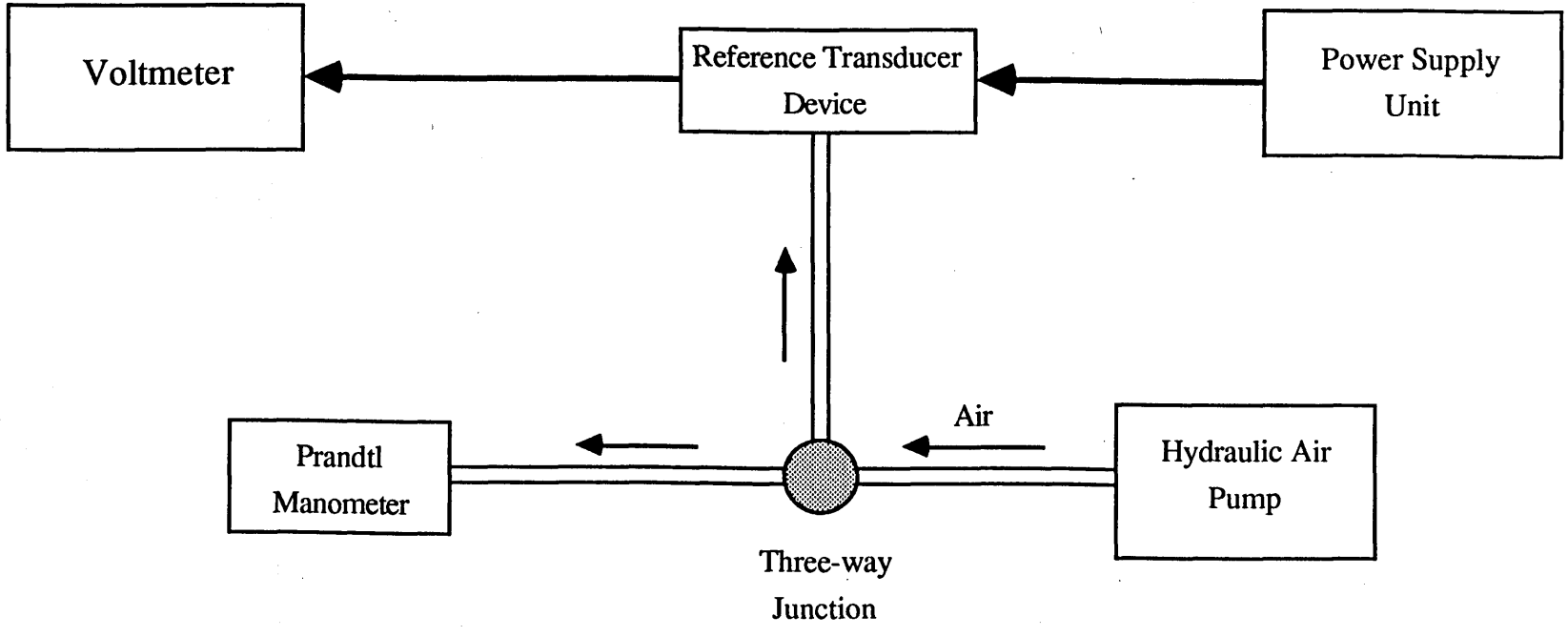

Figure 3.1. Schematic of the Reference Transducer Calibration Equipment

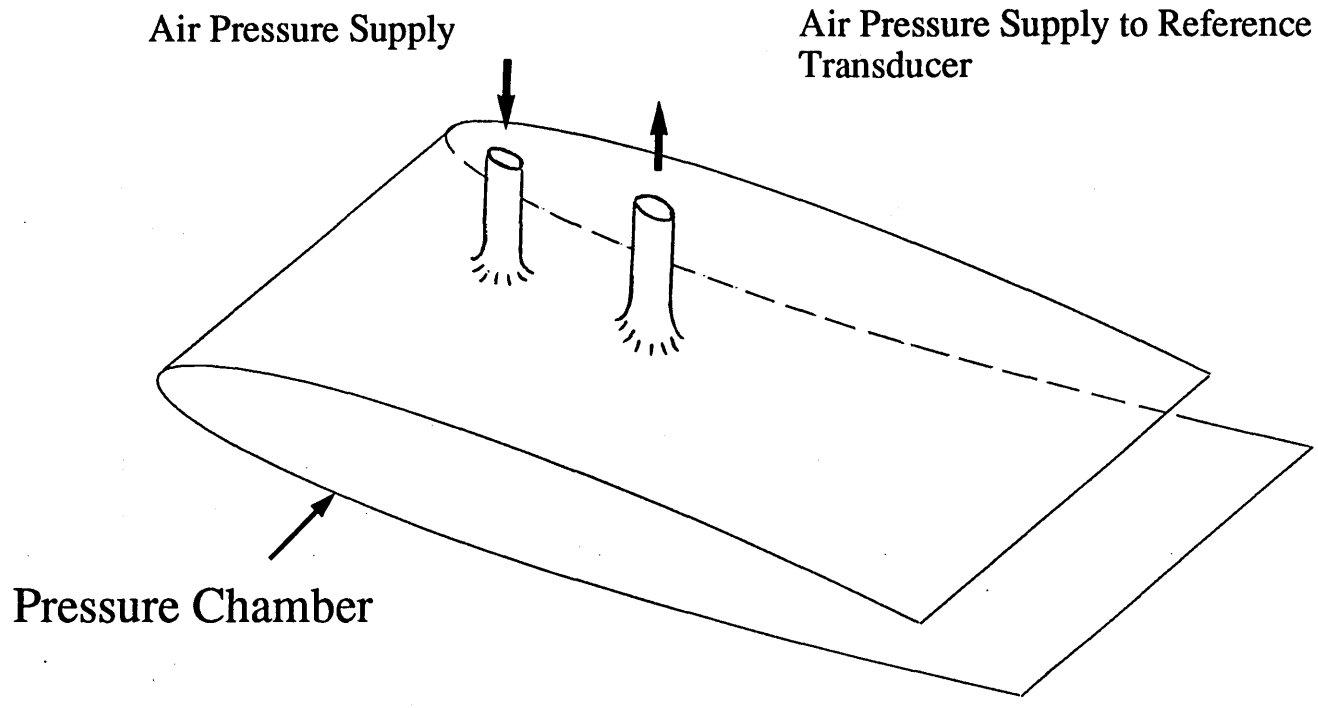

Figure 3.2. Pressure Chamber Arrangement for Transducer Calibration

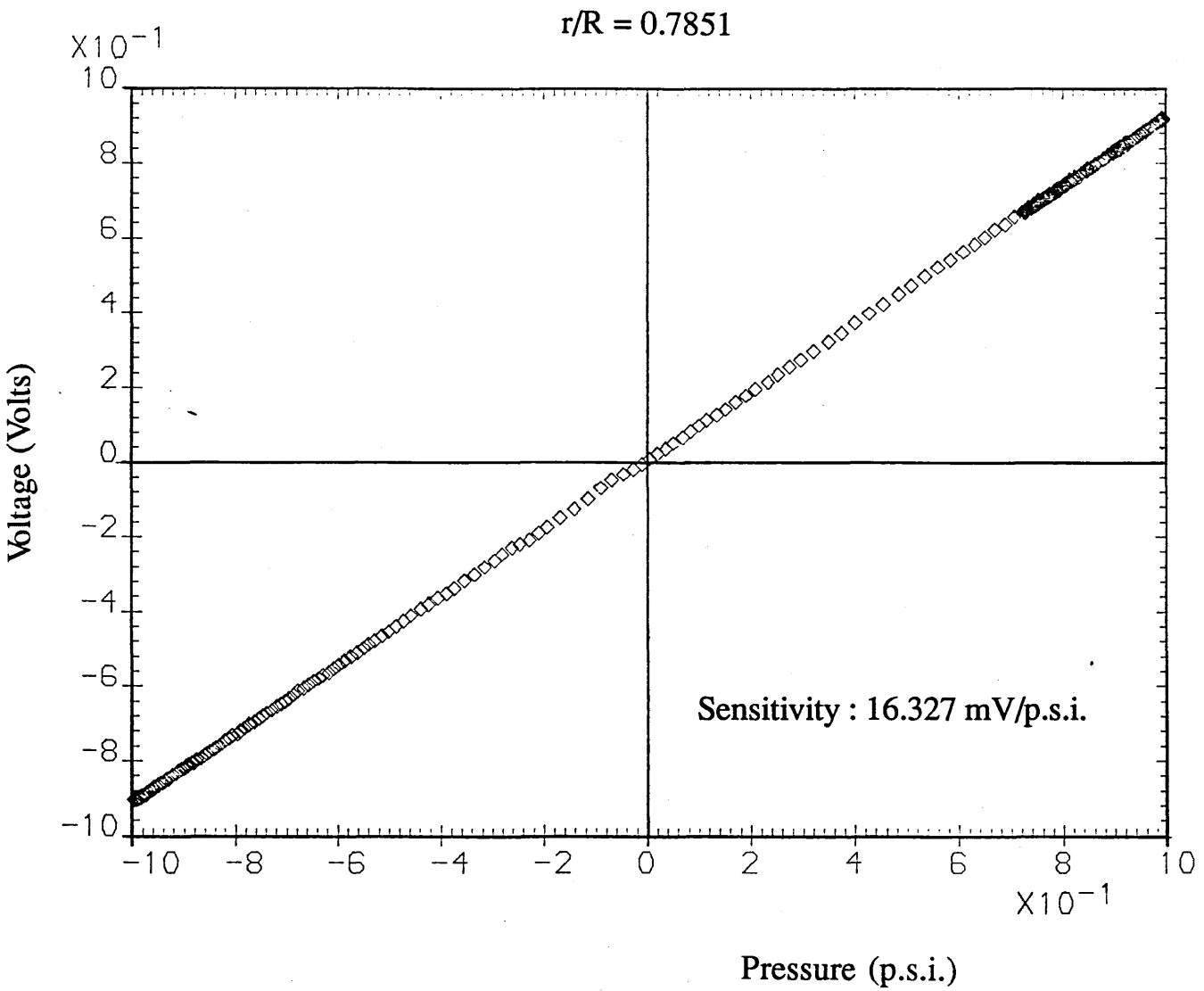

Figure 3.3. A Typical Calibration Curve (Channel No. 9, x/c=0.20604)

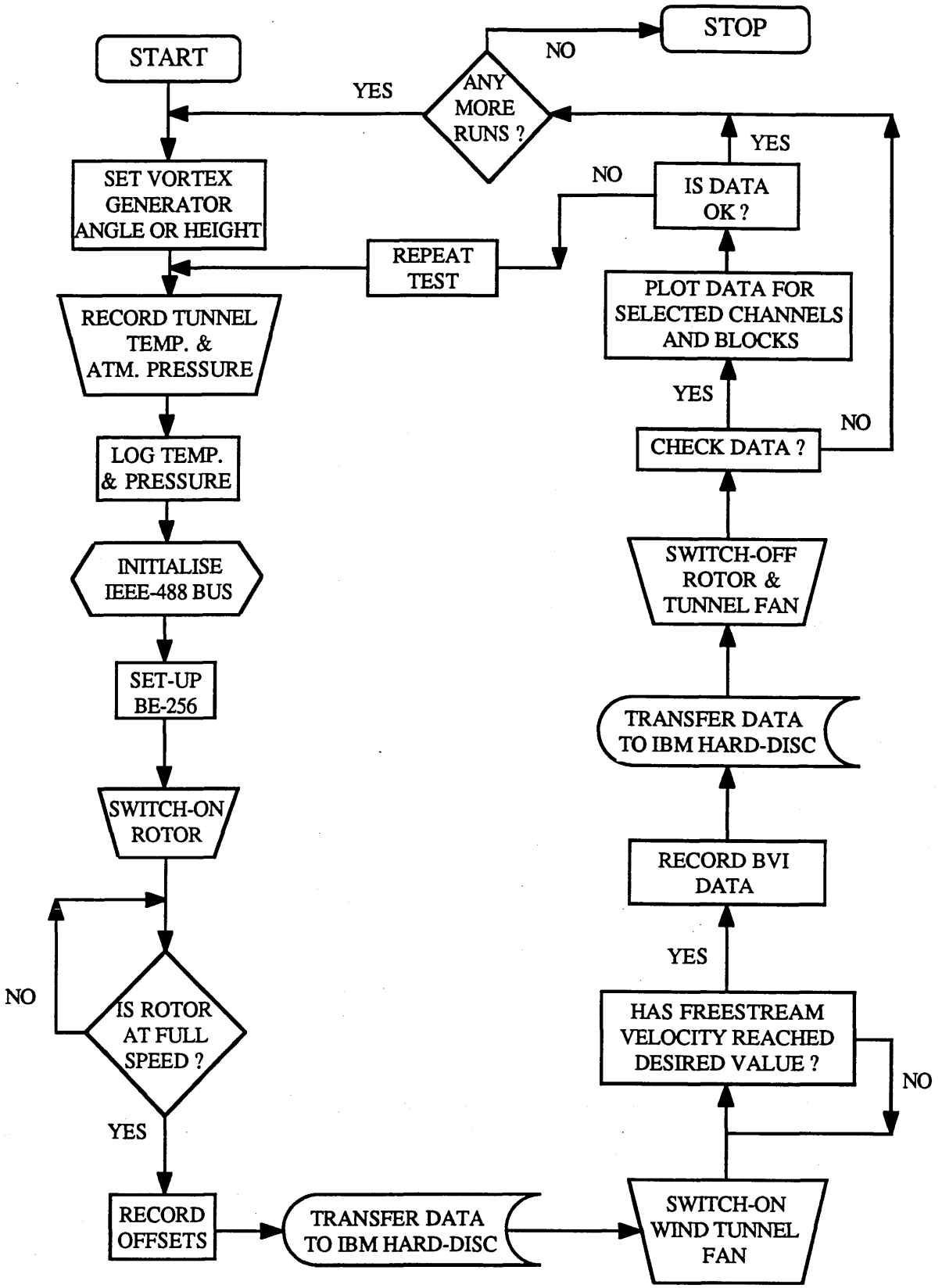

Figure 3.4. Flowchart Diagram Illustrating the Sequence of Events During a Blade-Vortex Interaction Test Run

"PARALLEL" B.V.I. TEST

RUN REFERENCE NUMBER : 36521

Blade Section :	" NACA - 0015 "	Vortex Strength :	6.70 m^2/s
Spanwise Position,	r/R = 0.7056	Vortex Separation,	Yv/C = 0.4000
Tip Reynolds Number,	Re = 600000		Zv/C = 0.0000
Tip Mach Number,	M_t = 0.174	Blade - Vortex Intersection Angle	= 90.000

AVERAGED DATA

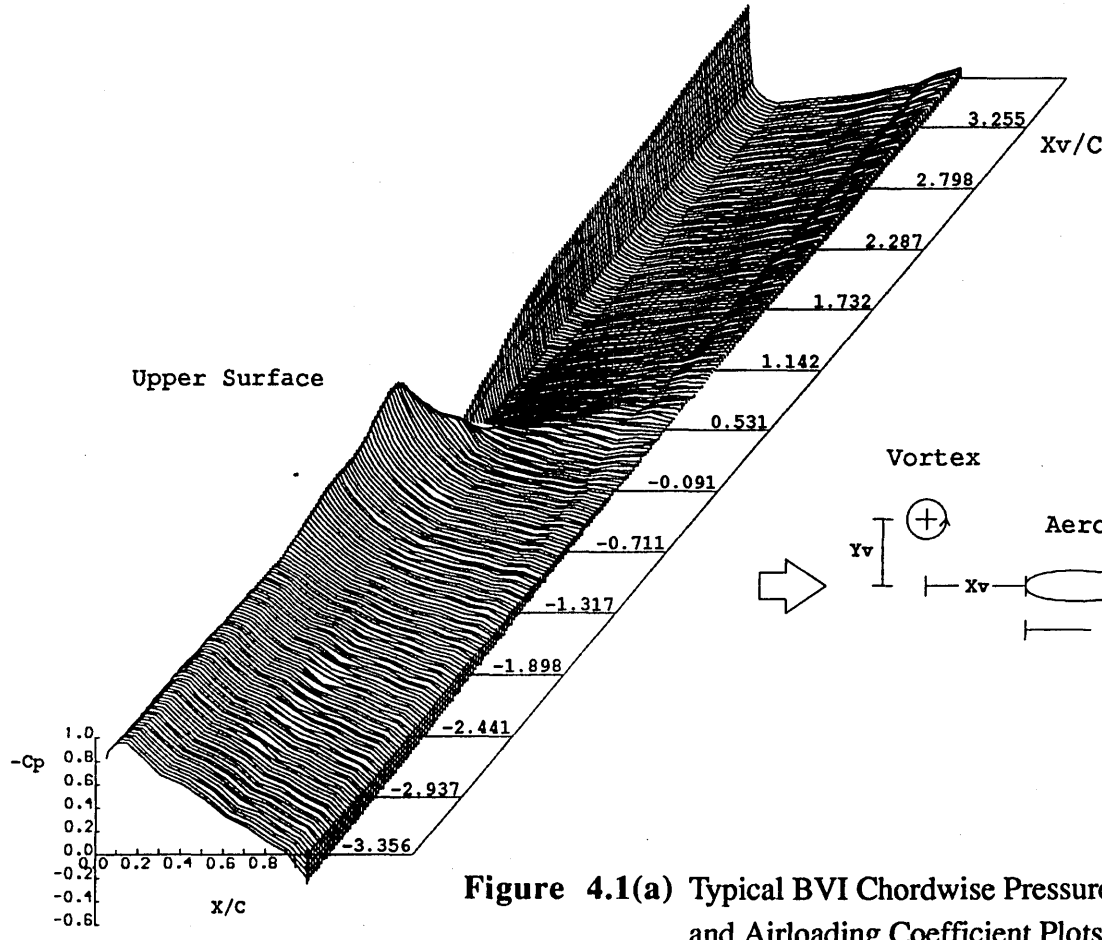

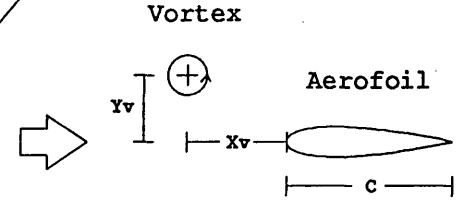

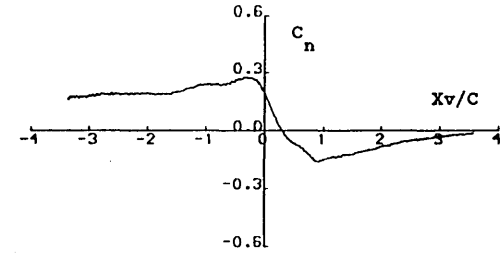

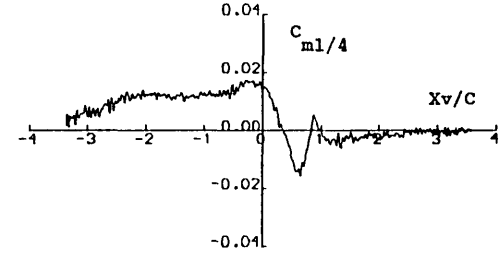

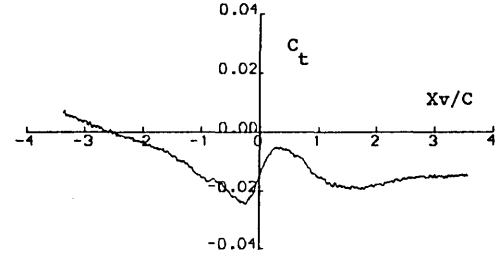

Figure 4.1(a) Typical BVI Chordwise Pressure Distributions (Upper Surface) and Airloading Coefficient Plots for Various Azimuth Locations

"PARALLEL" B.V.I. TEST

RUN REFERENCE NUMBER : 36521

Blade Section :	" NACA - 0015 "	Vortex Strength :	6.70 m^2/s
Spanwise Position,	r/R = 0.7056	Vortex Separation,	Yv/C = 0.4000
Tip Reynolds Number,	Re = 600000		Zv/C = 0.0000
Tip Mach Number,	M_t = 0.174	Blade - Vortex Intersection Angle	= 90.000

AVERAGED DATA

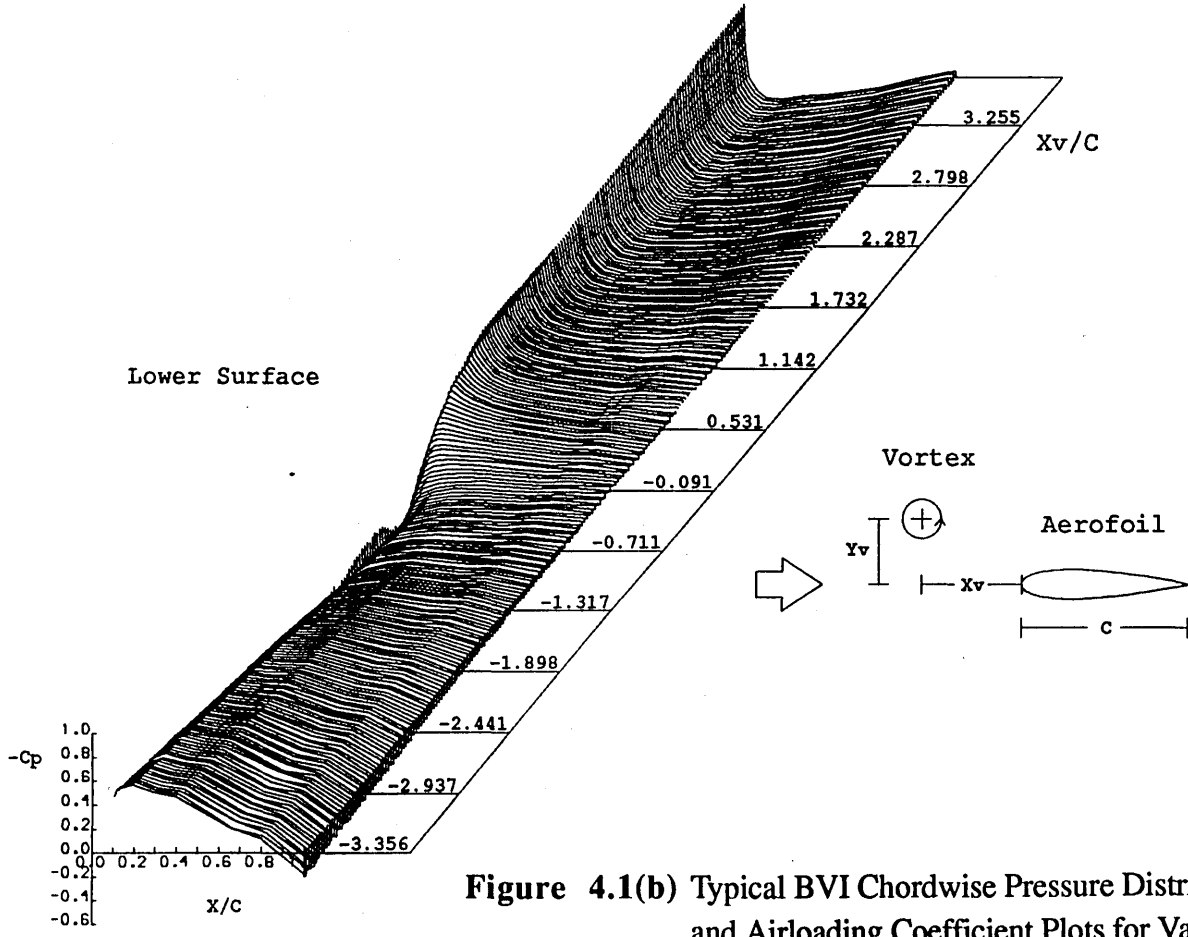

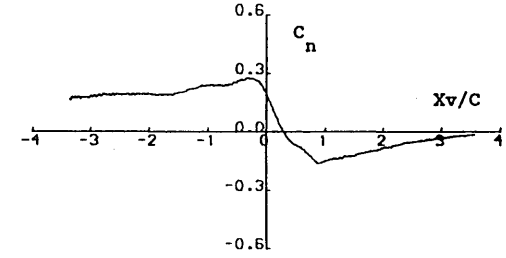

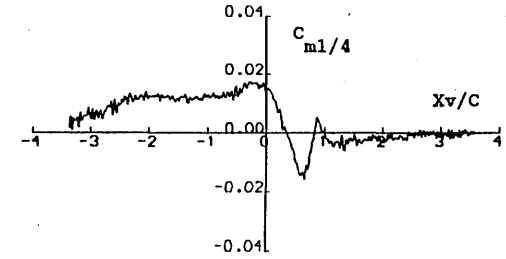

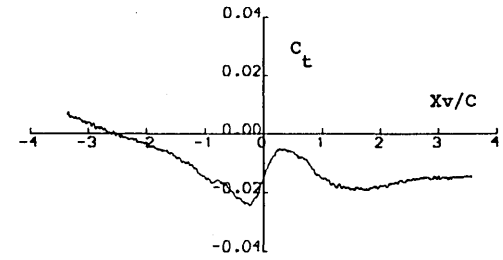

Figure 4.1(b) Typical BVI Chordwise Pressure Distributions (Lower Surface) and Airloading Coefficient Plots for Various Azimuth Locations

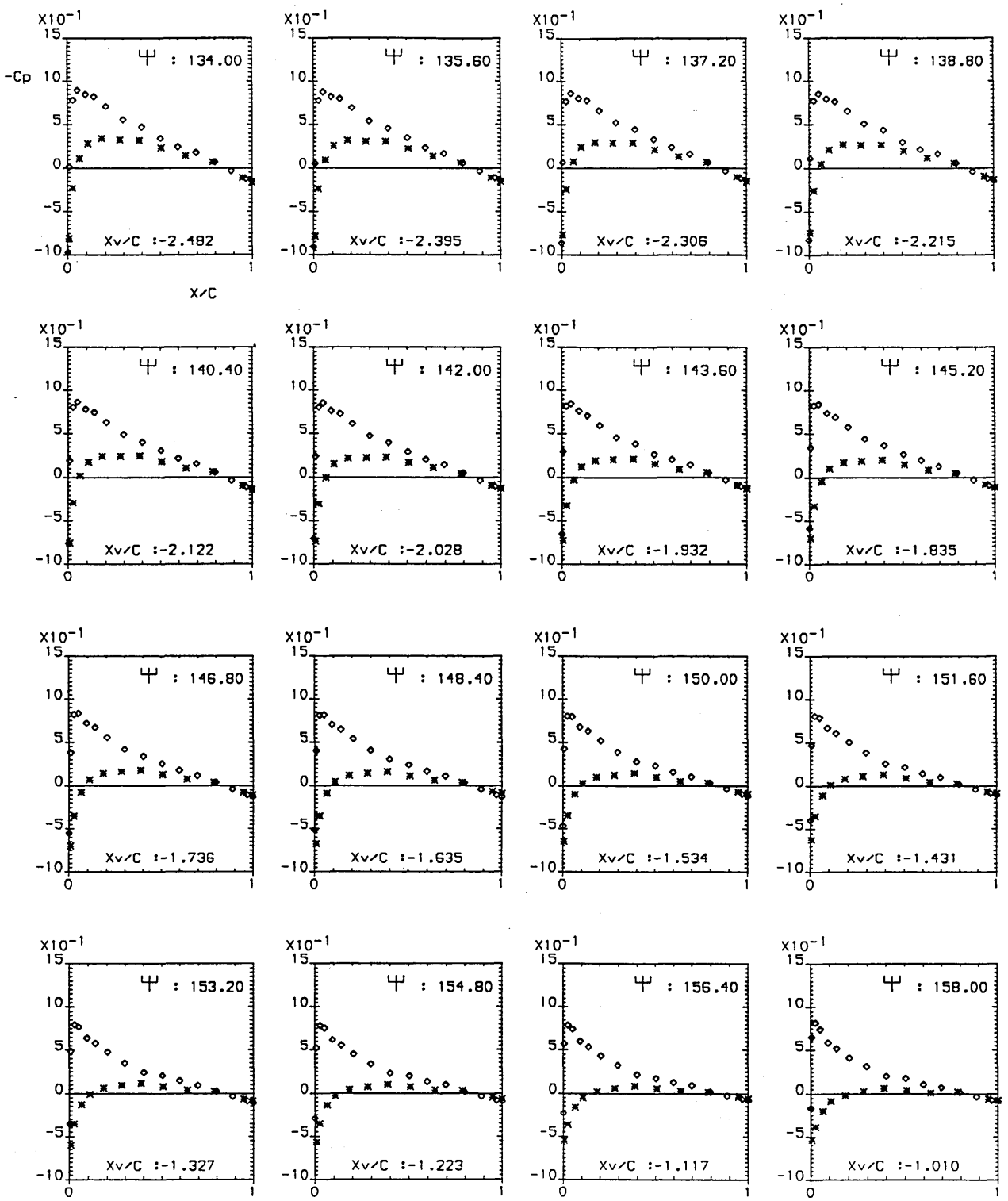

Figure 4.1.1. Instantaneous Surface Pressure Distributions during a Parallel BVI : r/R=0.62, Γ=6.70m^2/s, Y_v/c=-0.20

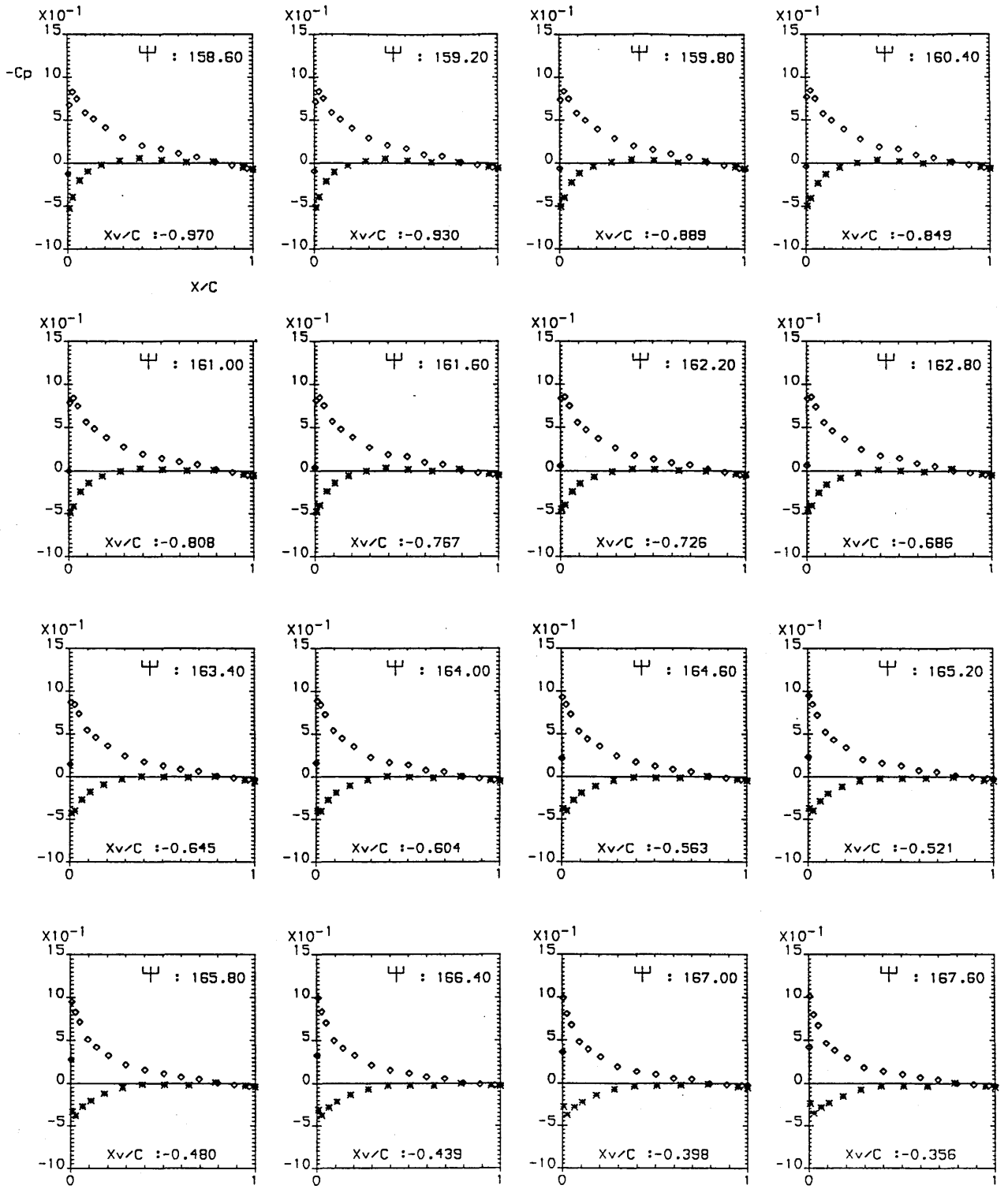

Figure 4.1.1 Continued...

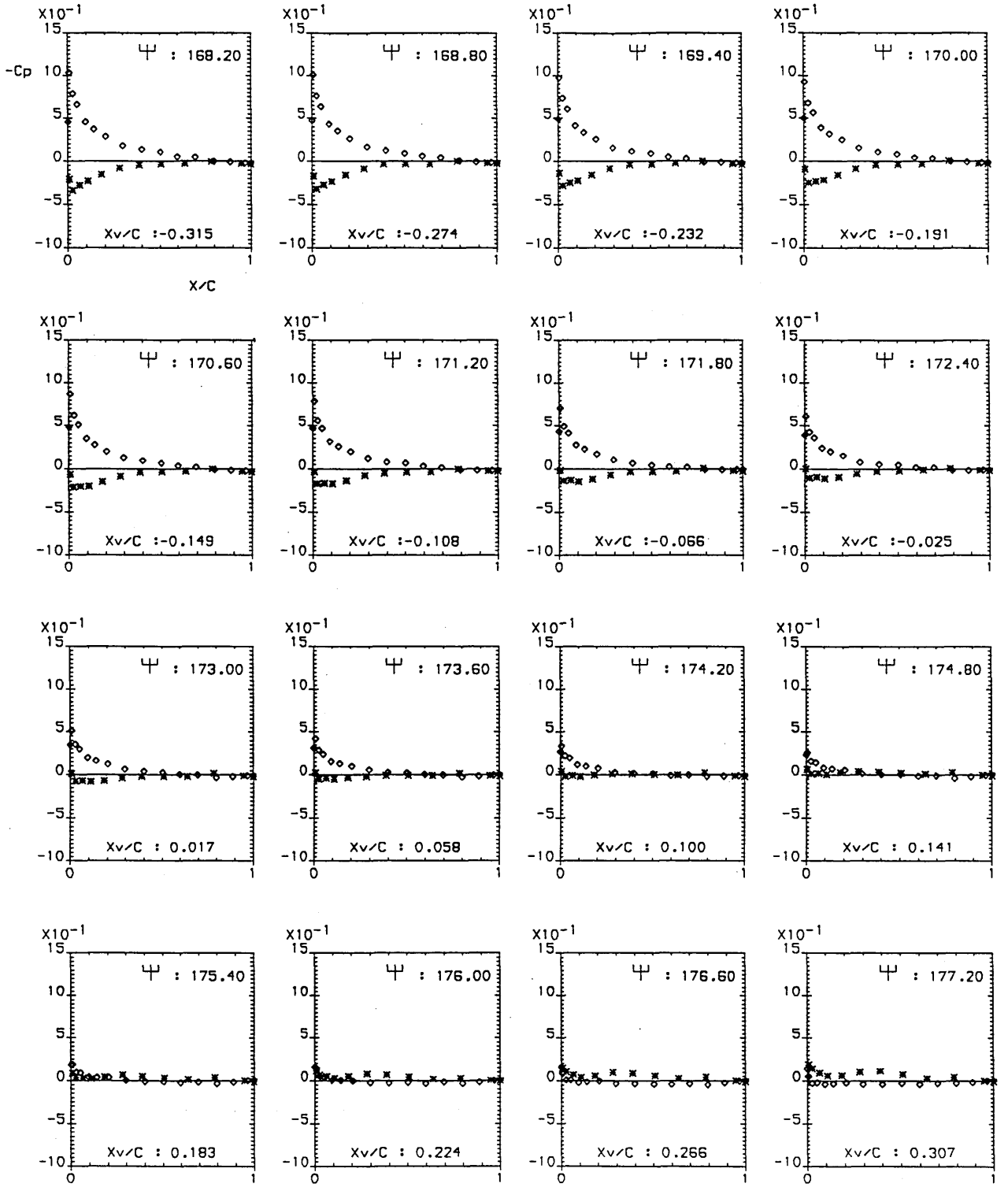

Figure 4.1.1 Continued...

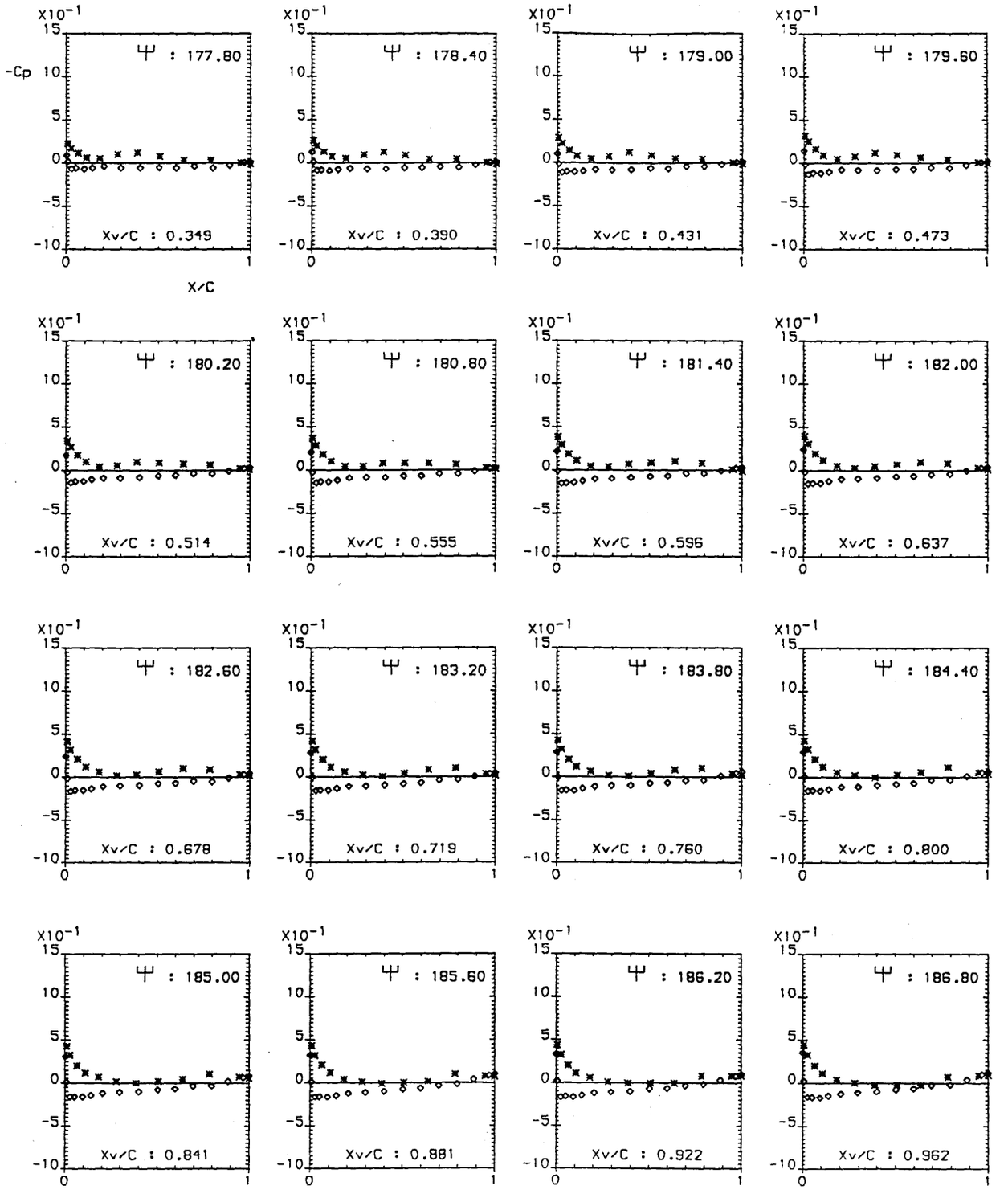

Figure 4.1.1 Continued...

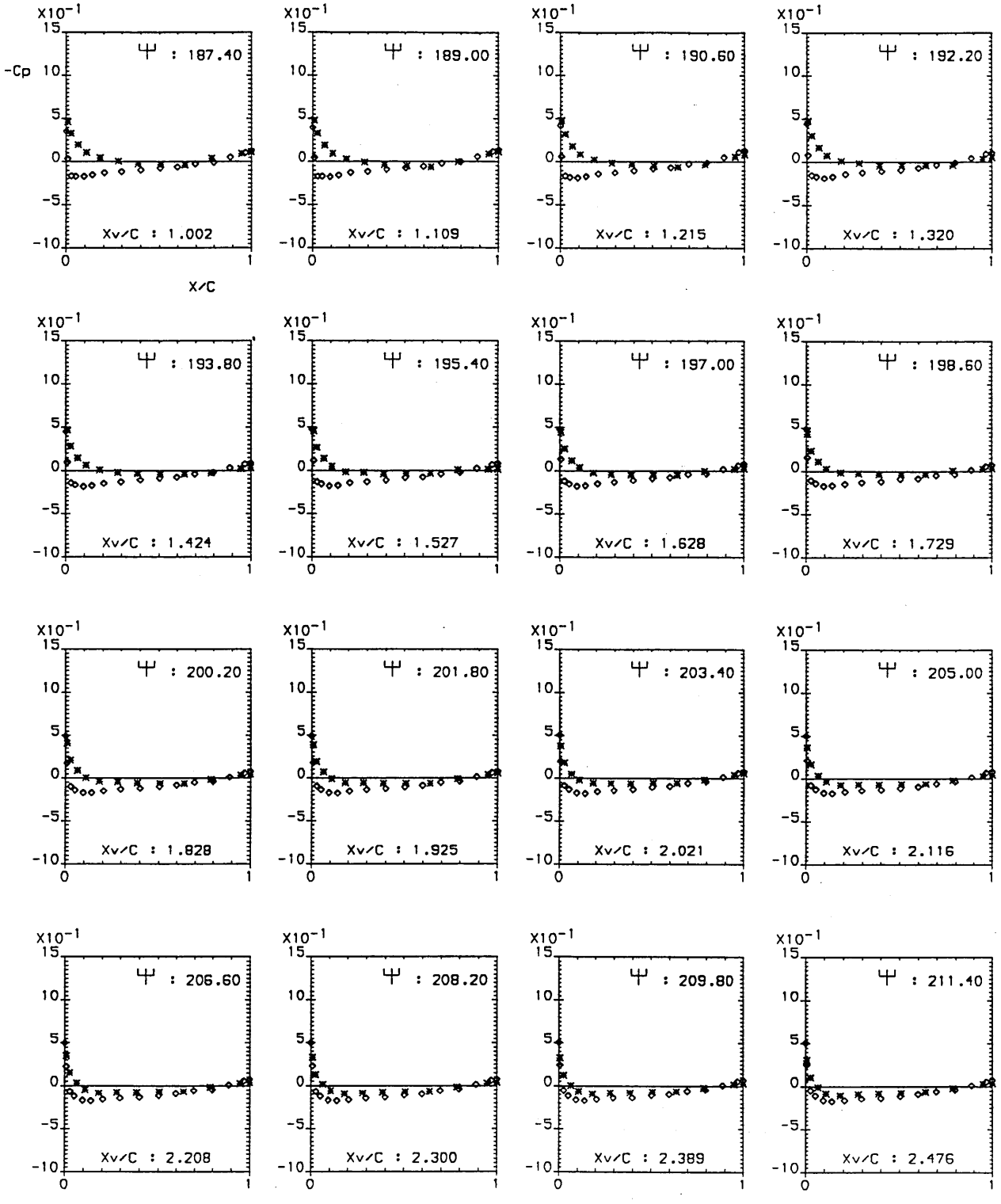

Figure 4.1.1 Concluded

"PARALLEL" B.V.I. TEST

RUN REFERENCE NUMBER : 35491

Blade Section :	" NACA - 0015 "	Vortex Strength :	6.70 m^2/s
Spanwise Position,	r/R = 0.6260	Vortex Separation,	Yv/C = -0.2000
Tip Reynolds Number,	Re = 600000		Zv/C = 0.0000
Tip Mach Number,	M_t = 0.174	Blade - Vortex Intersection Angle	= 90.000

AVERAGED DATA

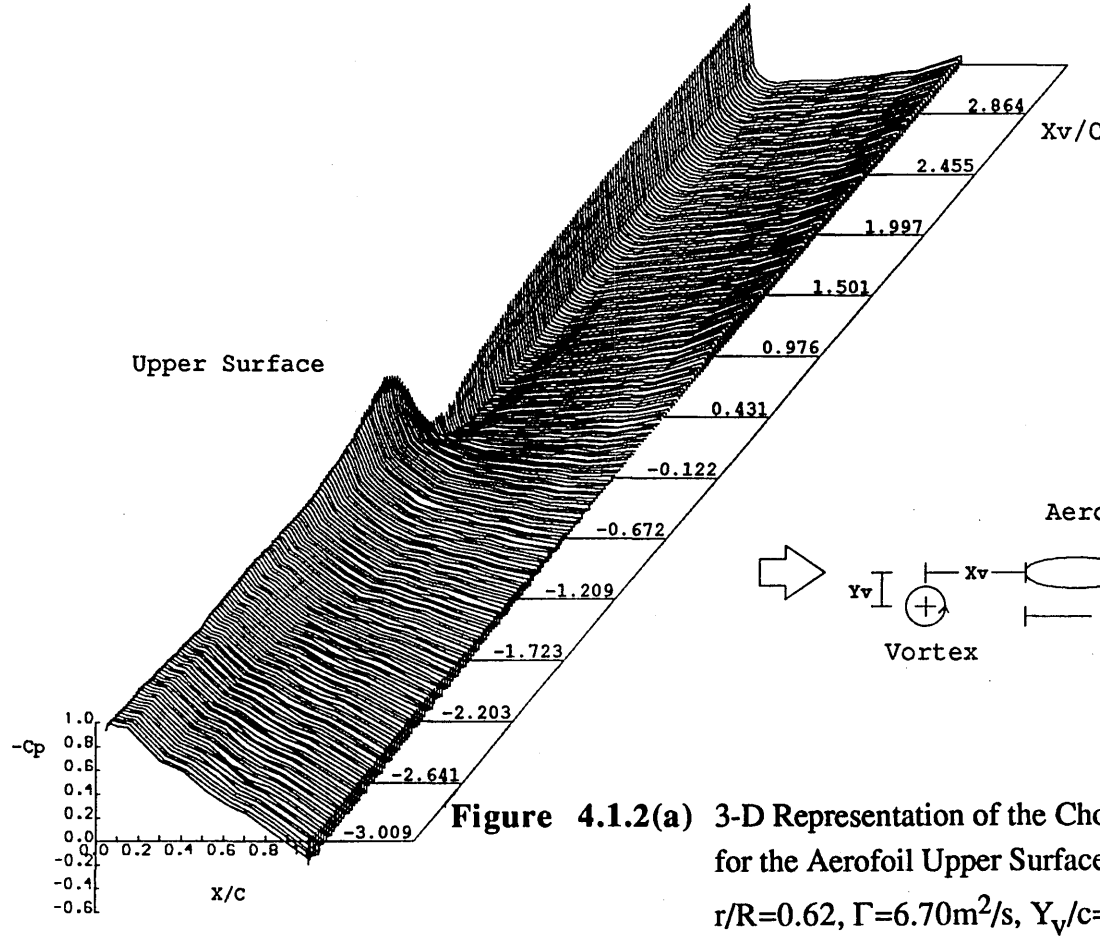

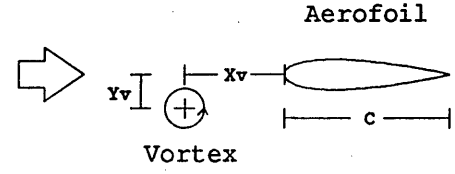

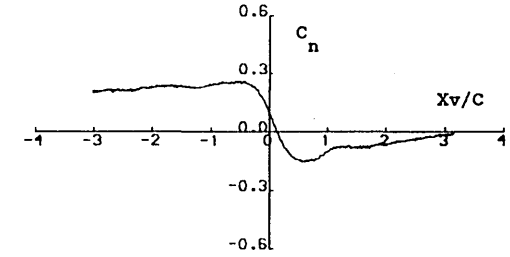

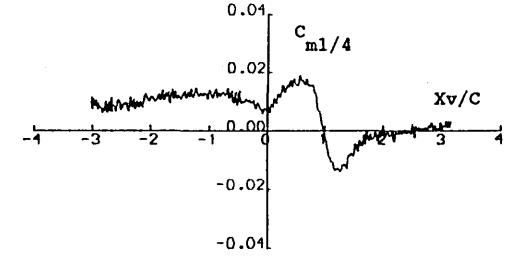

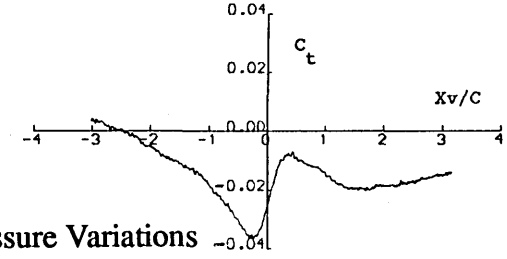

Figure 4.1.2(a) 3-D Representation of the Chordwise Pressure Variations for the Aerofoil Upper Surface During a Parallel BVI : r/R=0.62, Γ=6.70m^2/s, Y_v/c=-0.20

"PARALLEL" B.V.I. TEST

RUN REFERENCE NUMBER : 35491

Blade Section :	" NACA - 0015 "	Vortex Strength :	6.70 m^2/s
Spanwise Position,	r/R = 0.6260	Vortex Separation,	Yv/C = -0.2000
Tip Reynolds Number,	Re = 600000		Zv/C = 0.0000
Tip Mach Number,	M_t = 0.174	Blade - Vortex Intersection Angle	= 90.000

AVERAGED DATA

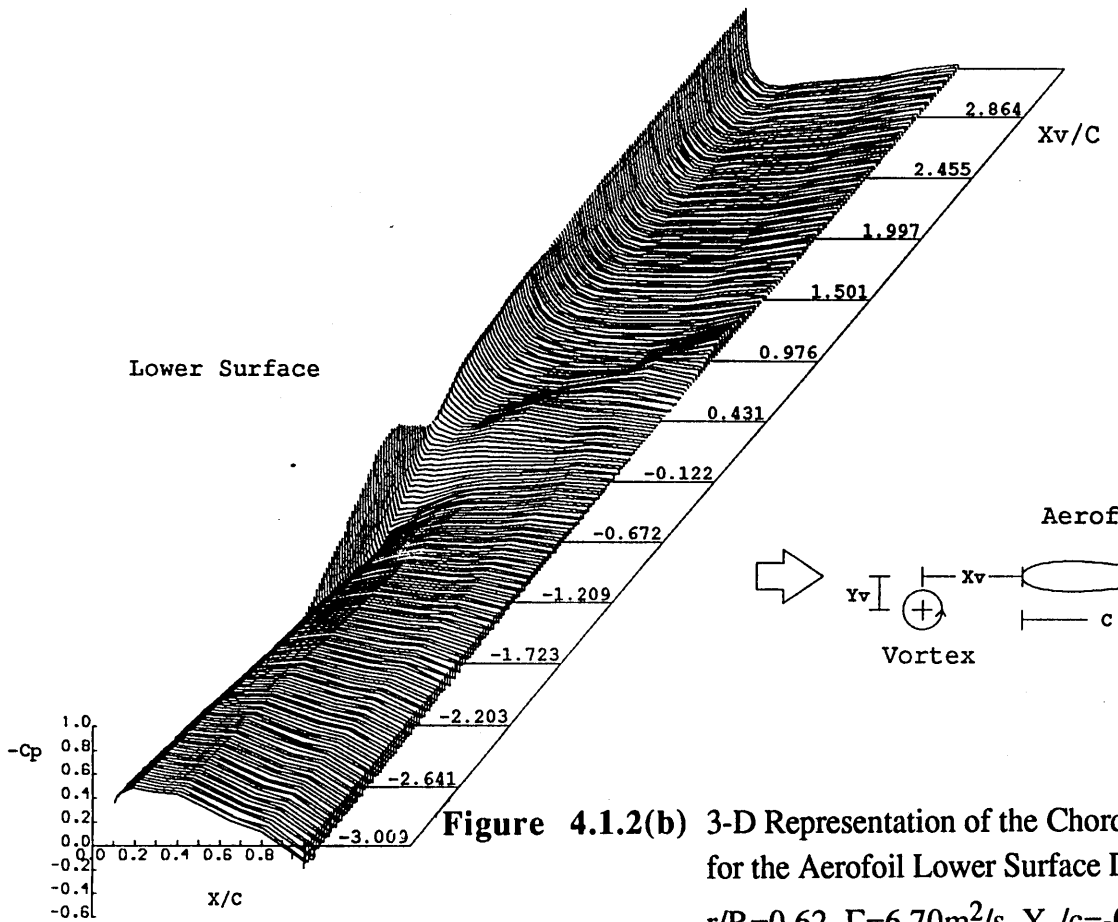

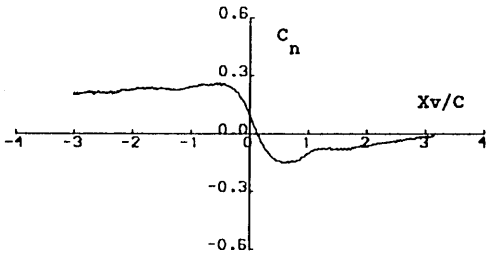

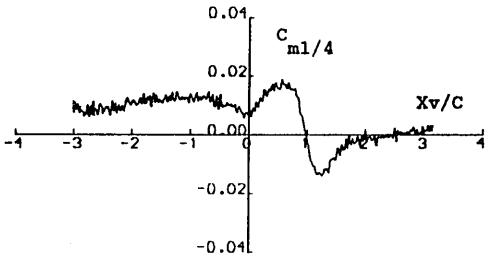

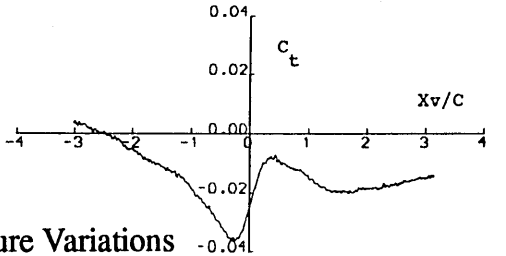

Figure 4.1.2(b) 3-D Representation of the Chordwise Pressure Variations for the Aerofoil Lower Surface During a Parallel BVI : r/R=0.62, Γ=6.70m^2/s, Y_V/c=-0.20

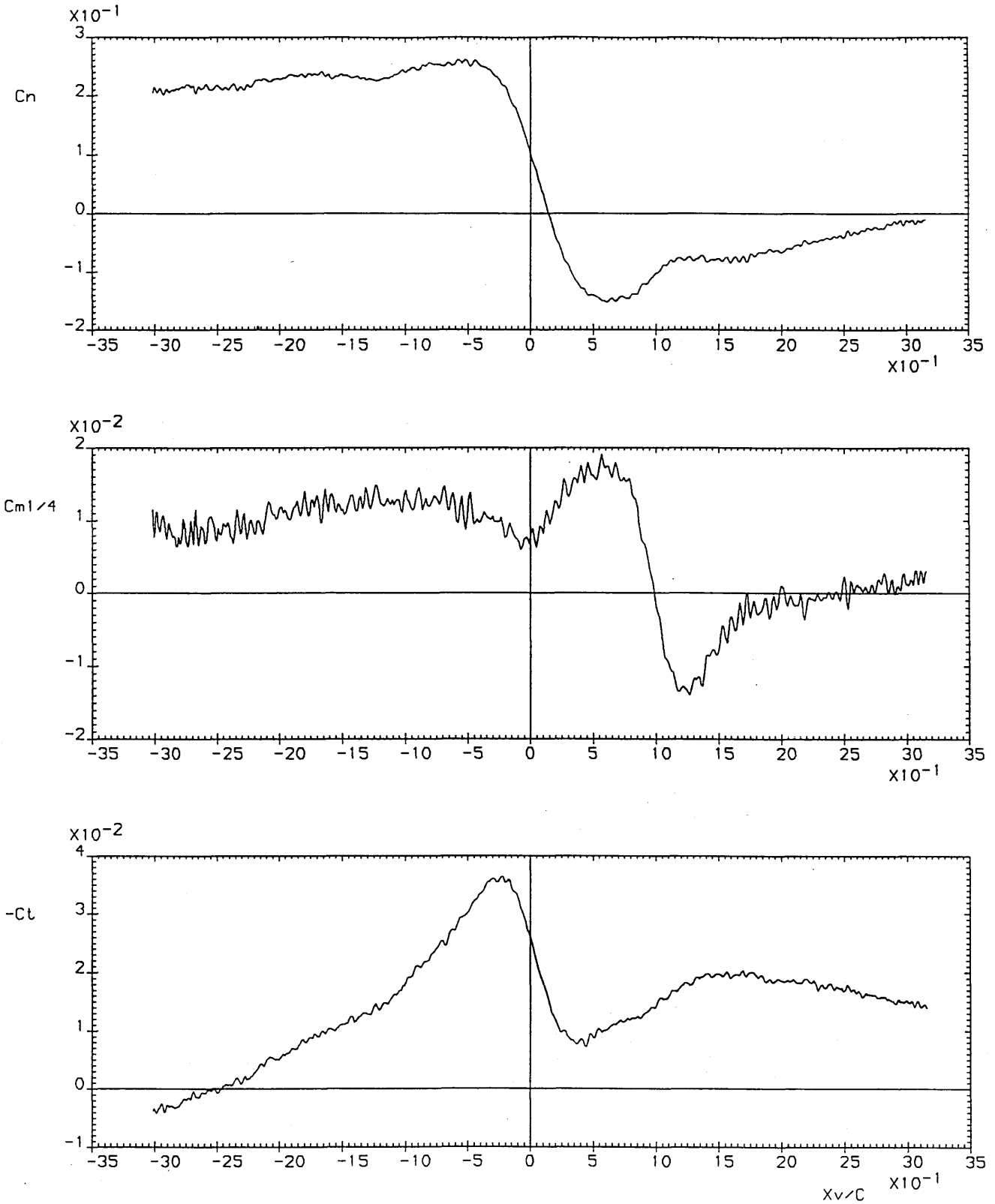

Figure 4.1.3. Aerodynamic Load Coefficient Variations for a Variety of Azimuthal Locations (X_v/c) During a Parallel BVI : r/R=0.62, Γ=6.70m^2/s, Y_v/c=-0.20

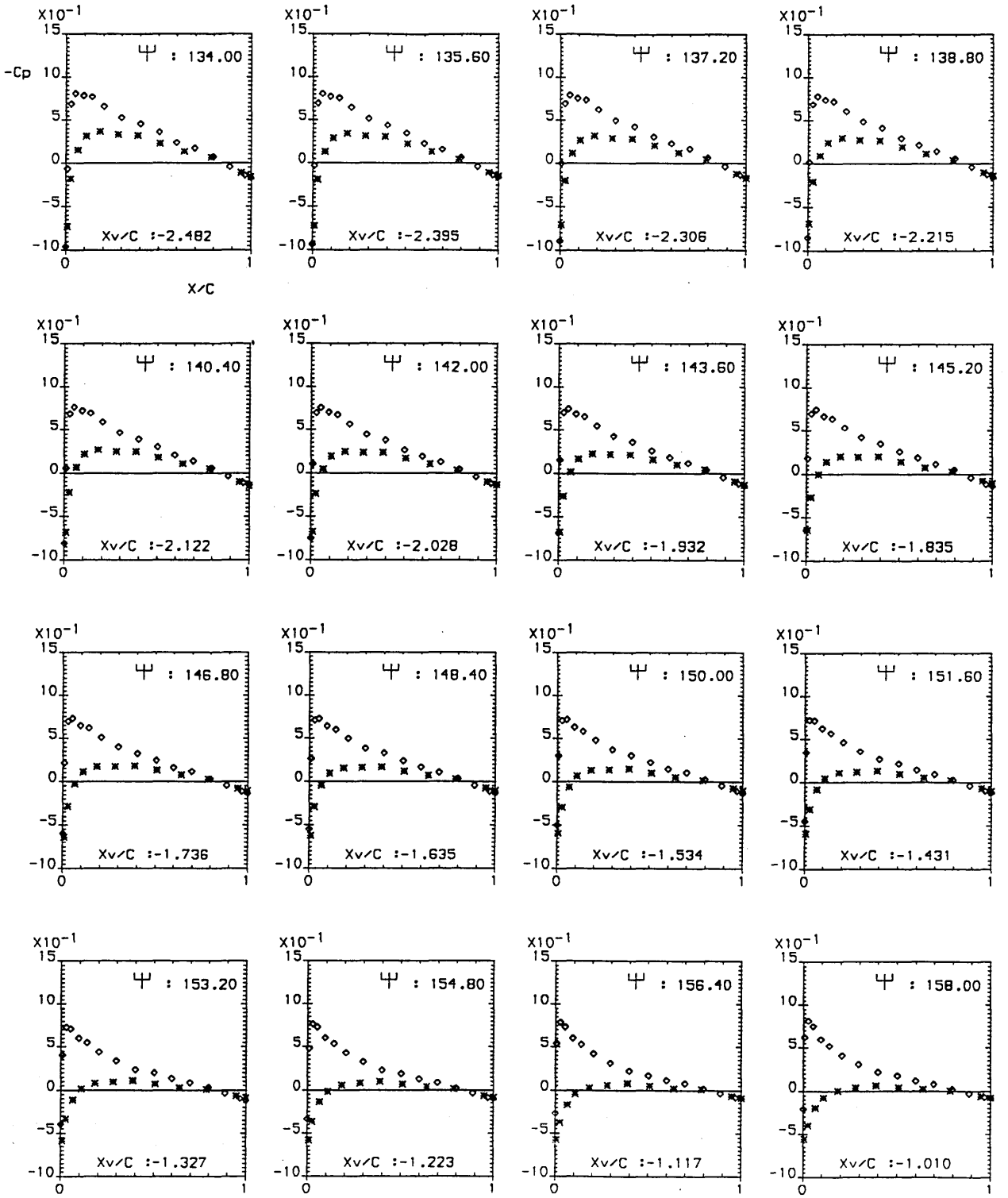

Figure 4.1.4. Instantaneous Surface Pressure Distributions During a Parallel BVI : r/R=0.62, Γ=6.70m^2/s, Y_v/c=0.00

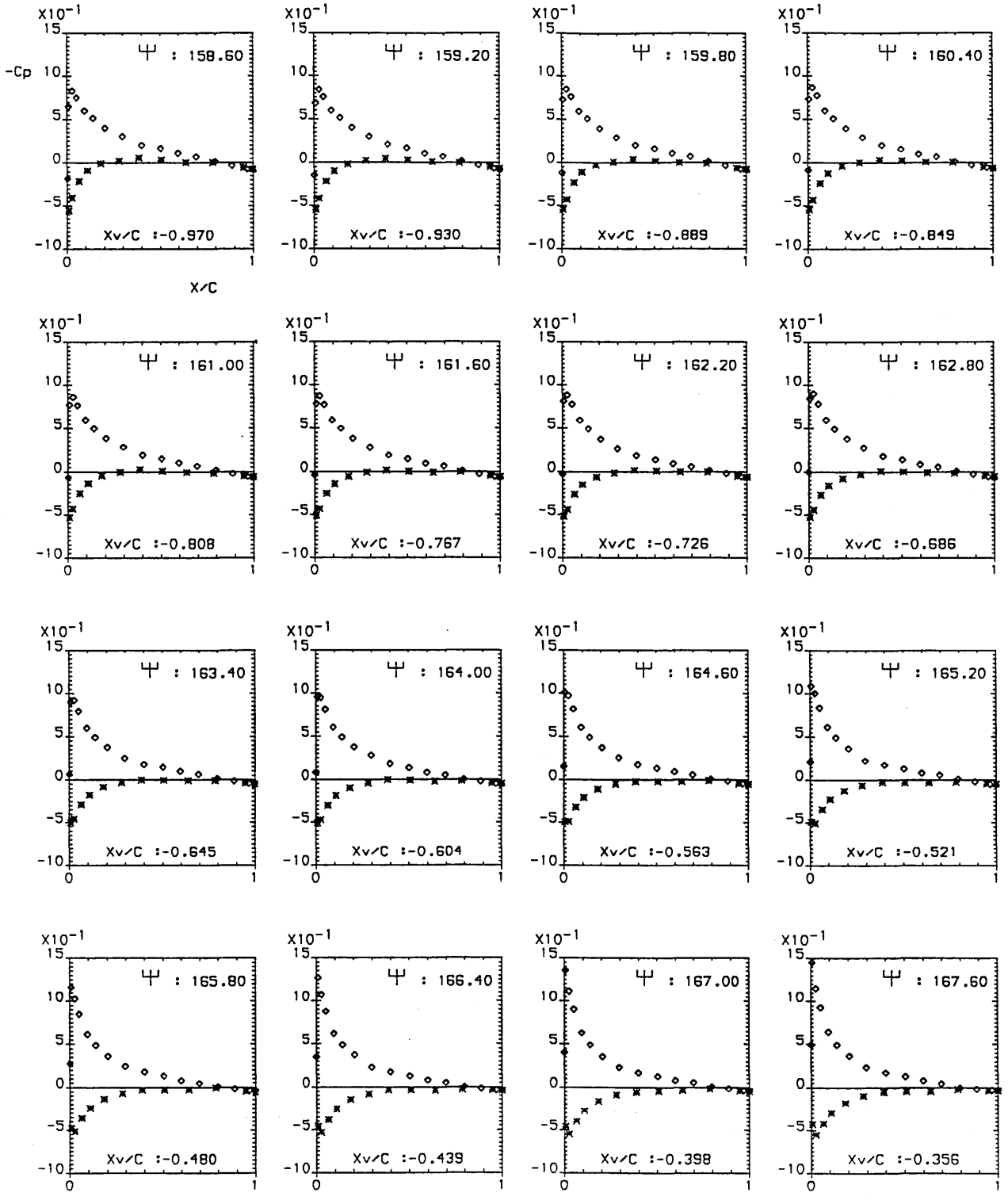

Figure 4.1.4 Continued...

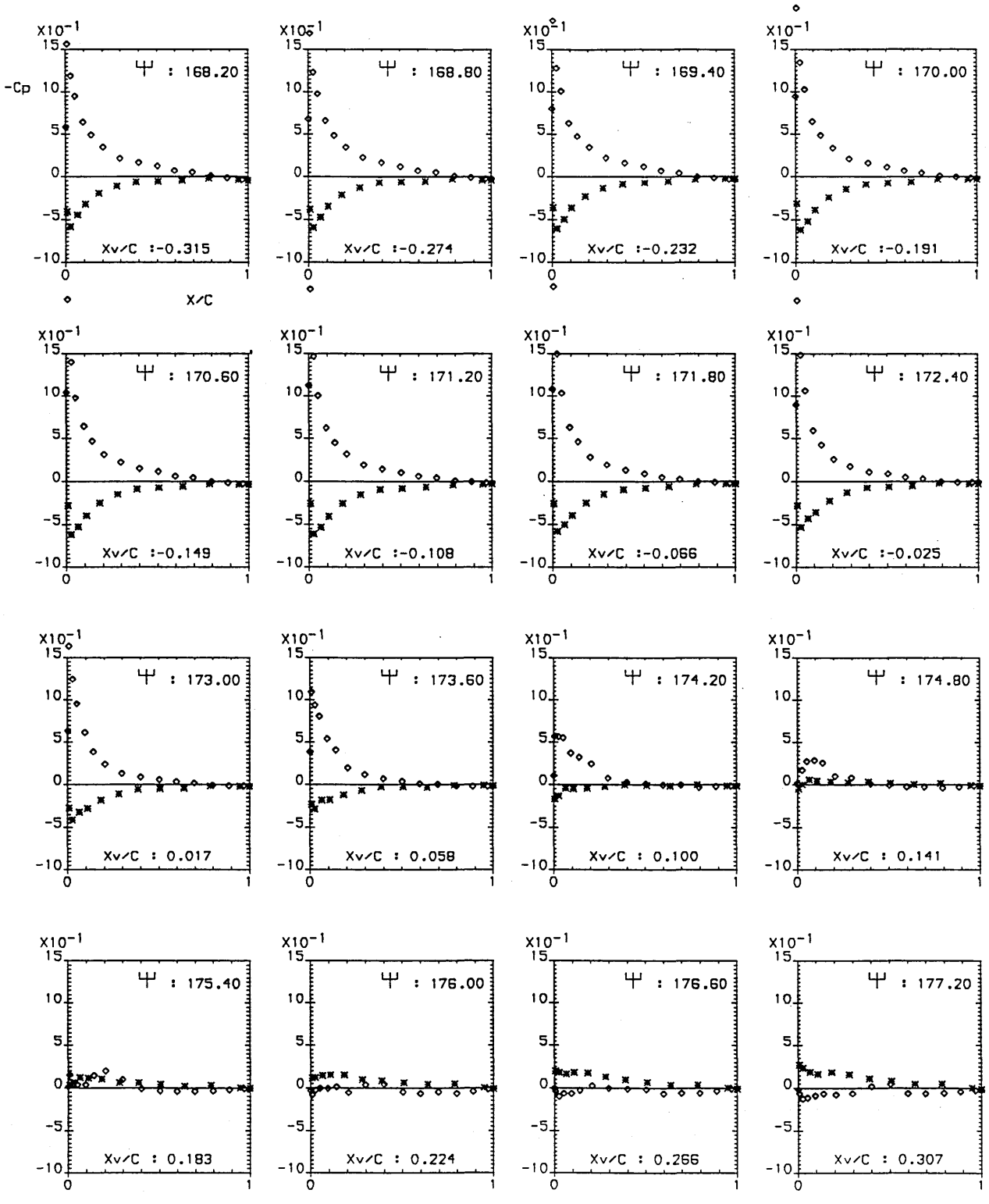

Figure 4.1.4 Continued...

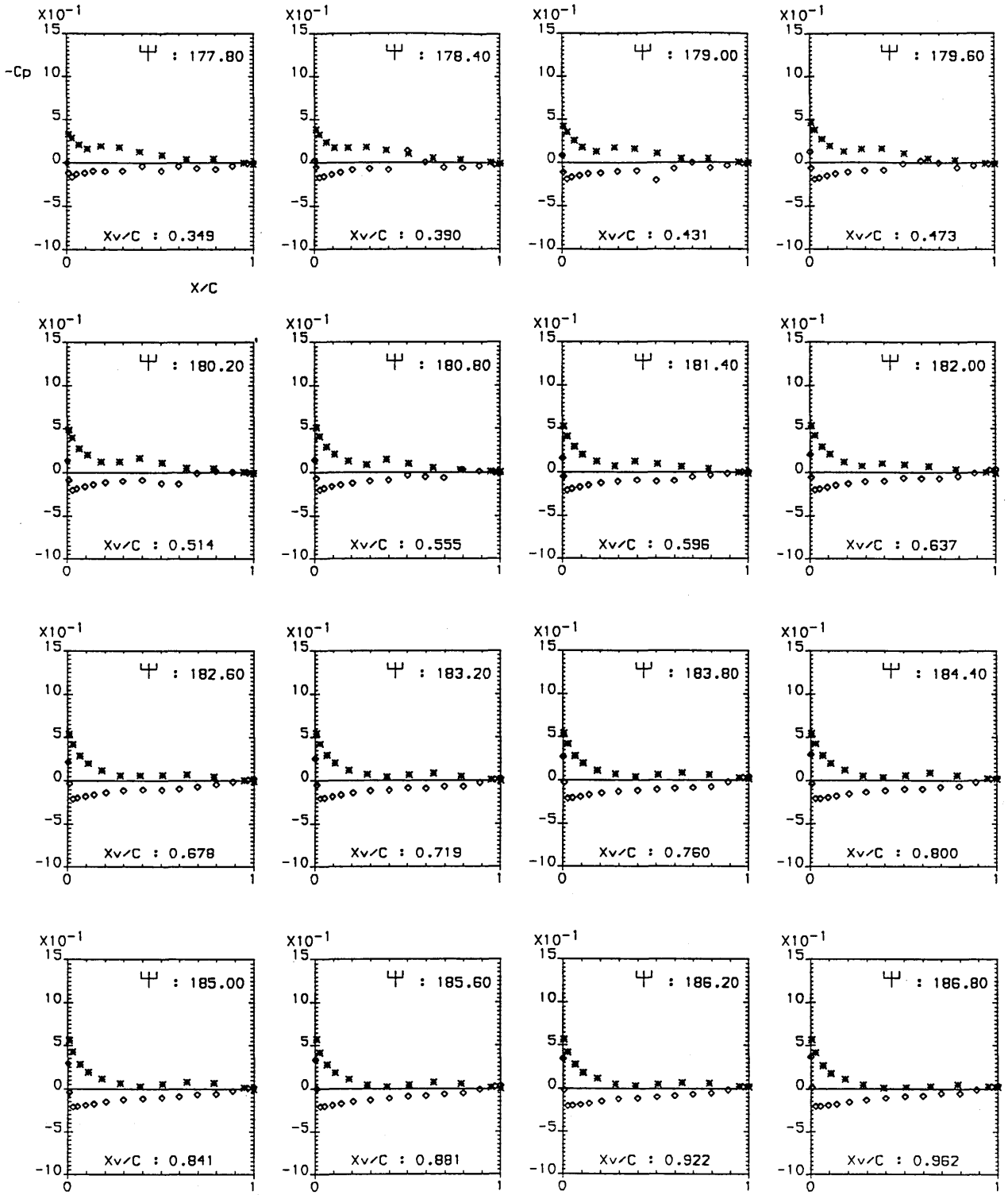

Figure 4.1.4 Continued...

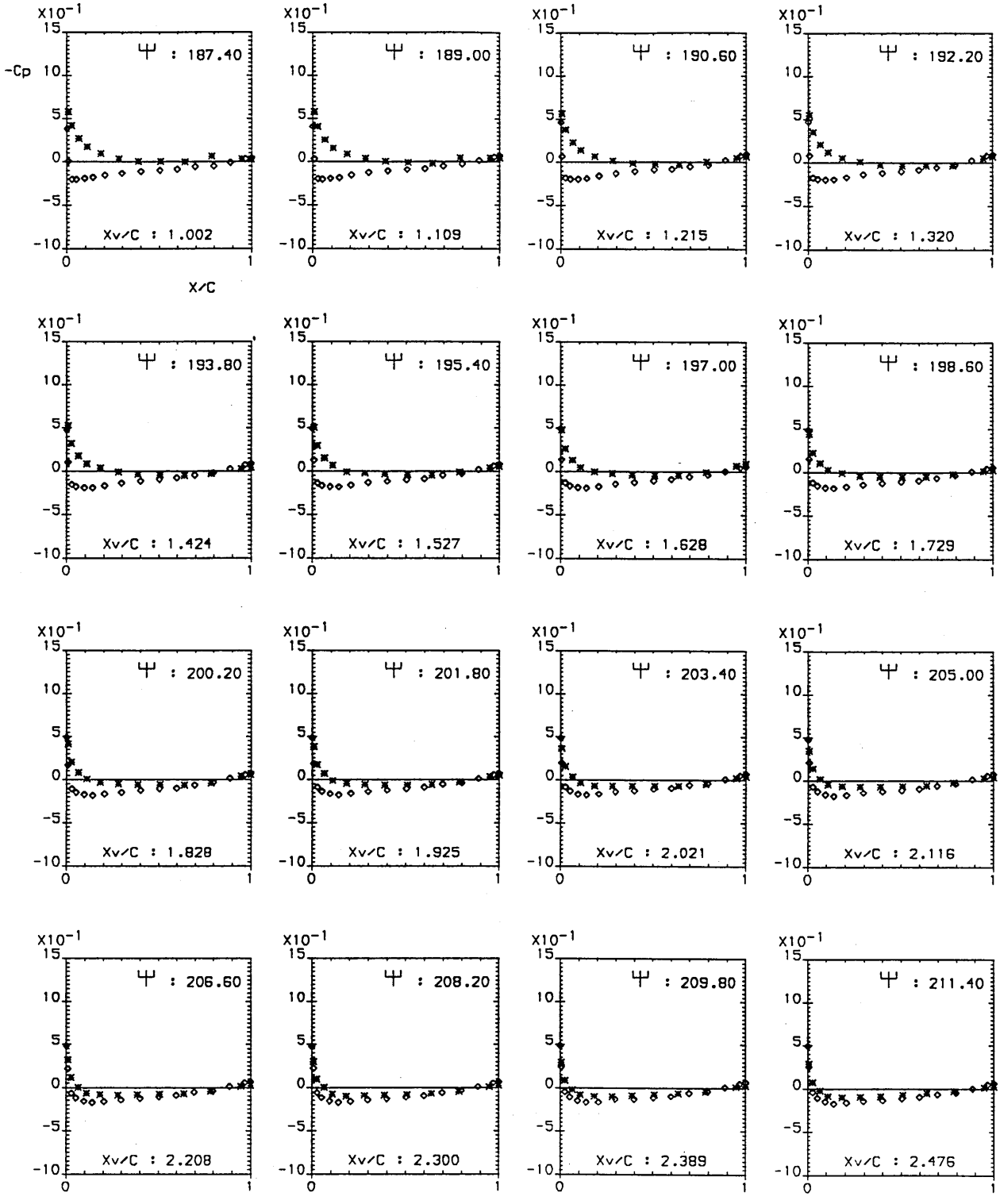

Figure 4.1.4 Concluded

"PARALLEL" B.V.I. TEST

RUN REFERENCE NUMBER : 35501

Blade Section :	" NACA - 0015 "	Vortex Strength :	6.70 m^2/s
Spanwise Position,	r/R = 0.6260	Vortex Separation,	Yv/C = 0.0000
Tip Reynolds Number,	Re = 600000		Zv/C = 0.0000
Tip Mach Number,	M_t = 0.174	Blade - Vortex Intersection Angle	= 90.000

AVERAGED DATA

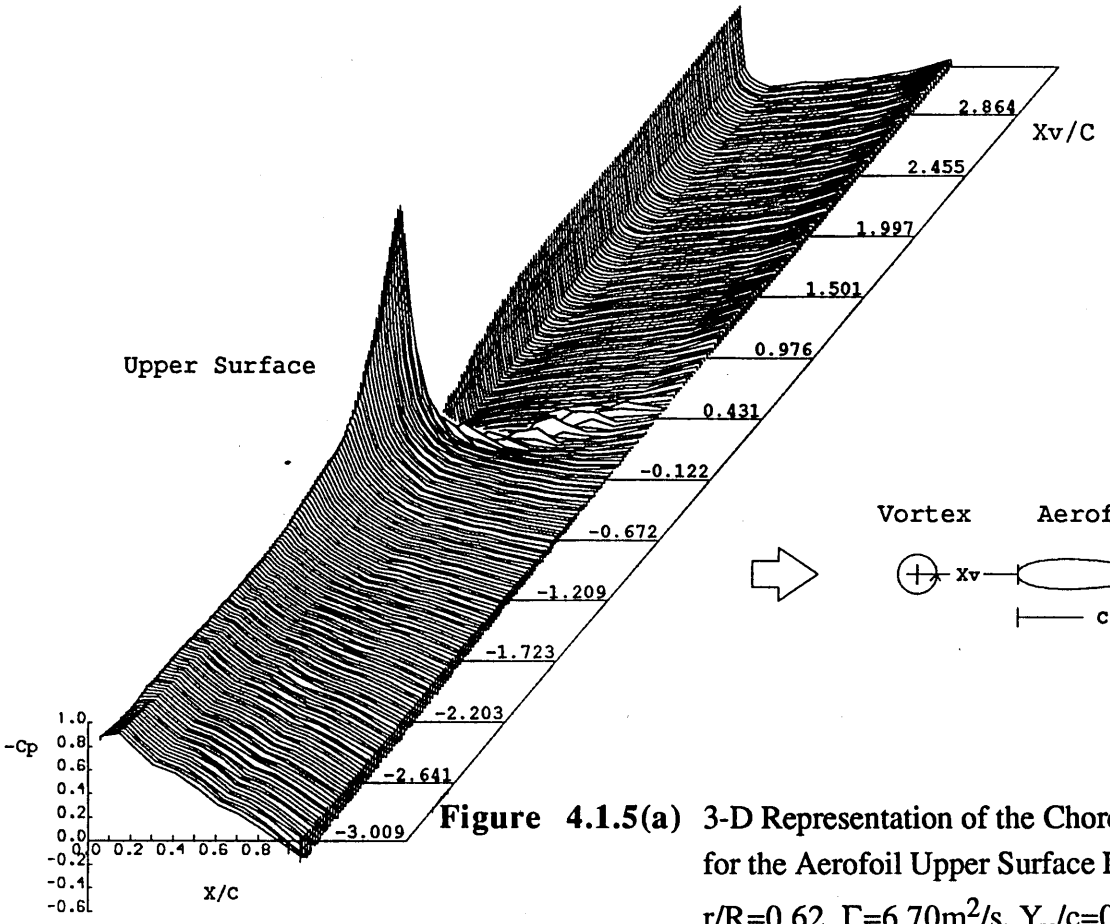

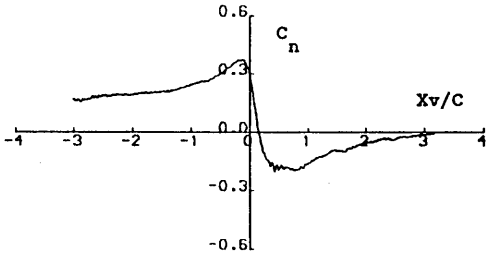

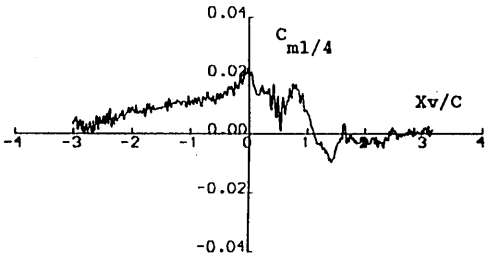

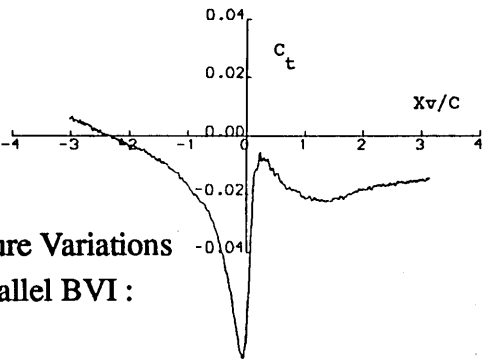

Figure 4.1.5(a) 3-D Representation of the Chordwise Pressure Variations for the Aerofoil Upper Surface During a Parallel BVI : r/R=0.62, Γ=6.70m^2/s, Y_v/c=0.00

"PARALLEL" B.V.I. TEST

RUN REFERENCE NUMBER : 35501

Blade Section :	" NACA - 0015 "	Vortex Strength :	6.70 m^2/s
Spanwise Position,	r/R = 0.6260	Vortex Separation,	Yv/C = 0.0000
Tip Reynolds Number,	Re = 600000		Zv/C = 0.0000
Tip Mach Number,	M_t = 0.174	Blade - Vortex Intersection Angle	= 90.000

AVERAGED DATA

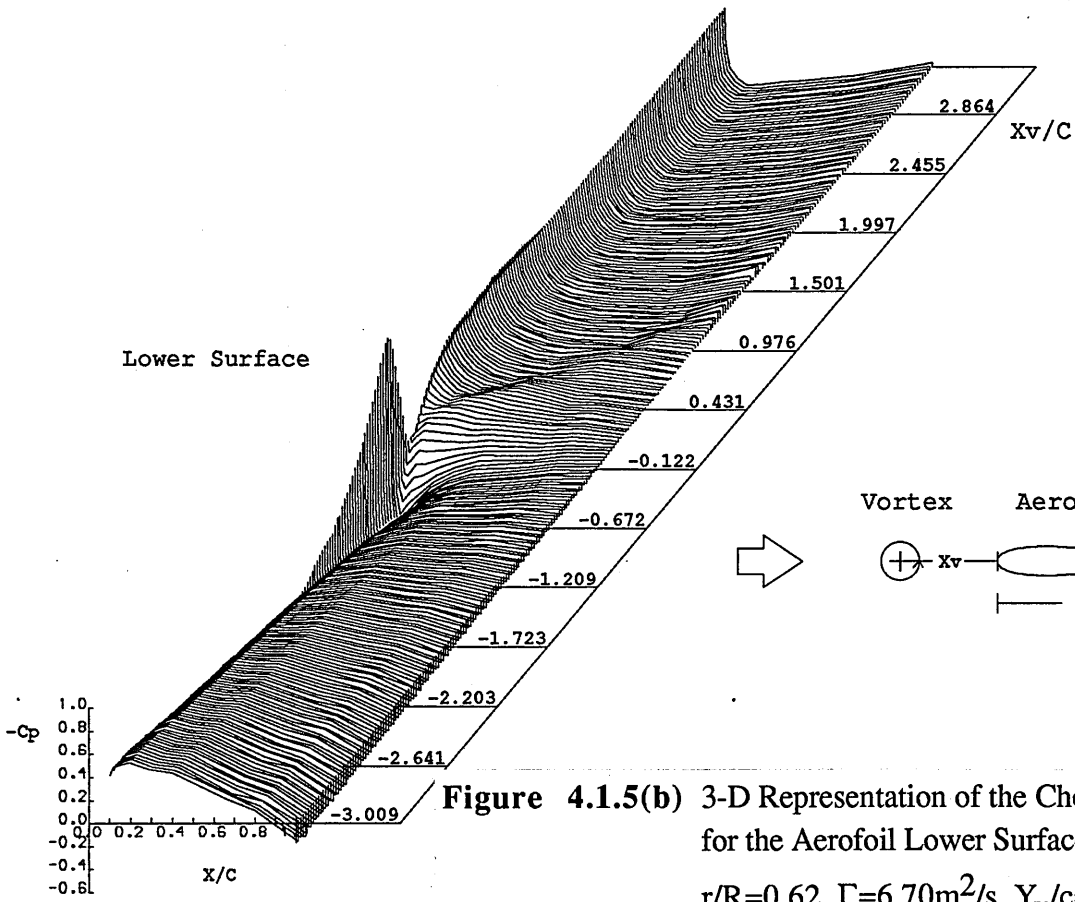

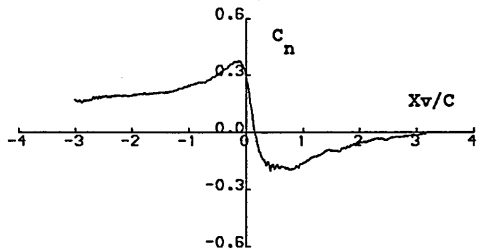

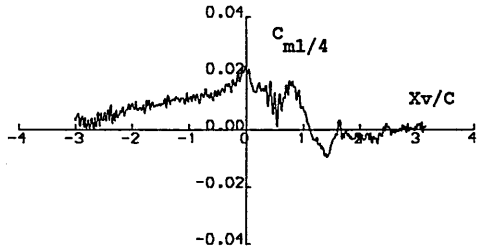

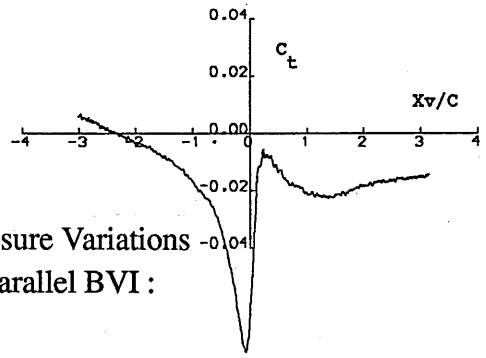

Figure 4.1.5(b) 3-D Representation of the Chordwise Pressure Variations for the Aerofoil Lower Surface During a Parallel BVI : r/R=0.62, Γ=6.70m^2/s, Y_v/c=0.00

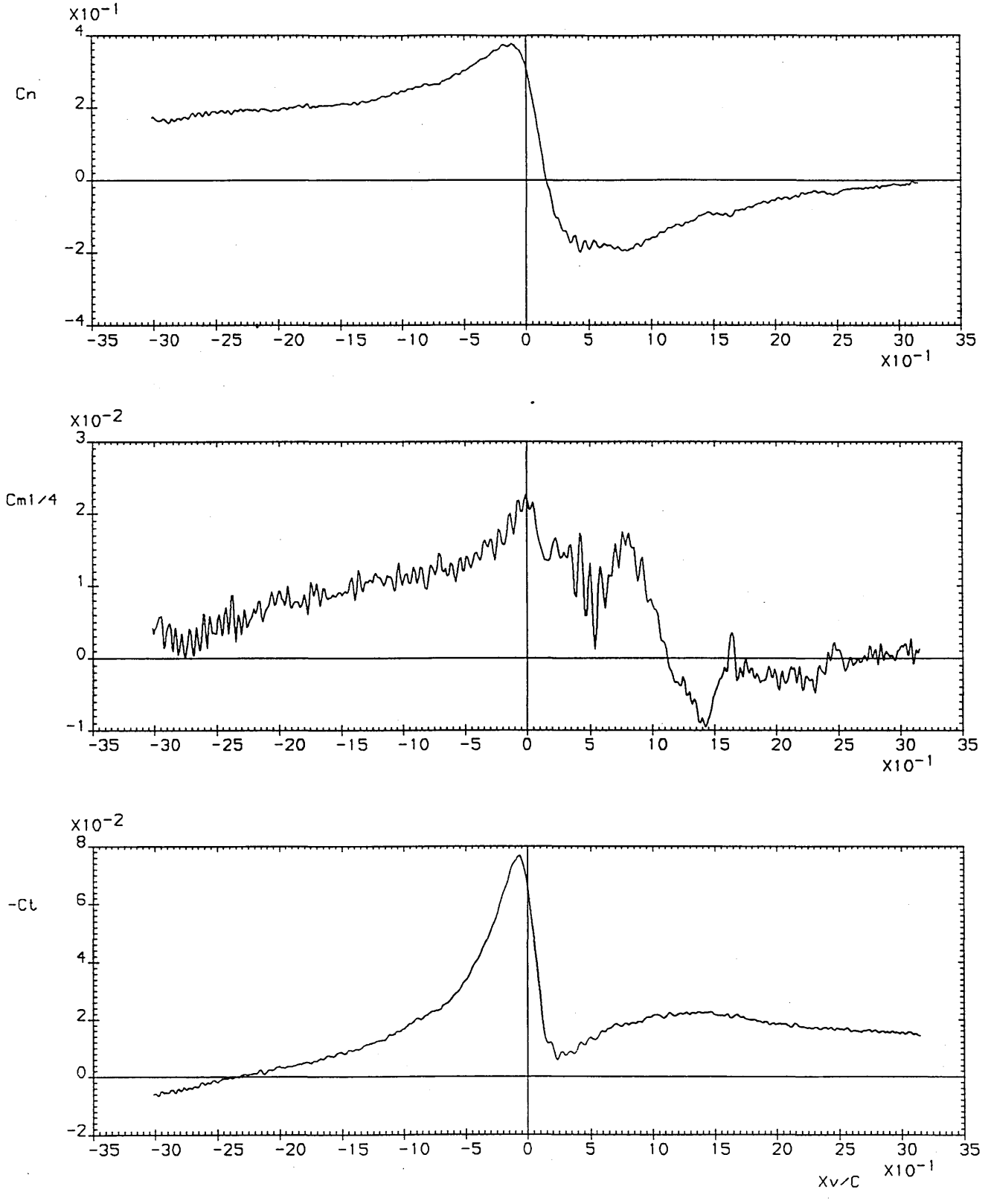

Figure 4.1.6. Aerodynamic Load Coefficient Variations for a Variety of Azimuthal Locations (X_v/c) During a Parallel BVI : r/R=0.62, Γ=6.70m^2/s, Y_v/c=0.00

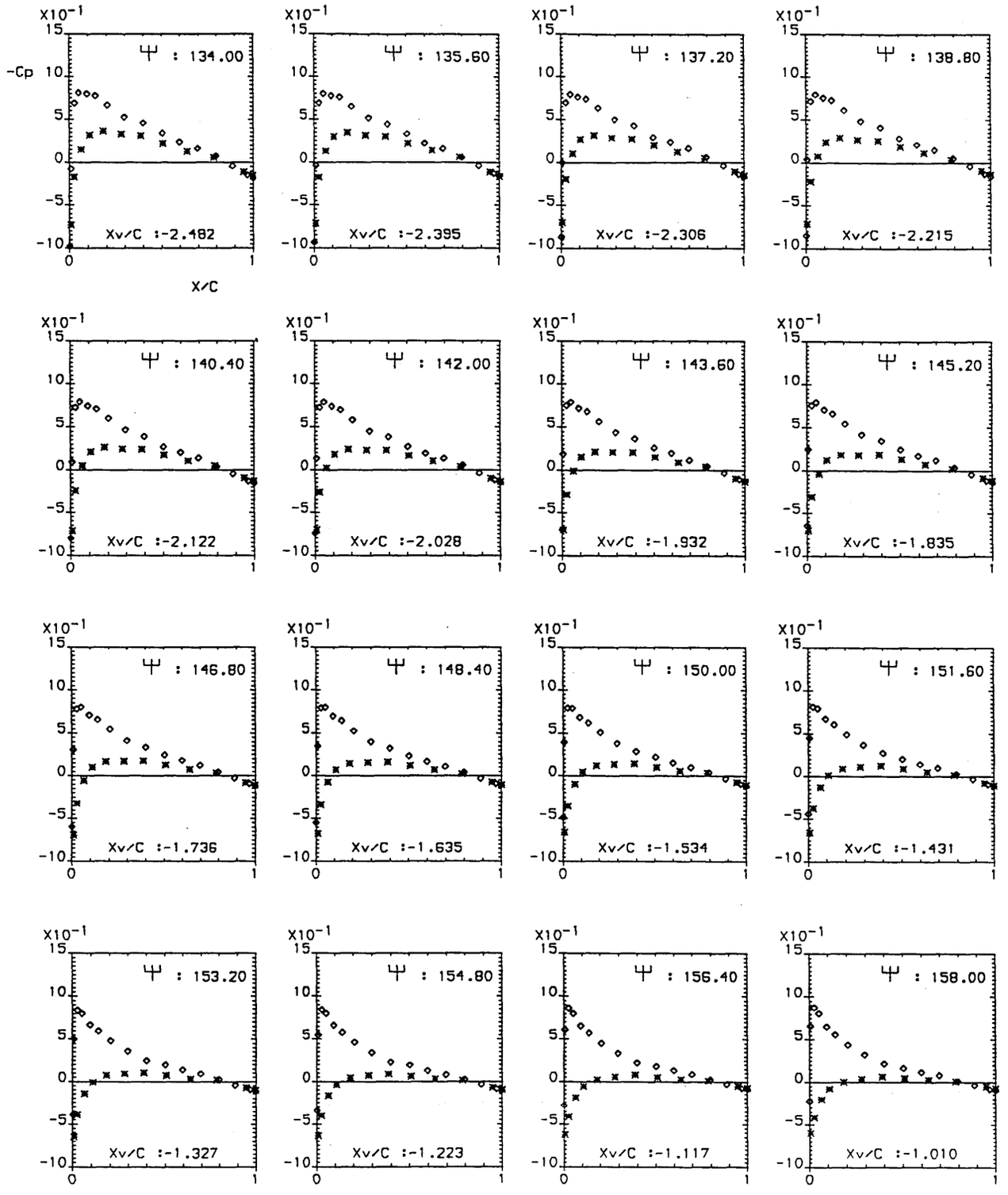

Figure 4.1.7. Instantaneous Surface Pressure Distributions During a Parallel BVI : r/R=0.62, Γ=6.70m^2/s, Y_v/c=0.20

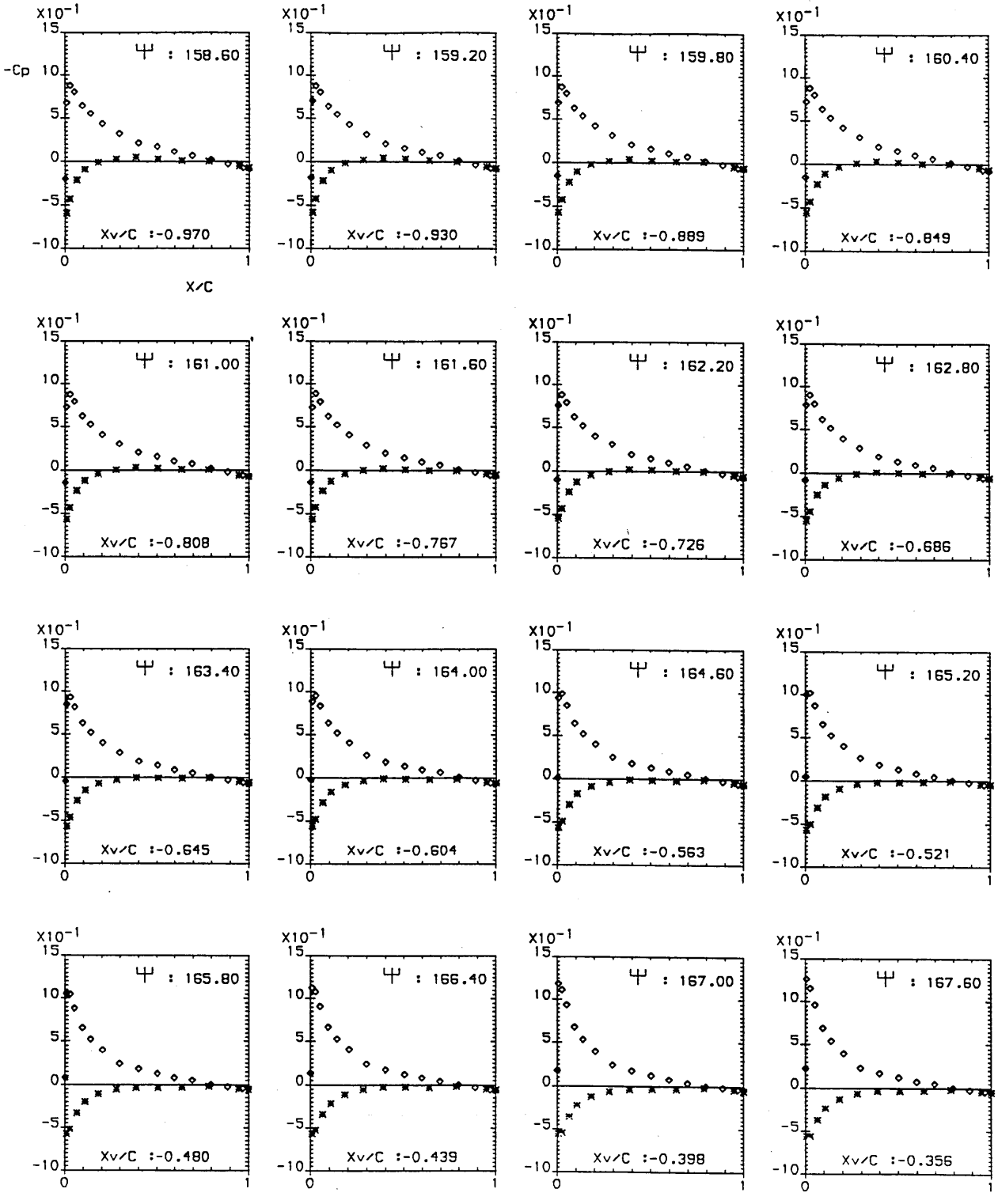

Figure 4.1.7 Continued...

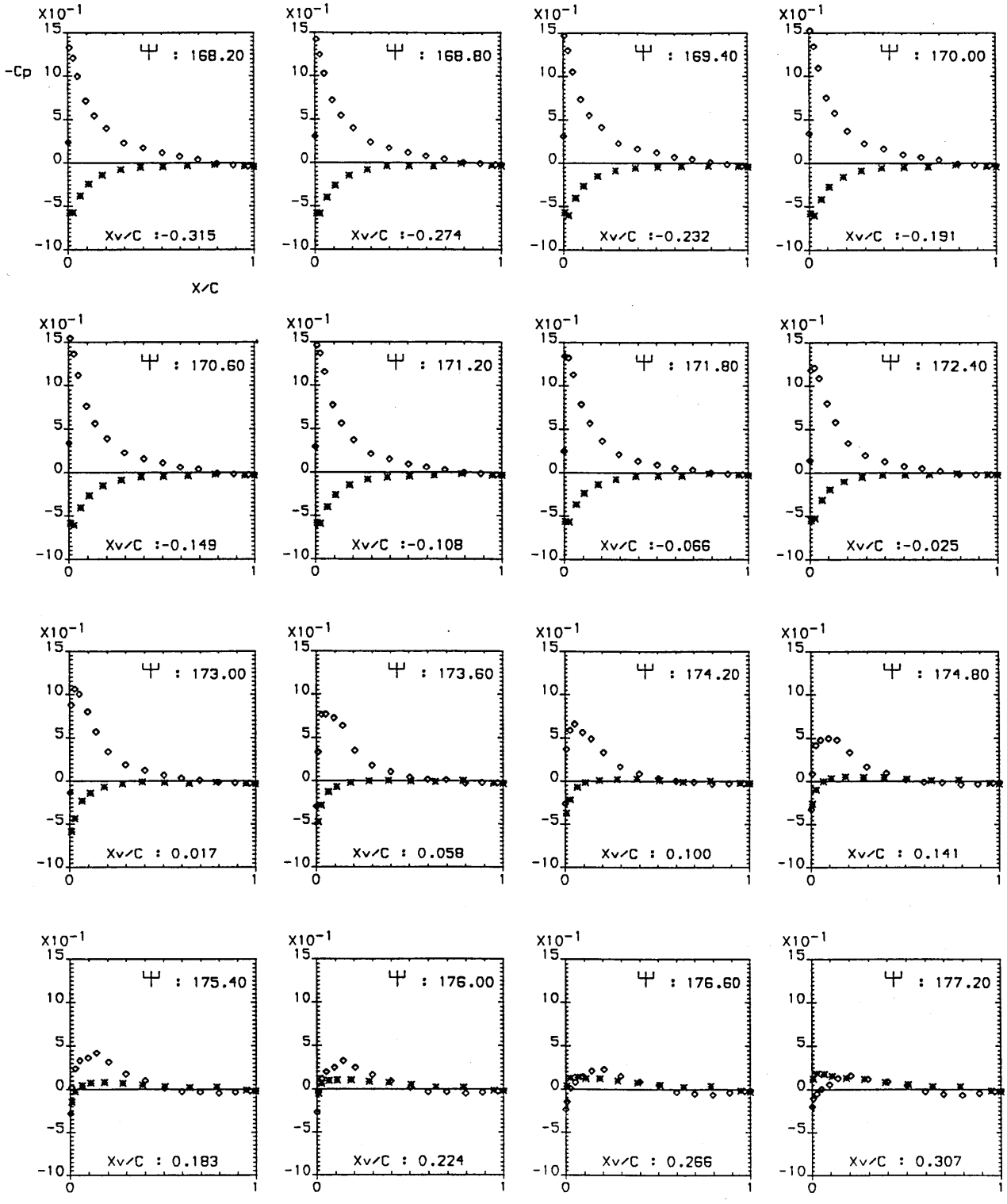

Figure 4.1.7 Continued...

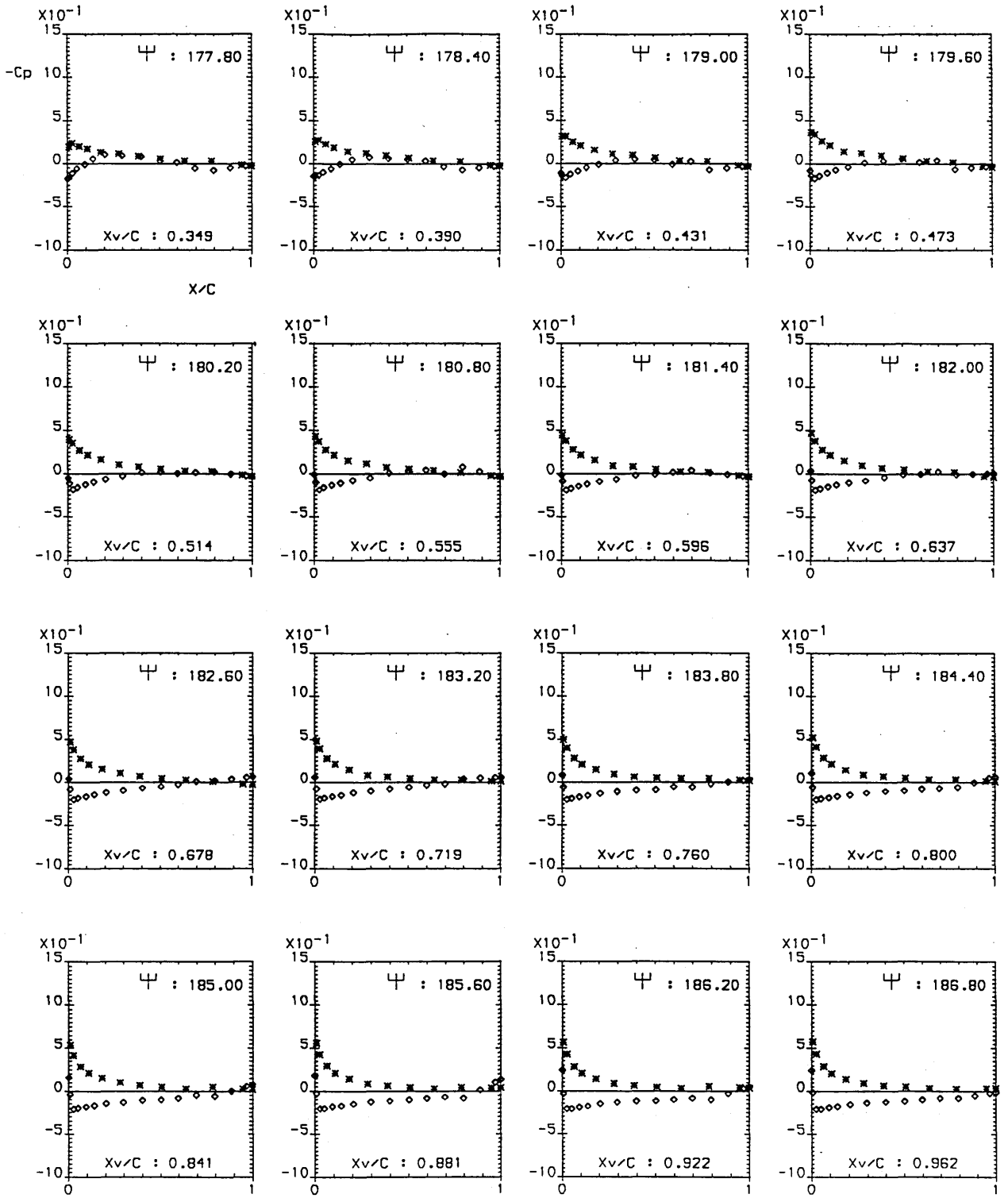

Figure 4.1.7 Continued...

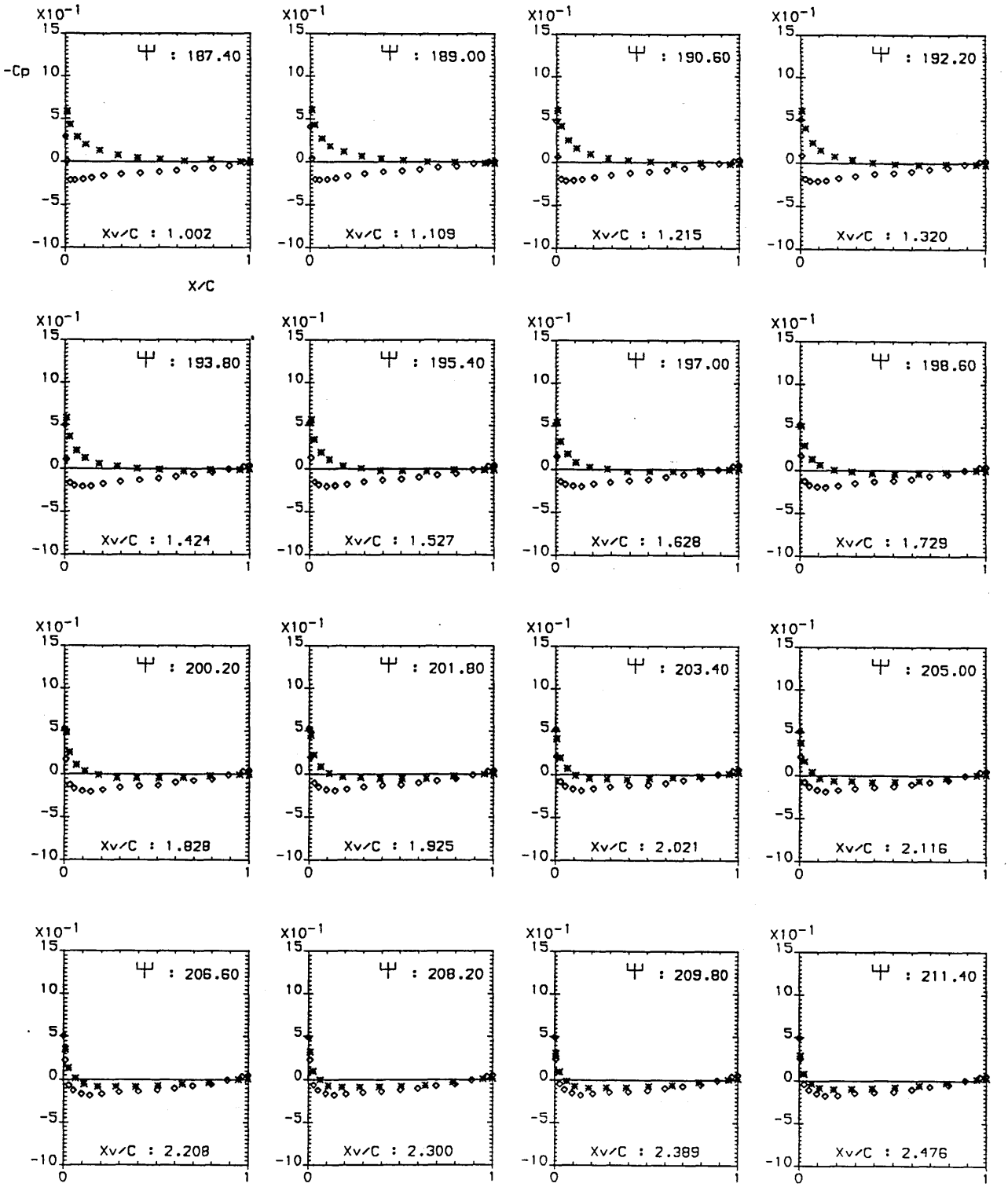

Figure 4.1.7 Concluded

"PARALLEL" B.V.I. TEST

RUN REFERENCE NUMBER : 35511

Blade Section :	" NACA - 0015 "	Vortex Strength :	6.70 m^2/s
Spanwise Position,	r/R = 0.6260	Vortex Separation,	Yv/C = 0.2000
Tip Reynolds Number,	Re = 600000		Zv/C = 0.0000
Tip Mach Number,	M_t = 0.174	Blade - Vortex Intersection Angle	= 90.000

AVERAGED DATA

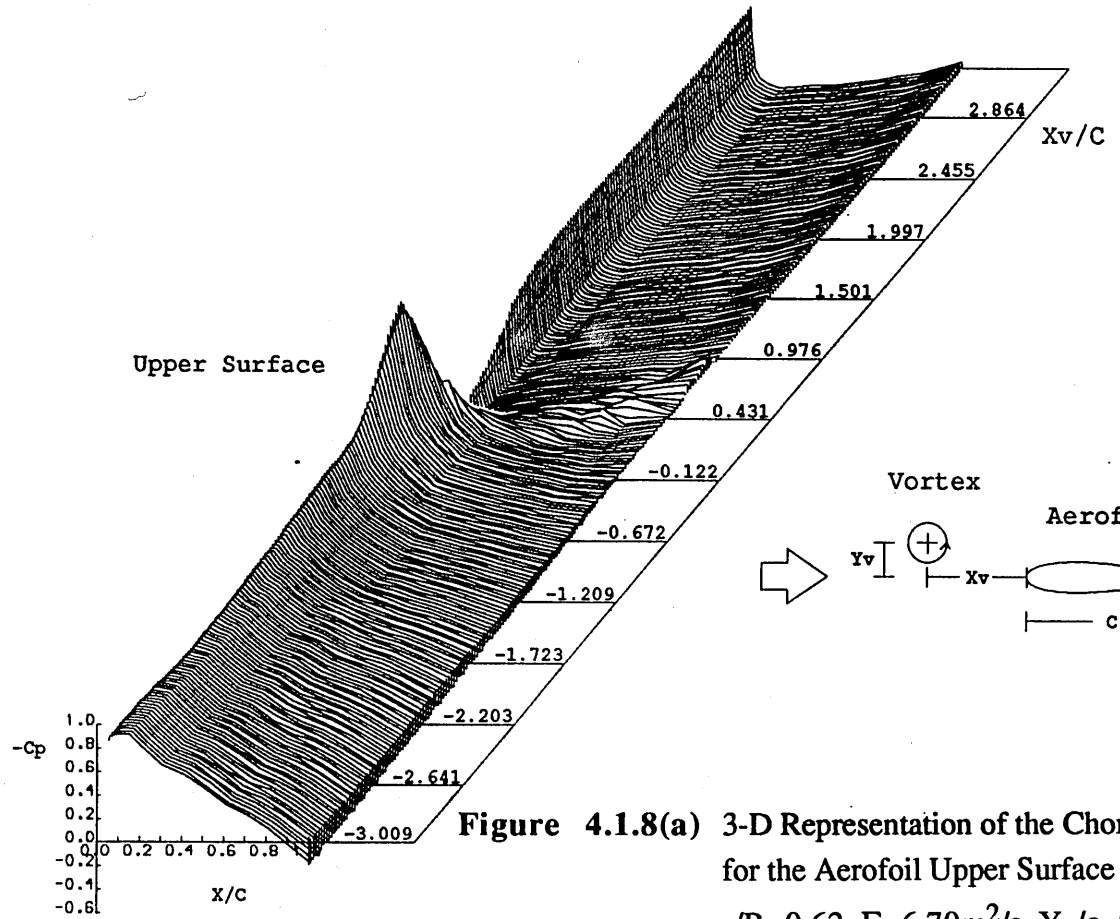

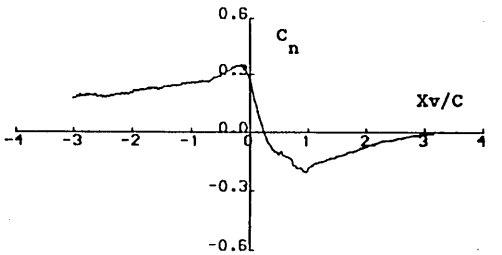

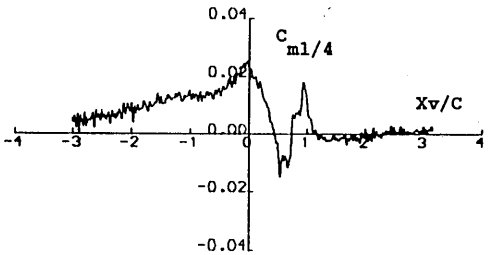

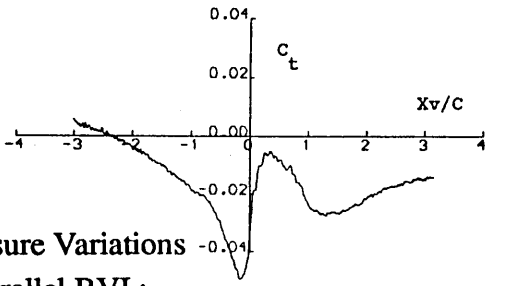

Figure 4.1.8(a) 3-D Representation of the Chordwise Pressure Variations for the Aerofoil Upper Surface During a Parallel BVI : r/R=0.62, Γ=6.70m^2/s, Y_v/c=0.20

"PARALLEL" B.V.I. TEST

RUN REFERENCE NUMBER : 35511

Blade Section :	" NACA - 0015 "	Vortex Strength :	6.70 m^2/s
Spanwise Position,	r/R = 0.6260	Vortex Separation,	Yv/C = 0.2000
Tip Reynolds Number,	Re = 600000		Zv/C = 0.0000
Tip Mach Number,	M_t = 0.174	Blade - Vortex Intersection Angle	= 90.000

AVERAGED DATA

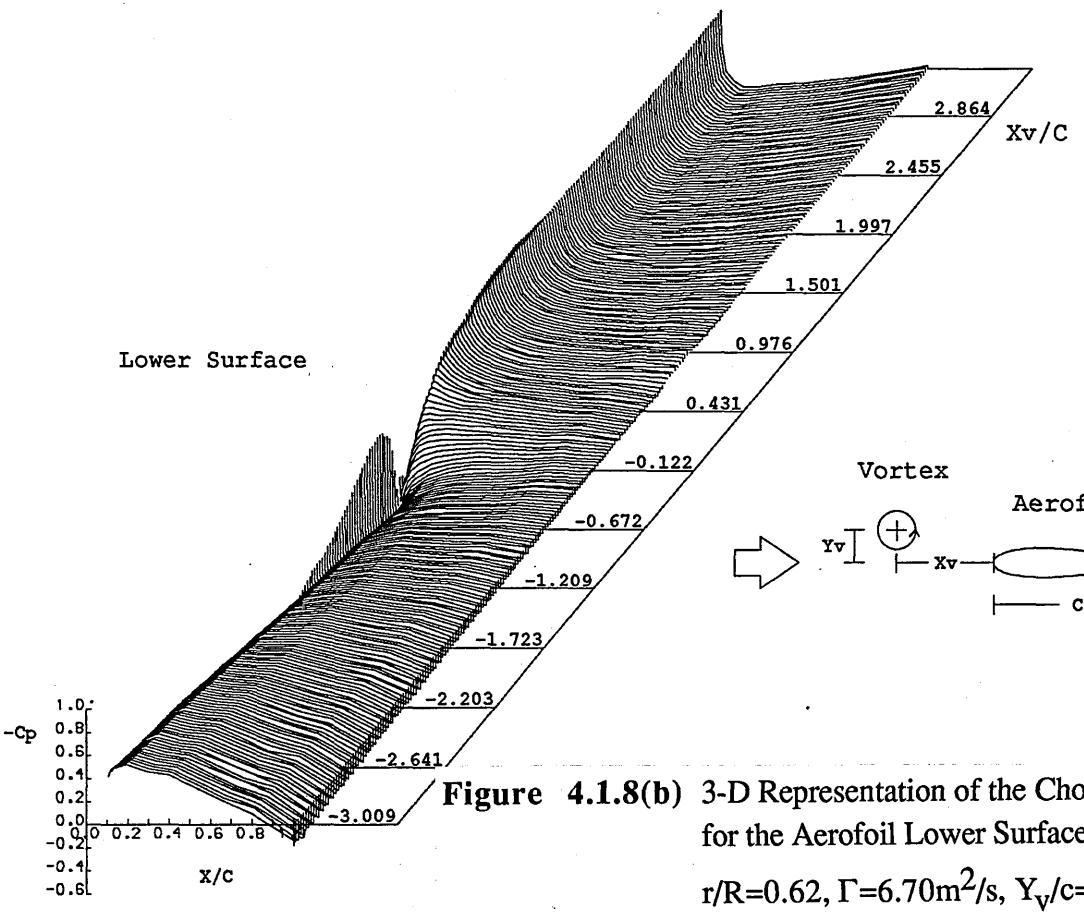

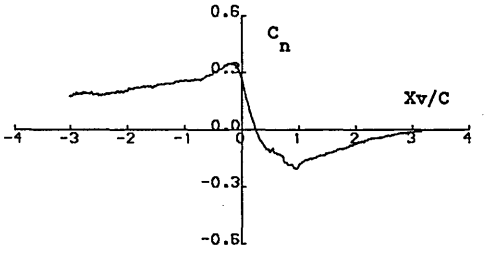

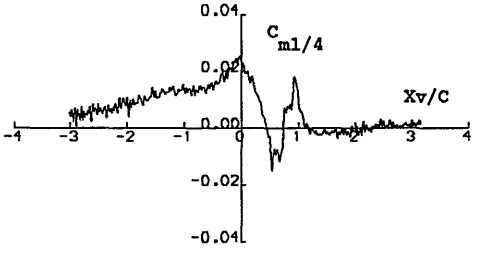

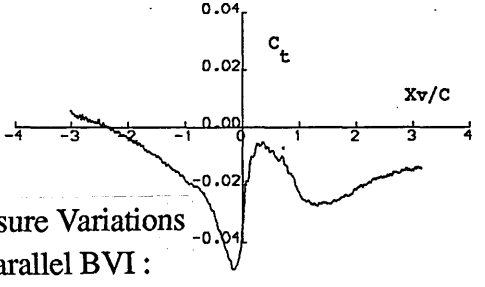

Figure 4.1.8(b) 3-D Representation of the Chordwise Pressure Variations for the Aerofoil Lower Surface During a Parallel BVI : r/R=0.62, Γ=6.70m^2/s, Y_v/c=0.20

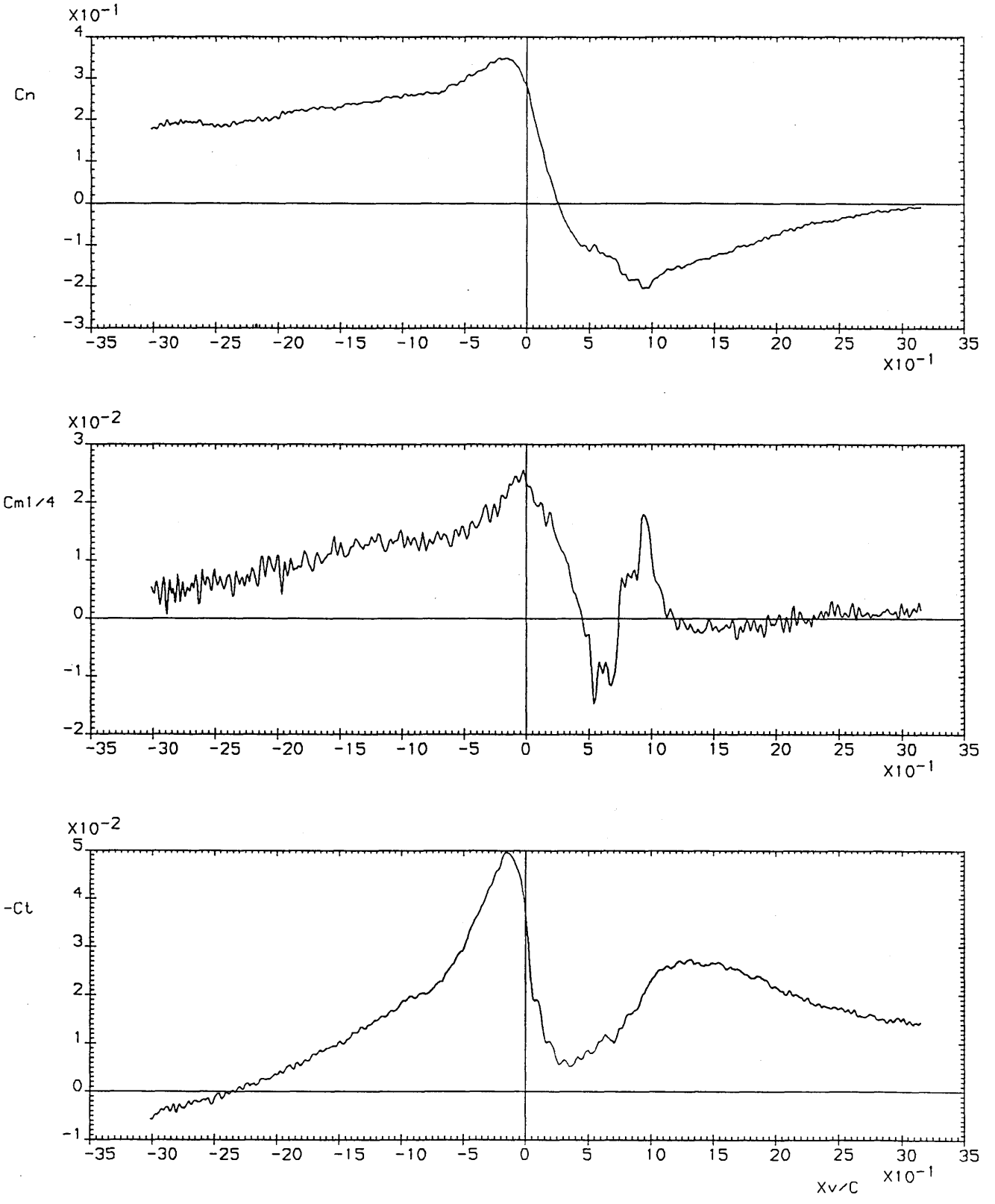

Figure 4.1.9 Aerodynamic Load Coefficient Variations for a Variety of Azimuthal Locations (X_V/c) During a Parallel BVI : r/R=0.62, Γ=6.70m^2/s, Y_V/c=0.20

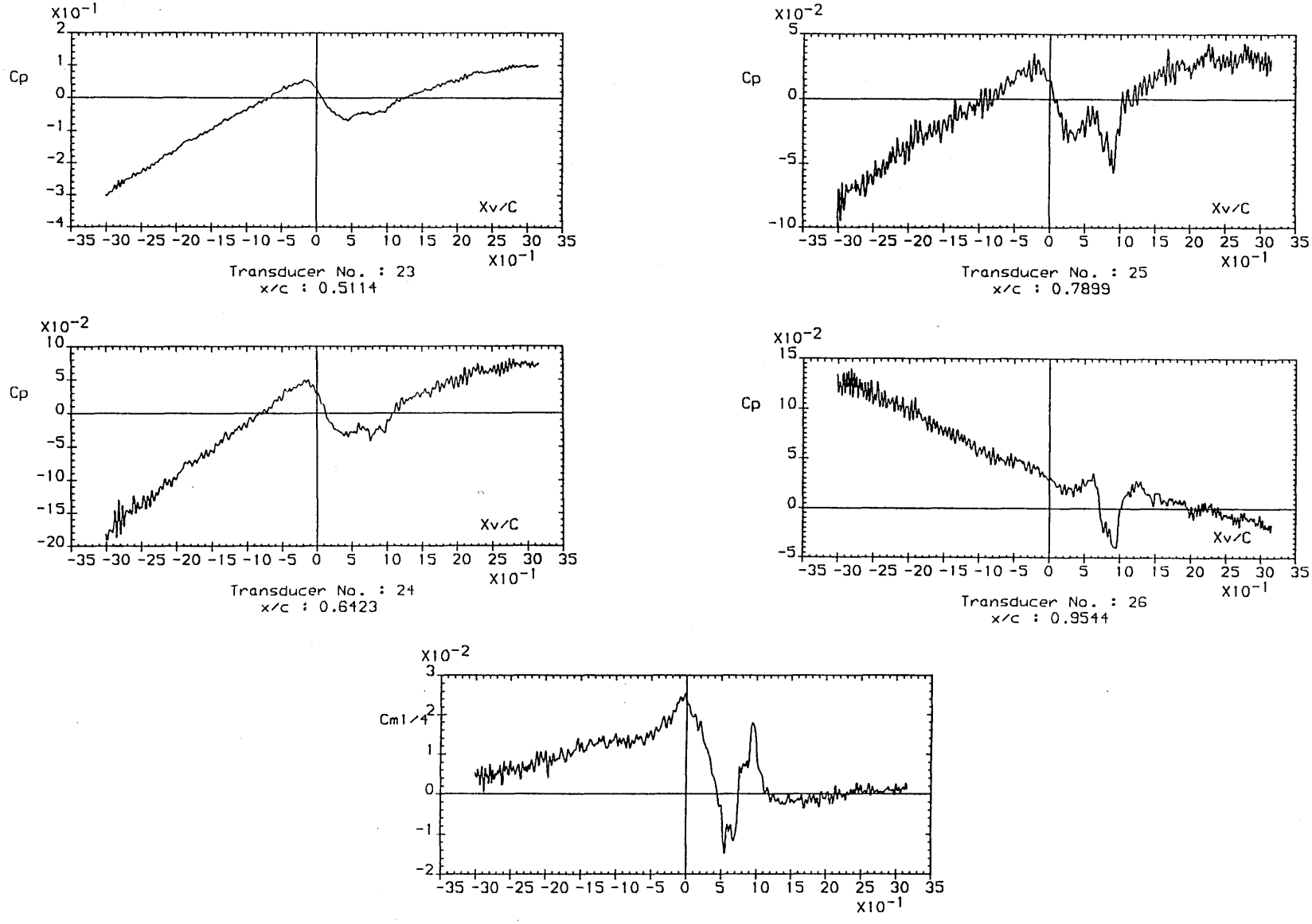

Figure 4.1.10 Comparison Between Selected Trailing Edge Surface Pressures and Quarter Chord Pitching Moment Coefficient During a Parallel BVI : r/R=0.62, Γ=6.70m^2/s, Y_V/c=0.20

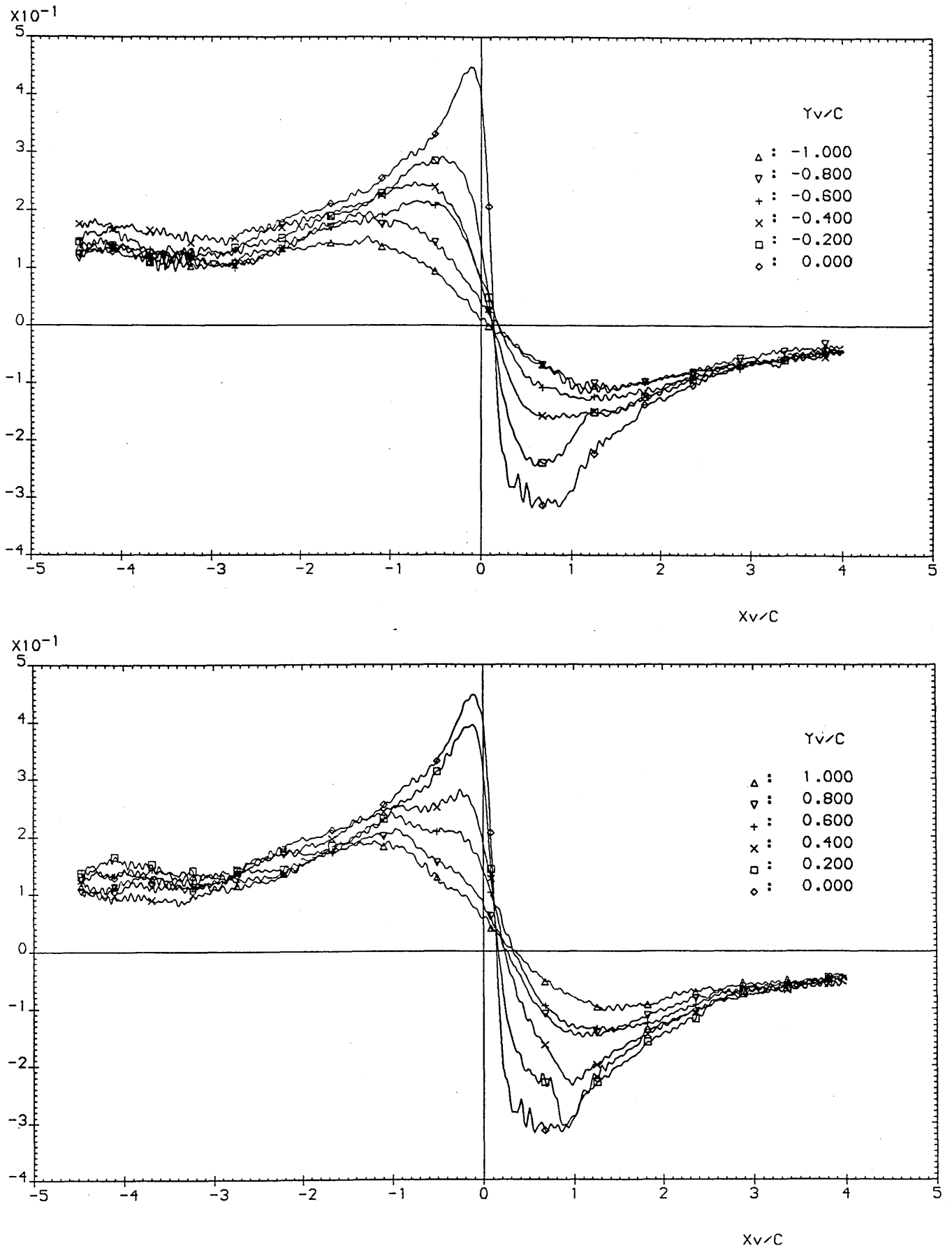

Figure 4.2.1 Typical Normal Force Coefficient Variations Due to Blade-Vortex Proximity Effect During a Parallel BVI : r/R=0.86, Γ=6.70m^2/s

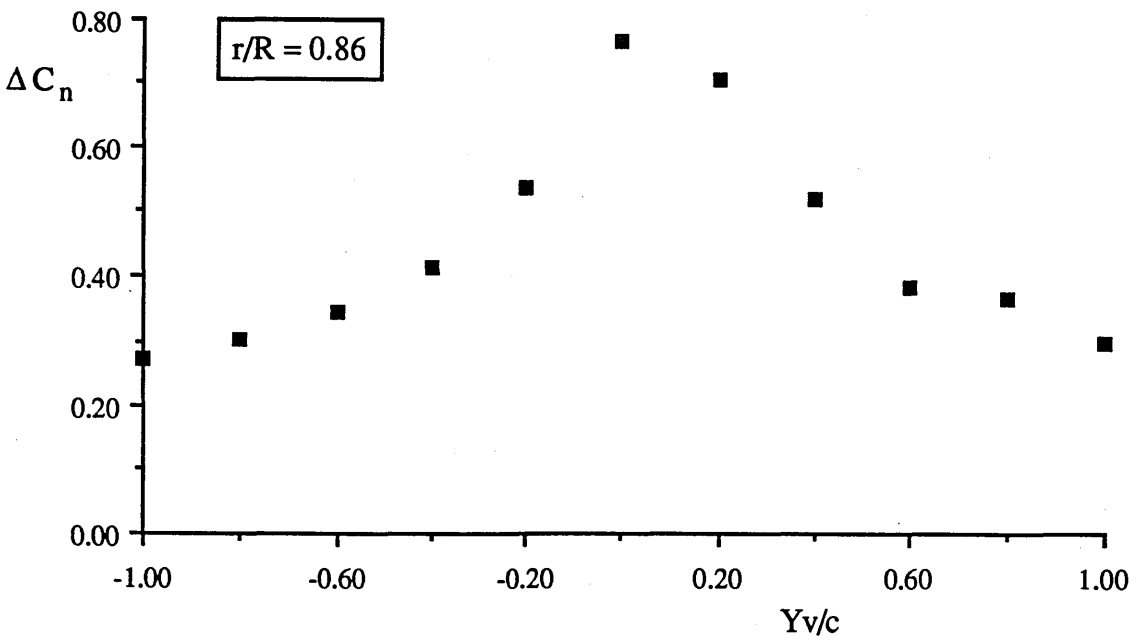

Figure 4.2.3 Differential Normal Force Coefficient Variations with Blade-Vortex Proximity for a Parallel BVI : r/R=0.86, Γ=6.70m^2/s

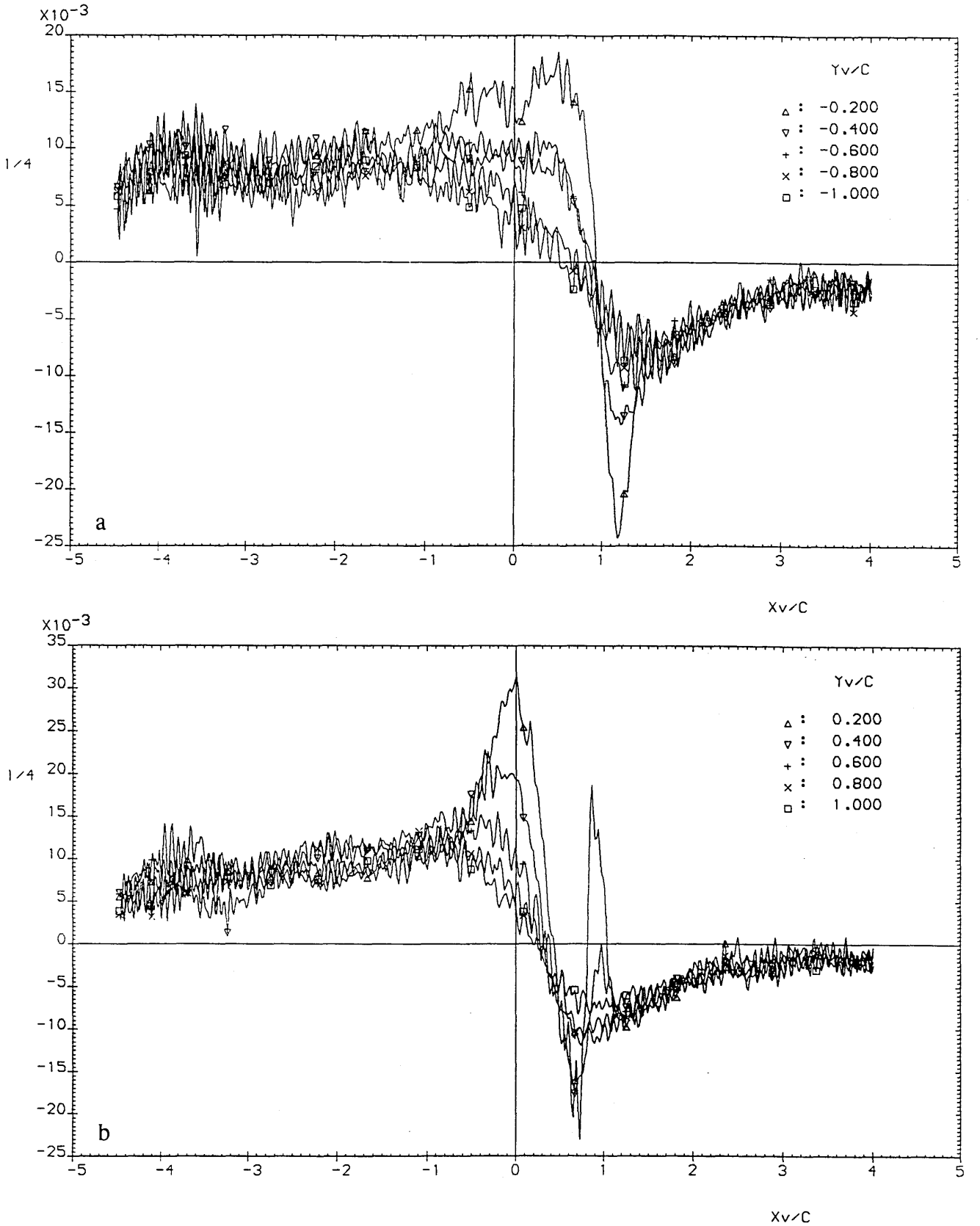

Figure 4.2.4 Typical Quarter Chord Pitching Moment Coefficient Variations Due to Blade-Vortex Proximity Effect During a Parallel BVI : r/R=0.86, Γ=6.70m^2/s

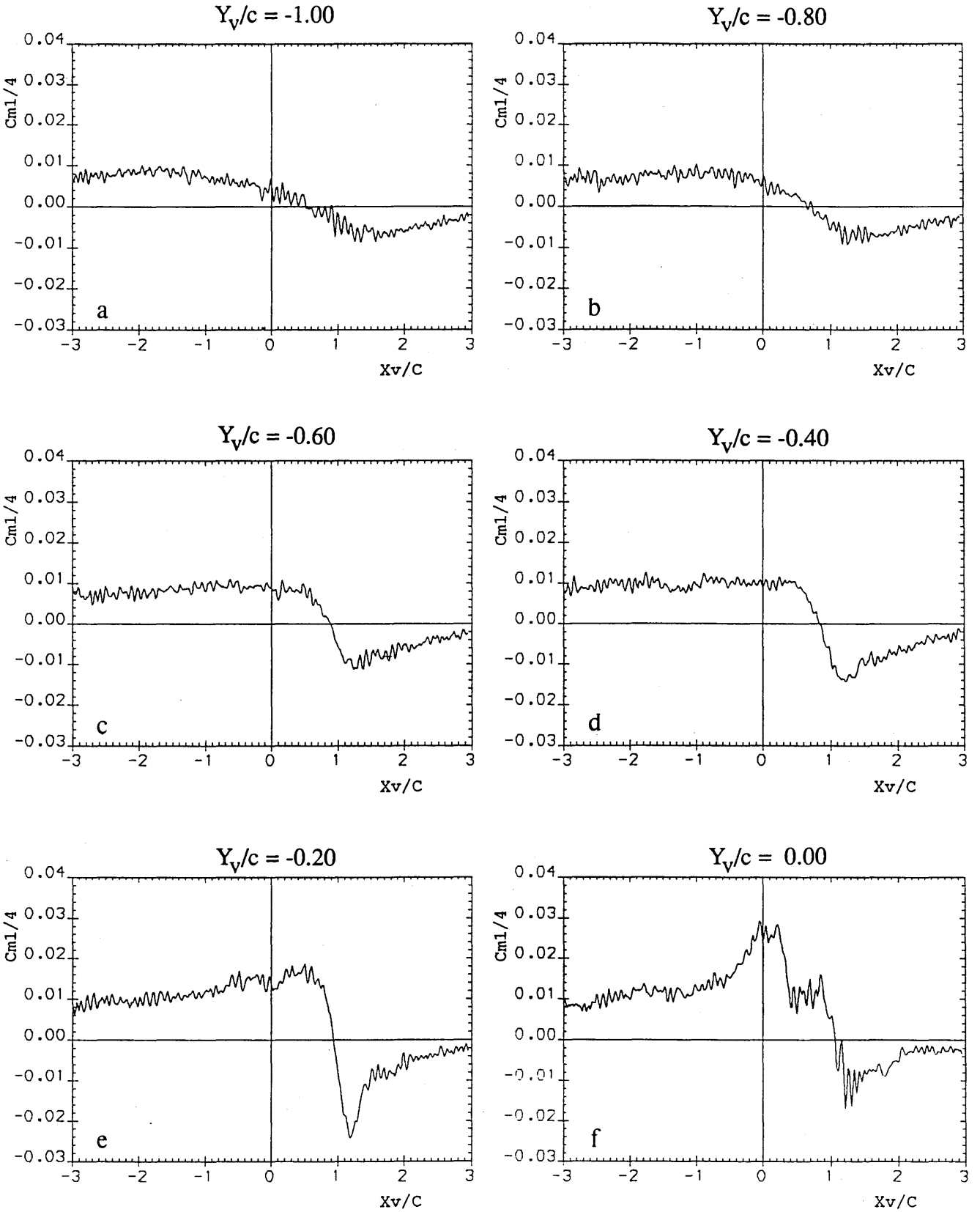

Figure 4.2.5 Quarter Chord Pitching Moment Coefficient Variations with Blade-Vortex Proximity During a Parallel BVI : r/R=0.86, Γ=6.70m^2/s

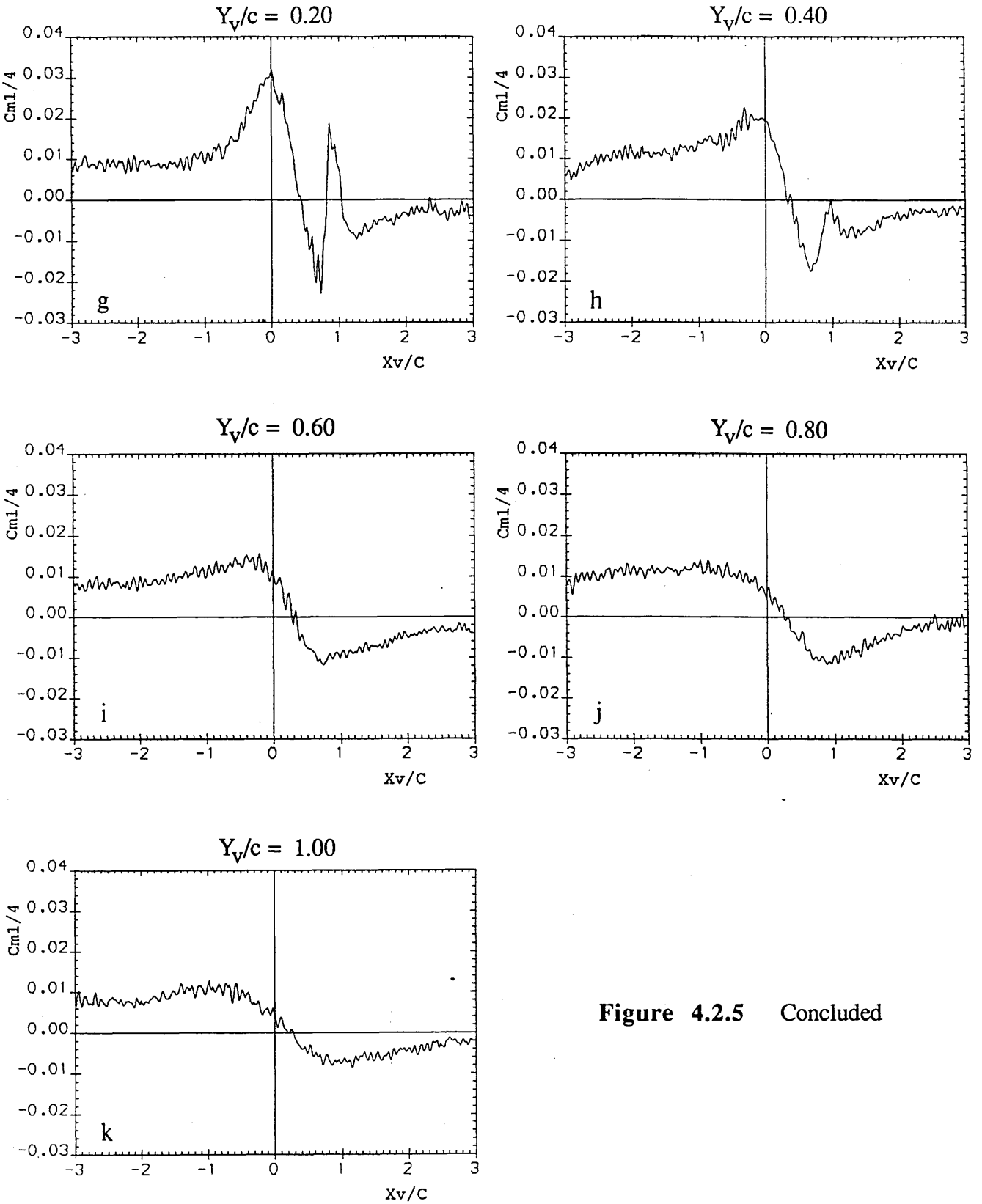

Figure 4.2.5 Concluded

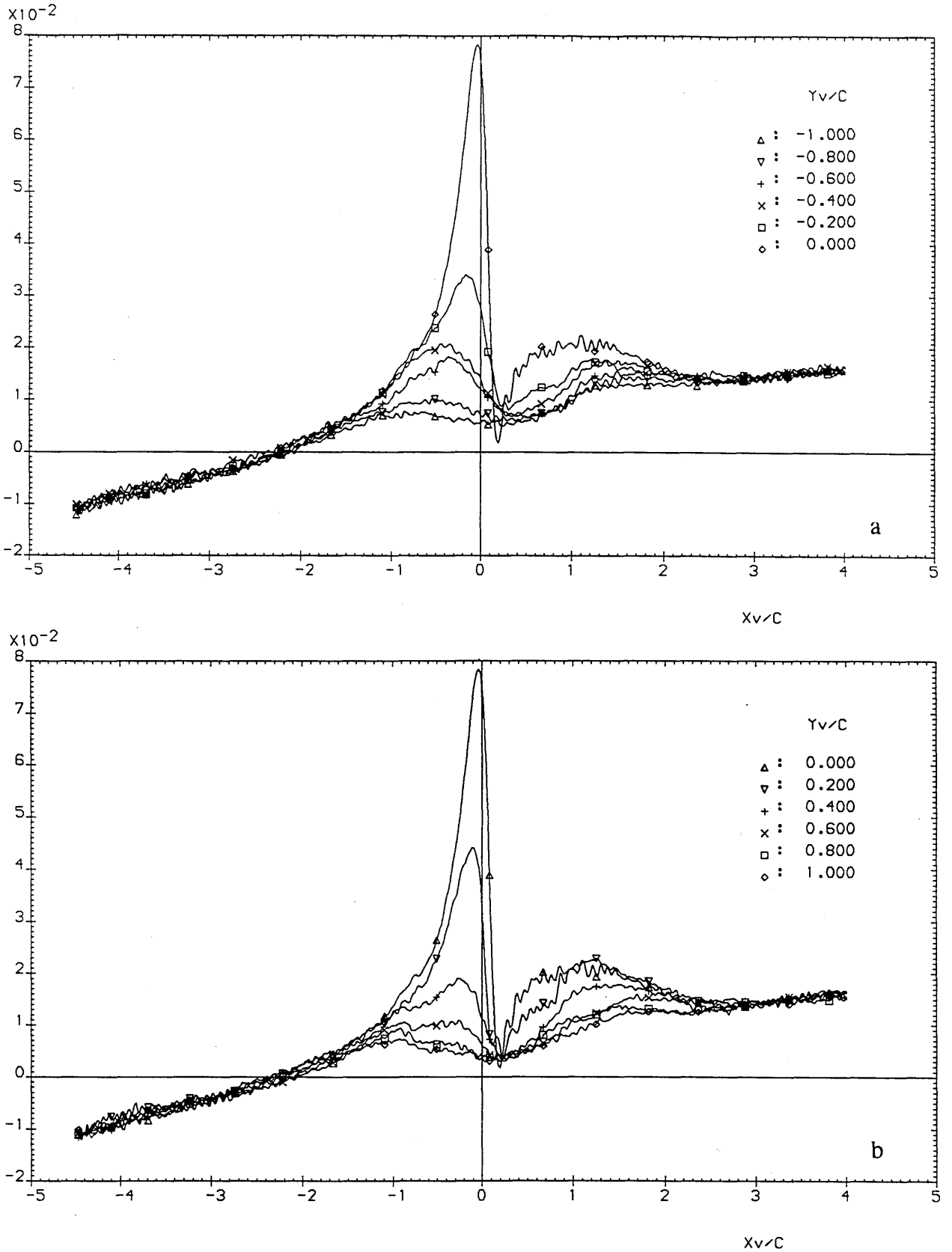

Figure 4.2.6 Typical Pressure Drag Coefficient Variations Due to Blade-Vortex Proximity Effect During a Parallel BVI : r/R=0.86, Γ=6.70m^2/s

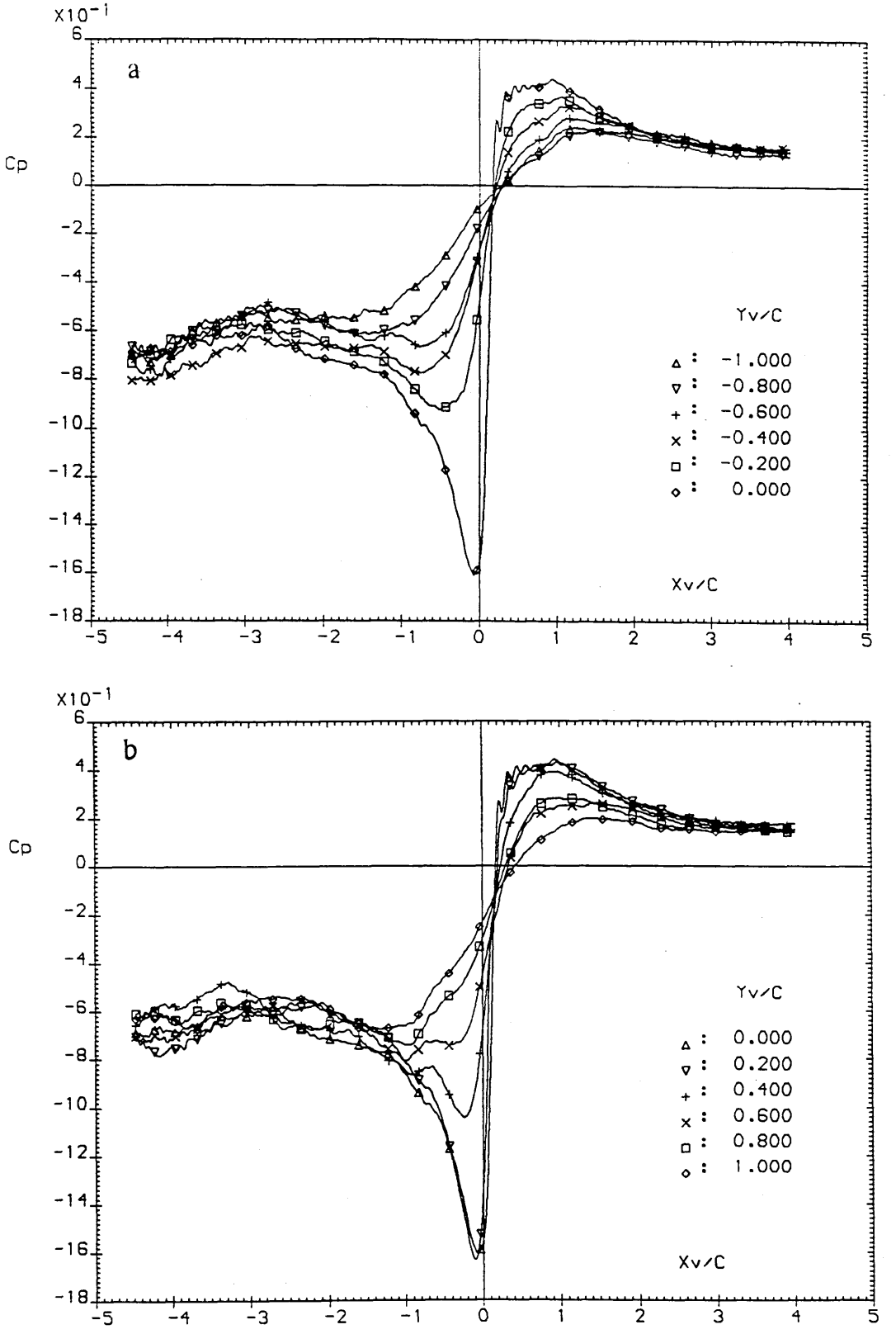

Figure 4.2.7 Azimuthal Pressure Variation Histories at x/c=0.0260 (Upper Surface) as a Function of Blade-Vortex Proximity : r/R=0.86, Γ=6.70m^2/s

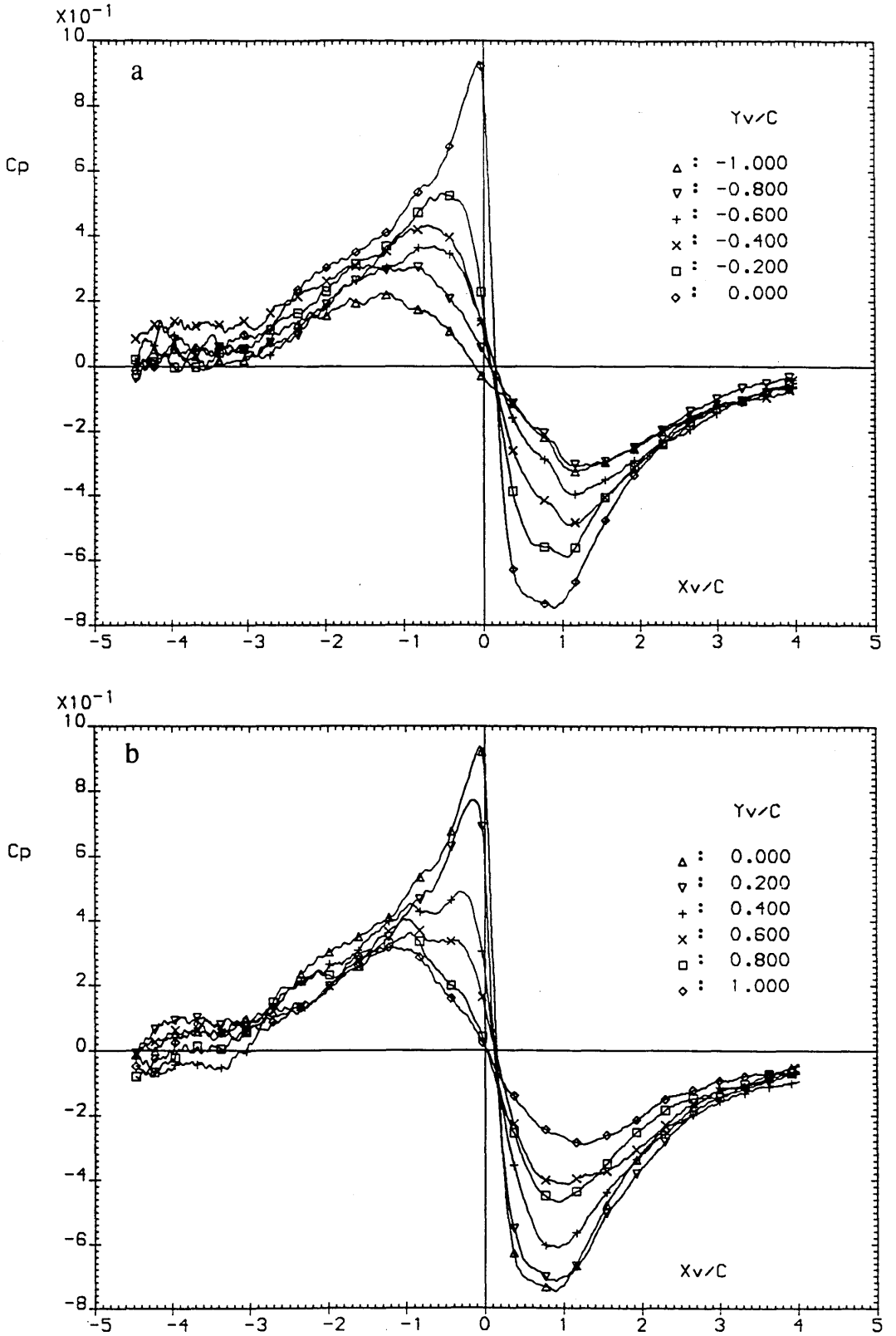

Figure 4.2.8 Azimuthal Pressure Variation Histories at x/c=0.0253 (Lower Surface) as a Function of Blade-Vortex Proximity : r/R=0.86, Γ=6.70m^2/s

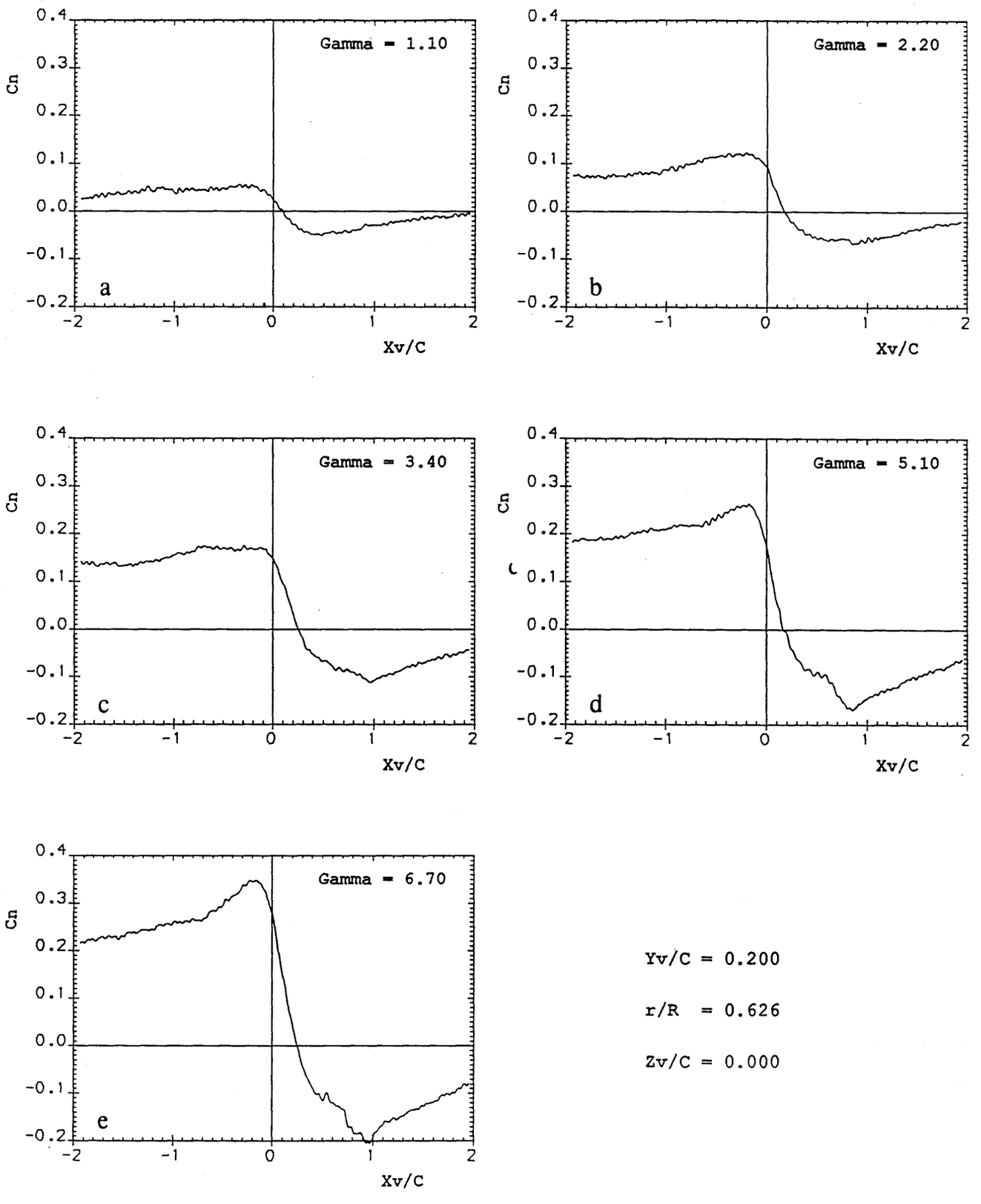

Figure 4.3.1 Azimuthal Normal Force Coefficient Variations with Vortex Strength During Parallel BVIs : r/R=0.62, Y_V/c=0.20

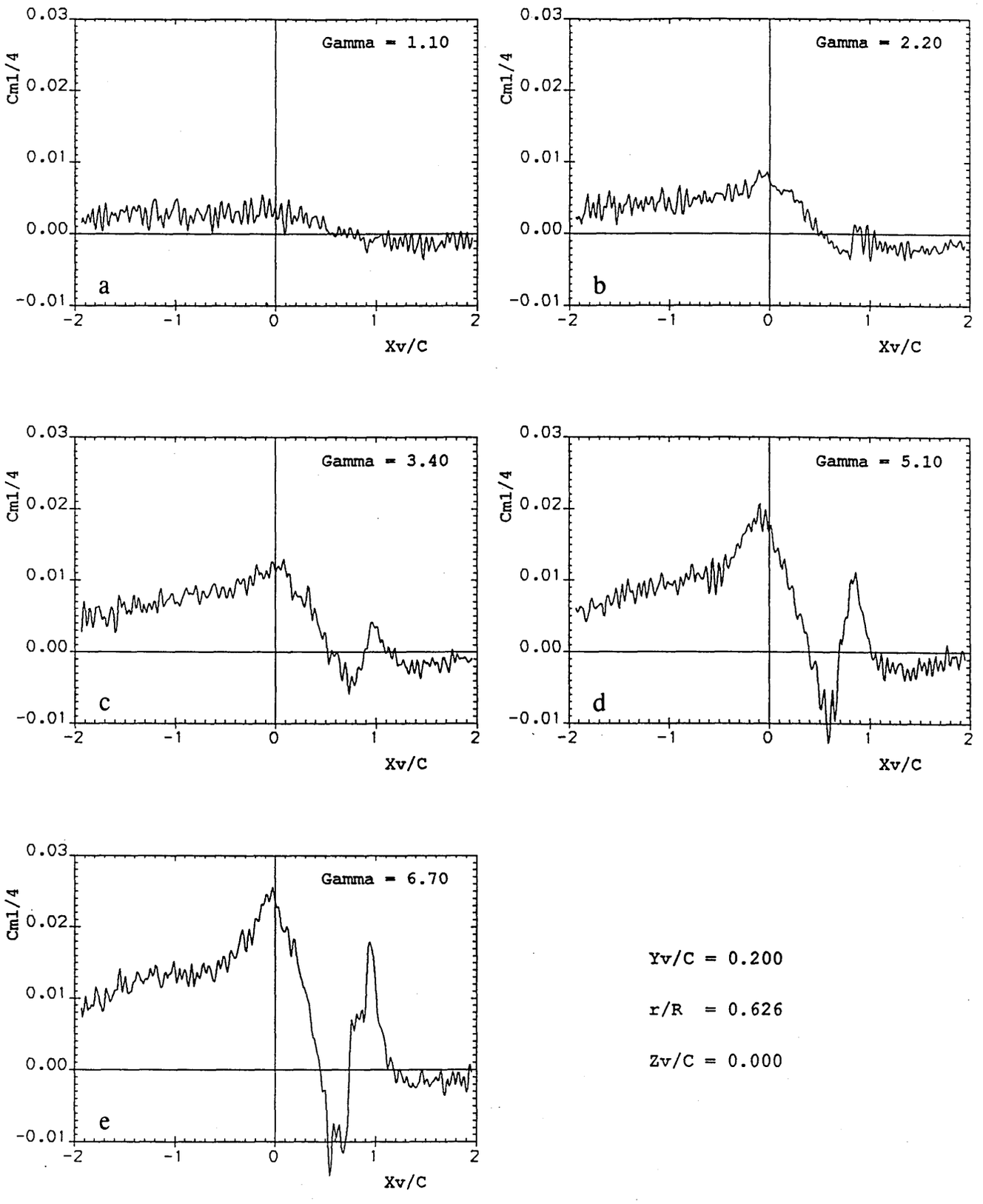

Yv/C = 0.200

r/R = 0.626

Zv/C = 0.000

Figure 4.3.2 Azimuthal Quarter Chord Pitching Moment Coefficient Variations with Vortex Strength During Parallel BVIs : r/R=0.62, Y_v/c=0.20

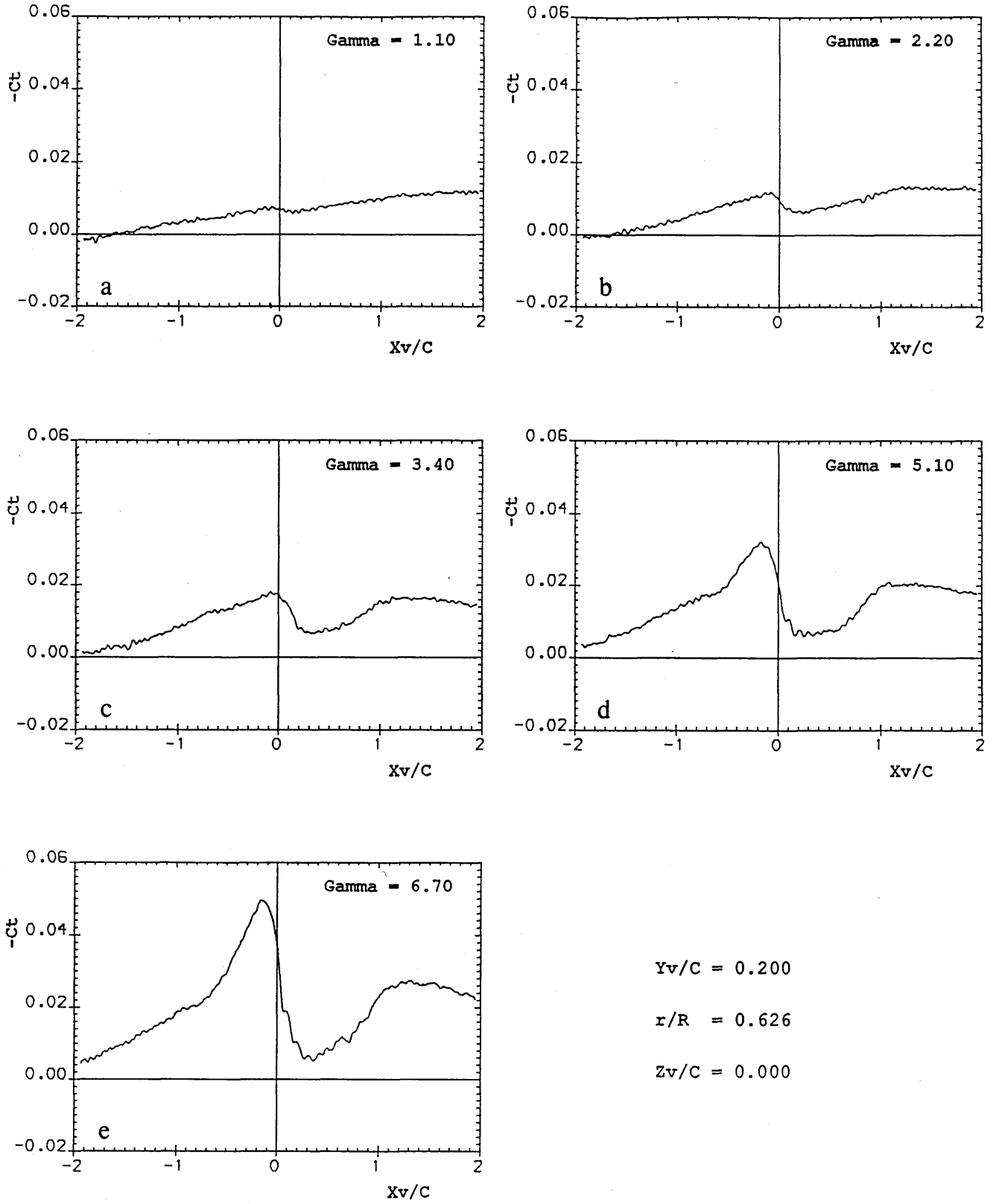

Figure 4.3.3 Azimuthal Pressure Drag Coefficient Variations with Vortex Strength During Parallel BVIs : r/R=0.62, Y_V/c=0.20

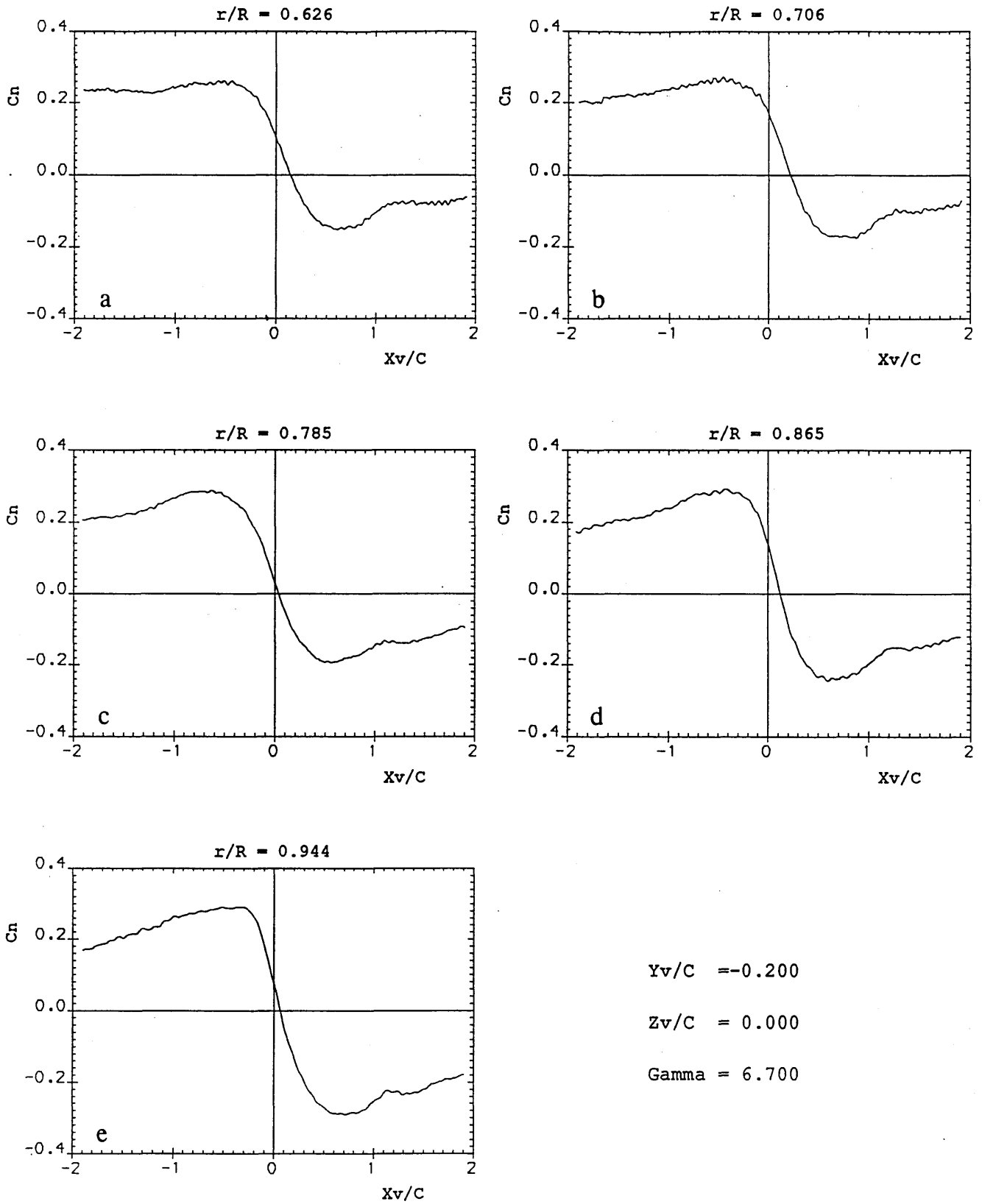

Figure 4.4.1 Azimuthal Normal Force Coefficient Variations with Radial Position During Parallel BVIs : Y_v/c=-0.20, Γ=6.70m^2/s

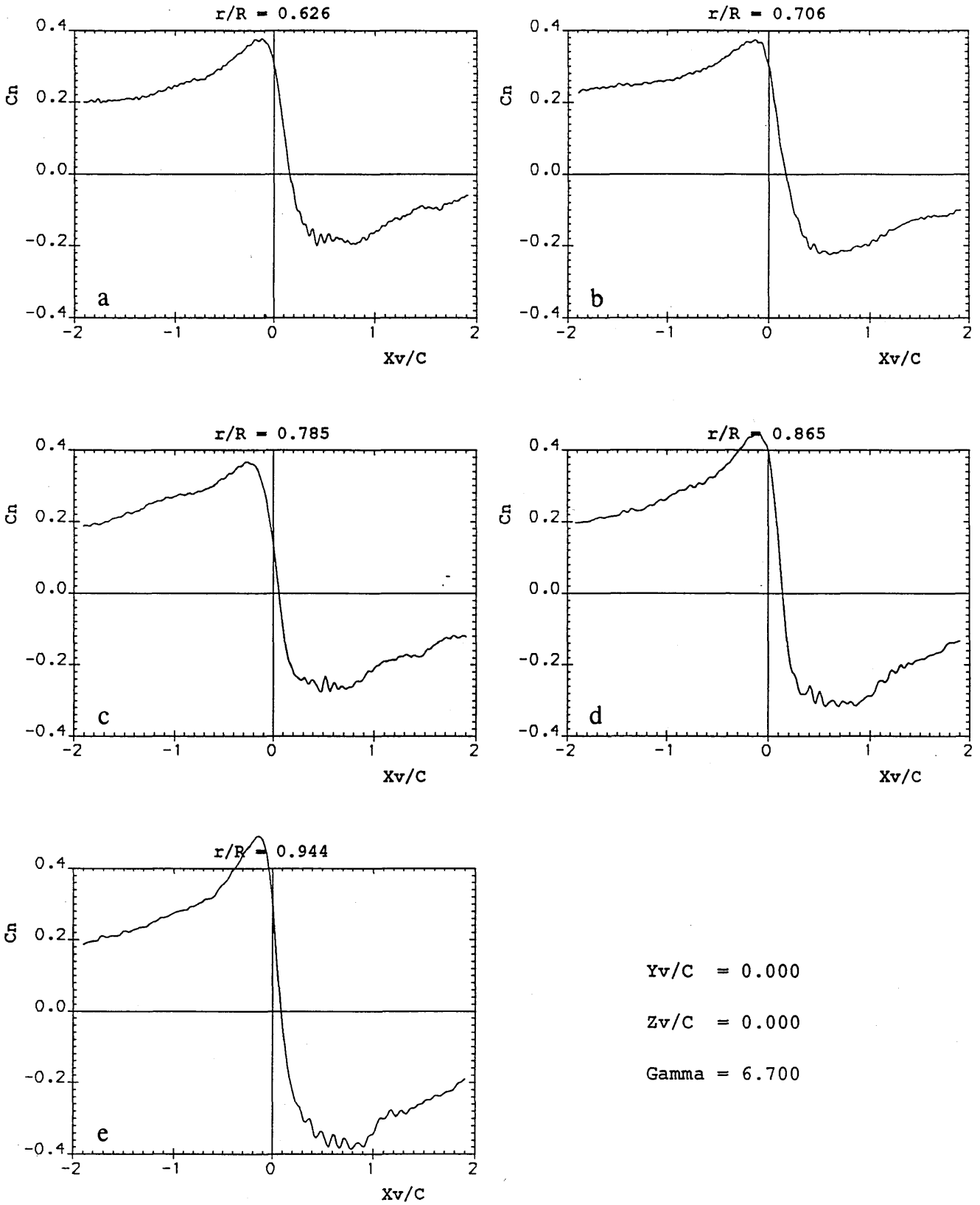

Figure 4.4.2 Azimuthal Normal Force Coefficient Variations with Radial Position During Parallel BVIs : Y_v/c= 0.00, Γ=6.70m^2/s

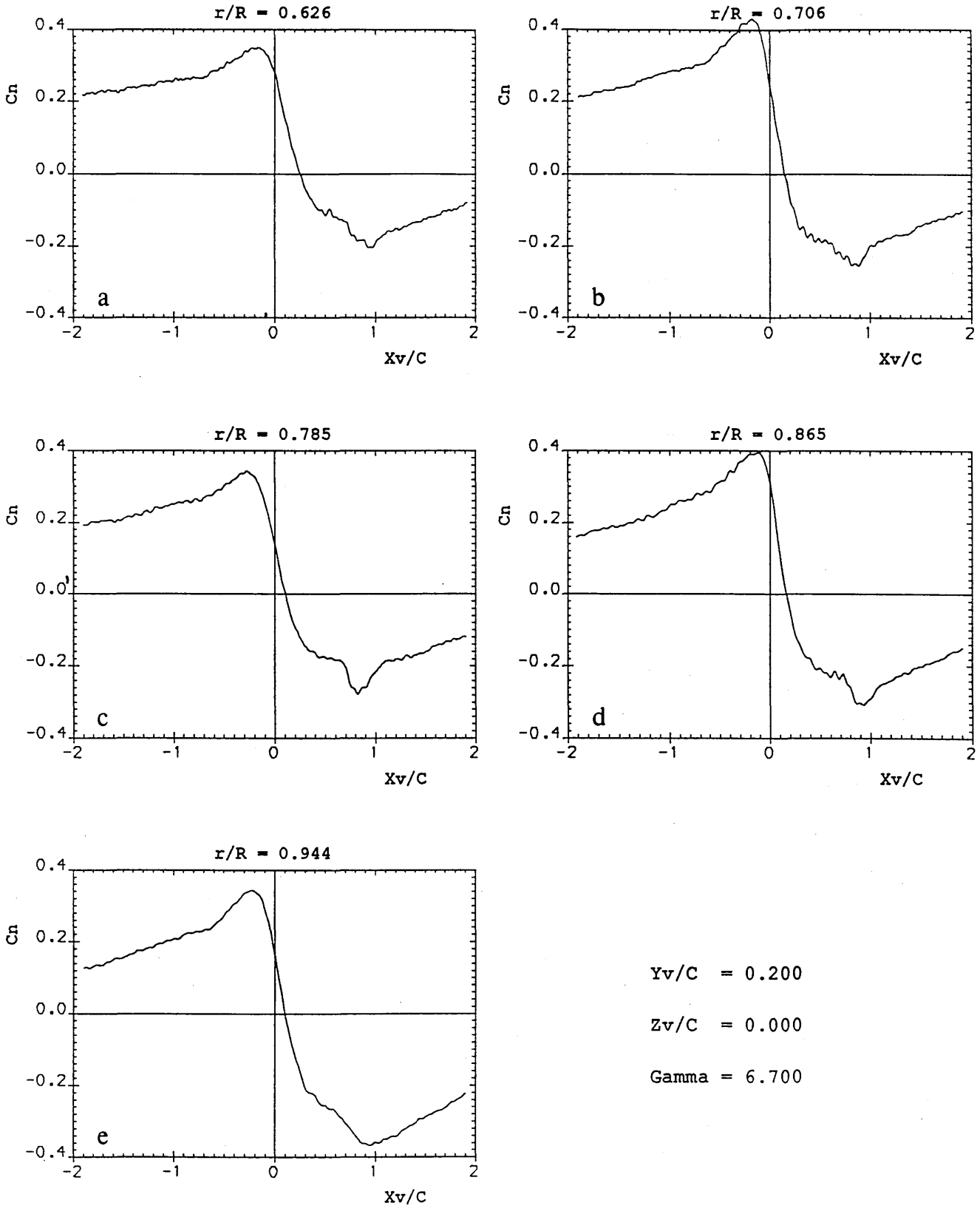

Figure 4.4.3 Azimuthal Normal Force Coefficient Variations with Radial Position During Parallel BVIs : Y_v/c= 0.20, Γ=6.70m^2/s

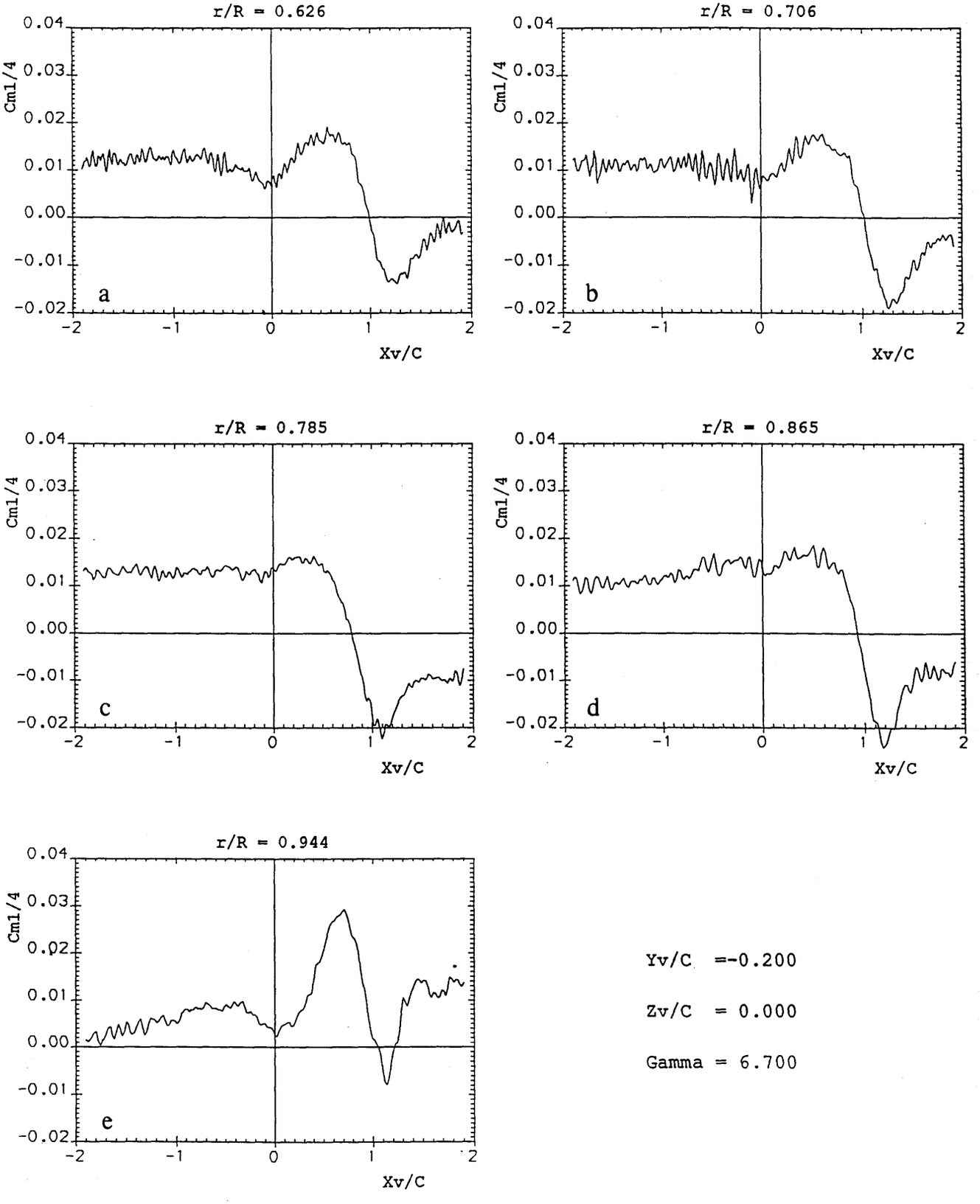

Figure 4.4.4 Azimuthal Quarter Chord Pitching Moment Coefficient Variations with Radial Position During Parallel BVIs : Y_V/c= -0.20, Γ=6.70m^2/s

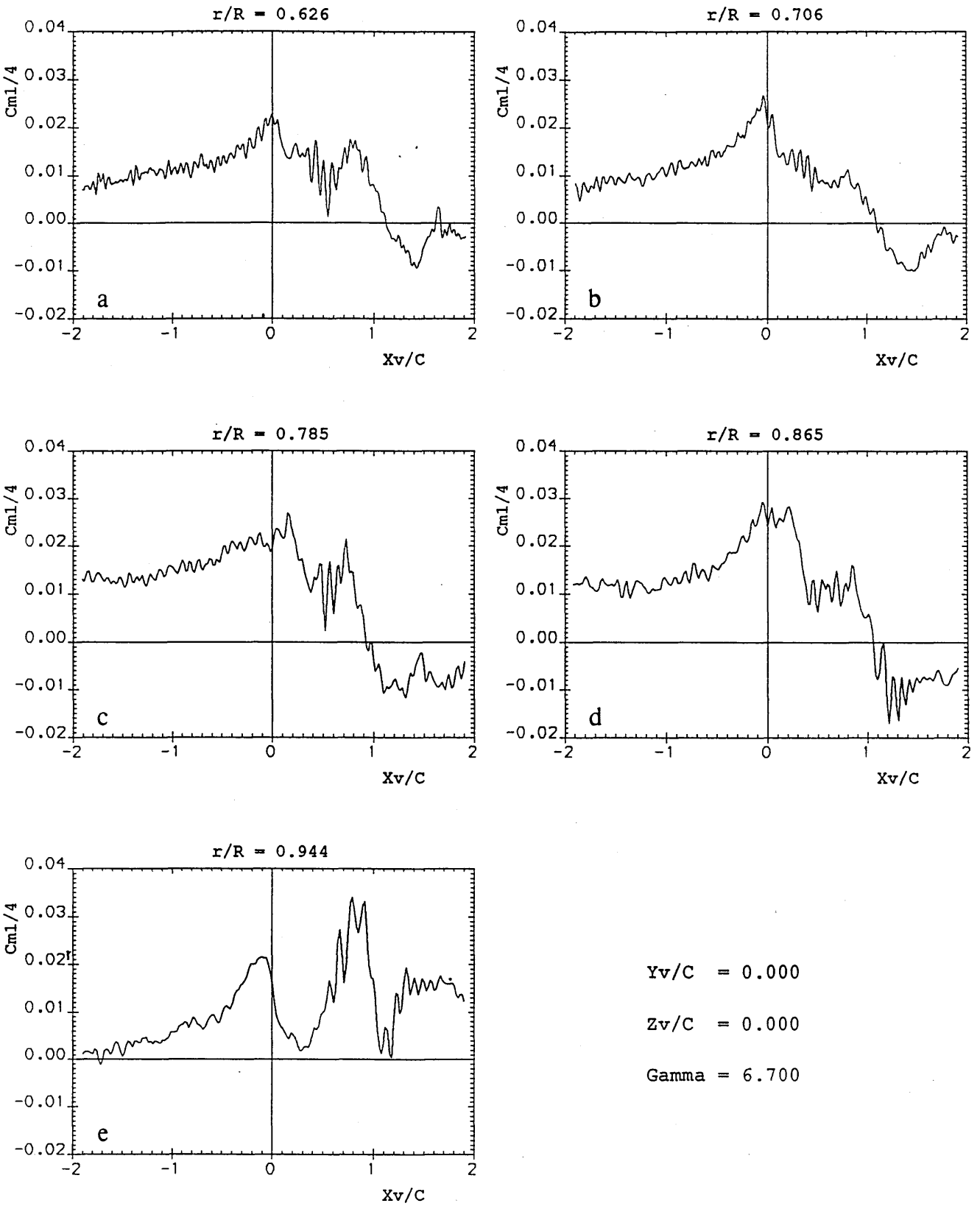

Figure 4.4.5 Azimuthal Quarter Chord Pitching Moment Coefficient Variations with Radial Position During Parallel BVIs : Y_v/c= 0.00, Γ=6.70m^2/s

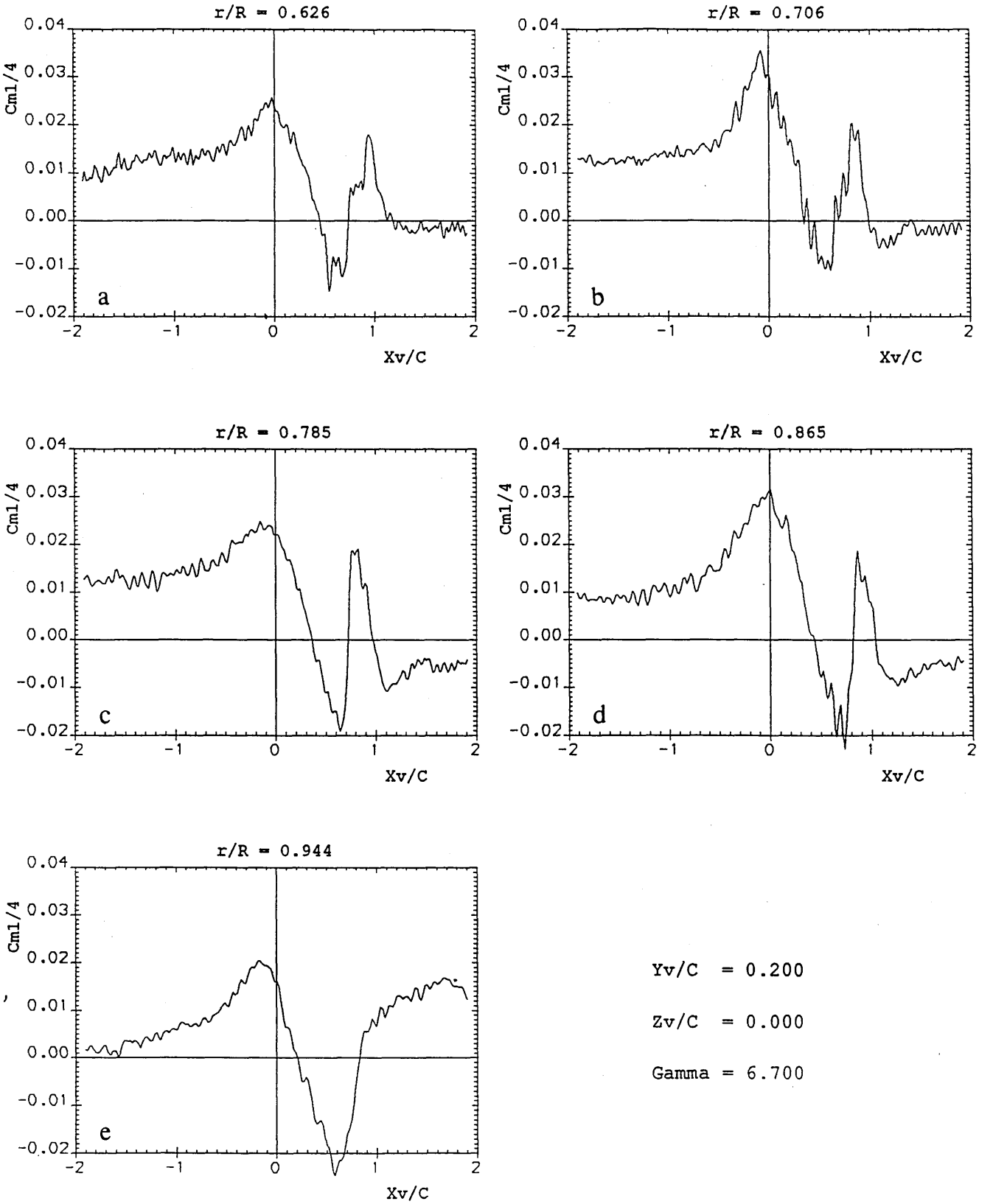

Figure 4.4.6 Azimuthal Quarter Chord Pitching Moment Coefficient Variations with Radial Position During Parallel BVIs : Y_V/c= 0.20, Γ=6.70m^2/s

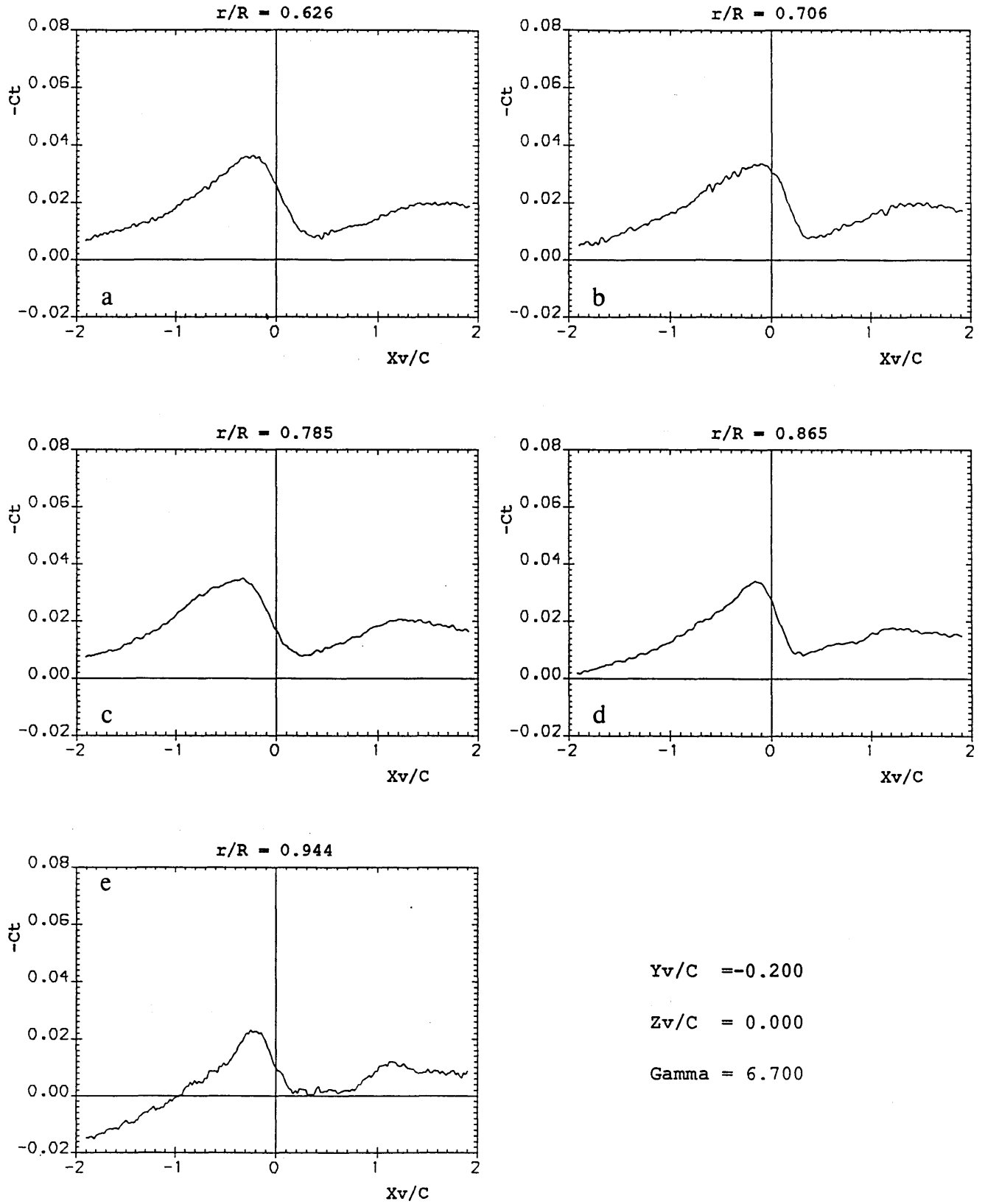

Figure 4.4.7 Azimuthal Pressure Drag Coefficient Variations with Radial Position During Parallel BVIs : Y_v/c=-0.20, Γ=6.70m^2/s

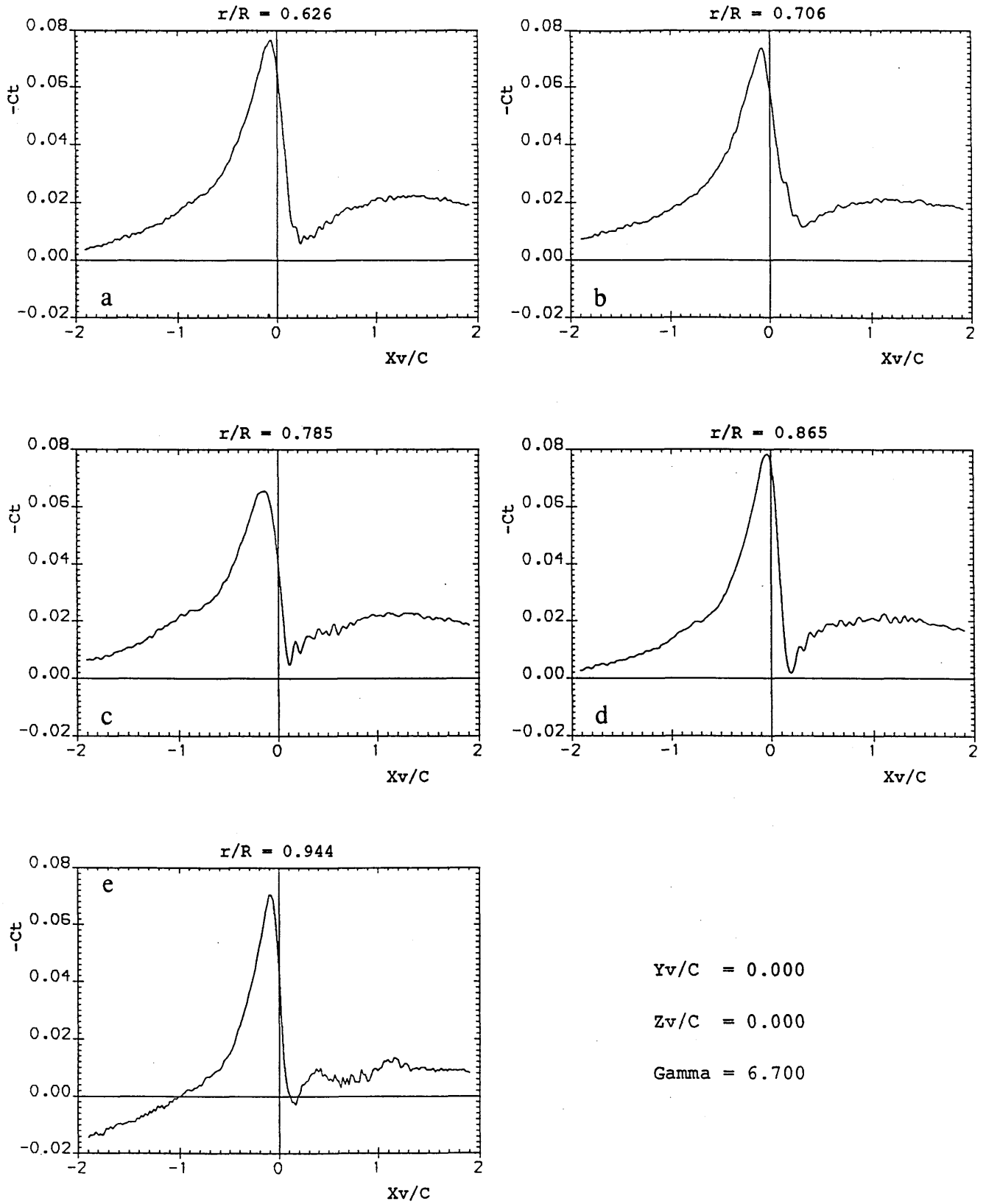

Figure 4.4.8 Azimuthal Pressure Drag Coefficient Variations with Radial Position During Parallel BVIs : Y_V/c= 0.00, Γ=6.70m^2/s

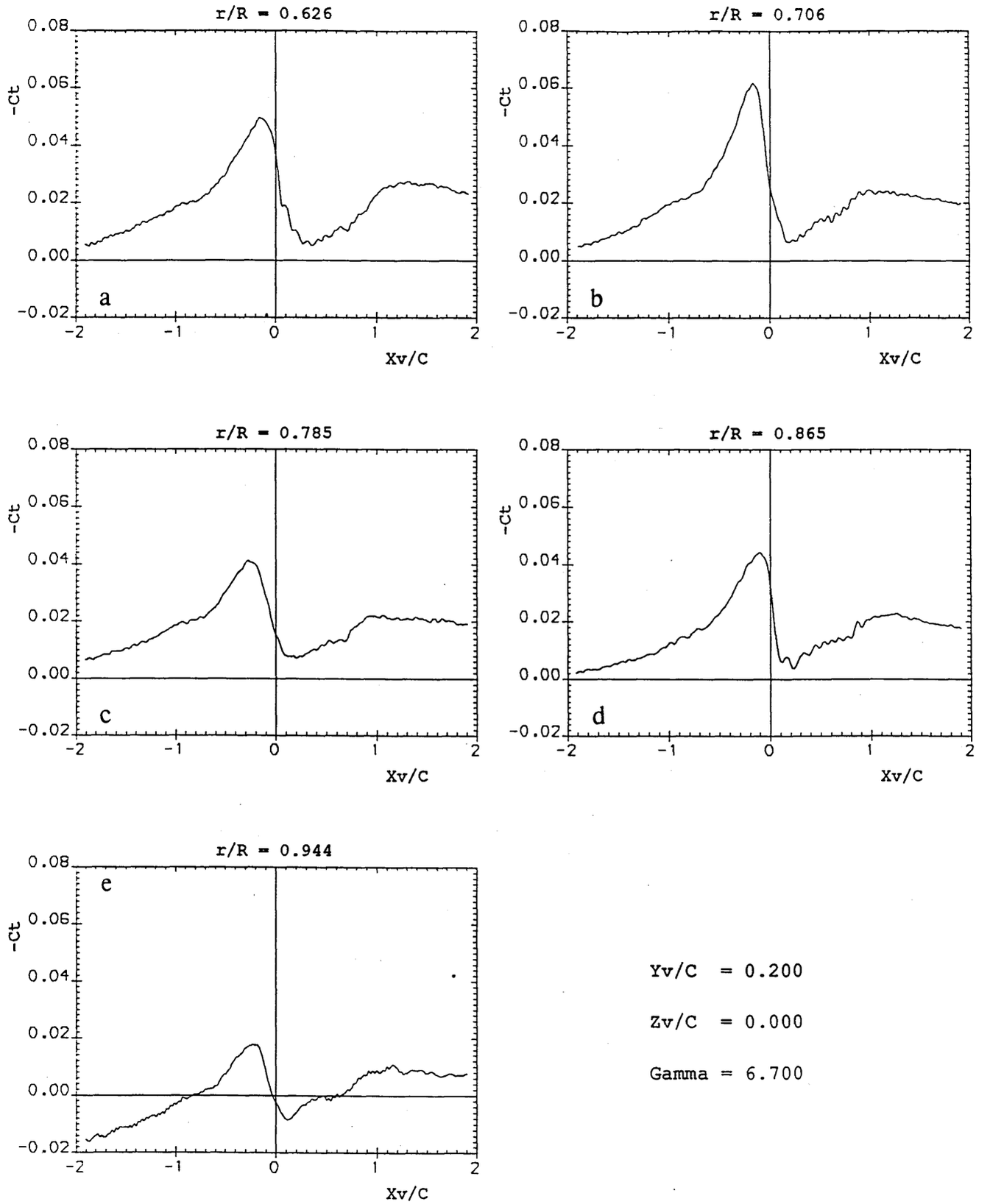

Figure 4.4.9 Azimuthal Pressure Drag Coefficient Variations with Radial Position During Parallel BVIs : Y_v/c= 0.20, Γ=6.70m^2/s

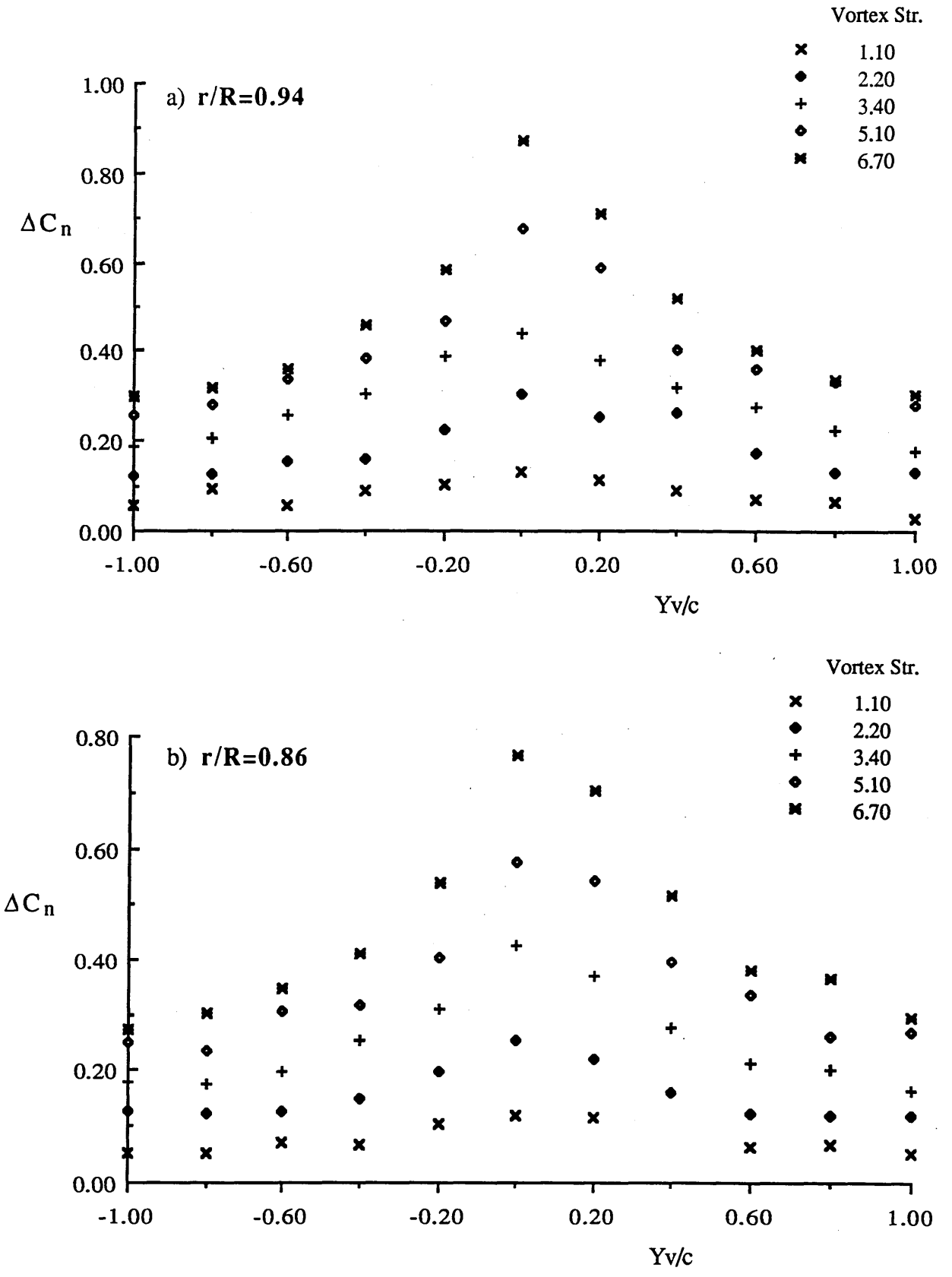

Figure 4.5.1 Maximum Section Lift Coefficient Difference Variations with Vortex Strength and Blade-Vortex Proximity

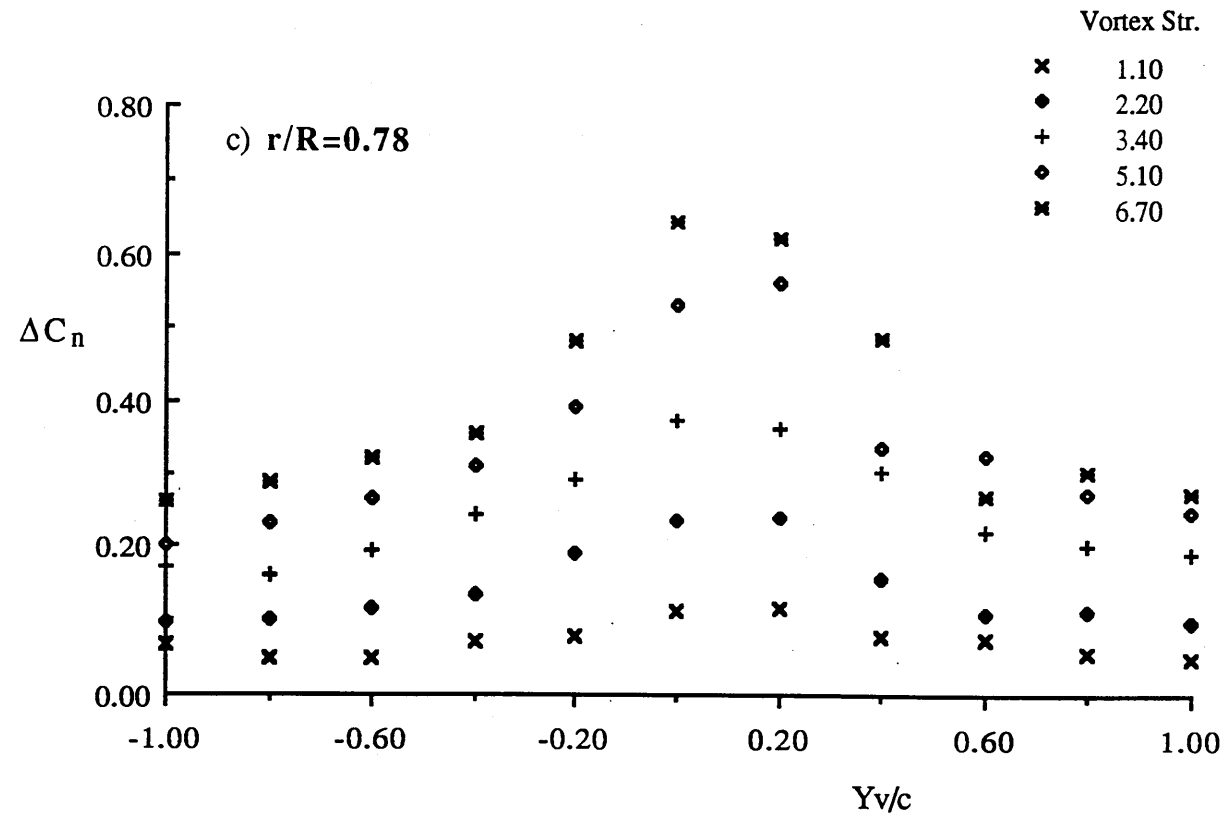

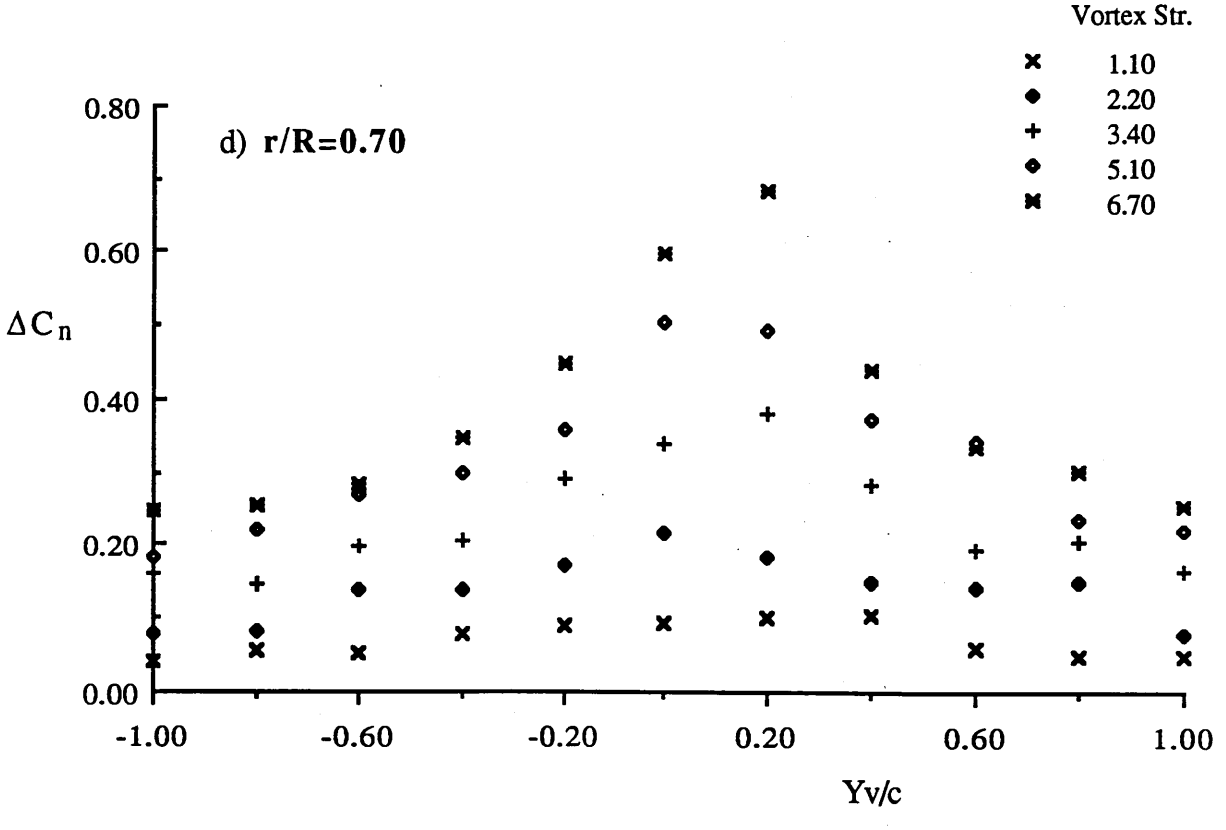

Figure 4.5.1 Continued...

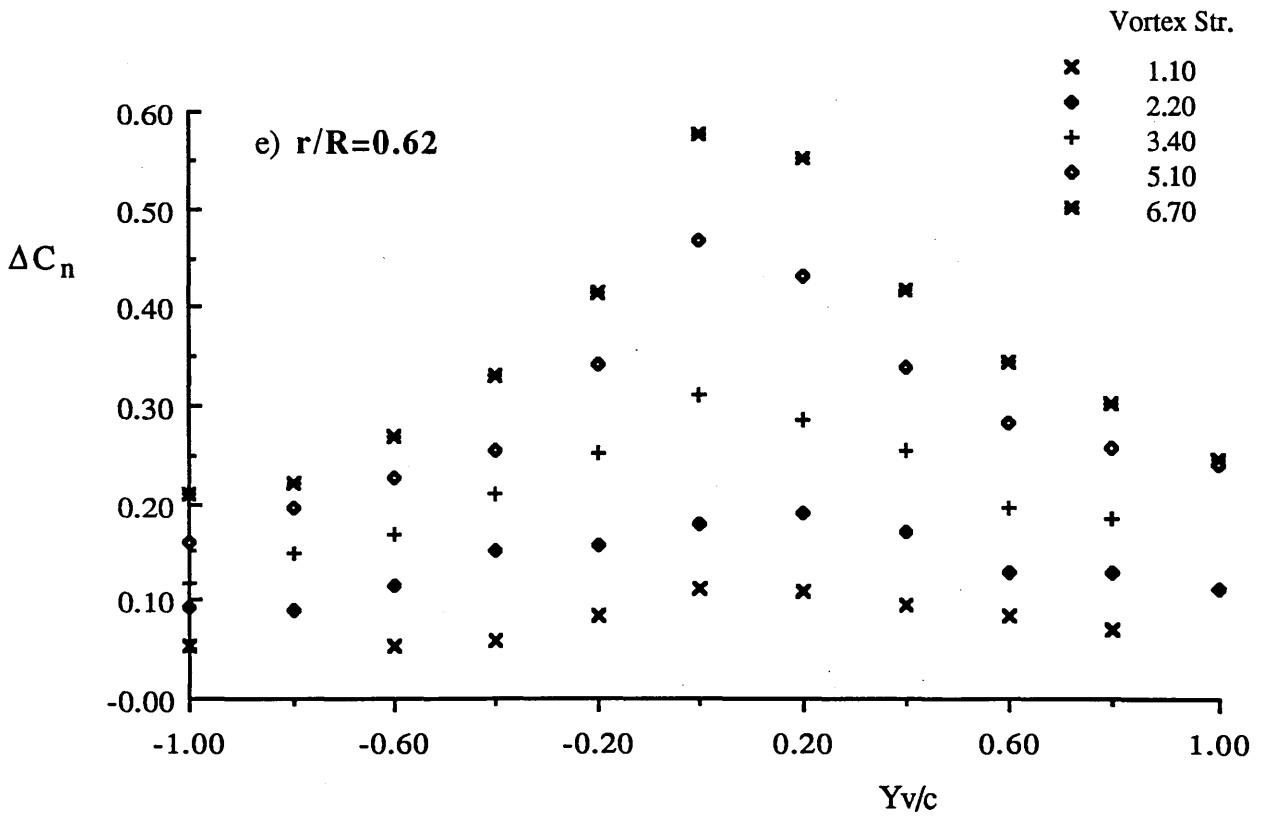

Figure 4.5.1 Concluded

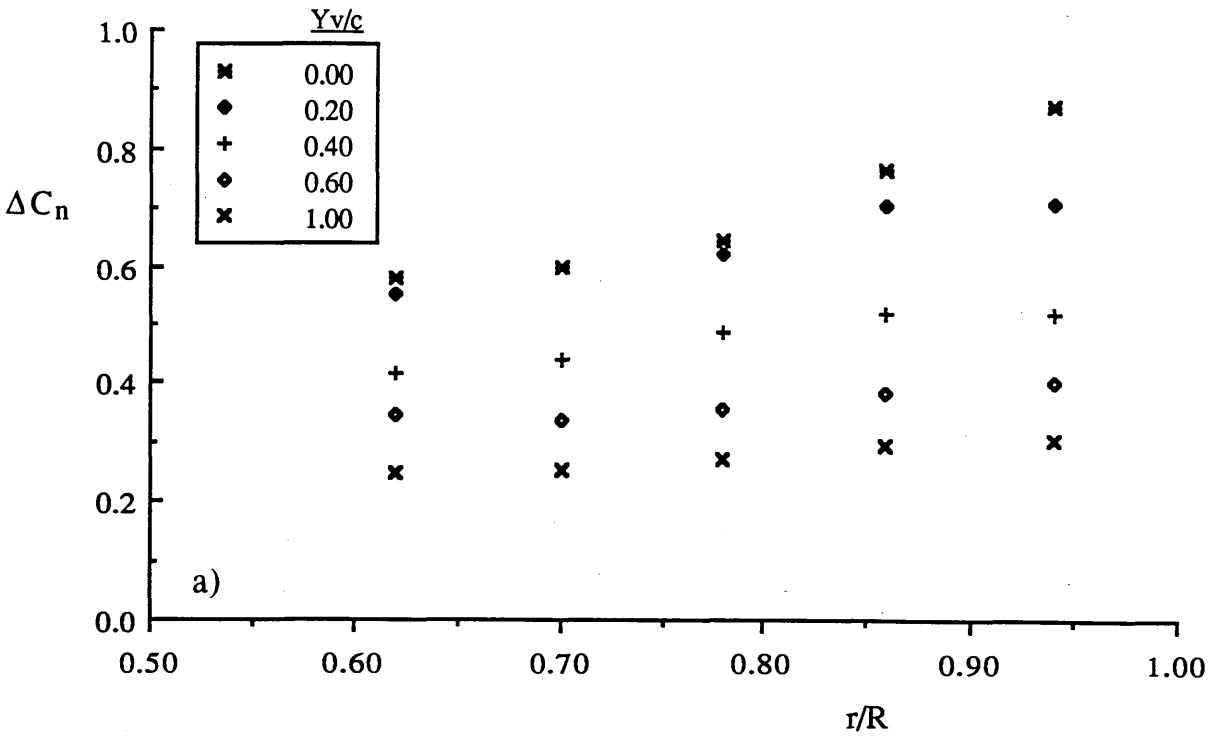

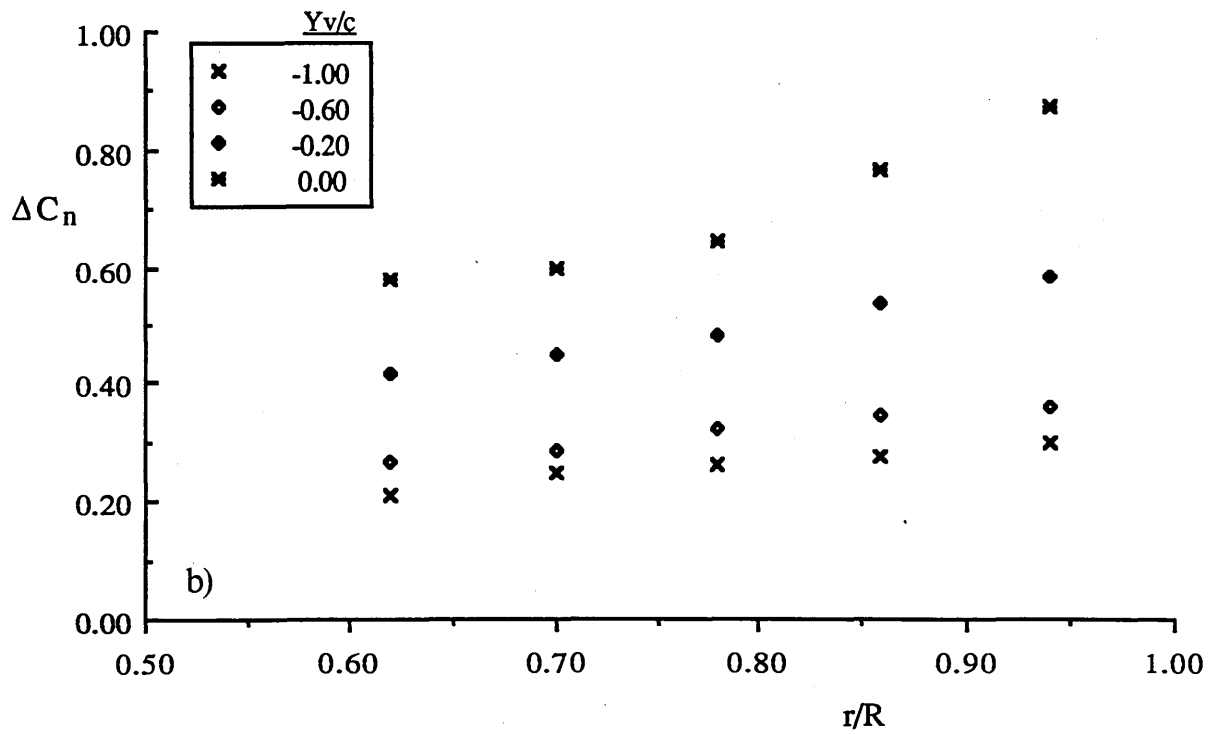

Figure 4.5.2 Maximum Section Lift Coefficient Difference Variations with Blade-Span Location (Γ=6.70m^2/s)

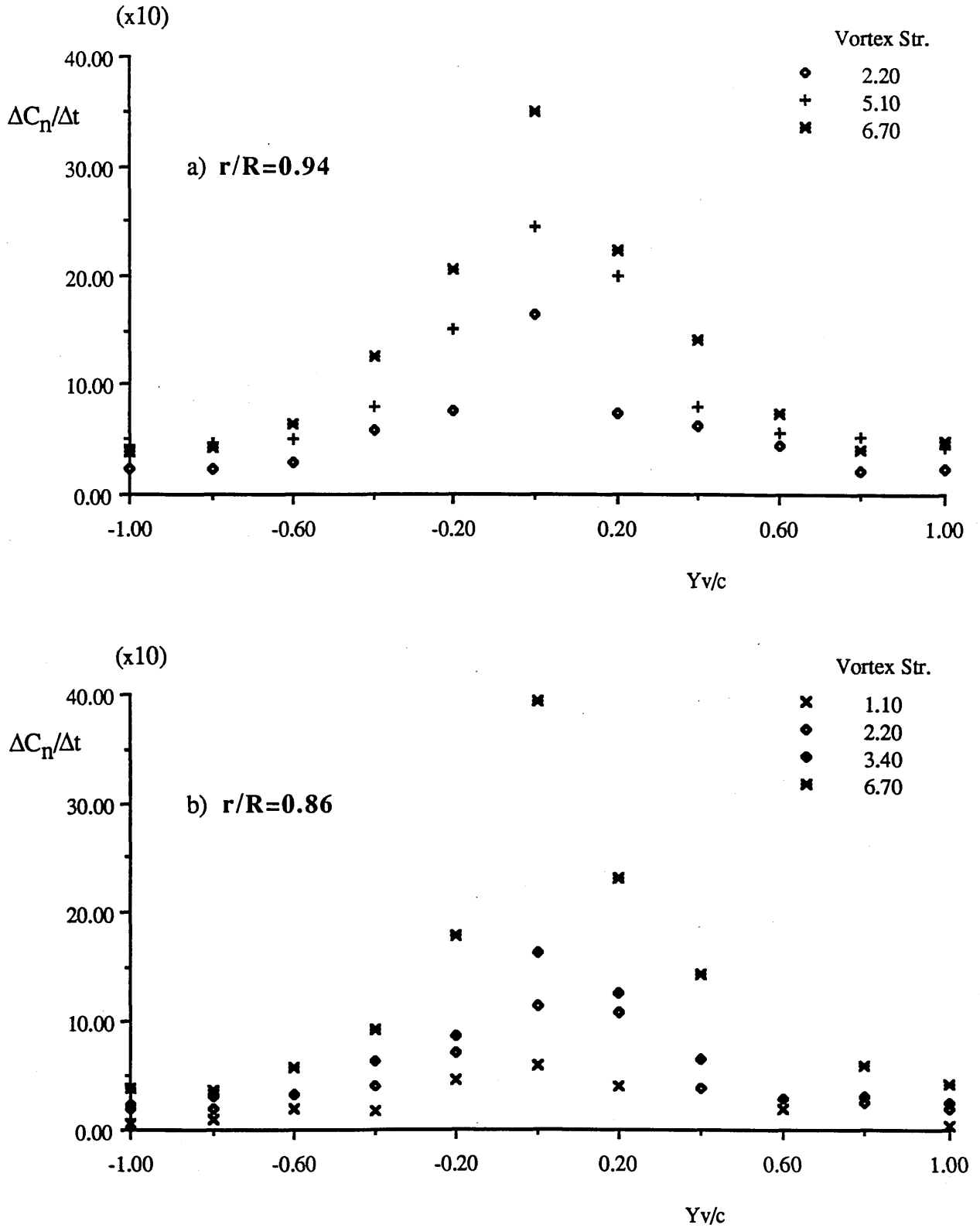

Figure 4.5.3 Illustrations of Time-Rate-Changes of ΔC_n with Vortex Strength and Blade-Vortex Proximity

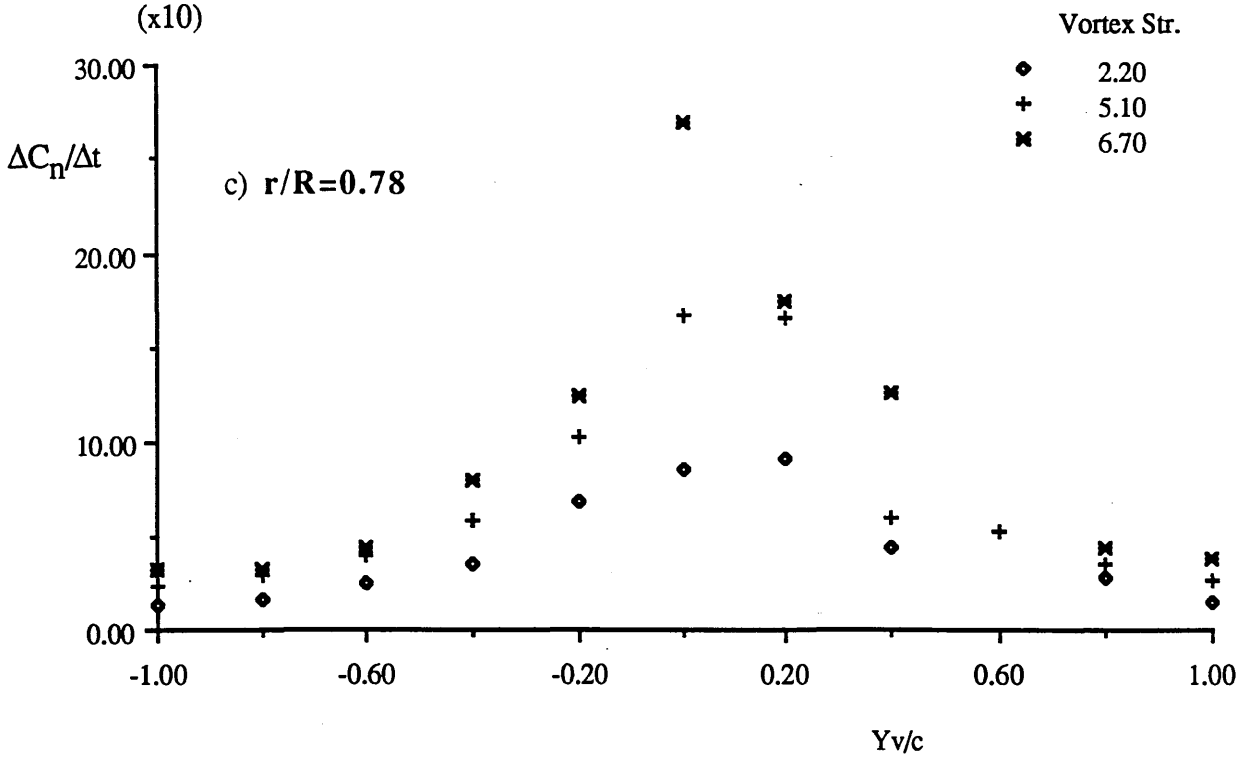

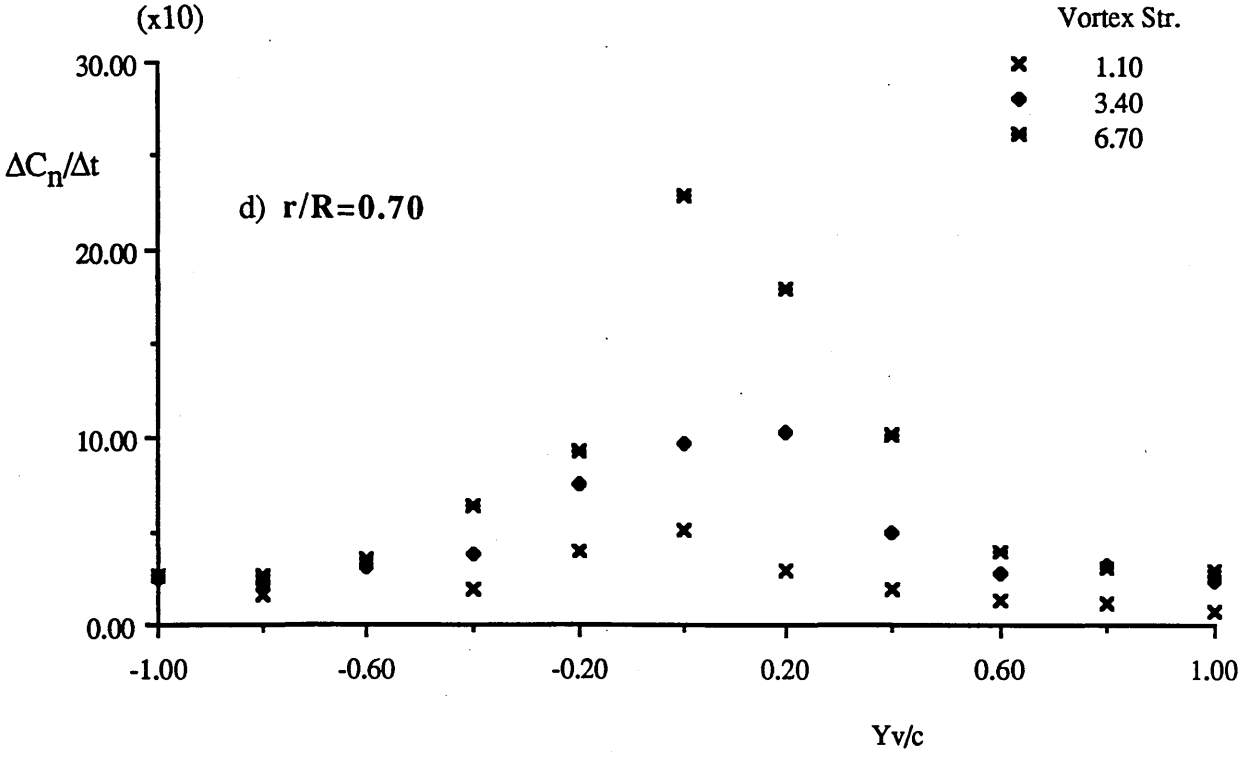

Figure 4.5.3 Continued...

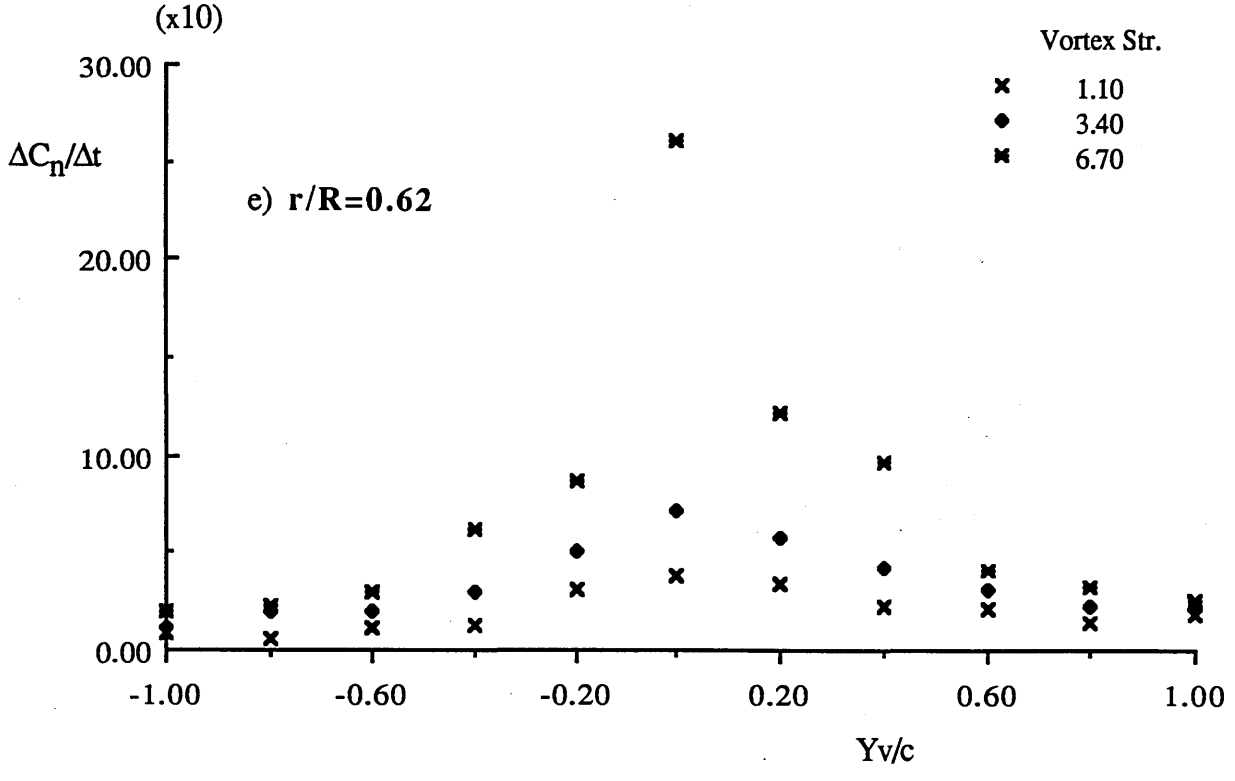

Figure 4.5.3 Concluded

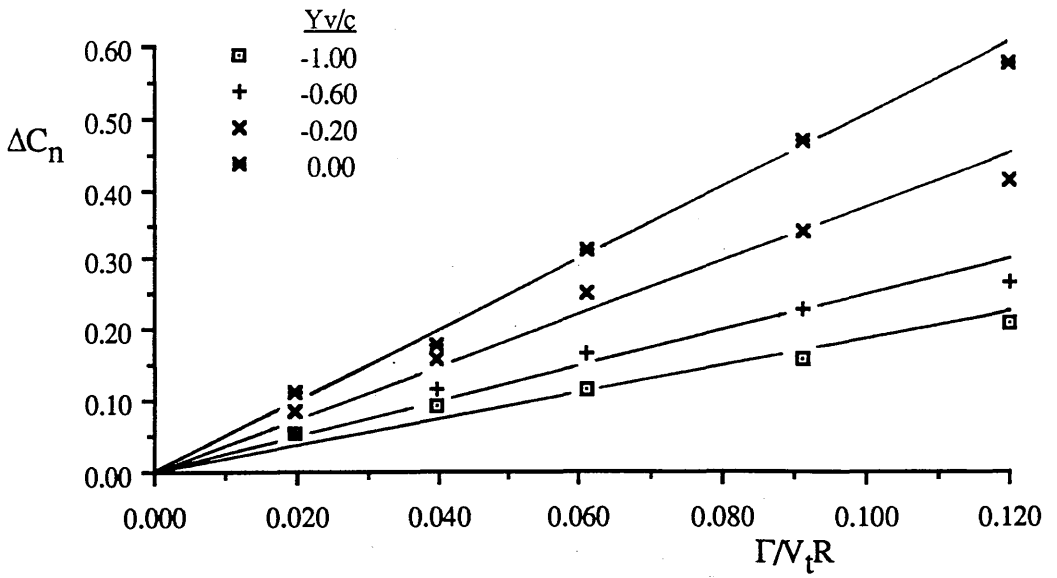

a

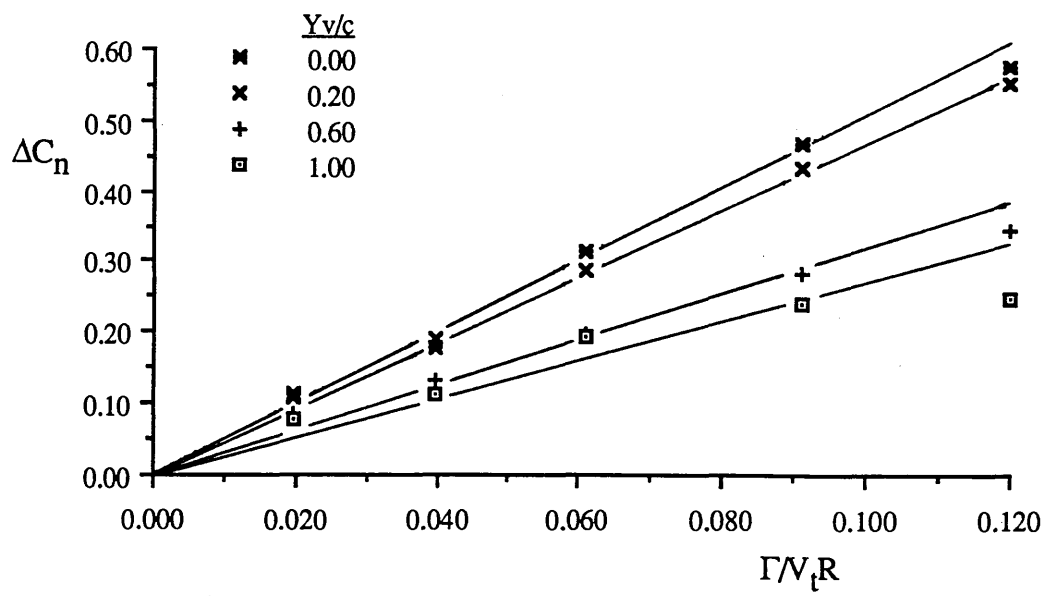

b

Figure 4.5.4 Maximum Section Lift Coefficient Difference Variations with Vortex Strength for the Radial Station r/R=0.62

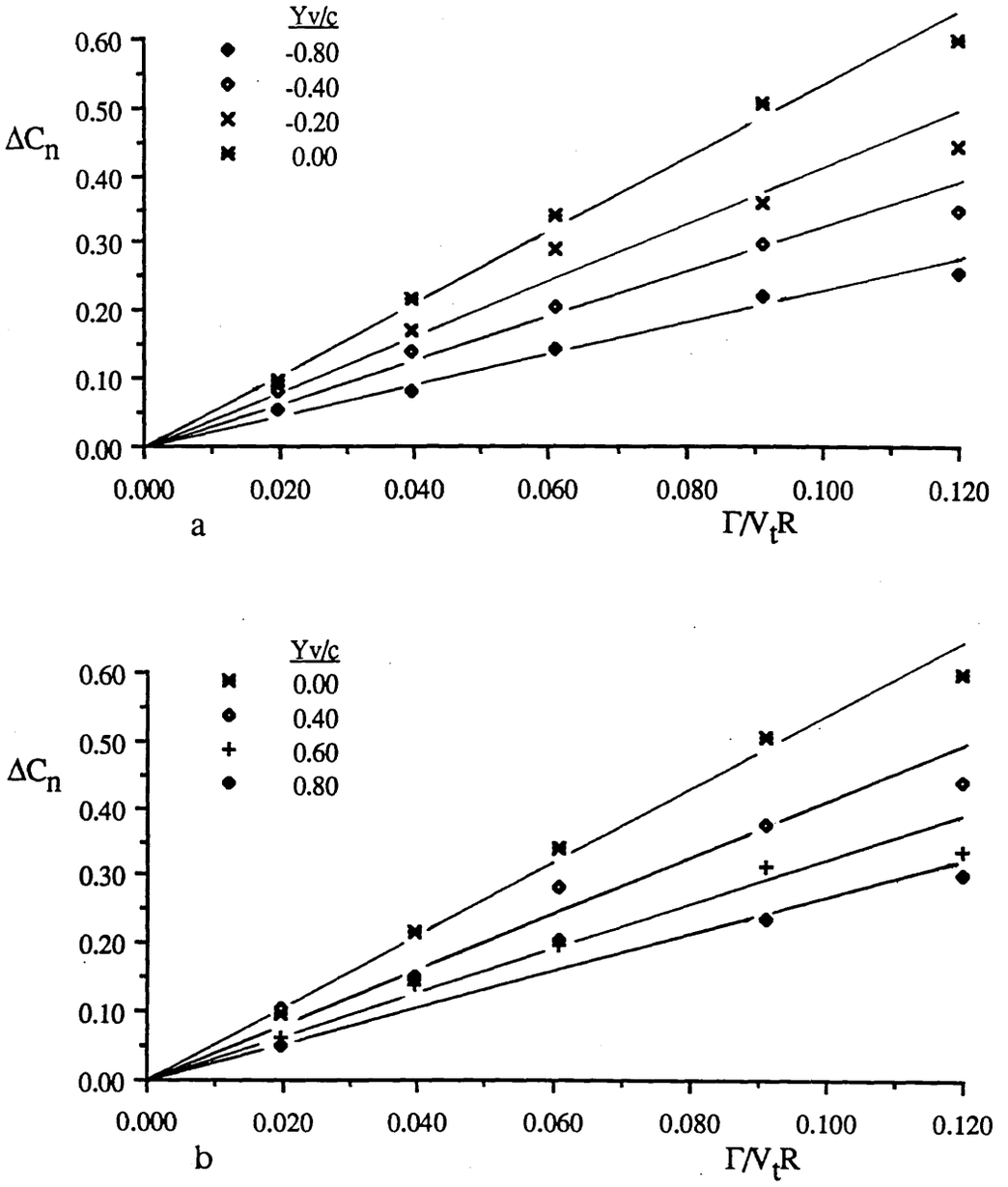

Figure 4.5.5 Maximum Section Lift Coefficient Difference Variations with Vortex Strength for the Radial Station r/R=0.70

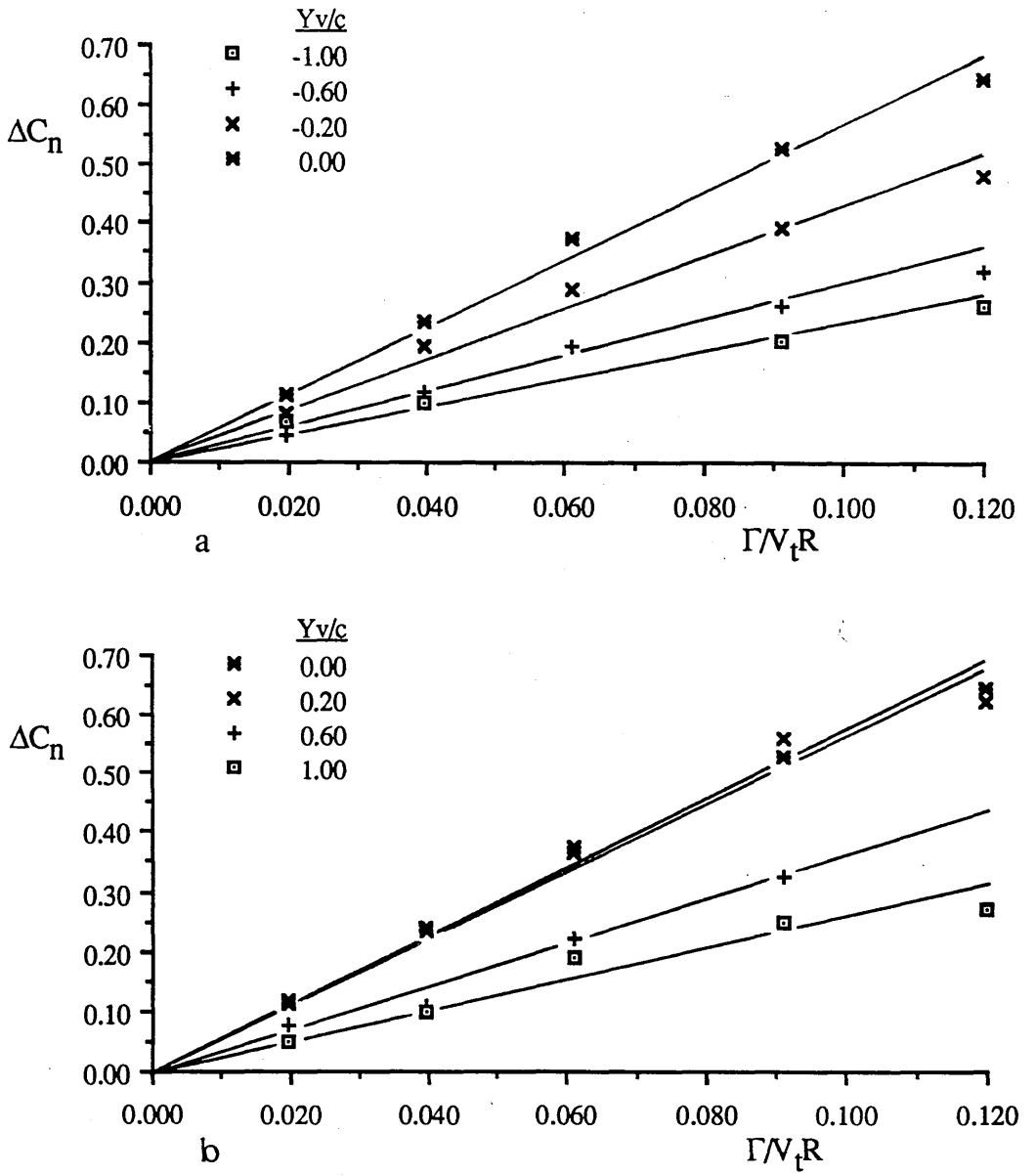

Figure 4.5.6 Maximum Section Lift Coefficient Difference Variations with Vortex Strength for the Radial Station r/R=0.78

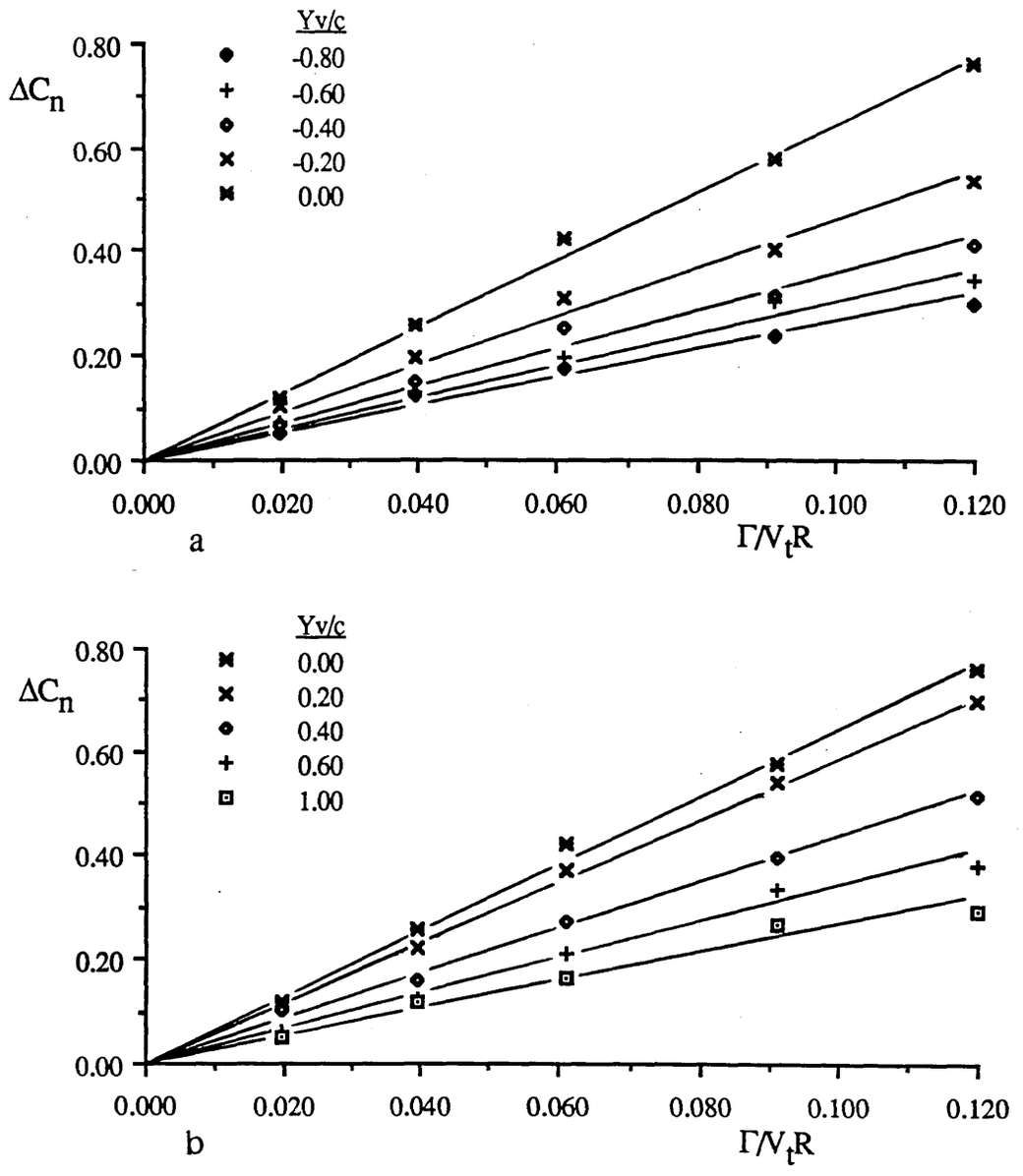

Figure 4.5.7 Maximum Section Lift Coefficient Difference Variations with Vortex Strength for the Radial Station r/R=0.86

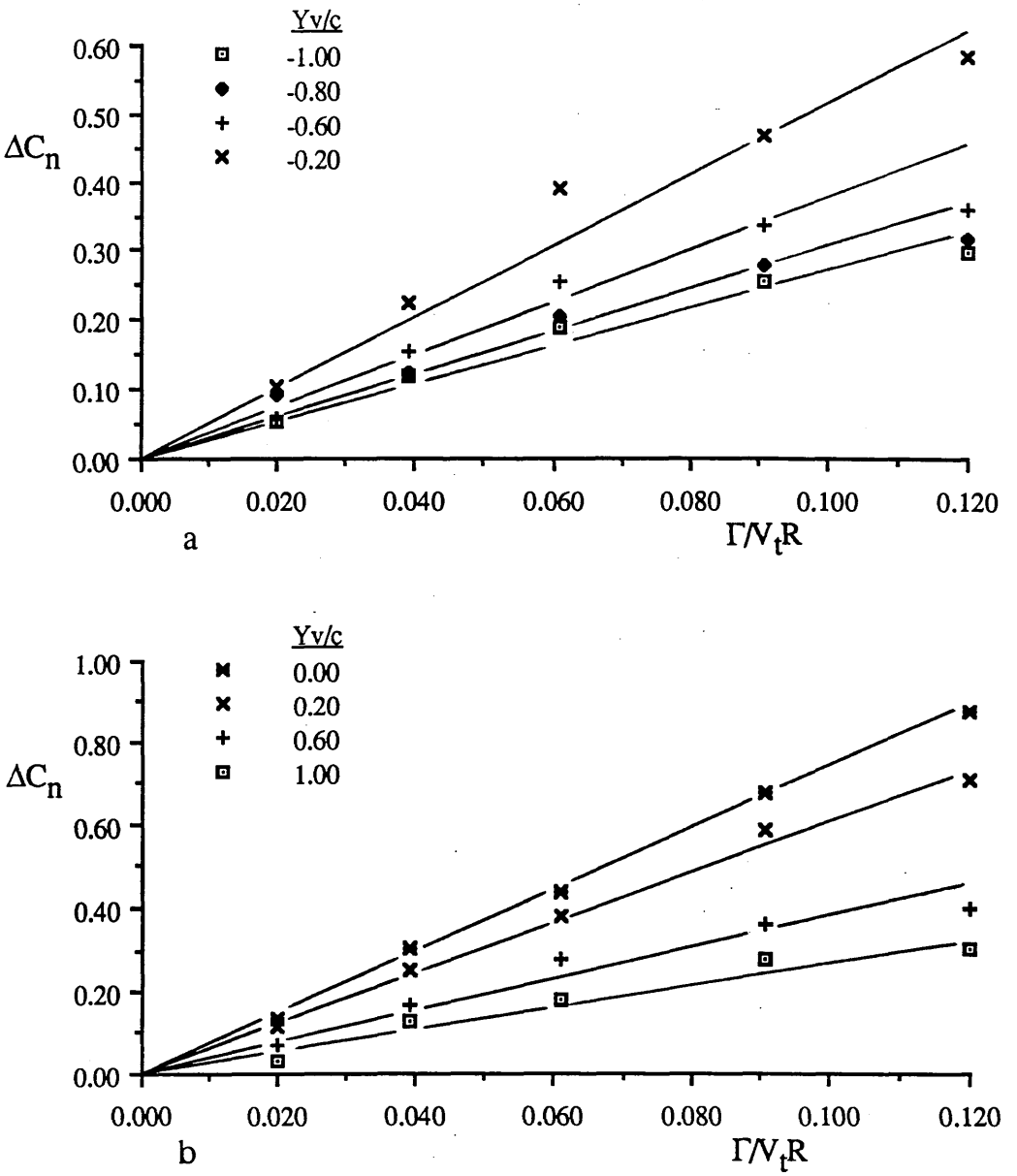

Figure 4.5.8 Maximum Section Lift Coefficient Difference Variations with Vortex Strength for the Radial Station r/R=0.94

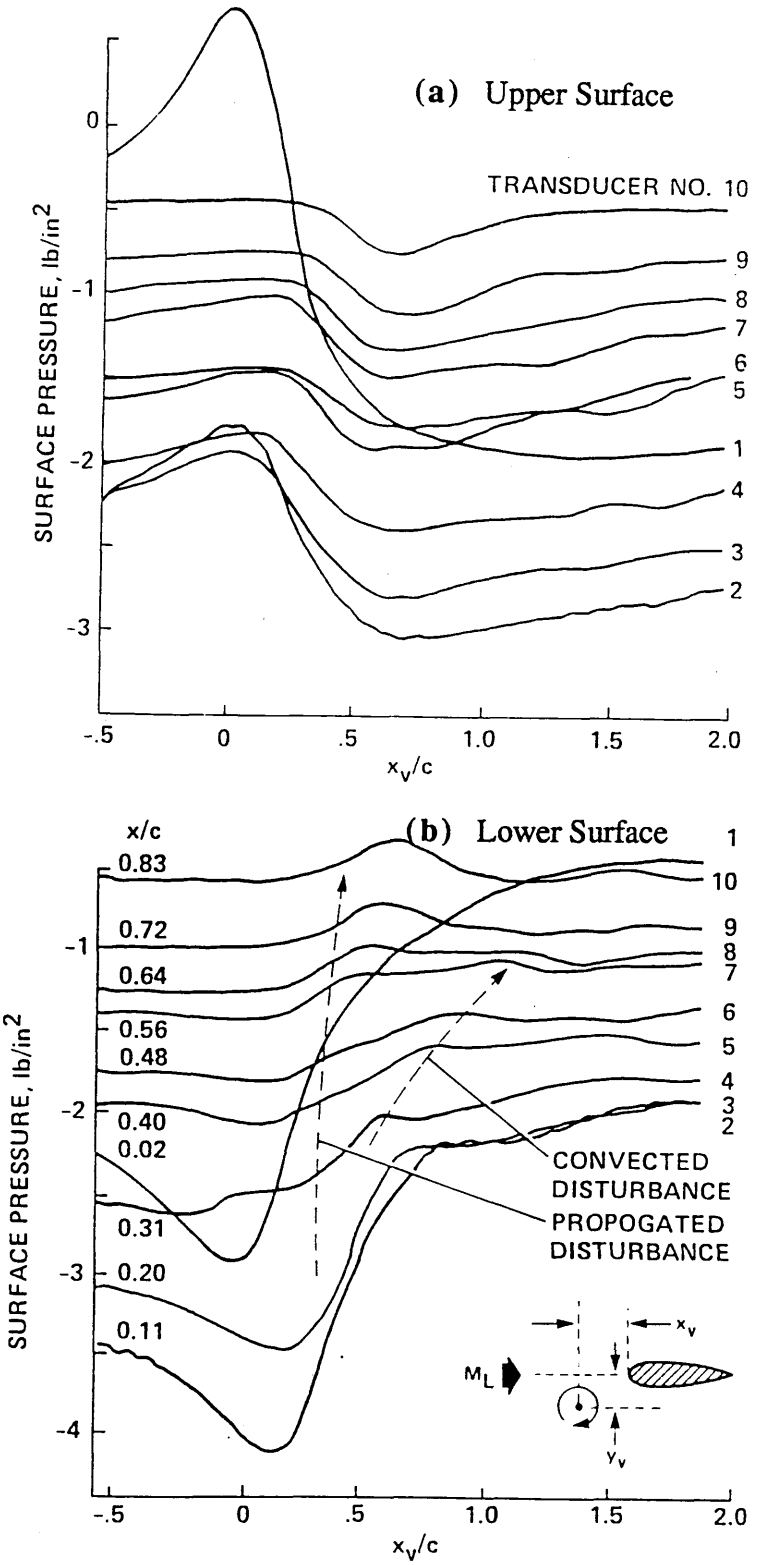

Figure 5.1.1 Vortex Induced Surface Pressure Variations over a NACA-0012 Rotor Blade Aerofoil : $M_l = 0.624$, $C_{lv} = 0.62$, $Y_v/c = -0.22$, $r/R = 0.893$ [**34**]

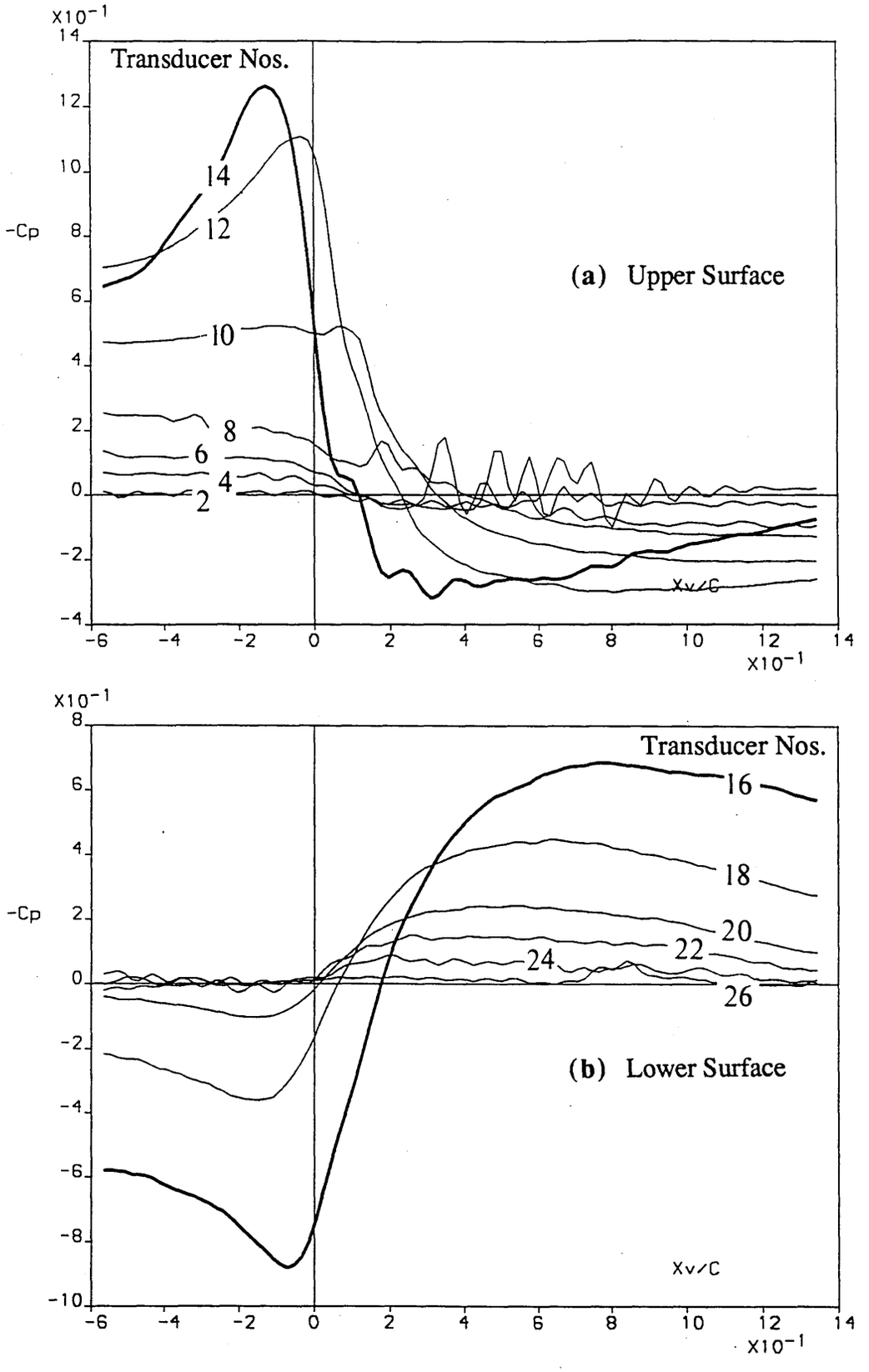

Figure 5.1.2 Vortex Induced Surface Pressure Variations over a NACA-0015 Rotor Blade Aerofoil : $Y_v/c=0.20$, $r/R=0.86$ and $\Gamma=5.10$ m^2/s.

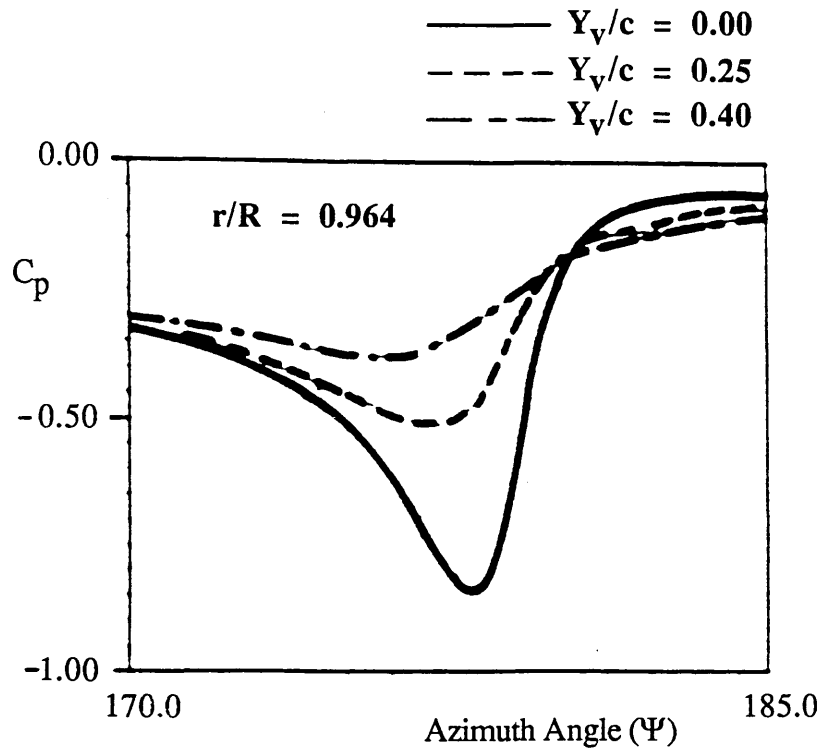

Figure 5.1.3(a) Pressure Effects of the Parallel BVI captured by a Leading Edge Pressure Transducer for Various Blade-Vortex Separation Distances : $M_t = 0.70$, $\mu = 0.20$ and $x/c = 0.02$ **[35]**

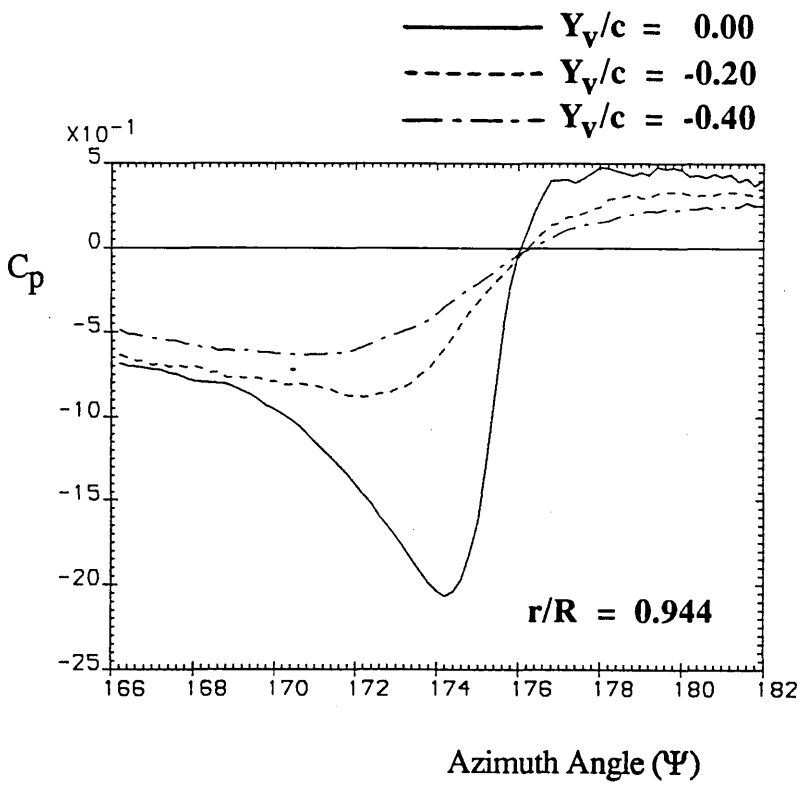

Figure 5.1.3(b) Pressure Effects of the Parallel BVI captured by a Leading Edge Pressure Transducer for Various Blade-Vortex Separation Distances : $\Gamma = 6.70 m^2/s$ and $x/c = 0.0260$ (Present Data)

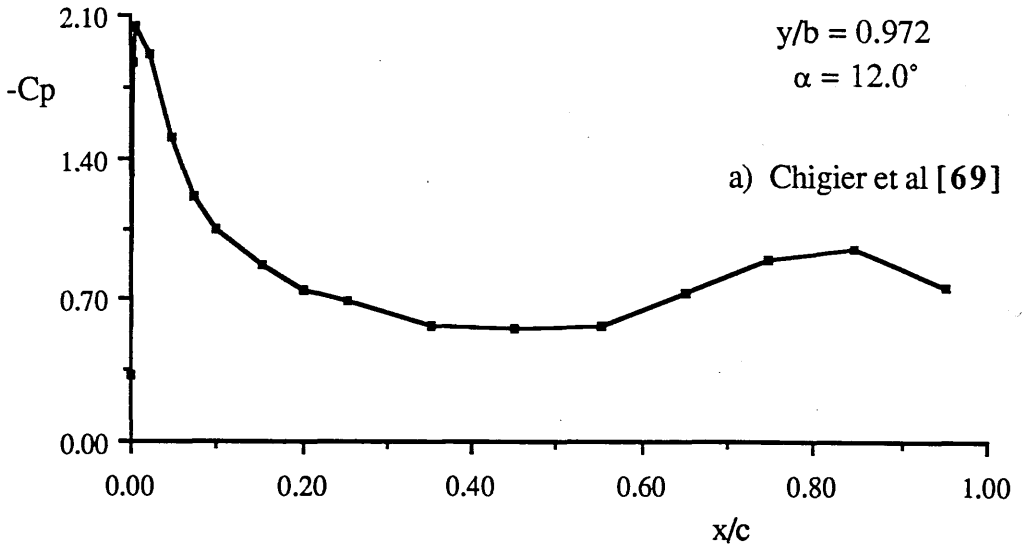

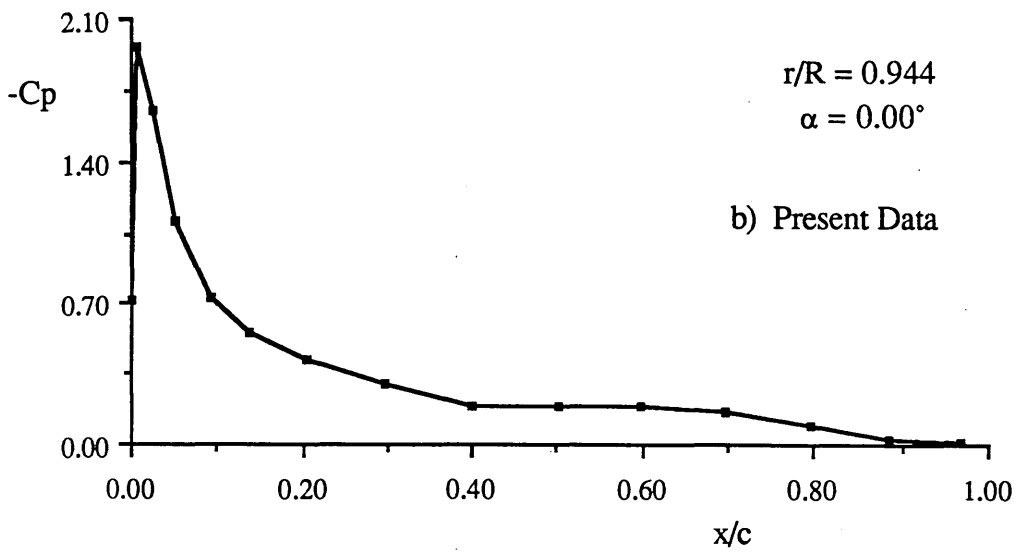

Figure 5.1.4 Upper Surface Pressure Coefficient Distributions from NACA-0015 Aerofoil Wings near the Tip Region a) Chigier et al [**69**] and b) Present Data

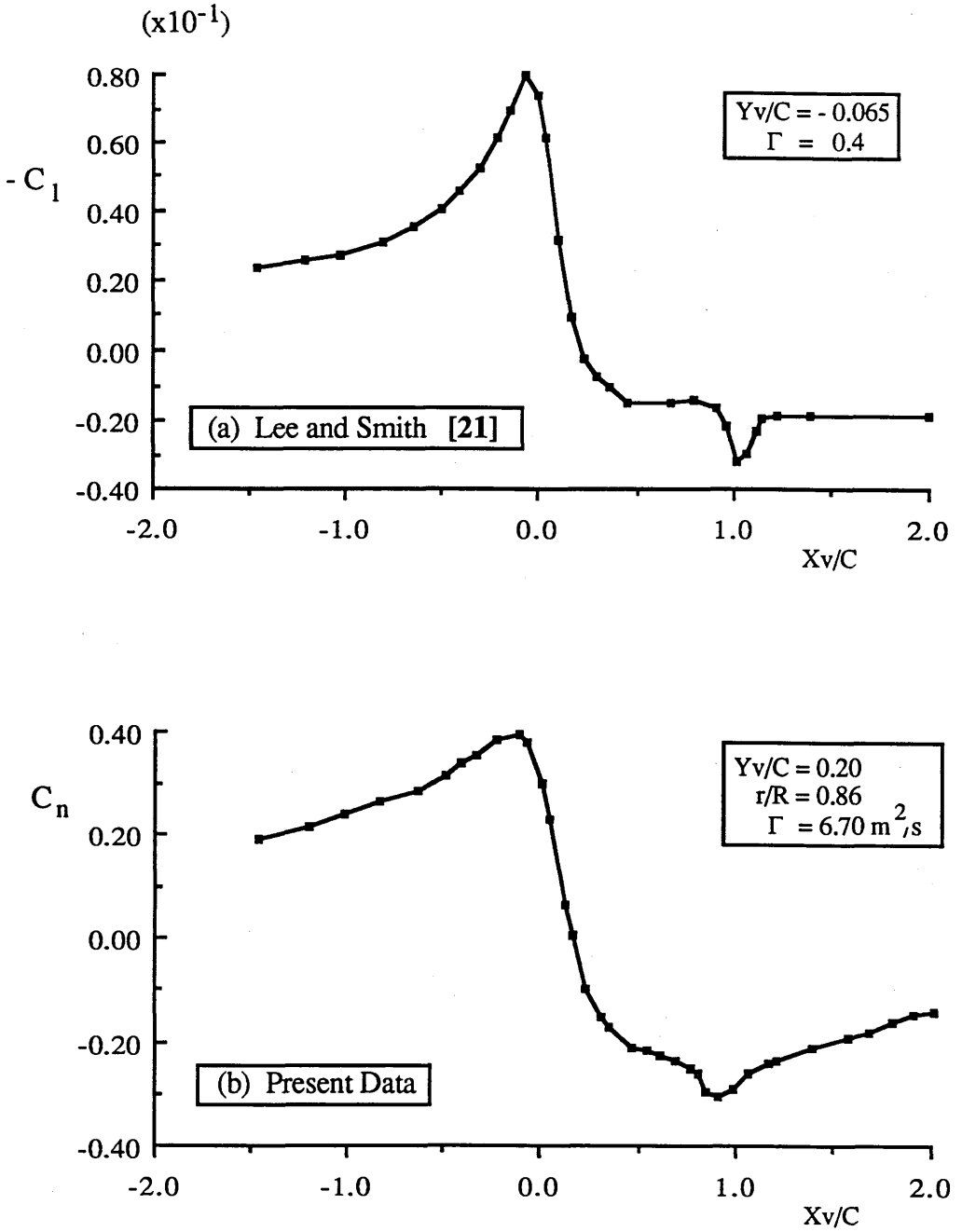

Figure 5.2.1 Comparison of Lift Coefficient Variations with Xv/c During a Parallel BVI ; a) Lee and Smith [21] and b) Present Data

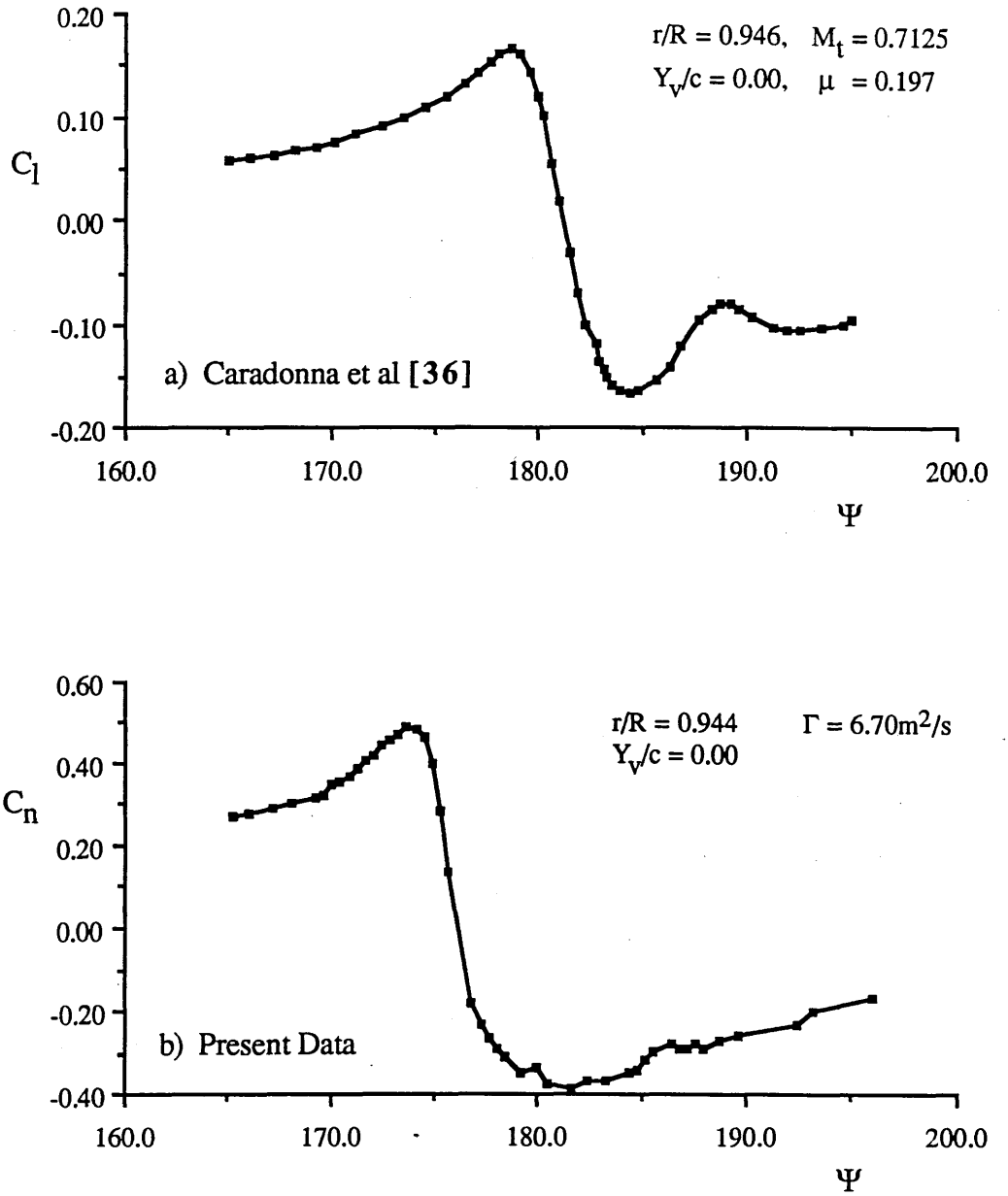

Figure 5.2.2 Comparison of Lift Coefficient Variations with Azimuth Angle During a Parallel BVI ; a) Caradonna et al [**36**] and b) Present Data

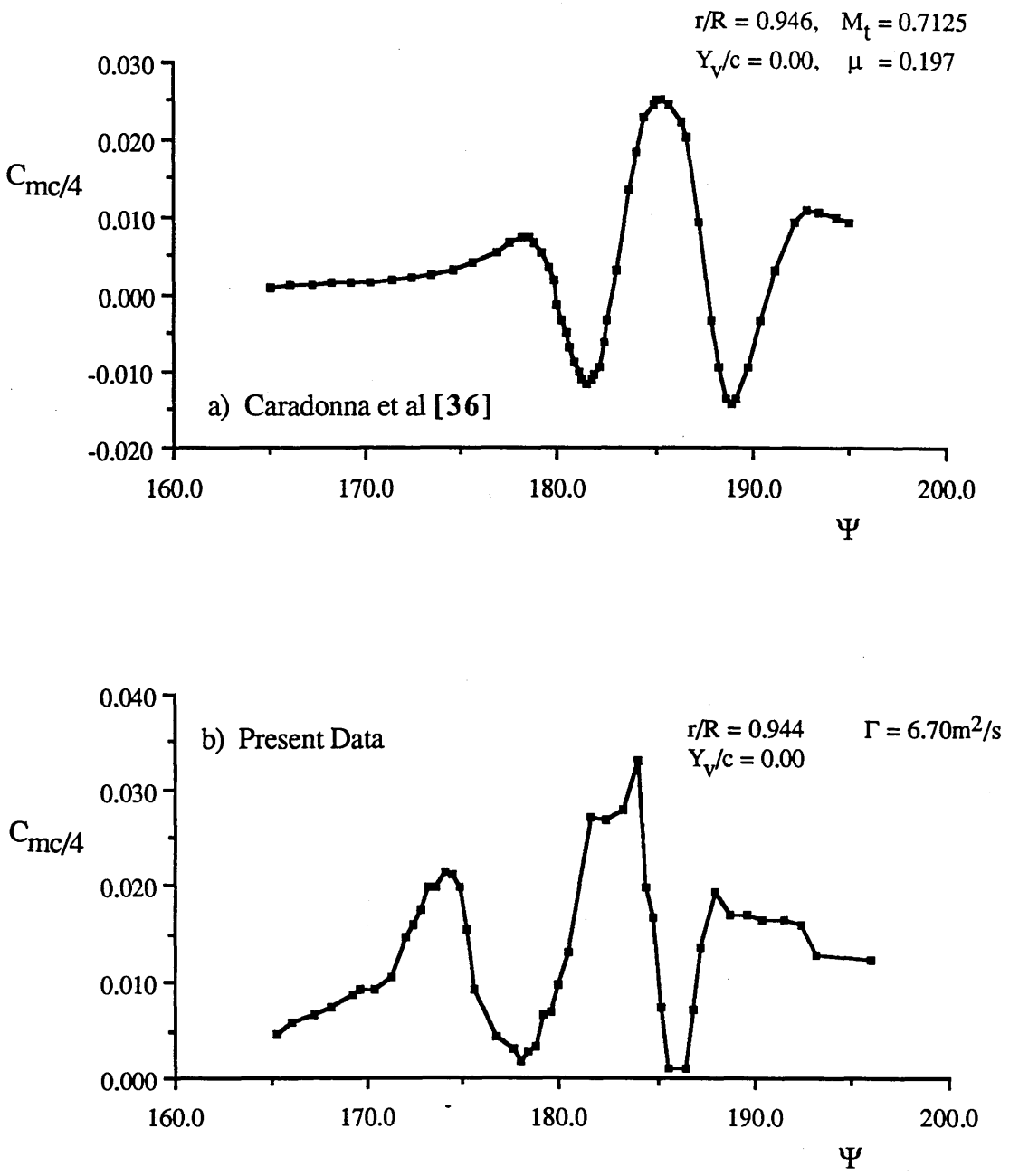

Figure 5.2.3 Comparison of Quarter Chord Pitching Moment Coefficient Variations with Azimuth Angle During a Parallel BVI ; a) Caradonna et al [36] and b) Present Data

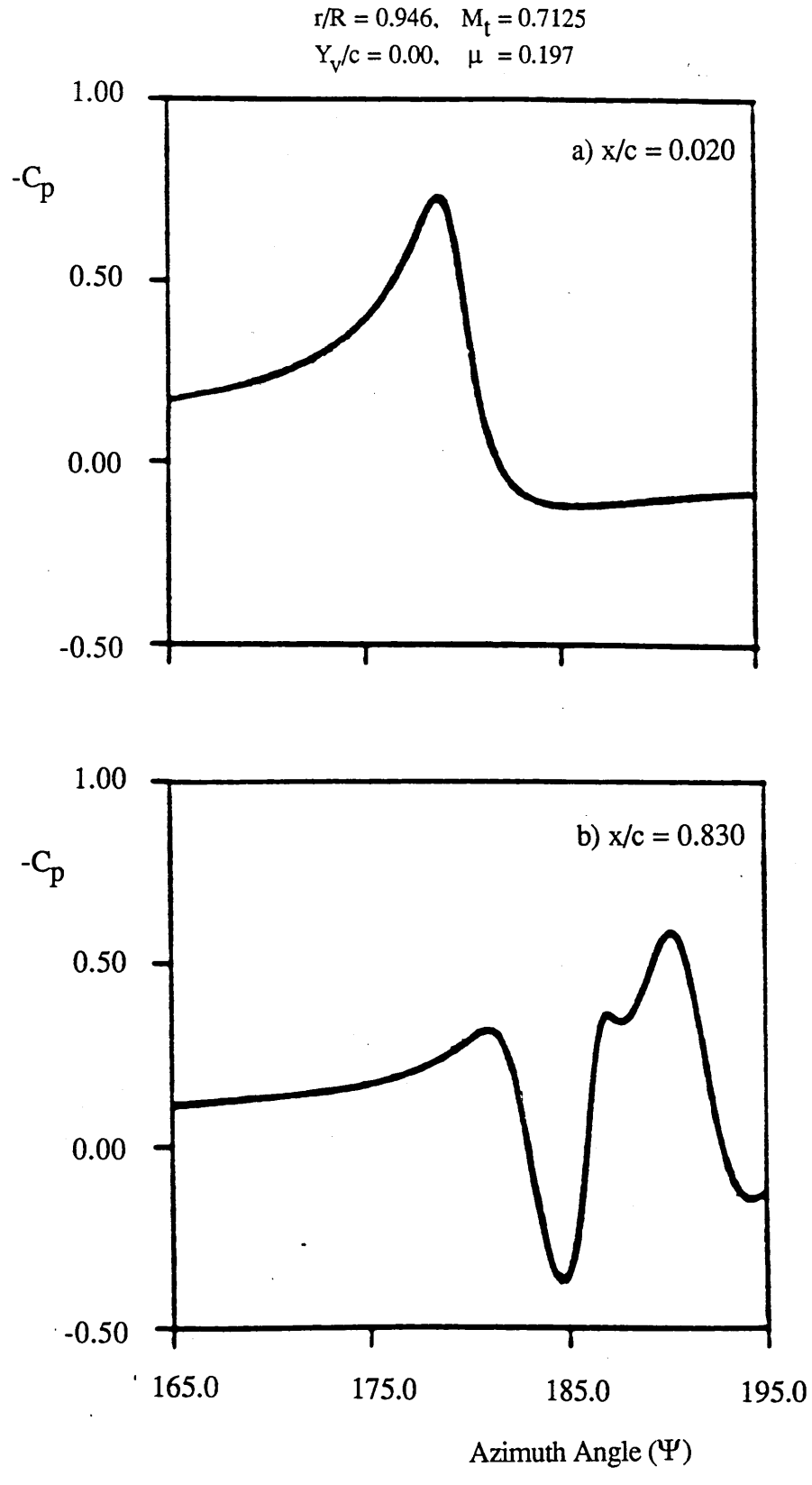

Figure 5.2.4 Pressure Coefficient Variations with Azimuth Angle During a Parallel BVI [**36**] ; a) x/c = 0.02 and b) x/c = 0.83

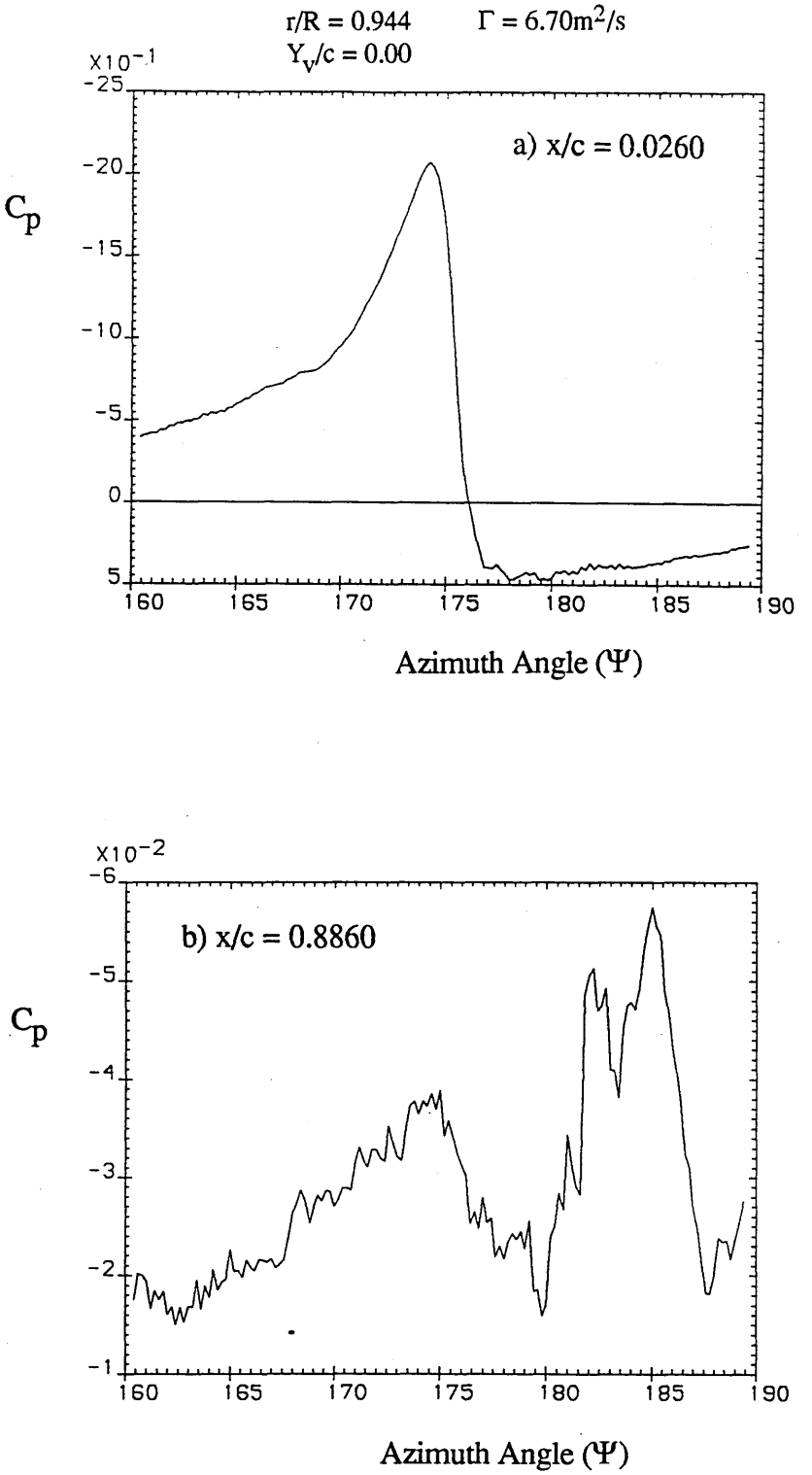

Figure 5.2.5 Pressure Coefficient Variations with Azimuth Angle During a Parallel BVI (Present Data) ; a) x/c = 0.026 and b) x/c = 0.886

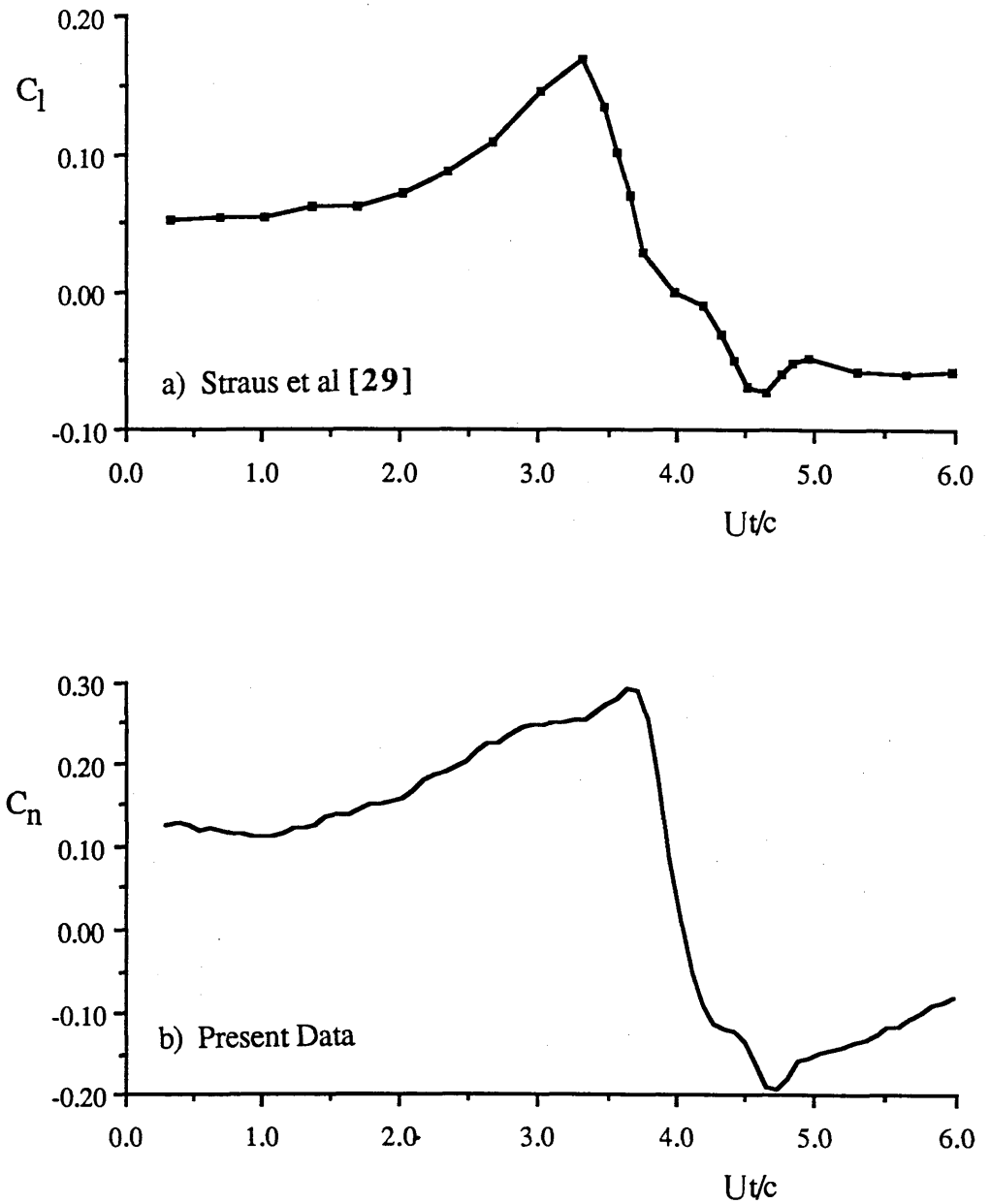

Figure 5.2.6 Comparison of Lift Coefficient Variations with Chord-Time Intervals During a Parallel BVI ; a) Straus et al [29] and b) Present Data

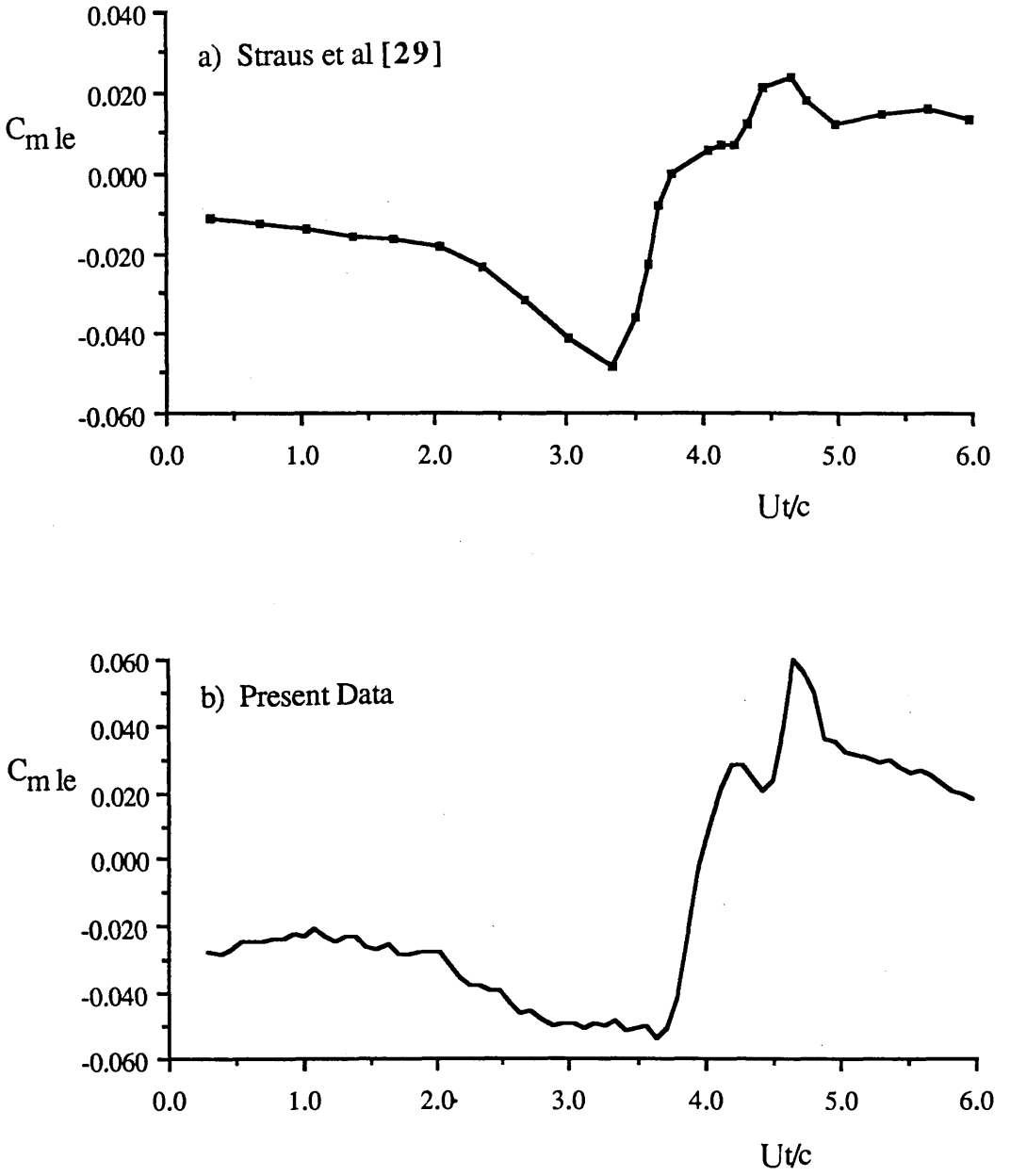

Figure 5.2.7 Comparison of Leading Edge Pitching Moment Coefficient Variations with Chord-Time Intervals During a Parallel BVI ; a) Straus et al [29] and b) Present Data

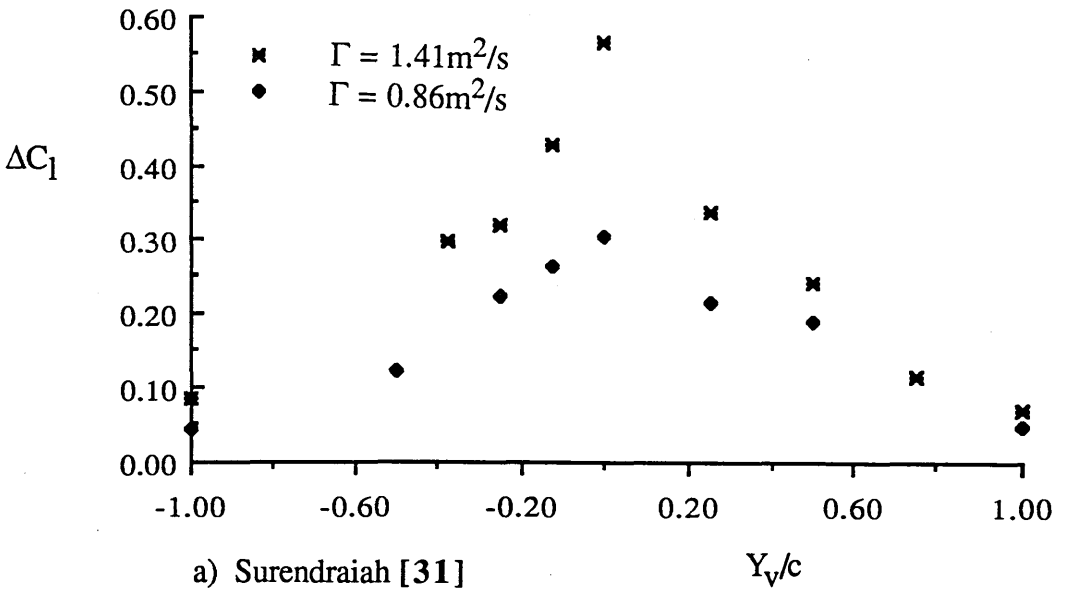

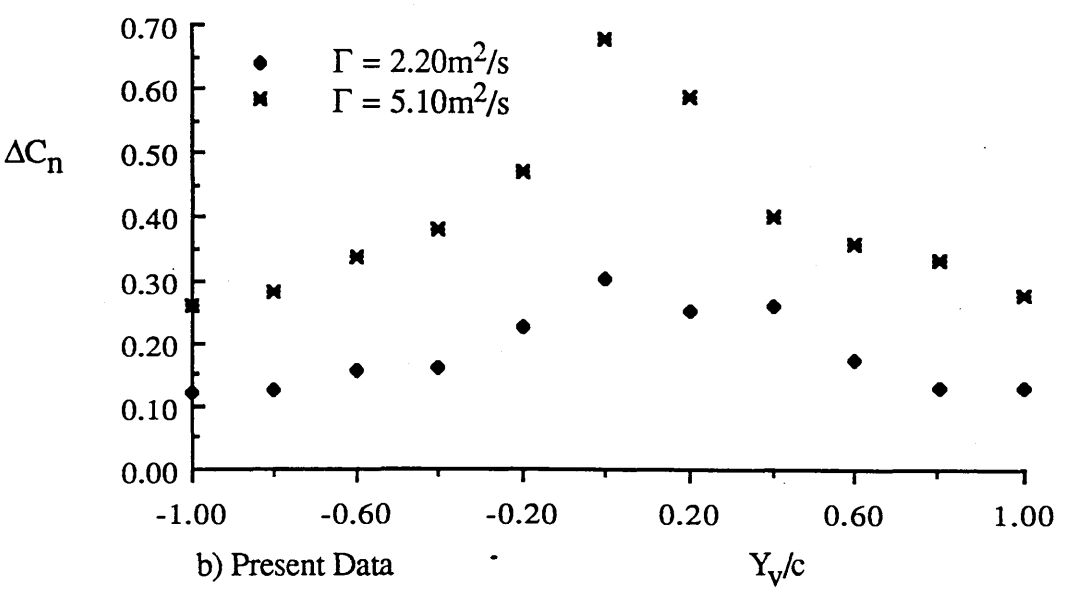

Figure 5.2.8 Comparison of Maximum Lift Coefficient Difference Variations with Blade-Vortex Proximity and Vortex Strength ; a) Surendraiah [31] and b) Present Data

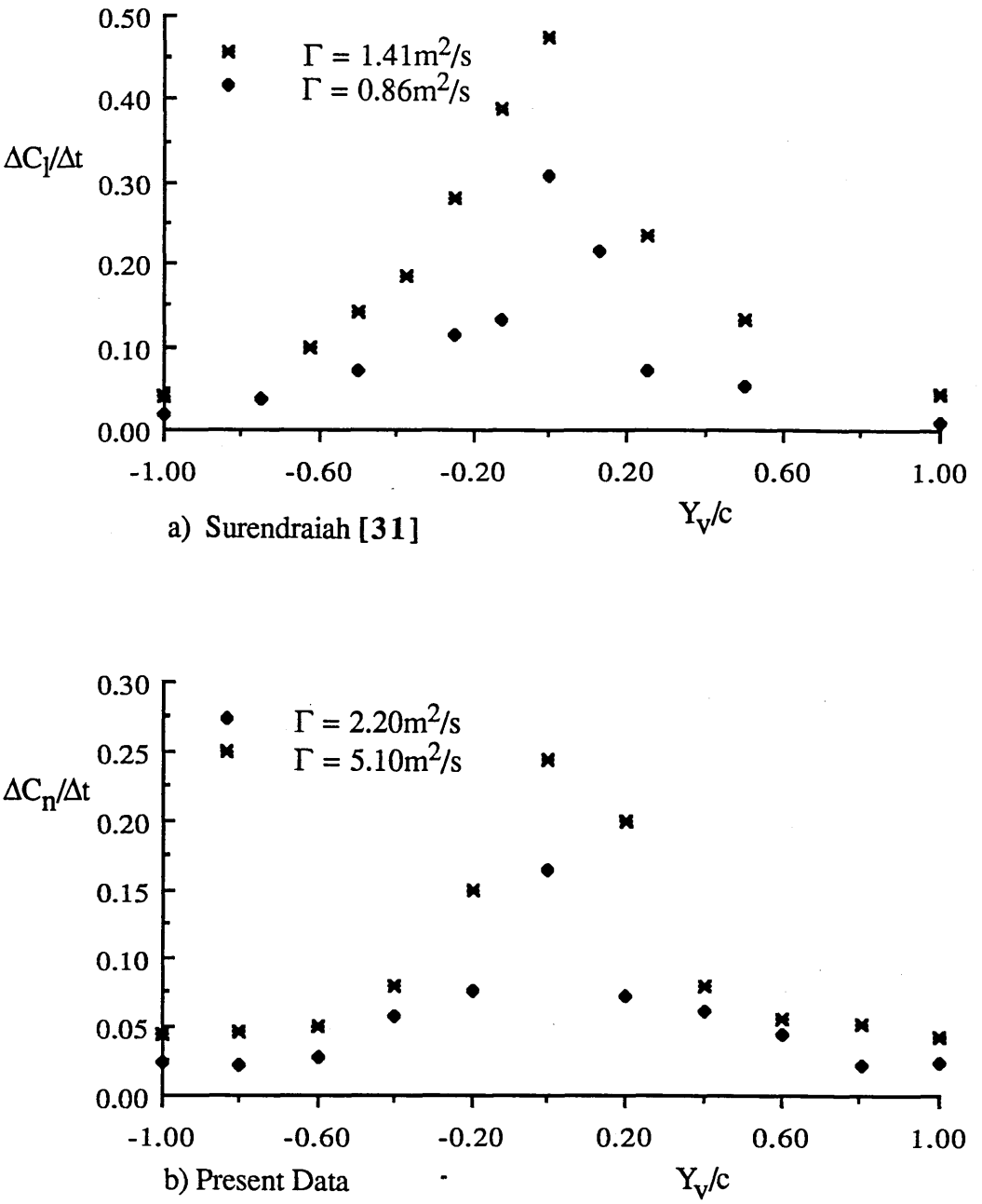

Figure 5.2.9 Comparison of Time-Rate-Changes of Maximum Lift Coefficient Difference Variations with Blade-Vortex Proximity and Vortex Strength ; a) Surendraiah **[31]** and b) Present Data

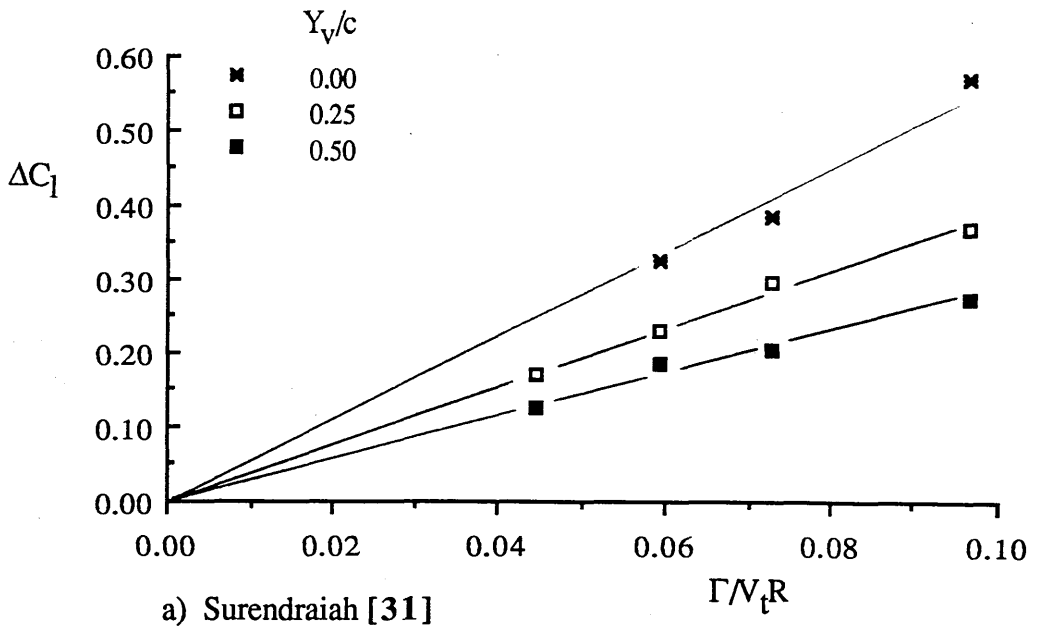

a) Surendraiah [31]

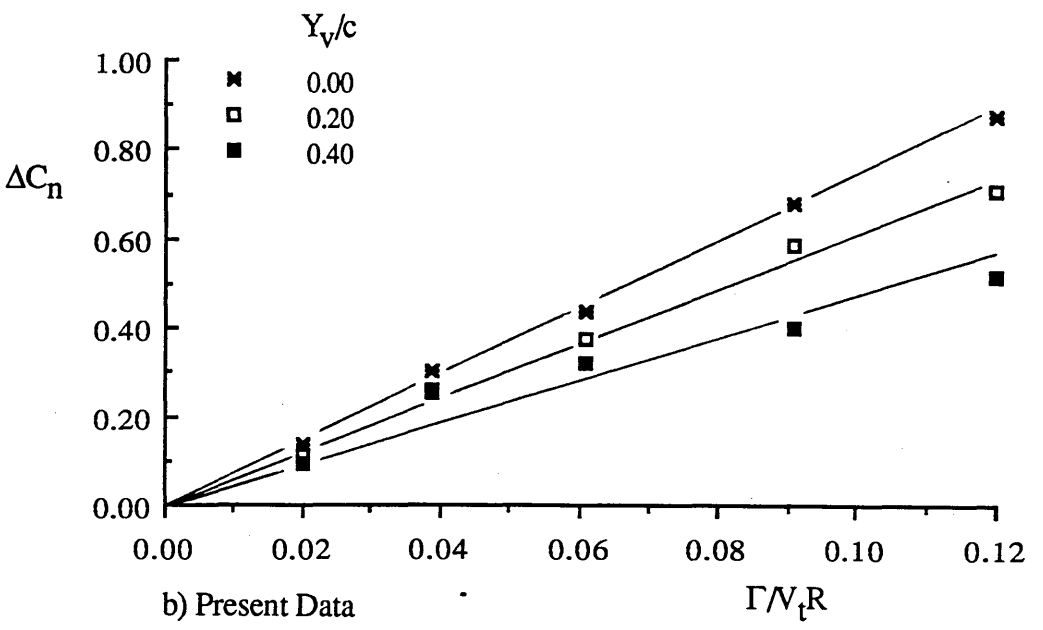

b) Present Data

Figure 5.2.10 Comparison of Maximum Lift Coefficient Difference Variations with Vortex Strength and Various Blade-Vortex Separation Distances ; a) Surendraiah [31] and b) Present Data

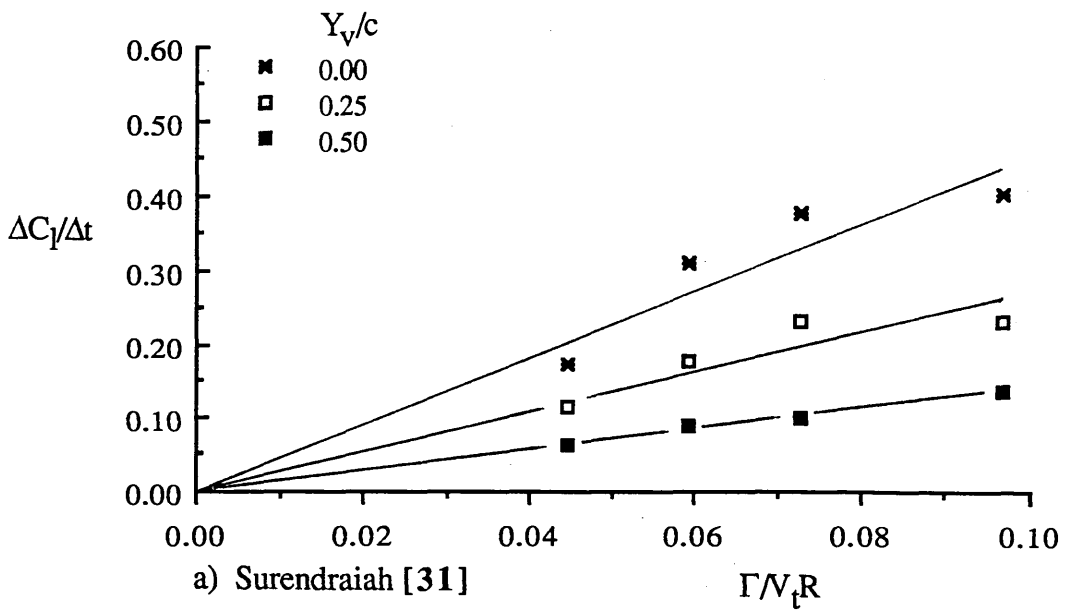

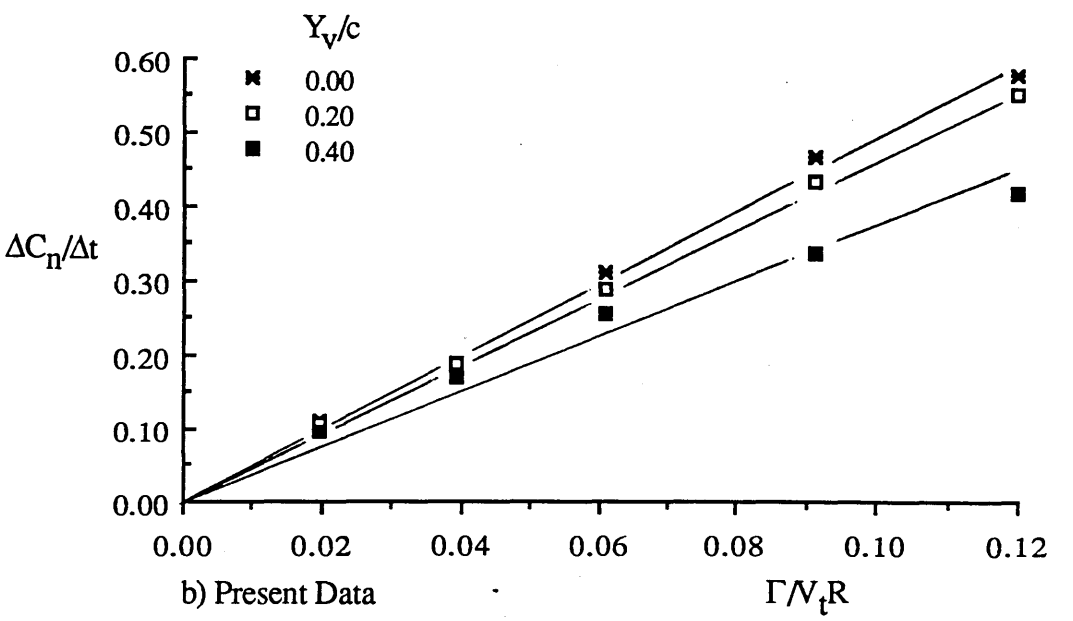

Figure 5.2.11 Comparison of Time-Rate-Changes of Maximum Lift Coefficient Difference with Vortex Strength and Various Blade-Vortex Separation Distances ; a) Surendraiah [**31**] and b) Present Data

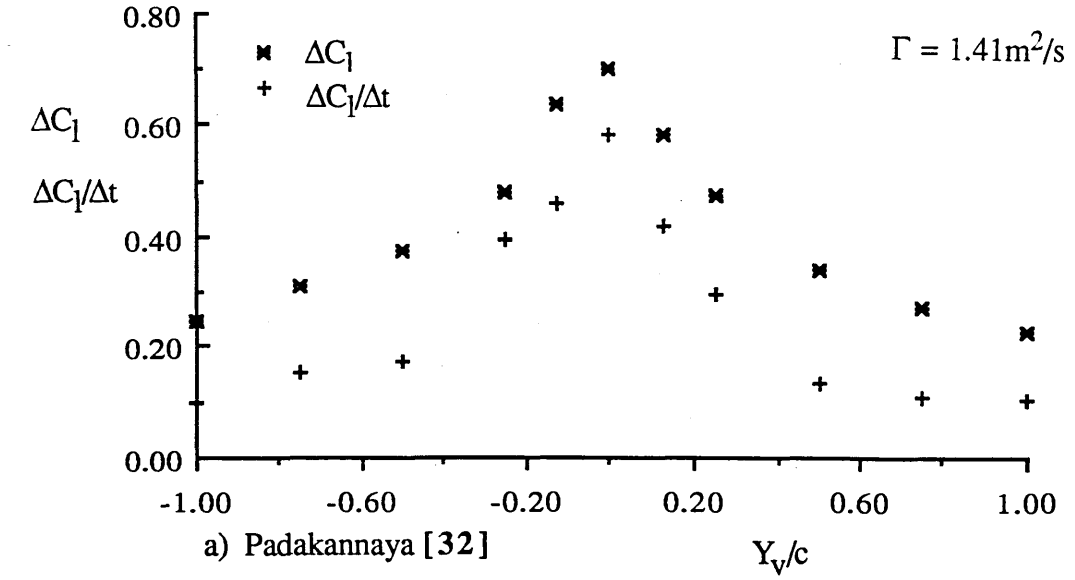

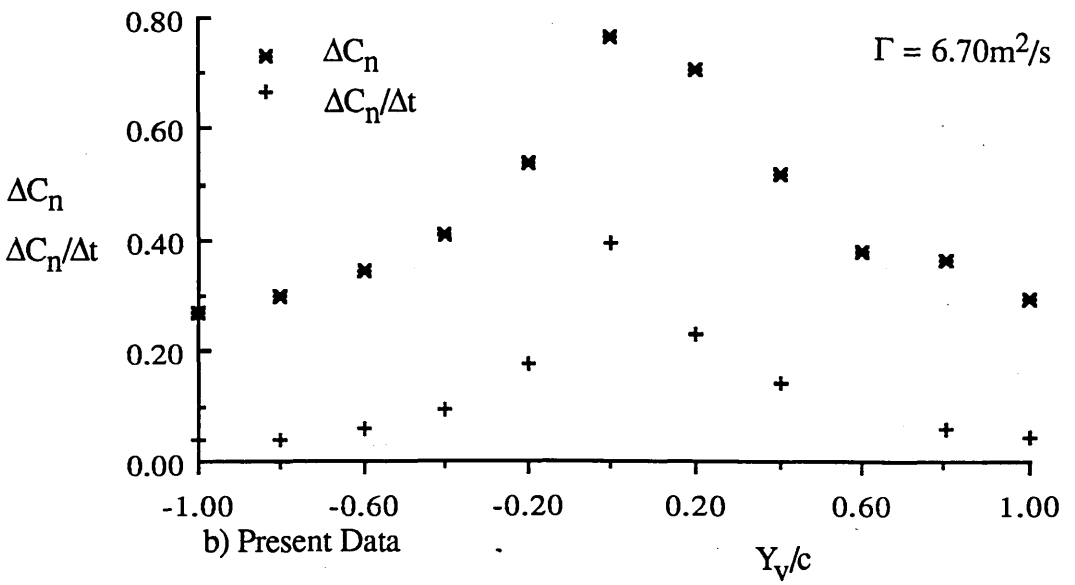

Figure 5.2.12 Comparison of ΔC_l and ΔC_n and Their Time-Rate-Changes with Blade-Vortex Proximity ; a) Padakannaya [32] and b) Present Data

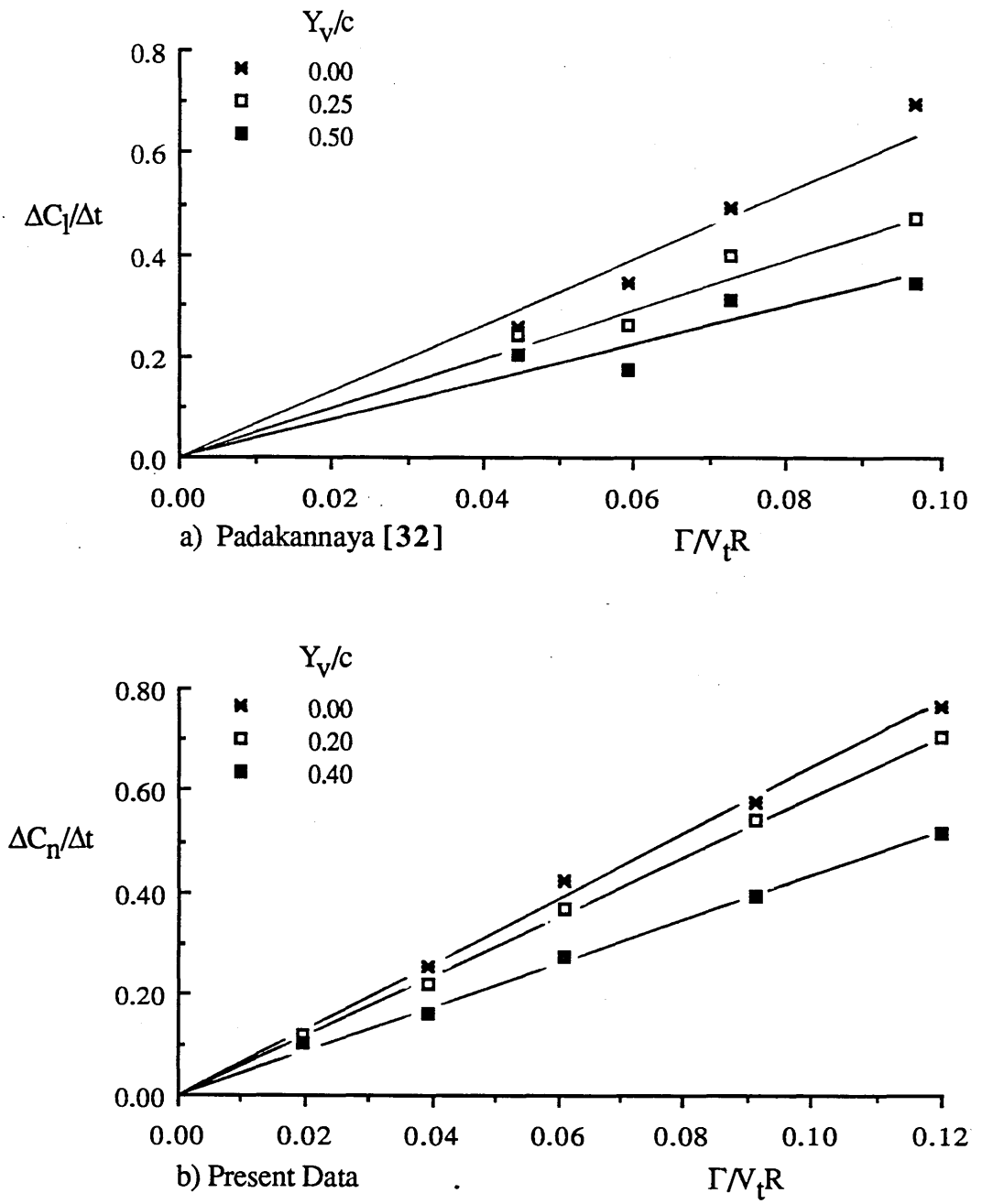

Figure 5.2.13 Comparison of Time-Rate-Changes of Maximum Lift Coefficient Difference Variations with Vortex Strength and Various Blade-Vortex Separation Distances ; a) Padakannaya [32] and b) Present Data